

CCIW
APR 10 1987

National Hydrology Research Institute

NHRI PAPER NO. 30

IWD SCIENTIFIC SERIES NO. 149

Hydraulic Characterization of a Small Ground-Water Flow System in Fractured Monzonitic Gneiss

K.G. Raven

GB
707
C335
no. 149E

NHRI

NATIONAL HYDROLOGY RESEARCH INSTITUTE
INLAND WATERS DIRECTORATE
OTTAWA, CANADA, 1986

(Disponible en français sur demande)



Environment
Canada

Environnement
Canada

National Hydrology Research Institute

NHRI PAPER NO. 30

IWD SCIENTIFIC SERIES NO. 149

Hydraulic Characterization of a Small Ground-Water Flow System in Fractured Monzonitic Gneiss

K.G. Raven

NHRI

**NATIONAL HYDROLOGY RESEARCH INSTITUTE
INLAND WATERS DIRECTORATE
OTTAWA, CANADA, 1986**

(Disponible en français sur demande)

© Minister of Supply and Services Canada 1986

Cat. No. En 36-502/149E

ISBN 0-662-14814-2

Contents

	Page
ABSTRACT	vii
RÉSUMÉ	vii
ACKNOWLEDGMENTS	ix
INTRODUCTION	1
SITE DESCRIPTION	1
Location	1
Geology	4
DRILLING PROGRAM	4
FRACTURE SYSTEM CHARACTERIZATION	7
Surface fracture mapping	7
Borehole fracture logging	7
BOREHOLE CASING INSTALLATION	13
STRADDLE-PACKER INJECTION TESTS	14
Method	14
Results	16
HYDRAULIC INTERFERENCE TESTS	17
Method	17
Results	19
Fracture zone No. 1	21
Fracture zone No. 2	28
Fracture zone No. 3	29
Fracture zone No. 4	30
Vertical flow properties of the rock mass	31
HYDRAULIC HEAD MONITORING	33
Hydraulic head distribution	33
Rock mass	33
Fracture zones Nos. 1, 2, 3 and 4	36
HYDRAULIC CONDUCTIVITY TENSOR DETERMINATIONS	38
Model description	38
Results	39
SUMMARY	42
REFERENCES	44
APPENDIX A. Fracture hydrology logs, boreholes FS-1 to FS-17	47
APPENDIX B. Straddle-packer injection test data, boreholes FS-1 to FS-17	105
APPENDIX C. Plots of drawdown versus log time, borehole FS-10	117
APPENDIX D. Hydraulic conductivity tensors	127

Tables

	Page
1. Summary of borehole length and orientation statistics	7
2. Summary of borehole collar elevation and location statistics	7
3. Mean orientation of major fracture sets identified by surface and borehole fracture mapping.	9
4. Mean orientation of major subsurface fracture sets by three subareas.	9
5. FS test interval statistics	13
6. Hydraulic properties of FS test intervals	17
7. Summary of hydraulic interference tests	20
8. Hydraulic properties of the rock mass surrounding fracture zone No. 1 determined from FS-10 pump tests using Gringarten uniform-flux fracture model	26
9. Equivalent single-fracture aperture — fracture zone No. 1	28
10. Fracture storativity — fracture zone No. 1	28
11. Equivalent single-fracture aperture — fracture zones Nos. 2 and 4	29
12. Fracture storativity — fracture zones Nos. 2 and 4	29
13. Equivalent single-fracture aperture — fracture zone No. 3	29
14. Fracture storativity — fracture zone No. 3	29
15. Vertical hydraulic diffusivity	33
16. Equilibrium hydraulic head of FS test intervals	35

Illustrations

Figure 1. Approach for investigating the ground-water flow characteristics of fractured rock.	1
Figure 2. Location map of Chalk River Nuclear Laboratories	2
Figure 3. Location map of NHRI hydrogeologic test site	3
Figure 4. Location of CRNL ground-water flow study site with respect to major and minor fracture zones and faults as identified by air photo lineament analysis and ground EM-VLF surveys	5
Figure 5. Map of CRNL ground-water flow study site	6
Figure 6. Contoured plot of poles to fractures measured in surface outcrops of CRNL ground-water flow study area.	8
Figure 7. Contoured plot of poles to fractures surveyed in FS-series boreholes using borehole television.	10
Figure 8. Contoured plot of poles to fractures logged in FS-series boreholes using borehole acoustic televiewer	11
Figure 9. Site map and fracture orientation data determined from surface and borehole mapping	12
Figure 10. Schematic of multiple-packer, multiple-standpipe casing installed in each FS-series borehole.	13
Figure 11. Schematic of surface test equipment used during straddle-packer injection tests and casing-packer withdrawal tests	15
Figure 12. Schematic of subsurface test equipment used during straddle-packer injection tests and casing-packer withdrawal tests	15
Figure 13. Schematic of straddle-packer injection test of a single fracture.	16

Illustrations (Cont.)

	Page
Figure 14. Distribution of the common logarithm of equivalent rock mass hydraulic conductivity, K_{erm} , in boreholes FS-1 to FS-17 measured with straddle-packer injection tests	17
Figure 15. Schematic of a two-borehole constant-discharge hydraulic interference test . .	18
Figure 16. Vertical cross section through centre of CRNL ground-water flow study site showing four fracture zones identified from hydraulic testing. . . .	21
Figure 17. Drawdown versus log-time response for pumping borehole and observation intervals intersecting fracture zone No. 1, FS-10 pump test, August 20-27, 1982	22
Figure 18. Drawdown versus log-time response for pumping borehole and observation intervals intersecting fracture zone No. 1, FS-10 pump test, September 27-29, 1983.	22
Figure 19. Log-drawdown versus log-time response for pumping borehole and observation intervals intersecting fracture zone No. 1, FS-10 pump test, August 20-27, 1982.	23
Figure 20. Log-drawdown versus log-time response for pumping borehole and observation intervals intersecting fracture zone No. 1, FS-10 pump test, September 27-29, 1983	24
Figure 21. Recovery response for pumping borehole FS-10 and observation interval FS 9-2 intersecting fracture zone No. 1.	24
Figure 22. Log-drawdown versus log-time response in fracture zone No. 1 during two pump tests from borehole FS-10, with best-fit type curves of the Gringarten and Ramey (1974) single horizontal, uniform-flux fracture model.	25
Figure 23. Log-drawdown versus log-time response for observation intervals intersecting fracture zone No. 1 with best-fit Theis curves, FS 7-3 pump test, October 1, 1982.	27
Figure 24. Log-drawdown versus log-time response for observation intervals intersecting fracture zone No. 1 with best-fit Theis curves, FS 8-2 pump test, October 2, 1982.	27
Figure 25. Log-drawdown versus log-time response for observation intervals intersecting fracture zone No. 1 with best-fit Theis curves, FS 9-2 pump test, October 4, 1982.	27
Figure 26. Log-drawdown versus log-time response for observation intervals intersecting fracture zone No. 1 with best-fit Theis curves, FS 10-1 pump test, October 5, 1982.	27
Figure 27. Log-drawdown versus log-time response for observation intervals intersecting fracture zone No. 2 with best-fit Theis curves, FS 4-2 pump test, August 16-19, 1982	28
Figure 28. Log-drawdown versus log-time response for observation intervals intersecting fracture zone No. 3 with best-fit Theis curves, FS 6-1 pump test, October 13-16, 1982	30
Figure 29. Log-drawdown versus log-time response for observation intervals intersecting fracture zone No. 3 with best-fit Theis curves, FS 6-1 pump test, October 27, 1983.	30
Figure 30. Log-drawdown versus log-time response for observation intervals intersecting fracture zone No. 3 with best-fit Theis curves, FS 11-2 pump test, October 27-29, 1982.	30
Figure 31. Log-drawdown versus log-time response for observation intervals intersecting fracture zone No. 3 with best-fit Theis curves, FS 15-3 pump test, October 24-26, 1983.	30

Illustrations (Cont.)

	Page
Figure 32. Drawdown versus log-time data for observation intervals in borehole FS-7 showing vertical response to pumping fracture zone No. 1 (high K zone) intersecting interval FS 7-3	32
Figure 33. Drawdown versus log-time data for observation intervals in borehole FS-3 showing vertical response to pumping fracture zone No. 1 (high K zone) located below the bottom of borehole FS-3	32
Figure 34. Hydrograph for test intervals in inclined borehole FS-2 for the period January 1982 to November 1984	34
Figure 35. Patterns of ground-water flow in fracture zone No. 2 estimated from equilibrium hydraulic head data recorded on December 15, 1982, and on November 1, 1984	37
Figure 36. Patterns of ground-water flow in fracture zone No. 3 estimated from equilibrium hydraulic head data recorded on December 15, 1982, and on November 1, 1984	37
Figure 37. Distribution of the common logarithm of effective fracture aperture, $2b_{eff}$, in boreholes FS-1 to FS-17 determined from straddle-packer injection tests and borehole acoustic televiewer logs	39
Figure 38. Hydraulic conductivity ellipsoid and reference axes in three directions	39
Figure 39. Stereographic plot of poles to K_1 , K_2 principal hydraulic conductivity planes for FS test intervals.	41
Figure 40. Plot of vertical hydraulic diffusivity determined from pump tests versus the harmonic mean of vertical hydraulic conductivity calculated from the fracture orientation-aperture model	42
Figure 41. Isometric sketch of CRNL ground-water flow study site showing the location of test boreholes, fracture zone No. 1 and diabase dyke	44
Figure 42. Isometric sketch of CRNL ground-water flow study site showing the location of test boreholes, fracture zones Nos. 2, 3 and 4, and diabase dyke.	44

Abstract

The hydraulic characteristics of a small ground-water flow system active in a block (200 m by 150 m by 50 m deep) of fractured monzonitic gneiss located at Chalk River, Ontario, have been determined from surface and borehole investigations. Surface investigations including air photo lineament analysis, ground and airborne geophysics and fracture mapping were used to define the local and regional fracture system, locate the study site, and direct the exploratory drilling program. Subsurface investigations were completed in 17 boreholes and included fracture logging, systematic straddle-packer injection testing, hydraulic interference testing, and long-term hydraulic head monitoring. The interference tests and monitoring were conducted in 90 packer-isolated test intervals created by installation of multiple-packer casings in each borehole. Hydraulic interference tests provided detailed information on the equivalent single-fracture aperture and storativity of four major (>50-m extent) fracture zones and the vertical hydraulic diffusivity of the rock mass of the study site. Fracture logs and injection test data were combined to generate a tensorial representation of hydraulic conductivity for each test interval. The results of the detailed investigations are presented and interpreted to provide a complete three-dimensional description of the ground-water flow system.

A gravity-controlled flow system occurs at the Chalk River study site. Ground-water flow in the rock is primarily vertical to a low hydraulic-head fracture zone at a depth of 33 to 50 m, with a horizontal component of flow determined by surface topography. An impermeable diabase dyke and three additional high-permeability fracture zones are important hydrogeologic features influencing flow at the study site. The results of the investigations also show that characterization of the geometric and hydraulic properties of large structural discontinuities is essential to understanding the flow of fluids in fractured rock.

Résumé

Les propriétés hydrauliques d'un petit système d'écoulement souterrain dans un bloc de gneiss monzonitique fracturé de 200 m par 150 m par 50 m de profondeur situé à Chalk River, Ontario, ont été déterminées à partir d'études en surface et de sondages. Des études en surface, notamment des analyses par photographie aérienne des arrangements structuraux, des examens géophysiques au sol et aériens et la cartographie des fractures, ont permis de déterminer le système de fractures à l'échelle locale et régionale, de connaître les caractéristiques du site étudié et d'orienter le programme de forages d'exploration. Des études de reconnaissance du sous-sol (17 trous de sondage) ont été achevées et comportaient, notamment l'obtention de diagraphies de fractures, des essais systématiques d'injection à packer double, des essais d'interférence hydraulique et la surveillance à long terme des hauteurs piézométriques. Les essais d'interférence et la surveillance ont été effectués dans 90 intervalles d'essais isolés par l'installation de tubages à packers multiples dans chacun des trous de sondage. Des essais d'interférence hydraulique ont fourni des renseignements détaillés sur l'ouverture calculée pour une seule fracture et le coefficient d'emménagement équivalents de quatre grandes zones de fractures (supérieures à 50 m), et sur la diffusivité hydraulique verticale de la masse rocheuse à l'étude. Les diagraphies de fractures et les données obtenues lors des essais d'injection ont permis de produire une représentation tensorielle de la conductivité hydraulique de chacun des intervalles soumis aux essais. Les résultats des études détaillées de reconnaissance sont présentés et interprétés afin de fournir une description tridimensionnelle complète du système d'écoulement souterrain.

Un système d'écoulement par gravité existe au site à l'étude de Chalk River. Dans la roche, l'écoulement souterrain est essentiellement vertical et atteint une zone fracturée à faible hauteur piézométrique située entre 33 et 50 m de profondeur; la composante horizontale de l'écoulement est régie par la topographie de la surface. Un dyke imperméable de diabase et trois autres zones fracturées à grande perméabilité sont des caractéristiques hydrogéologiques importantes qui influent sur l'écoulement dans le site à l'étude. Les résultats des études de reconnaissance montrent également qu'il est essentiel de déterminer les propriétés géométriques et hydrauliques des grandes discontinuités structurales afin de connaître l'écoulement des liquides dans des roches fracturées.

Acknowledgments

The author would like to acknowledge the able field assistance provided by C. Burge, B. Hannah, P. Kornelsen, B. Kueper, P. Lapcevic, C. Mangione, W. Stensrud and A. Vorauer in completing the hydraulic testing, casing installation and hydraulic head monitoring programs. Special thanks are extended to J.A. Smedley and R. A. Sweezey who supervised most of the field activities. The technical, mechanical and electrical support of the Chalk River Nuclear Laboratories shops is greatly appreciated. J.S.O. Lau, J.G. Bisson and F. Auger of the Geological Survey of Canada completed borehole television surveys and borehole acoustic televiewer logs.

This work was supported by funds provided by Atomic Energy of Canada Limited, Pinawa, Manitoba, as part of the Canadian Nuclear Fuel Waste Management Program. Earlier drafts of this report benefited from suggestions and review provided by A. Rouleau and K.S. Novakowski of the National Hydrology Research Institute, Environment Canada.

Hydraulic Characterization of a Small Ground-Water Flow System in Fractured Monzonitic Gneiss

K.G. Raven

INTRODUCTION

This report describes the results of borehole investigations completed on the property of the Chalk River Nuclear Laboratories (CRNL) to define the physical hydrogeology of a small ground-water flow system in fractured monzonitic gneiss. The work contained in this report forms part of a broad research project supported by Atomic Energy of Canada Limited (AECL) and the National Hydrology Research Institute (NHRI) of Environment Canada to study ground-water flow in shallow fractured rock. The activities in this report were completed in the period 1981 to 1983. Some of the 1981 research activities are also found in Raven and Smedley (1982).

Activities completed as part of the CRNL ground-water flow study include the collection and interpretation

of surface and borehole geological, geophysical and hydrogeological data; geomechanical studies; and numerical ground-water flow simulation. The approach adopted in this study to combine these various investigations (Raven *et al.*, 1985) is shown in Figure 1. The central components of the approach include development of a geological-structural model to guide hydrogeological investigations and a mathematical flow model to integrate hydrogeological data. In reference to Figure 1, this report includes the results of (1) borehole and surface fracture geometry characterization studies; (2) hydraulic tests for the measurement of hydraulic conductivity (K_{ij}), specific storage (S_s) and natural ground-water flow and pressure boundaries; and (3) hydraulic head monitoring.

The data assembled in this report provide a detailed description of the fluid flow properties and hydraulic boundaries of a block of fractured monzonitic gneiss measuring 200 m by 150 m by 50 m deep. Hydraulic conductivity tensors and both steady-state and transient (from long-term pump tests) hydraulic head data for 90 packer-isolated test intervals in 17 boreholes are reported. In addition to information on the fundamental nature of flow systems in fractured rock, the CRNL ground-water flow study site provides a relatively complete three-dimensional data set for the comparison and validation of numerical ground-water flow codes under both steady-state and transient conditions.

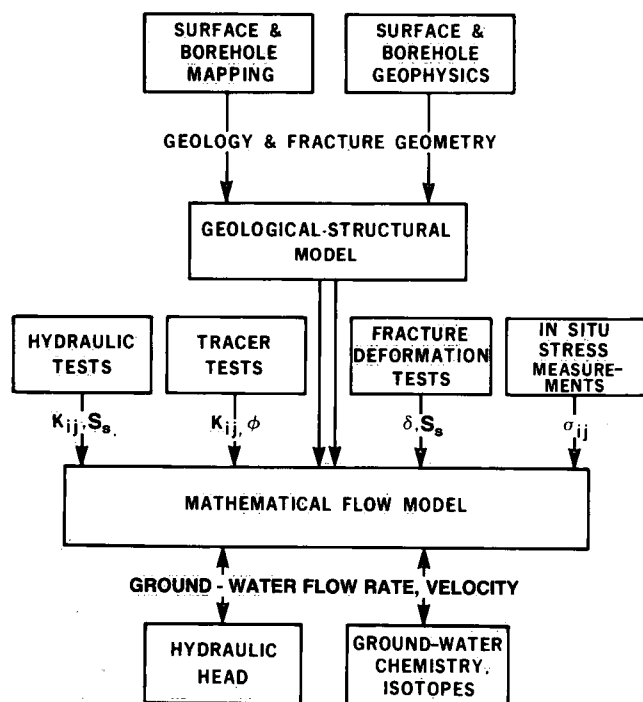


Figure 1. Approach for investigating the ground-water flow characteristics of fractured rock.

SITE DESCRIPTION

Location

The study site is located on the property of the Chalk River Nuclear Laboratories of Atomic Energy of Canada Limited, 200 km northwest of Ottawa, Ontario, near the town of Chalk River (Fig. 2). Since 1978, the National Hydrology Research Institute has developed several test sites on the CRNL property in the general area bounded by Maskinonge, Upper Bass and Lower Bass lakes. The CRNL ground-water flow study site is located on the eastern side of Maskinonge Lake in the upper half of the rectangular area identified as the NHRI hydrogeologic test site in Figure 3.

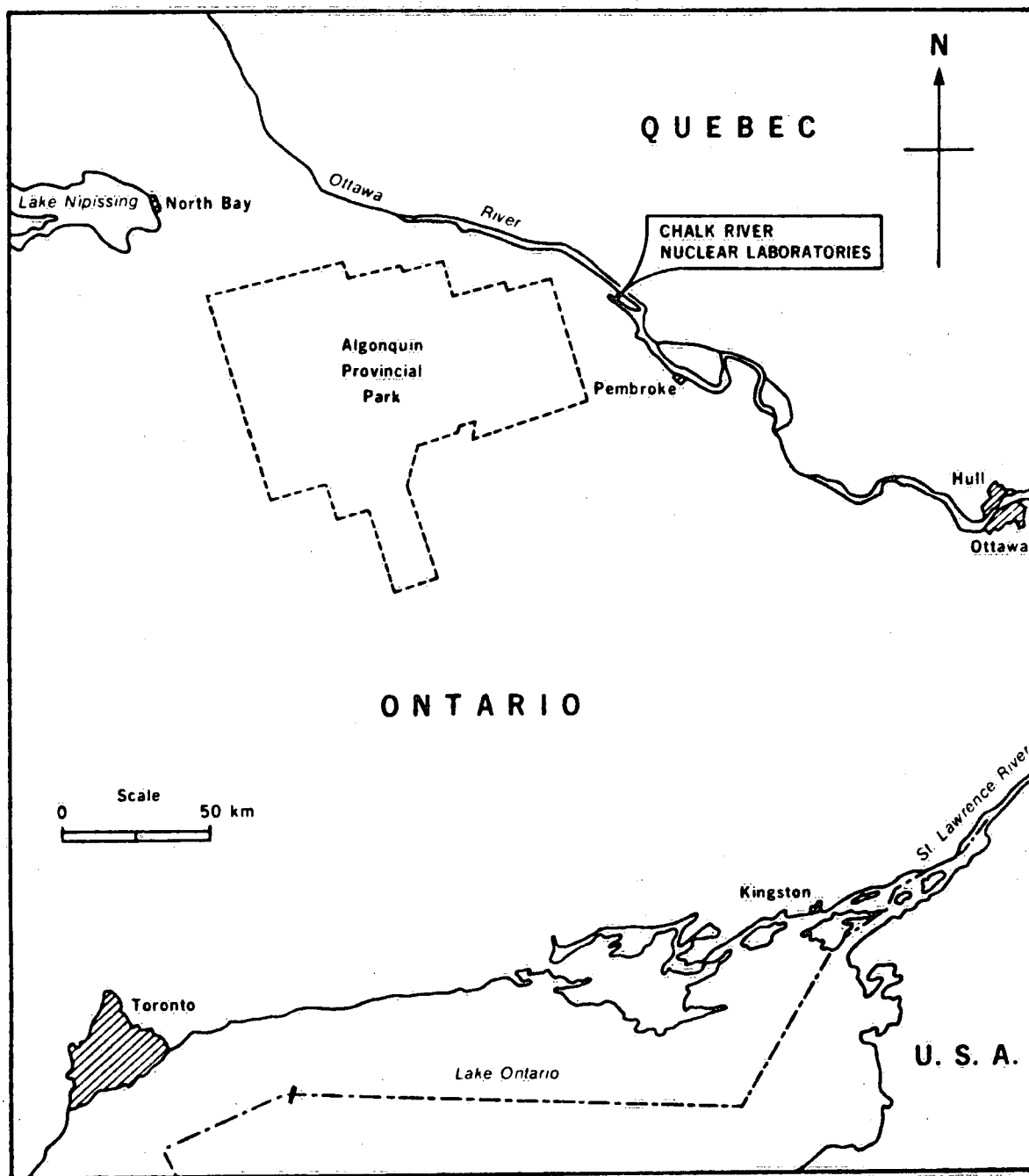


Figure 2. Location map of Chalk River Nuclear Laboratories.

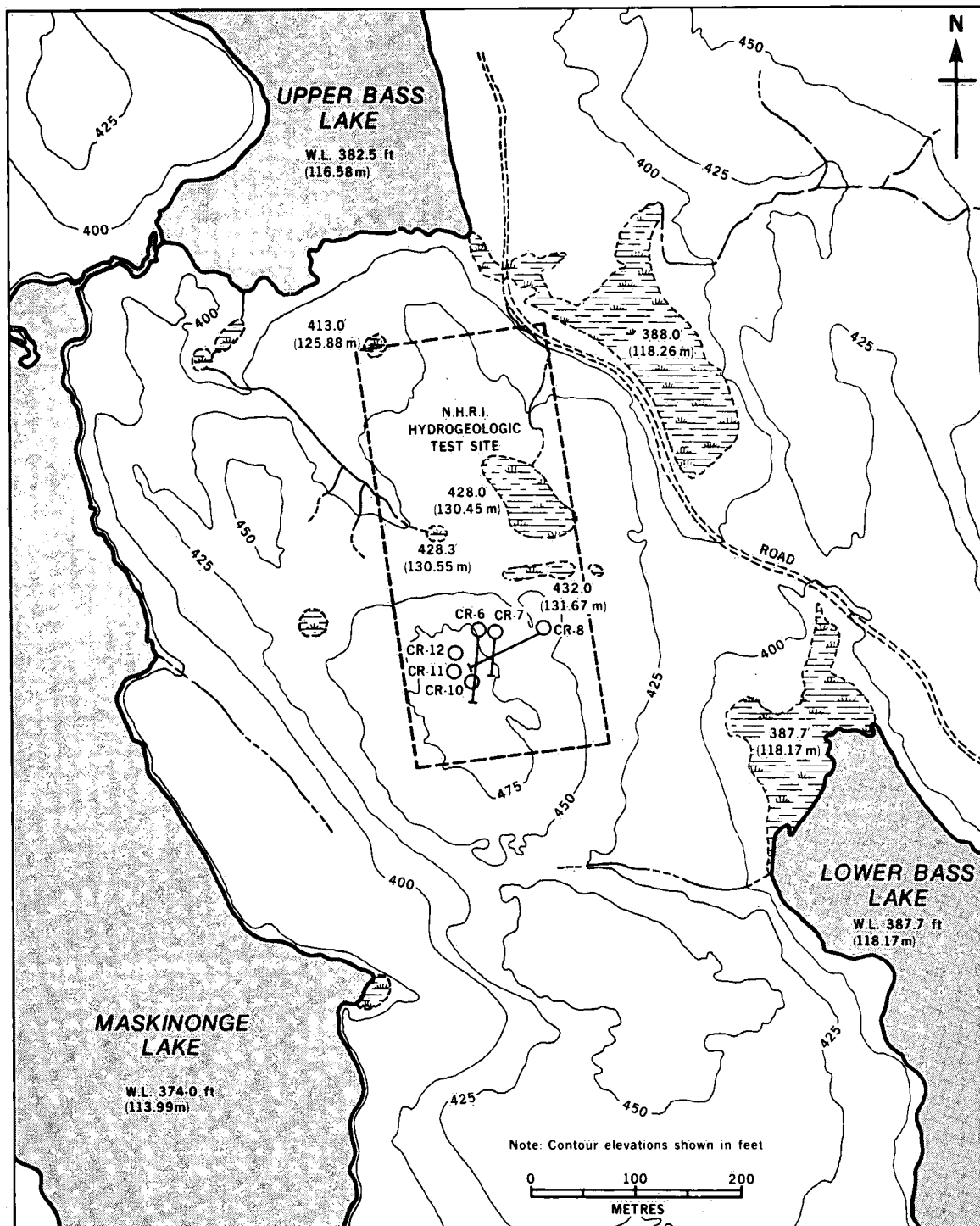


Figure 3. Location map of NHRI hydrogeologic test site. The CRNL ground-water flow study site is located in the upper half of the NHRI hydrogeologic test site.

Geology

The geology of the Chalk River area has been studied in detail by several workers (Lumbers, 1974; Brown and Thivierge, 1977; Brown and Rey, 1984). The area is both lithologically heterogeneous and structurally complex. The Chalk River area is underlain by rocks of the Grenville Province of the Canadian Shield and is situated within the Ottawa-Bonnechere graben system, a major fault zone striking northwesterly across the region. The main rock unit is a folded sheet of quartz monzonite, which is overlain and underlain by paragneiss and numerous inclusions of metagabbro, diabase and pegmatite. The early tectonic-metamorphic history includes polyphase deformation culminating in the formation of large-scale recumbent antiformal-synformal structures (Brown and Rey, 1984) and a highly complex fracture system. Faults and fracture zones from the centimetre to kilometre scales transect the Chalk River area.

The study site was selected on the basis of the results of air photo lineament analysis and surface and airborne EM (electromagnetic) surveys (Dence and Scott, 1980; Scott, 1984; Sinha and Hayles, 1984). These surveys were used to locate a 200-m by 150-m area of relatively uniform fracturing and presumably uniform subsurface fluid flow properties. Figure 4 shows the location of the selected site with respect to major and minor fracture zones and faults as identified by air photo lineament analysis (Raven and Smedley, 1982) and ground EM-VLF (very low frequency) surveys (Dence and Scott, 1980). The most notable structural feature in the vicinity of the study site strikes east-west, bisects the NHRI hydrogeologic test site, and forms the southern boundary of the CRNL ground-water flow study site. Two minor air photo lineaments trend northwesterly and intersect the northwest and southwest corners of the study site. A minor conductive zone identified by EM-VLF surveys transects the northwest corner of the study site. Identification of these large-scale structural features intersecting or bordering the study site is important, as these structures are likely to control the development of ground-water flow systems by acting as either constant pressure boundaries owing to enhanced permeability or impermeable boundaries as a result of reduced permeability.

The area selected for study is a well-exposed upthrown rock mass bounded on three and possibly four sides by faults or major fracture zones. The study area is presented in detail in Figure 5, which shows ground elevation and the location of boreholes, outcrops and surface water bodies. Bedrock exposure represents approximately 20% to 30% of the surface area. Local outcrops are composed of foliated granitic and monzonitic gneisses with

numerous pegmatite dykes and stringers. Local gneissosity reflects regional trends at $315^{\circ}/30^{\circ}$ NE, although outcrops in the southern end of the study area show more east-west strikes, possibly reflecting the major east-west trending structural fracture discussed above. A thin veneer of clean, medium-grained sand covers the remaining 70% of the site, generally thickening to a maximum of 1 to 3 m in the northwest.

DRILLING PROGRAM

Seventeen boreholes (FS-series) were drilled at the study site in the period 1981 to 1983. The average depths of the boreholes are 45 to 50 m. In May 1981, nine 155-mm diameter boreholes (FS-1 to 9) were drilled using air-percussion or downhole-hammer drilling techniques. Boreholes were drilled with air to prevent contamination of formation waters with drilling fluids. A polyvinyl chloride surface casing was grouted approximately 3 m into the bedrock for each air-percussion borehole. In May 1982, one borehole (FS-7) was deepened and five additional 155-mm diameter boreholes (FS-10 to 14) were air-percussion drilled. In June 1983, three HQ-size boreholes (FS-15 to 17) were diamond cored to provide detailed lithologic information and overcore stress measurements for the study site.

Both vertical and inclined boreholes were drilled. Boreholes FS-7, 8, 9, 12, 13, 14 and 17 were targeted to intersect major structural discontinuities. Boreholes FS-2, 8, 9 and 11 were inclined normal to the strike of the major joint sets identified from surface mapping (see section on "Surface Fracture Mapping"). Average borehole spacing is about 30 m. The location of the boreholes is shown in Figure 5. A summary of borehole length and orientation statistics is given in Table 1. Borehole collar elevations and locations determined from field surveys are listed in Table 2.

Lithology logs for each borehole were assembled from the recovered core and from chip samples collected during the air-percussion drilling process. These lithology logs are incorporated on fracture hydrology logs presented in Appendix A. Based on these logs the subsurface lithology of the site is characterized by a garnetiferous quartz-monzonitic gneiss with numerous lenses of pegmatite and metagabbro. A 5- to 10-m thick diabase dyke occupies the east-west striking lineament that forms the southern boundary of the study site.

Prior to geophysical logging and hydraulic testing, each air-percussion borehole was developed and cleaned using air flushing, pumping and brushing. Diamond drilled boreholes were developed with repeated pumping using a submersible electric pump.

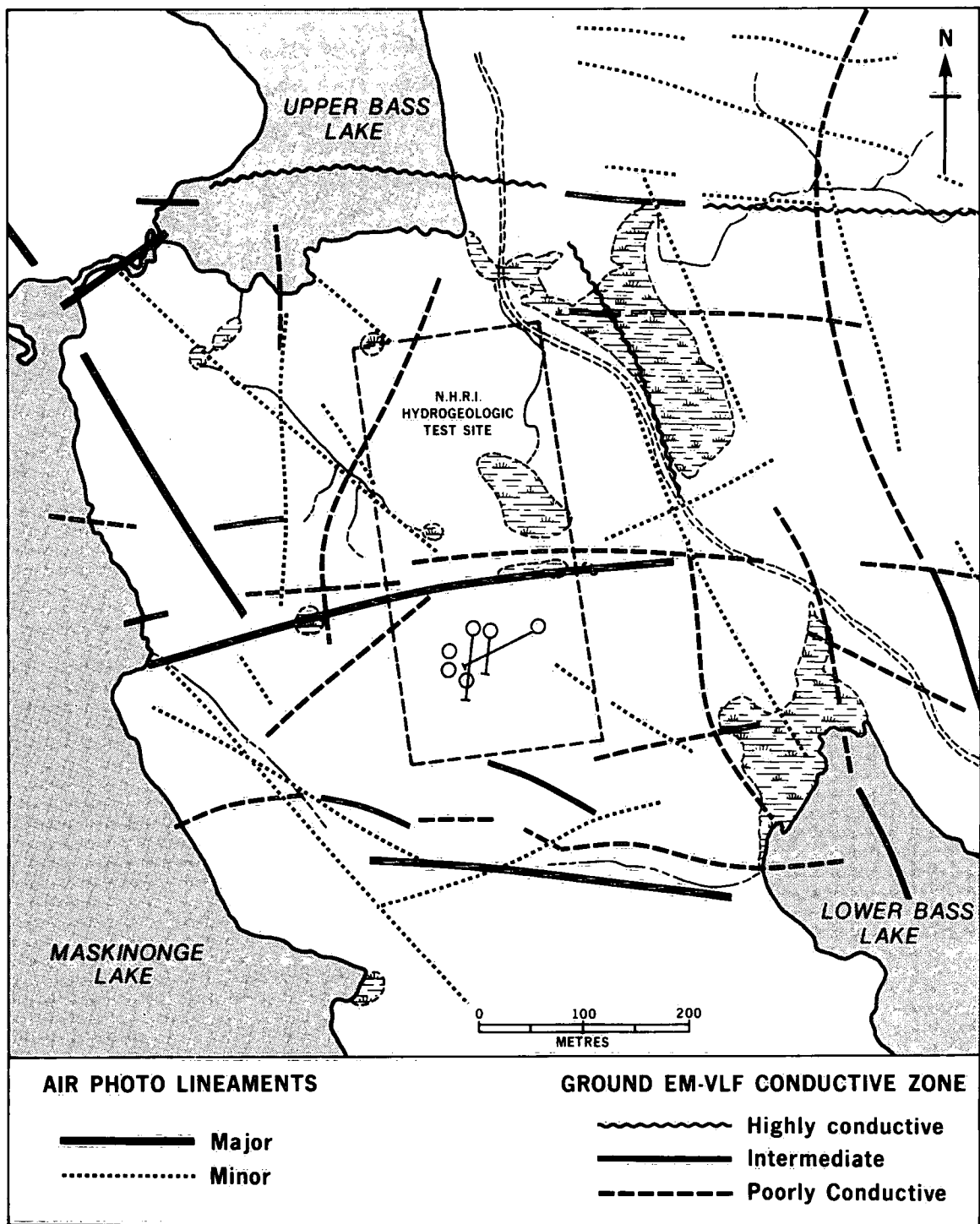


Figure 4. Location of CRNL ground-water flow study site with respect to major and minor fracture zones and faults as identified by air photo lineament analysis and ground EM-VLF surveys.

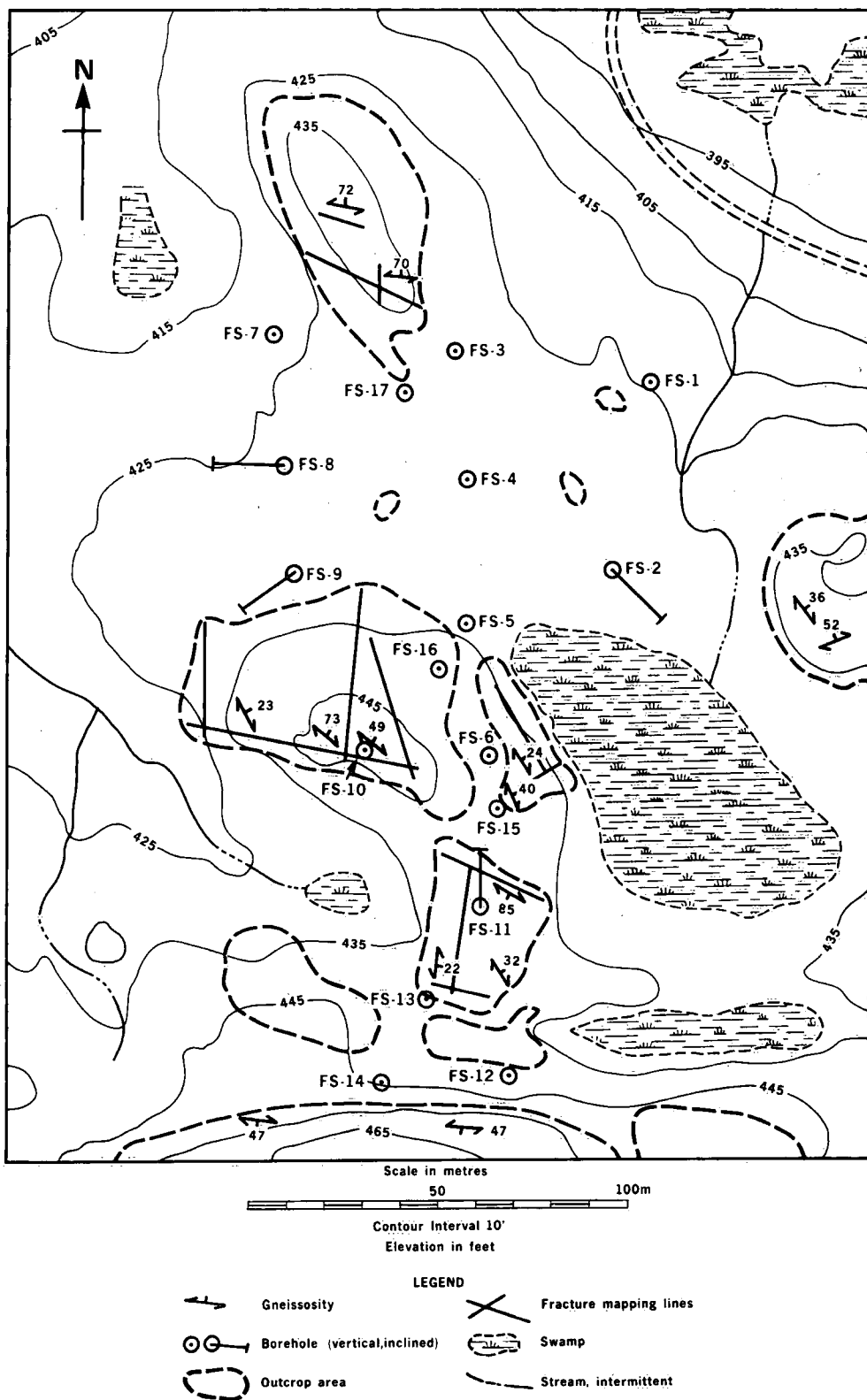


Figure 5. Map of CRNL ground-water flow study site.

Table 1. Summary of Borehole Length and Orientation Statistics

Borehole	Drilling method	Length (m B.C.T.*)	Orientation
FS-1	AP†	43.26	Vertical
FS-2	AP	43.60	130°/65°
FS-3	AP	41.50	Vertical
FS-4	AP	42.50	Vertical
FS-5	AP	41.60	Vertical
FS-6	AP	41.60	Vertical
FS-7	AP	74.15	Vertical
FS-8	AP	41.86	276°/70°
FS-9	AP	42.18	236°/70°
FS-10	AP	48.25	Vertical
FS-11	AP	43.53	0°/69°
FS-12	AP	43.50	Vertical
FS-13	AP	43.30	Vertical
FS-14	AP	42.13	Vertical
FS-15	DC‡	48.51	Vertical
FS-16	DC	50.34	Vertical
FS-17	DC	60.75	Vertical

*Below casing top.

†Denotes 155-mm diameter air percussion drilled.

‡Denotes HQ-size diamond core drilled.

Table 2. Summary of Borehole Collar Elevation and Location Statistics

Borehole	Collar elevation* (m.a.s.l.)	Collar location†	
		Northing	Westing
FS-1	130.03	1114.54	4857.09
FS-2	131.82	1070.36	4885.72
FS-3	131.22	1144.52	4900.63
FS-4	132.48	1109.32	4911.95
FS-5	132.63	1077.28	4928.21
FS-6	134.54	1038.89	4935.39
FS-7	129.48	1164.09	4945.66
FS-8	130.61	1130.50	4958.48
FS-9	132.74	1102.26	4967.31
FS-10	137.34	1054.38	4964.52
FS-11	135.22	1002.62	4954.37
FS-12	135.01	958.29	4965.77
FS-13	134.78	984.74	4977.23
FS-14	135.90	970.55	4997.21
FS-15	134.23	1026.19	4936.05
FS-16	133.99	1067.12	4938.86
FS-17	133.00	1135.80	4916.34

*Denotes elevation of low point on top of surface casing.

†Locations are relative to CRNL plant co-ordinates which are rotated 22° counterclockwise from true north.

FRACTURE SYSTEM CHARACTERIZATION

The fluid flow properties of fractured crystalline rock are generally controlled by a system of interconnected and discontinuous fractures. Detailed knowledge of the hydraulic and geometric properties of such discontinuous fracture systems is required to understand the patterns of fluid and solute movement in fractured rock. The hydraulic proper-

ties of fractures are usually expressed as an equivalent hydraulic opening or aperture, while the geometric properties of fractures include orientation, spacing and size. Data on the hydraulic and geometric properties of fractures may be integrated to describe the fluid flow properties of a rock mass using either deterministic (Snow, 1965) or statistical (Rouleau, 1984) methods. In this report (see section on "Hydraulic Conductivity Tensor Determinations"), data on fracture location, orientation and aperture have been combined using the deterministic approach of Snow (1965).

The geometry of the fracture system at the study site was investigated using surface mapping and borehole logging techniques.

Surface Fracture Mapping

Scan-line surveys were used to map the fracture system in outcrops at the study site. The location of these scan lines is shown on Figure 5. Fracture location, orientation, trace length, termination index (Priest and Hudson, 1981), and infilling characteristics were recorded for each fracture mapped in surface outcrops. Fractures with trace lengths less than 1.0 m were not mapped.

Fracture orientation data were plotted as poles to fracture planes and contoured on a lower-hemisphere equal-area projection to identify pole clusters or fracture sets. The resultant plot corrected for sampling orientation bias using the Terzaghi (1965) technique is shown in Figure 6. The contour diagram indicates the existence of three major fracture sets. In order of decreasing fracture density, the mean orientations of the sets determined from visual inspection are 105°/75° S, 235°/70° N and 150°/90°. The relative strengths of these fracture sets vary spatially in the study area outcrops, indicating statistically nonhomogeneous fracture characteristics at the scale of the study site (about 150 to 200 m). The dominant 105°/75° S fracture set is strongest in the most southerly outcrops proximal to the major east-west striking diabase dyke discussed previously and diminishes to a secondary set in the most northerly outcrop. Conversely, the 235°/70° N fracture set is dominant in the northern outcrop and diminishes significantly to the south. The 150°/90° fracture set maintains relatively uniform expression in all surface outcrops.

Borehole Fracture Logging

Borehole television surveys (Lau, 1980) and acoustic televiwer logging (Zemanek *et al.*, 1969) were carried out by the Geological Survey of Canada (Lau *et al.*, 1984) to map the subsurface fracture system intersecting each borehole. Fracture and vein orientation, location and character were identified in both borehole surveys. All boreholes were

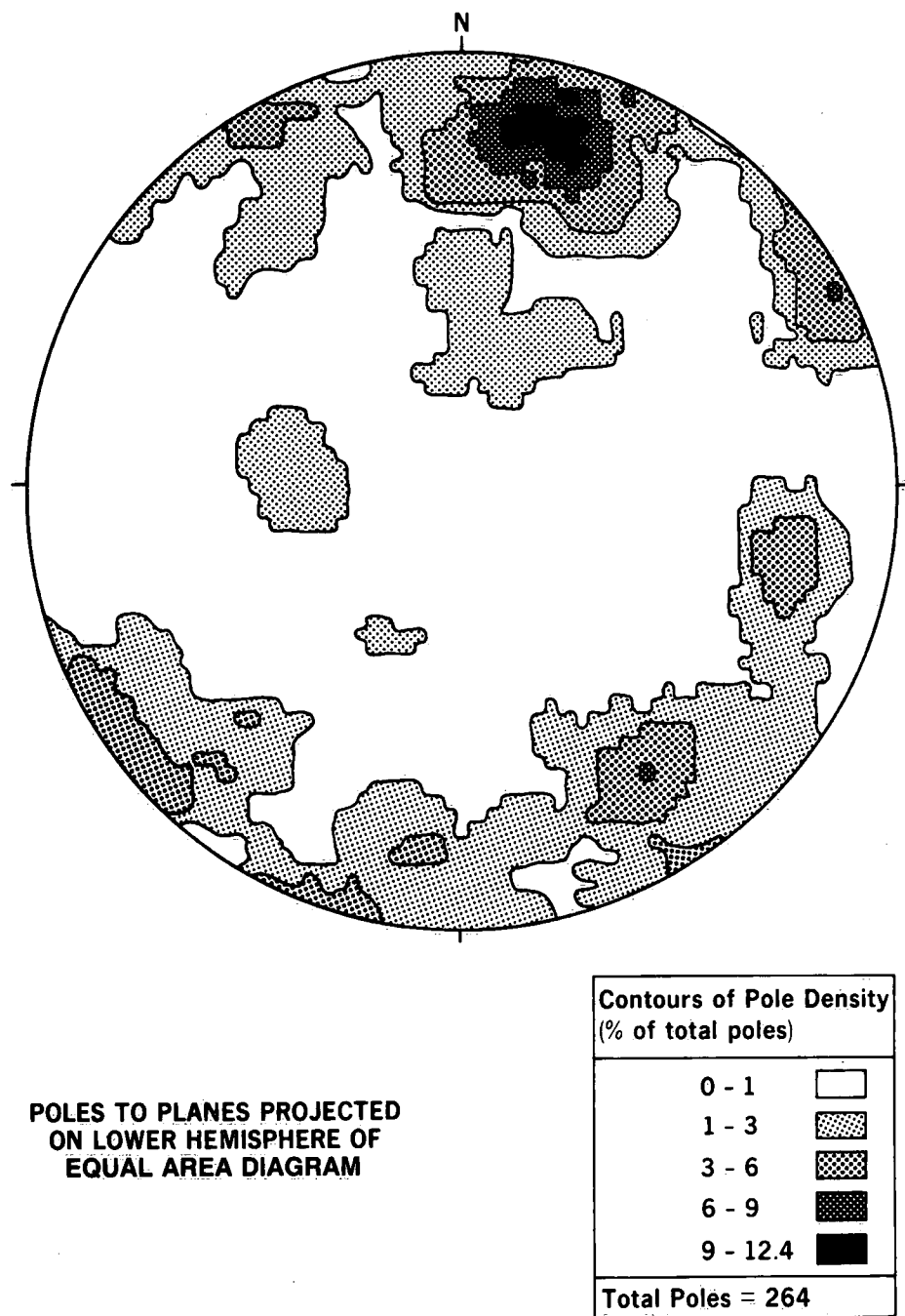


Figure 6. Contoured plot of poles to fractures measured in surface outcrops of CRNL ground-water flow study area.

surveyed using borehole television. Acoustic televiewer logging was completed in all boreholes except boreholes FS-15 and 16. The results of these surveys are included in fracture hydrology logs in Appendix A. Fractures and veins identified by borehole television have been plotted on the fracture hydrology logs as a straight line connecting the high and low points of the elliptical borehole wall trace. Acoustic televiewer fracture and vein logs have been schematically represented on the fracture hydrology logs as they appeared on 360° photographs of the borehole wall over 0.5-m intervals.

Orientation data from the fractures intersecting each borehole have been combined, plotted and contoured using the method described for surface fracture analysis. Figures 7 and 8 show the contoured polar plots for fractures identified by borehole television surveys and borehole acoustic televiewer logging, respectively. Fracture orientations measured within the highly fractured diabase dyke intersected by the top half of borehole FS-12 and the entire length of borehole FS-14 are excluded from both figures; indeed, these data were unreliable because of poor fracture definition and detection. The plot of acoustic televiewer data (Fig. 8) includes fracture orientation data for boreholes FS-15 and 16 measured by borehole television surveys.

The contoured polar plots from both borehole fracture mapping methods indicate the occurrence of similar subsurface fracture sets. The mean orientations of the major surface and subsurface fracture sets are listed in Table 3, in order of relative strength, decreasing from left to right. At the site scale, the surface fracture mapping identified all steeply dipping fracture sets. The relative

strengths of the two dominant fracture sets, however, were reversed between surface and subsurface mapping. This reversal reflects the spatial variation in fracture orientation and the bias of surface outcrops to the southern and central areas of the study site.

Spatial variability of subsurface fracturing was also investigated by grouping fracture orientation data into three subareas: northern, including data from boreholes FS-1, 2, 3, 4, 7 and 17; central, with data from boreholes FS-5, 6, 8, 9, 10 and 16; and southern, with data from boreholes FS-11, 12, 13 and 15. For this comparison we selected fracture orientation data determined from borehole acoustic televiewer logging. This data source was preferred to data from borehole television surveys because of the superior ability of the acoustic televiewer logs to identify fractures within hydrogeologically important mafic layers. The resulting contoured polar diagrams and the tabular listing of the major subsurface fracture sets are shown in Figure 9 and Table 4 for each of the three subareas of the study site. Figure 9 also shows the location of three major structural discontinuities that intersect the study site. The fracture orientation data in Figure 9 show a relative increase from north to south in the strength of the fracture set oriented at 240° to 260°/75° N and a relative decrease in the strength of the 150°/90° fracture set. The 105°/80° S fracture set shows relatively uniform expression in all three subareas. The relative strengths of the subsurface fracture sets reflect, among other geologic factors, the proximity of the boreholes to major structural features. The observed spatial variation in fracturing suggests that the fluid flow properties of the rock mass will also show significant spatial variability or heterogeneity. Because this variability in fluid

Table 3. Mean Orientation of Major Fracture Sets Identified by Surface and Borehole Fracture Mapping

Fracture detection method		Mean orientation of major fracture sets		
Surface fracture mapping	105°/70° S	235°/70° N	150°/90°	—
Borehole acoustic televiewer	250°/70° N	105°/75° S	145°/90°	Subhorizontal
Borehole television	250°/70° N	100°/65° S	145°/90°	Subhorizontal

Table 4. Mean Orientation of Major Subsurface Fracture Sets by Three Subareas

Subarea and boreholes		Mean orientation of major fracture sets		
North				
FS-1,2,3,4,7,17	105°/80° S	Subhorizontal	145°/90°	255°/80° N
Centre				
FS-5,6,8,9,10,16	105°/80° S	260°/80° N	250°/65° N	Subhorizontal 150°/90°
South				
FS-11,12,13,15	240°/75° N	105°/75° S	200°/80° N	Subhorizontal

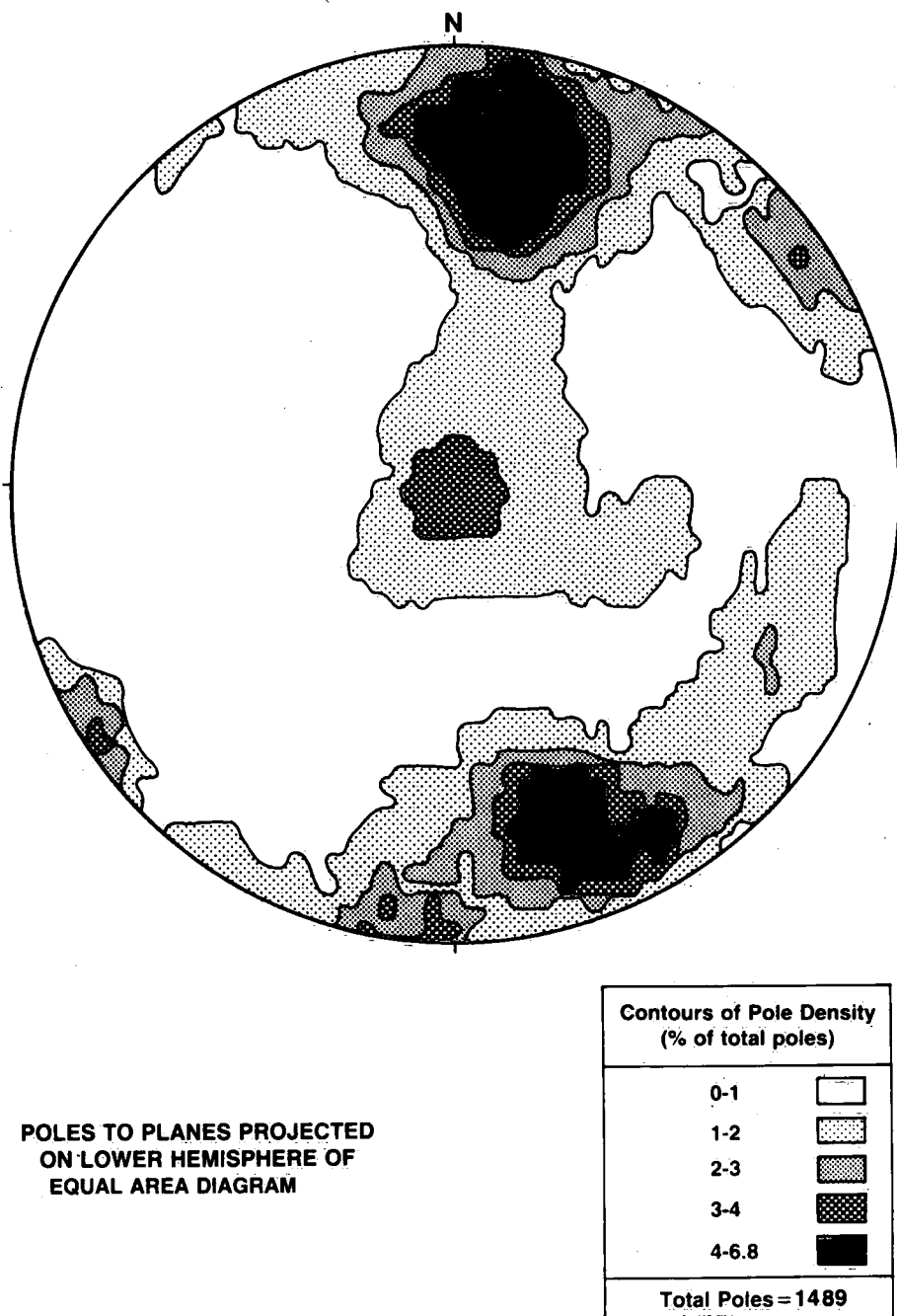
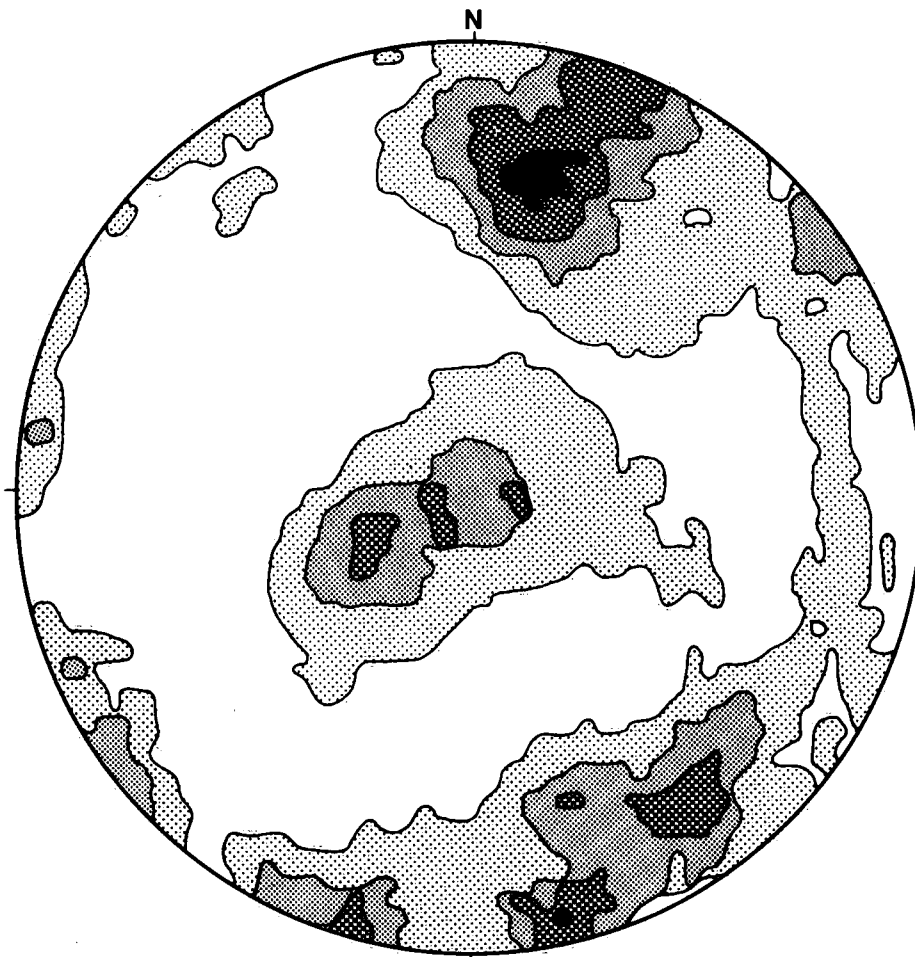


Figure 7. Contoured plot of poles to fractures surveyed in FS-series boreholes using borehole television.



POLES TO PLANES PROJECTED
ON LOWER HEMISPHERE OF
EQUAL AREA DIAGRAM

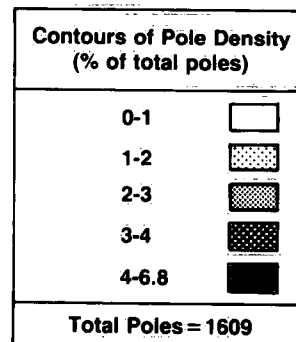


Figure 8. Contoured plot of poles to fractures logged in FS-series boreholes using borehole acoustic televiewer.

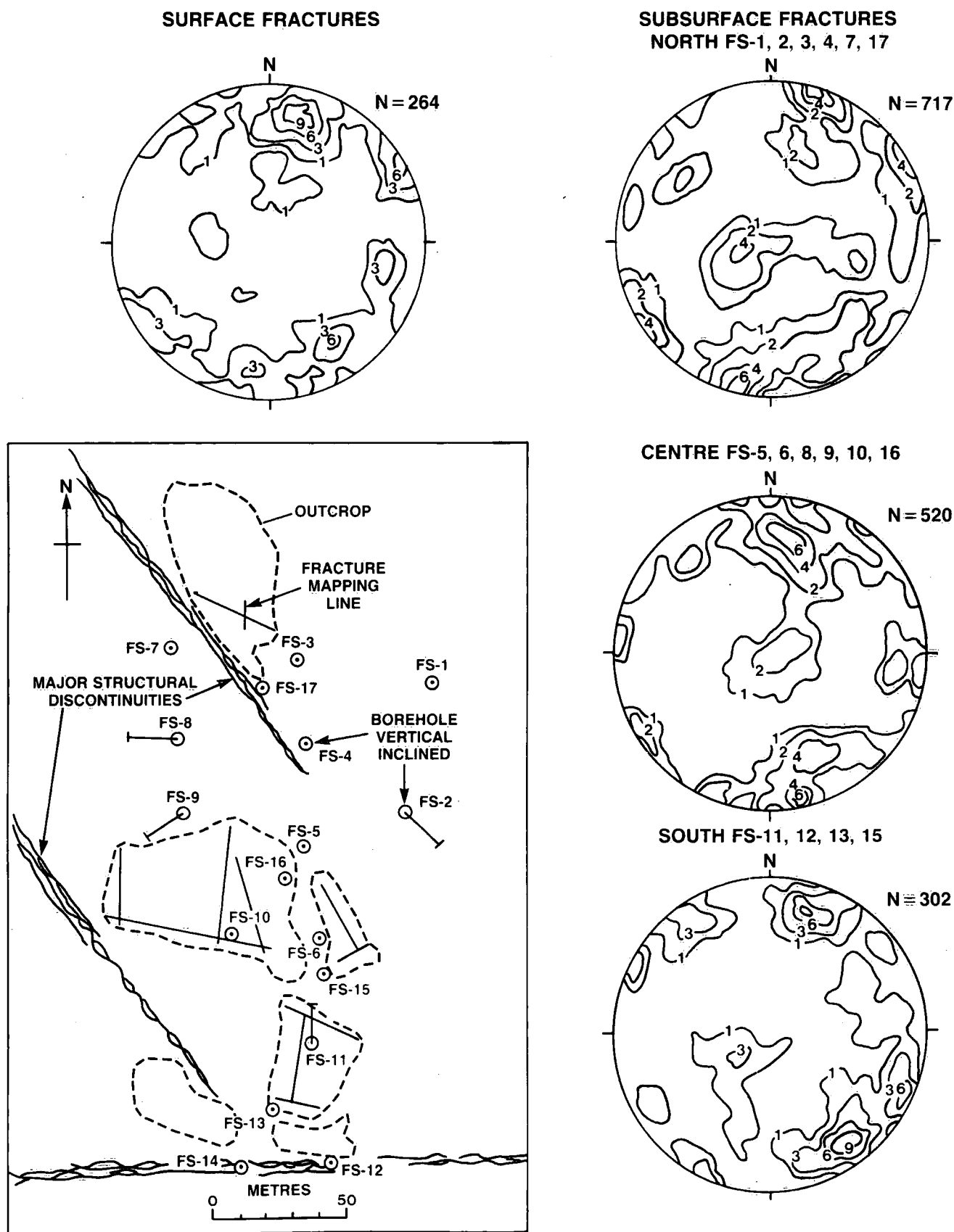


Figure 9. Site map and fracture orientation data determined from surface and borehole mapping. Stereographic plots show contours of poles to fractures in 1% surface area of lower-hemisphere equal-area projections.

flow properties will, in part, be related to the presence or absence of major structural discontinuities, definition of such discontinuities will be critical to the characterization of a rock mass for detailed hydrogeologic evaluation.

BOREHOLE CASING INSTALLATION

Each borehole was completed with a multiple-packer, multiple-standpipe casing to provide long-term access to hydraulically isolated test intervals. The casing system designed by NHRI, described by Raven and Smedley (1982) and shown schematically in Figure 10, provides simultaneous and continuous access to five to seven packer-isolated test intervals in each borehole. Each test interval is accessed by either 25-mm diameter polyvinyl chloride standpipes or 13-mm diameter nylon tubing. Air-inflated reinforced packers provide hydraulic seals in each borehole. Each packer is pressurized with air from surface using individual inflation lines. Monitoring of packer-inflation pressures at surface ensures long-term inflation and the integrity of test interval seals. Location of the casing packers in each bore-

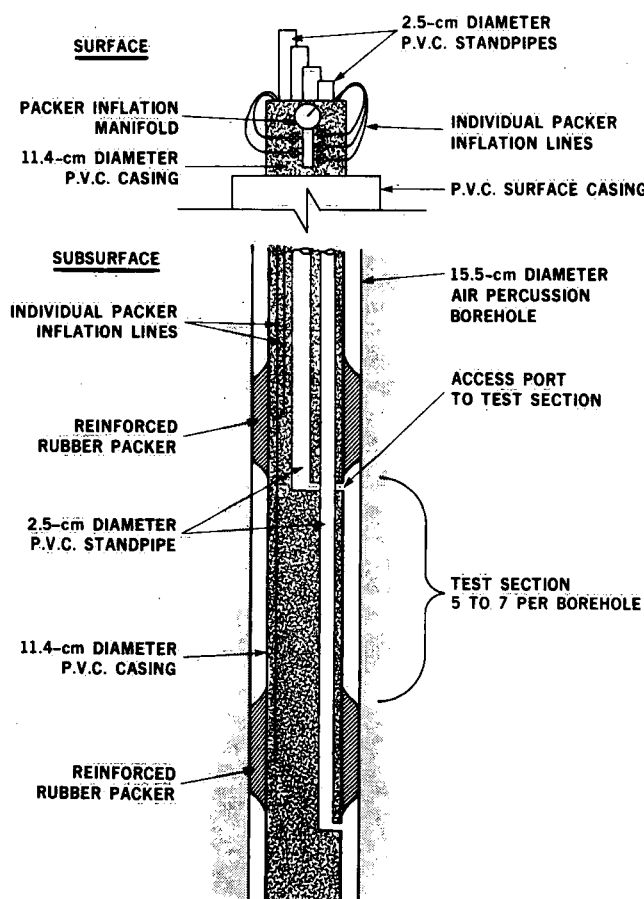


Figure 10. Schematic of multiple-packer, multiple-standpipe casing installed in each FS-series borehole.

hole is shown on fracture hydrology logs in Appendix A.

Prior to casing installation, all packers and O-ring-sealed casing lengths were pressure-tested at surface to ensure integrity of the casing system. Casing was installed in each borehole shortly after completion of drilling, geophysical surveys and straddle-packer testing. Casing was installed in boreholes FS-1 to 9 in August 1981, in boreholes FS-7 and FS-10 to 14 in July 1982, and in boreholes FS-15 to 17 in August 1983. A total of 78 packers were installed in the 17 boreholes at the study site. As of February 1985, only two of the 78 packers had failed. These failures occurred in packers FS 2-5 and FS 8-4.

Ninety test intervals in 17 boreholes provide the data base for study of the ground-water flow system at CRNL.

Table 5. FS Test Interval Statistics

Interval	Interval depth (m B.C.T.*)	Interval length (m)	Interval volume (L)
FS 1-1	37.19-43.26	6.07	47.2
FS 1-2	26.81-36.45	9.64	74.7
FS 1-3	16.44-26.06	9.62	74.6
FS 1-4	7.59-15.69	8.10	62.8
FS 1-5	2.03- 6.84	4.81	53.3
FS 2-1	34.31-43.60	9.29	72.1
FS 2-2	25.34-33.53	8.19	63.5
FS 2-3	16.58-24.63	8.05	62.4
FS 2-4	9.25-15.81	6.56	50.9
FS 2-5	3.05- 8.47	5.42	102.1
FS 3-1	32.10-41.50	9.40	72.9
FS 3-2	23.25-31.33	8.08	62.7
FS 3-3	15.91-22.47	6.56	50.9
FS 3-4	7.97-15.14	7.17	55.6
FS 3-5	4.59- 7.18	2.59	20.0
FS 3-6	3.05- 3.82	0.81	38.7
FS 4-1	33.00-42.50	9.50	134.0
FS 4-2	22.60-32.18	9.58	74.3
FS 4-3	15.15-21.81	6.67	51.7
FS 4-4	7.93-14.51	6.58	51.0
FS 4-5	5.18- 7.15	1.97	15.3
FS 4-6	3.05- 4.40	1.35	34.7
FS 5-1	32.25-41.60	9.35	72.5
FS 5-2	21.85-31.47	9.62	74.6
FS 5-3	12.97-21.09	8.12	63.0
FS 5-4	7.16-12.22	5.06	39.2
FS 5-5	2.06- 6.40	4.34	49.8
FS 6-1	30.70-41.60	10.90	84.5
FS 6-2	21.83-29.92	8.09	62.7
FS 6-3	16.94-21.06	4.12	31.9
FS 6-4	8.07-16.17	8.10	62.8
FS 6-5	2.03- 7.32	5.29	41.0
FS 7-1	61.65-74.15	12.50	96.9
FS 7-2	52.79-60.95	8.16	63.3
FS 7-3	44.82-52.10	7.28	56.5
FS 7-4	30.78-44.12	13.34	103.5

*Below casing top.

Table 5. Continued

Interval	Interval depth (m B.C.T.)	Interval length (m)	Interval volume (L)
FS 7-5	18.85-30.07	11.22	87.0
FS 7-6	7.89-18.17	10.28	79.7
FS 7-7	3.05- 7.16	4.11	64.3
FS 8-1	34.11-41.86	7.75	60.1
FS 8-2	23.73-33.33	9.60	74.5
FS 8-3	14.86-22.95	8.09	62.8
FS 8-4	4.16-14.11	9.95	77.2
FS 8-5	3.05- 3.42	0.37	56.3
FS 9-1	35.84-42.18	6.34	49.2
FS 9-2	28.50-33.03	6.53	50.6
FS 9-3	19.64-27.72	8.08	62.6
FS 9-4	9.25-18.90	9.65	74.9
FS 9-5	4.31- 8.49	4.18	32.4
FS 9-6	3.05- 3.55	0.50	57.2
FS 10-1	39.31-48.75	9.44	73.2
FS 10-2	28.92-38.59	9.67	75.0
FS 10-3	23.08-28.19	5.11	39.6
FS 10-4	15.13-22.37	7.24	56.2
FS 10-5	9.28-14.44	5.16	40.0
FS 10-6	1.50- 8.62	7.12	16.4
FS 11-1	37.13-43.53	6.40	49.6
FS 11-2	28.29-36.45	8.16	63.3
FS 11-3	20.92-27.56	6.64	51.5
FS 11-4	12.93-20.20	7.27	56.4
FS 11-5	4.09-12.25	8.16	63.3
FS 11-6	2.00- 3.38	1.38	36.6
FS 12-1	35.61-43.50	7.89	61.2
FS 12-2	27.66-34.93	7.27	56.4
FS 12-3	19.71-26.95	7.24	56.2
FS 12-4	7.76-19.01	11.25	87.3
FS 12-5	3.50- 7.07	3.57	89.3
FS 13-1	35.33-43.30	7.97	61.8
FS 13-2	29.54-34.67	5.13	39.8
FS 13-3	22.21-28.86	6.65	51.6
FS 13-4	14.86-21.51	6.65	51.6
FS 13-5	7.48-14.13	6.65	51.6
FS 13-6	1.50- 6.80	5.30	57.3
FS 14-1	38.10-42.13	4.03	31.3
FS 14-2	30.77-37.41	6.64	51.5
FS 14-3	18.88-30.10	11.22	87.0
FS 14-4	7.86-18.18	10.32	80.0
FS 14-5	5.80- 7.15	1.35	133.7
FS 15-1	45.49-48.51	3.02	13.3
FS 15-2	38.17-44.84	6.67	29.3
FS 15-3	30.85-37.49	6.64	29.2
FS 15-4	15.95-30.10	14.15	62.1
FS 15-5	0.70-15.26	14.56	53.8
FS 16-1	47.90-50.34	2.44	10.7
FS 16-2	37.50-47.21	9.71	42.6
FS 16-3	30.20-36.83	6.63	29.1
FS 16-4	16.39-29.49	13.10	57.5
FS 16-5	0.52-15.70	15.18	49.2
FS 17-1	51.78-60.75	8.97	39.4
FS 17-2	40.45-51.12	10.67	46.8
FS 17-3	27.01-39.79	12.78	56.1
FS 17-4	19.70-26.37	6.67	29.3
FS 17-5	0.69-19.05	18.36	63.9

Depth, length and annulus volume statistics of these test intervals are given in Table 5. Test interval lengths vary from 3 to 13 m.

Vertical and lateral hydraulic interference and tracer tests, ground-water sampling, and long-term hydraulic-head monitoring have been completed using the packer-standpipe casing. This casing system provides more accurate test data for this type of field study than are otherwise obtainable from open boreholes because it reduces (1) natural intra-borehole ground-water flow and (2) the interval volume, mixing and storage effects. A series of small diameter tools have also been developed (Raven and Smedley, 1982) for testing in conjunction with the casing system.

STRADDLE-PACKER INJECTION TESTS

Method

A comprehensive program of straddle-packer injection testing was completed to measure the near-field hydraulic properties of each borehole. Air-inflated straddle-packers were used to isolate systematically test intervals of 1.5 to 2.0 m in length. Over 350 injection tests were completed in 17 boreholes.

During an injection test, the steady-state flow rate (Q) into a test interval was measured for an injection pressure or hydraulic head (ΔH) imposed above ambient or equilibrium conditions. A single injection head was used in each test. Step injection or multiple flow-rate tests were not conducted as part of the injection test program.

Completion of straddle-packer injection tests requires the assembly of surface and borehole test equipment. Schematics of the surface and borehole test equipment used at the CRNL ground-water flow study site are shown in Figures 11 and 12. Detailed descriptions of these equipment and testing procedures are given by Raven (1980) and Raven and Smedley (1982). Figures 11 and 12 also show the surface and borehole equipment used to complete pump or withdrawal tests from multiple-packer, multiple-standpipe casings.

During each test fluid injection pressure was monitored continuously using downhole pressure transducers and maintained constant with the use of large surface pressure reservoirs. A triple transducer probe, as shown in Figure 12, was frequently used to monitor injection pressure in the test interval and pressures above and below the packer assembly. Monitoring of pressures above and below the test interval assists in the detection of leakage of injection fluid around the packer seals. Combined nonlinearity,

INJECTION/WITHDRAWAL TESTS SURFACE EQUIPMENT SCHEMATIC

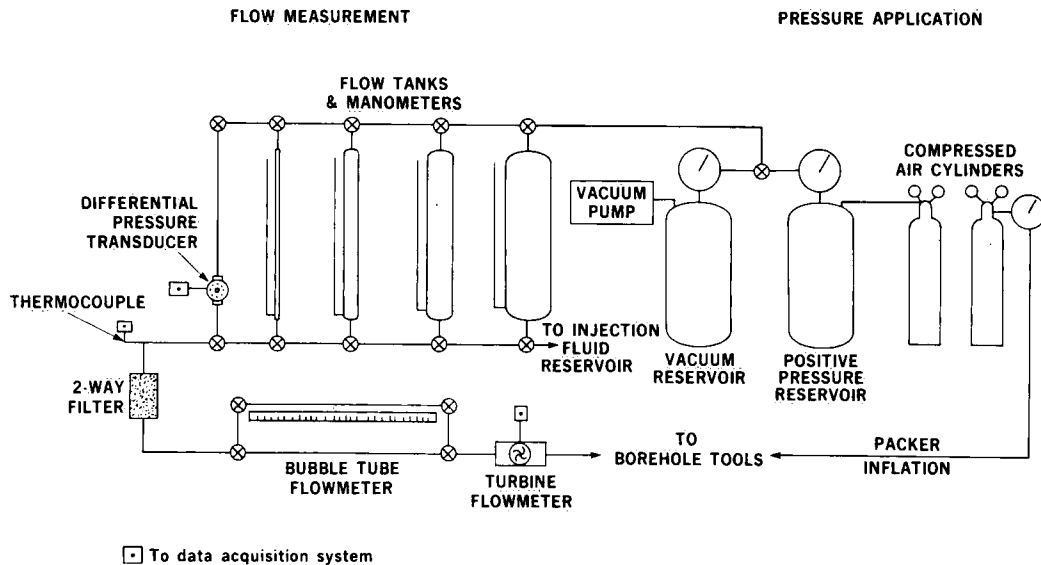


Figure 11. Schematic of surface test equipment used during straddle-packer injection tests and casing-packer withdrawal tests.

INJECTION/WITHDRAWAL TESTS BOREHOLE EQUIPMENT SCHEMATIC

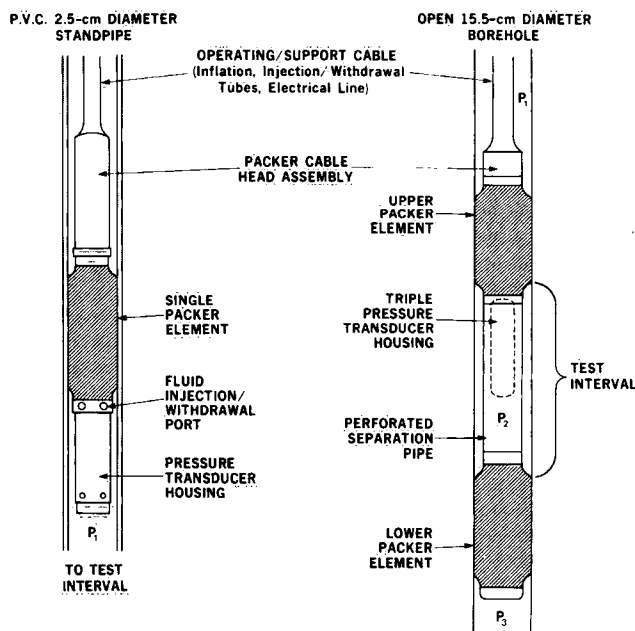


Figure 12. Schematic of subsurface test equipment used during straddle-packer injection tests and casing-packer withdrawal tests.

repeatability and sensitivity specifications of the downhole pressure transducers and surface recording equipment result in a system sensitivity of 0.01-m hydraulic head. Injection heads of 5 to 25 m were used during most of the tests.

Injection flow rates were measured at surface using a series of constant-head flow tanks of different diameters (Raven, 1980), a turbine flow meter and a bubble-tube flow meter (Gale *et al.*, 1979). This flow rate measurement system is effective over a measurement range of about six orders of magnitude. The lowest reliable measurement of flow rate was approximately $4 \times 10^{-10} \text{ m}^3 \cdot \text{s}^{-1}$. This lower limit was determined by thermal expansion and compressibility effects of the injection fluid and the test equipment (flexible tubing, packers, etc.). The upper flow rate measurement limit was approximately $1.0 \times 10^{-4} \text{ m}^3 \cdot \text{s}^{-1}$. This limit was determined from the frictional head loss characteristics of the injection tubing and the requirement of a minimum downhole injection head of 0.10 m.

Fluid injection periods for each test varied from 30 to 120 min. During this period, measurements of flow rate, injection pressure and fluid temperature were recorded in digital form and graphically with multiple-pen strip chart recorders.

Prior to testing in each borehole, the straddle-packer probe was tested at surface for leaks and accuracy of flow rate measurement in a 6-m length plastic pipe.

Results

Each borehole was systematically tested from the static water table down to the bottom of the hole with test interval overlap of 0.05 to 0.27 m. The measured flow rate (Q) and injection head (ΔH) data expressed as a ratio $Q/\Delta H$ reflect the conductive properties of the test interval. The flow rate per unit injection head ($Q/\Delta H$) data for the test site based on 1.5- to 2.0-m test interval lengths range from $5.0 \times 10^{-4} \text{ m}^2 \cdot \text{s}^{-1}$ to less than $1.5 \times 10^{-11} \text{ m}^2 \cdot \text{s}^{-1}$.

The flow rate per unit injection head data have been plotted on summary fracture hydrology logs for each borehole in Appendix A and tabulated for each borehole in Appendix B.

Two conceptual flow models may be appropriate in analyzing the injection test data. Assuming flow is equally distributed through a porous media equivalent of the section of fractured rock under test, an equivalent rock mass hydraulic conductivity (K_{erm}) may be calculated (Hvorslev, 1951):

$$K_{erm} = \frac{Q}{\Delta H 2\pi L} \ln(r_b/r_w) \quad (1)$$

where L is the test interval length, r_b is the radius to constant pressure boundary, and r_w is the radius of borehole.

Alternatively, if one assumes all of the measured flow is the result of a single fracture intersecting the test interval, the injection test data may be used to calculate an equivalent single-fracture aperture ($2b_{esf}$). This flow model assumes laminar, radial flow in a horizontal fracture represented as a smooth parallel-plate opening. This flow model with injection test data is schematically represented in Figure 13. The equivalent single-fracture aperture is determined from (Gale, 1977):

$$2b_{esf} = \left\{ \frac{Q}{\Delta H} \frac{12\mu}{2\pi\rho g} \ln(r_b/r_w) \right\}^{1/3} \quad (2)$$

where μ is dynamic viscosity of the fluid, ρ is fluid density, and g is acceleration of gravity.

Assuming the equivalent porous media flow model and r_b to be equal to 10 m, the minimum and maximum $Q/\Delta H$ correspond to equivalent rock mass hydraulic conductivities of $2.9 \times 10^{-12} \text{ m} \cdot \text{s}^{-1}$ and $2.4 \times 10^{-4} \text{ m} \cdot \text{s}^{-1}$. These $Q/\Delta H$ data also represent equivalent single fracture apertures of 2.7 and 900 μm . Because most test intervals intersect more than one fracture and the apertures of the fracture system are nonuniform, a realistic model of flow to analyse the injection test data is likely intermediate between these two models.

STRADDLE PACKER INJECTION TEST

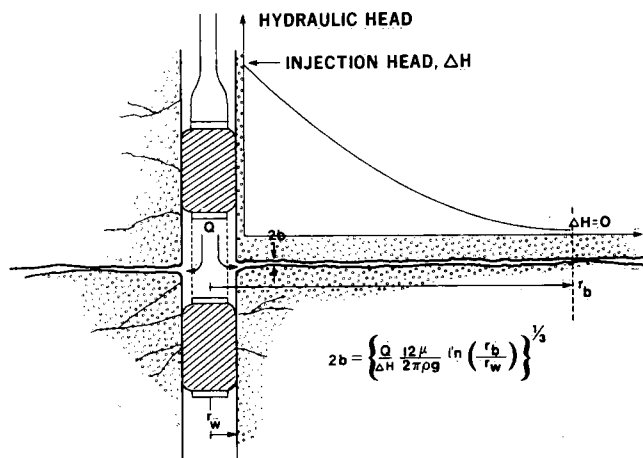


Figure 13. Schematic of straddle-packer injection test of a single fracture.

The results of the injection testing identified several zones of significantly high permeability. In many instances these zones are associated with fracturing in thin (<1 m thick) metagabbro layers within the monzonitic gneiss. The high-permeability zones also define large single fractures or narrow interconnected fracture zones at the study site. Four major fracture zones were identified at the study site based on the results of hydraulic interference tests. These fracture zones are discussed in detail in the section on results of hydraulic interference tests.

The lowest permeability test intervals were located in borehole FS-14. Borehole FS-14 was drilled into a 5- to 10-m wide vertical diabase dyke. The injection test results in borehole FS-14 confirm the results of hydraulic interference tests completed across the dyke, which indicate that the dyke behaves as a local impermeable barrier to ground-water flow.

The results of all injection tests and some withdrawal tests have been analyzed to determine the distribution of equivalent rock mass hydraulic conductivity (K_{erm}) at the study site. The distribution of the common logarithm of 340 measurements of hydraulic conductivity is shown in Figure 14. The distribution is truncated at approximately $10^{-11} \text{ m} \cdot \text{s}^{-1}$ (lower measurement limit for injection tests) and is skewed to the right to higher hydraulic conductivity values. The geometric mean of all hydraulic conductivity determinations for the study site is $2.1 \times 10^{-9} \text{ m} \cdot \text{s}^{-1}$.

The results of the injection tests completed on test intervals of 1.5 to 2.0 m length have also been summed to determine the $Q/\Delta H$ values for the longer test intervals

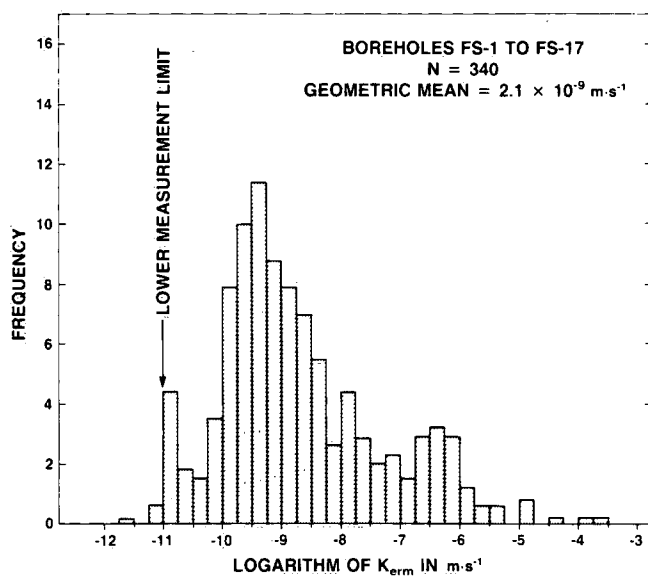


Figure 14. Distribution of the common logarithm of equivalent rock mass hydraulic conductivity, K_{erm} , in boreholes FS-1 to FS-17 measured with straddle-packer injection tests.

isolated by the multiple-packer casings. The $Q/\Delta H$ values as well as estimates of isotropic equivalent rock mass hydraulic conductivity (K_{erm}) for each casing interval are listed in Table 6. Hydraulic conductivity was determined for the casing intervals because equilibrium and transient hydraulic head data and ground-water geochemistry were measured in the casing intervals. To evaluate the ability of numerical models of ground-water flow to describe the CRNL ground-water flow system requires field measurements of hydraulic head, hydraulic conductivity and ground-water geochemistry on the same test intervals.

Estimates of anisotropic hydraulic conductivity (K_{ij}) were also calculated for each casing interval by integrating fracture orientation data measured with borehole acoustic televiewer and fracture apertures calculated from injection tests. The method and results of these hydraulic conductivity tensor determinations are discussed in the section on "Hydraulic Conductivity Tensor Determinations."

HYDRAULIC INTERFERENCE TESTS

Method

Hydraulic interference tests were completed from open boreholes and in casing test intervals to evaluate the hydraulic properties of the rock mass. Both constant discharge and constant drawdown pump tests were conducted at the study site during the period 1982 to 1984.

Table 6. Hydraulic Properties of FS Test Intervals

Interval	Flow rate per unit head $Q/\Delta H$ ($m^2 \cdot s^{-1}$)	Equivalent rock mass hydraulic conductivity, K_{erm} ($m \cdot s^{-1}$)*
FS 1-1	6.3×10^{-10}	8.0×10^{-11}
FS 1-2	1.3×10^{-8}	1.0×10^{-9}
FS 1-3	8.0×10^{-8}	6.4×10^{-9}
FS 1-4	1.8×10^{-8}	1.7×10^{-9}
FS 1-5	6.2×10^{-10}	1.0×10^{-10}
FS 2-1	2.5×10^{-9}	2.1×10^{-10}
FS 2-2	2.9×10^{-9}	2.7×10^{-10}
FS 2-3	1.1×10^{-6}	1.0×10^{-7}
FS 2-3†	6.5×10^{-7}	6.2×10^{-8}
FS 2-4	4.4×10^{-8}	5.2×10^{-9}
FS 2-5	3.9×10^{-8}	5.5×10^{-9}
FS 3-1	2.9×10^{-8}	2.3×10^{-9}
FS 3-2	8.5×10^{-8}	8.1×10^{-9}
FS 3-2†	7.8×10^{-8}	7.4×10^{-9}
FS 3-3	4.9×10^{-8}	5.7×10^{-9}
FS 3-4	8.0×10^{-9}	8.6×10^{-10}
FS 3-5	2.7×10^{-10}	8.0×10^{-11}
FS 3-6 N.D.	—	—
FS 4-1	2.8×10^{-9}	2.3×10^{-10}
FS 4-2	2.9×10^{-6}	1.5×10^{-7}
FS 4-2†	2.2×10^{-6}	1.8×10^{-7}
FS 4-3	2.8×10^{-6}	3.2×10^{-7}
FS 4-4	1.6×10^{-5}	1.9×10^{-6}
FS 4-5 N.D.	—	—
FS 4-6 N.D.	—	—
FS 5-1	6.5×10^{-7}	5.3×10^{-8}
FS 5-1†	8.0×10^{-7}	6.6×10^{-8}
FS 5-2	1.5×10^{-8}	1.2×10^{-9}
FS 5-3	5.4×10^{-9}	5.1×10^{-10}
FS 5-4	7.2×10^{-9}	1.1×10^{-9}
FS 5-5	2.3×10^{-7}	4.1×10^{-8}
FS 6-1	5.1×10^{-6}	3.6×10^{-7}
FS 6-1†	8.0×10^{-7}	5.6×10^{-8}
FS 6-2	5.3×10^{-9}	5.0×10^{-10}
FS 6-3	5.5×10^{-9}	1.0×10^{-9}
FS 6-4	9.8×10^{-9}	9.3×10^{-10}
FS 6-5 N.D.	—	—
FS 7-1	2.9×10^{-8}	1.8×10^{-9}
FS 7-2	1.4×10^{-7}	1.3×10^{-8}
FS 7-3	5.0×10^{-4}	5.3×10^{-5}
FS 7-4	5.0×10^{-6}	2.9×10^{-7}
FS 7-5	1.7×10^{-8}	1.2×10^{-9}
FS 7-6	4.4×10^{-9}	3.3×10^{-10}
FS 7-7	3.0×10^{-7}	5.6×10^{-8}
FS 8-1	4.0×10^{-9}	4.0×10^{-10}
FS 8-2	1.8×10^{-5}	1.4×10^{-6}
FS 8-3	1.7×10^{-9}	1.6×10^{-10}
FS 8-4	2.5×10^{-9}	1.9×10^{-10}
FS 8-5 N.D.	—	—

* Determined from 1.5- to 2.0-m interval, 30- to 120-min duration constant-pressure injection tests unless otherwise indicated.

† Determined from 72-h duration, constant-pressure withdrawal test in casing interval.

‡ Determined from bail recovery test in casing interval.

N.D. — Not determined owing to insufficient data.

Table 6. Continued

Interval	Flow rate per unit head $Q/\Delta H$ ($m^2 \cdot s^{-1}$)	Equivalent rock mass hydraulic conductivity, K_{erm} ($m \cdot s^{-1}$)
FS 9-1	2.2×10^{-7}	2.7×10^{-8}
FS 9-2	1.3×10^{-4}	1.5×10^{-5}
FS 9-3	3.0×10^{-8}	2.8×10^{-9}
FS 9-4	5.4×10^{-8}	4.3×10^{-9}
FS 9-5 N.D.	—	—
FS 9-6 N.D.	—	—
FS 10-1	3.4×10^{-5}	2.8×10^{-6}
FS 10-2	9.4×10^{-9}	7.5×10^{-10}
FS 10-3	1.7×10^{-9}	2.5×10^{-10}
FS 10-4	3.7×10^{-9}	3.9×10^{-10}
FS 10-5	8.3×10^{-9}	1.2×10^{-9}
FS 10-6 N.D.	—	—
FS 11-1	1.5×10^{-6}	1.8×10^{-7}
FS 11-2	2.7×10^{-6}	2.5×10^{-7}
FS 11-2†	1.3×10^{-6}	1.2×10^{-7}
FS 11-3	1.7×10^{-9}	1.9×10^{-10}
FS 11-4	1.1×10^{-10}	1.2×10^{-11}
FS 11-5	7.0×10^{-9}	6.6×10^{-10}
FS 11-6 N.D.	—	—
FS 12-1	2.2×10^{-8}	2.1×10^{-9}
FS 12-2	9.3×10^{-10}	9.8×10^{-11}
FS 12-3	1.3×10^{-8}	1.4×10^{-9}
FS 12-4†	4.5×10^{-8}	3.1×10^{-9}
FS 12-5 N.D.	—	—
FS 13-1	2.4×10^{-6}	2.3×10^{-7}
FS 13-2	6.7×10^{-8}	1.0×10^{-8}
FS 13-3	1.1×10^{-8}	1.3×10^{-9}
FS 13-4	6.6×10^{-7}	7.6×10^{-8}
FS 13-5	1.7×10^{-7}	2.0×10^{-9}
FS 13-6 N.D.	—	—
FS 14-1†	1.5×10^{-11}	2.9×10^{-12}
FS 14-2†	2.0×10^{-10}	2.3×10^{-11}
FS 14-3†	3.3×10^{-8}	2.3×10^{-9}
FS 14-4†	3.3×10^{-8}	2.4×10^{-9}
FS 14-5 N.D.	—	—
FS 15-1	1.6×10^{-6}	4.5×10^{-7}
FS 15-2	2.9×10^{-7}	3.7×10^{-8}
FS 15-3	3.7×10^{-6}	4.7×10^{-7}
FS 15-4	2.8×10^{-6}	1.7×10^{-7}
FS 15-5	1.5×10^{-7}	8.7×10^{-9}
FS 16-1	1.6×10^{-5}	5.6×10^{-6}
FS 16-2	1.4×10^{-6}	1.2×10^{-7}
FS 16-3	8.1×10^{-8}	1.0×10^{-8}
FS 16-4	3.0×10^{-8}	1.9×10^{-9}
FS 16-5	3.4×10^{-8}	1.9×10^{-9}
FS 17-1	7.6×10^{-6}	7.2×10^{-7}
FS 17-2	1.2×10^{-5}	9.5×10^{-7}
FS 17-3	4.1×10^{-5}	2.7×10^{-6}
FS 17-4	8.9×10^{-7}	1.1×10^{-7}
FS 17-5	9.8×10^{-7}	4.5×10^{-8}

Most of the interference tests were configured and analyzed as constant discharge or pump tests. The principles of a constant discharge or pump test are shown schematically in Figure 15. Drawdown versus time response in an

observation interval is monitored for a constant discharge or injection stimulus in an activation interval. The response measured at the observation interval is typically a function of the hydraulic properties of the medium or rock mass and the response characteristics of the activation and observation test intervals. One of the most important response characteristics of both the activation and observation test intervals is their storage capacity. This capacity is expressed as a dimensionless wellbore storage coefficient \bar{C} (Earlougher, 1977):

$$\bar{C} = \frac{V\beta}{r_w^2 S} \quad (3)$$

where V is the test interval volume, β is the test interval compressibility, r_w is the radius of the borehole, and S is the storativity of medium tested. The compressibility β is a measure of the changing volume (ΔV) and changing hydraulic head (ΔH) relationships of the test interval:

$$\beta = \frac{\Delta V}{V\Delta H} \quad (4)$$

HYDRAULIC INTERFERENCE TEST

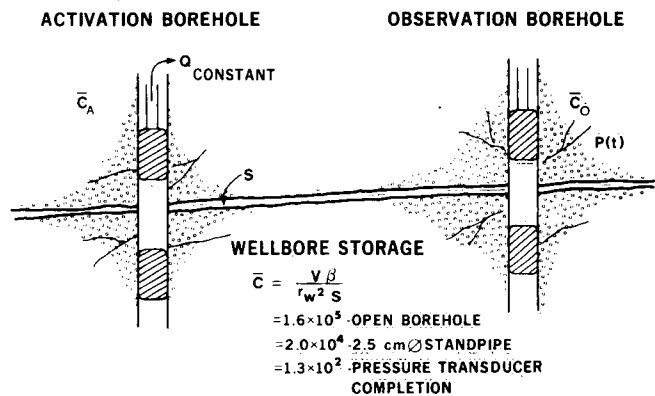


Figure 15. Schematic of a two-borehole constant-discharge hydraulic interference test. Drawdown response data, $P(t)$, used to determine interborehole hydraulic properties are influenced by wellbore storage \bar{C} at both activation and observation boreholes. The magnitude of \bar{C} is proportional to the volume (V) - compressibility (β) product of the borehole test interval and equipment.

Wellbore or test interval storage capacity will often mask the early-time drawdown response during interference tests and failure to consider such effects in conventional (Theis) analyses will underestimate transmissivity and overestimate storativity of the medium. The magnitude of this error increases with decreasing borehole spacing, decreasing transmissivity (T) of the medium and increasing dimensionless wellbore-storage coefficient.

Jargon (1976) has shown that the time at which the activation test interval storage effect will become negligible at an observation test interval is given by:

$$t = (230 + 15s) \left\{ \frac{\bar{C}}{(r/r_w)^2} \right\}^{0.86} \frac{Sr^2}{T} \quad (5)$$

where s is the dimensionless skin factor (Agarwal *et al.*, 1970) and r is the borehole spacing. Application of Equation 5 to an open borehole with zero skin yields the approximate equation of Papadopoulos and Cooper (1967) for the time after which wellbore storage is negligible in a pumping well:

$$t \approx 250 \frac{r_w^2}{T} \quad (6)$$

Because fractured crystalline rocks typically possess low transmissivity, it is essential to design interference tests to minimize test interval storage effects. At the CRNL study site, boreholes were completed with multiple-packer, multiple-standpipe casings, and pressure transducers were often used to monitor drawdowns. As shown in Figure 15, this typically resulted in a decrease in dimensionless wellbore storage coefficient, \bar{C} , from 1.6×10^5 for an open borehole to 1.3×10^2 for a borehole completed with a packer and pressure transducer. For an interference test in fractured rock with $T = 1 \times 10^{-6} \text{ m}^2 \cdot \text{s}^{-1}$, $S = 2 \times 10^{-5}$, $r = 25 \text{ m}$ and $r_w = 0.08 \text{ m}$, this reduction in pumping borehole storage capacity reduces the period of storage-dominated flow at an observation interval from 7300 to 160 min. This reduction is significant, particularly as long-term drawdown data from pumping tests in fractured rock may often reflect complex and uncertain far-field boundary effects. Therefore, assessment of interborehole hydraulic properties often requires reliable test data at early to intermediate time.

For the interference tests completed at the CRNL site ground water was withdrawn from (1) open boreholes using a 76-mm diameter submersible electric pump and (2) casing test intervals using either air-lift pumping or a surface peristaltic pump. Discharge flow rates were monitored using a turbine flowmeter and measured with a stop watch and graduated cylinder or bucket.

Drawdown response was measured in open pumped boreholes using either an electric-contact, water-level tape or a submersible pressure transducer. Both level-sensing devices have sensitivity of 0.01 m. No drawdown was measured in casing test intervals subjected to air-lift pumping. Drawdown was measured in casing test intervals pumped with a peristaltic pump. The peristaltic pump was connected to 22-mm diameter packer-piezometer probe

inflated at the bottom of the 25 mm-diameter PVC standpipe (Fig. 12). The packer-piezometer probe significantly reduced the wellbore storage coefficient of the pumped interval, resulting in more reliable drawdown data. A pressure transducer housed within the packer-piezometer probe measured drawdowns to within 0.01 m.

Drawdown in observation test intervals was measured in three ways: (1) using an electric-contact, water-level tape; (2) with a submersible pressure transducer both with and without inflatable packer; and (3) with water-level probes based on the capacitance principle. The first two methods accurately measured drawdowns to within 0.01 m. The water-level probes were accurate to within 1.0 mm. Packers were used with the submersible pressure transducers to reduce observation test interval storage effects and to obtain reliable early-time drawdown data.

Flow rate, pressure and water-level data were recorded using a real-time datalogger and multiple-pen strip charts. The pressure and water-level measurements recorded with the datalogger were converted to hydraulic head and tabulated as drawdown versus time. The drawdown and time data were plotted on diagnostic log-log diagrams (Gringarten, 1982) and analyzed using various type-curve techniques.

Results

Many hydraulic interference tests were completed at the CRNL ground-water flow study site. Nineteen of these tests provided response data suitable for detailed analysis and interpretation. In each interference test, drawdown response was monitored in several test intervals. Table 7 summarizes the 19 interference tests giving information on activation borehole or test interval, date of test, withdrawal flow rate, test duration, responding observation intervals and the hydrogeological features evaluated in each test. Hydraulic interference tests provided detailed information on the hydraulic properties of discrete narrow fracture zones and of the bulk rock mass.

During interference tests at the CRNL study site, drawdown response was observed initially along horizontal, high hydraulic-conductivity fracture zones and subsequently in test intervals located vertically above and below the fracture zones. This response sequence indicates that the interference tests provide information on the lateral flow properties of the horizontal fracture zones and the vertical flow properties of the surrounding rock mass. The response sequence also demonstrates the importance of high hydraulic-conductivity fracture zones on the response characteristics of a rock mass to pumping and some of the potential difficulties in analysis and interpretation of

Table 7. Summary of Hydraulic Interference Tests

Activation borehole or test interval	Date	Flow rate Q ($\text{m}^3 \cdot \text{s}^{-1}$)	Test duration (min)	Responding observation interval, FS	Hydrogeological features evaluated
FS-7	82/05/15	Variable*	150	5-1,8-2,9-2	Fracture zone No. 1
FS-10	82/07/20-27	1.5×10^{-4}	10 060	5-1,7-3,8-2,9-2,13-2 All remaining intervals in FS-1 to 14	Fracture zone No. 1 Vertical flow properties of rock mass
FS-10	82/08/20-27	1.5×10^{-4}	14 430	5-1,7-3,8-2,9-2,13-2 All remaining intervals in FS-1 to 14	Fracture zone No. 1 Vertical flow properties of rock mass
FS 7-3	82/10/01	6.0×10^{-5}	270	5-1,8-2,9-2,10-1,13-2	Fracture zone No. 1
FS 8-2	82/10/02	3.0×10^{-5}	180	5-1,7-3,9-2,10-1,13-2	Fracture zone No. 1
FS 9-2	82/10/04	6.0×10^{-5}	180	5-1,7-3,8-2,10-1,13-2	Fracture zone No. 1
FS 10-1	82/10/05	3.0×10^{-5}	180	5-1,7-3,8-2,9-2,13-2	Fracture zone No. 1
FS-10	83/06/17-21	2.0×10^{-4}	6 145	5-1,5-2,5-3,5-4,5-5 6-1,6-2,6-3,6-4,6-5	Drawdown response for geomechanical experiment
FS-10	83/09/27-29	2.2×10^{-4}	2 900	9-2,15-1,16-2,17-1 All remaining intervals in FS-15,16,17	Fracture zone No. 1 Vertical flow properties of rock mass
FS 2-3	82/09/25-28	3.5×10^{-6}	4 200	3-2,4-4,4-2,5-2 2-1, 2-2	Fracture zones No. 2 and No. 4 Vertical flow properties of rock mass
FS 4-2	82/08/16-19	3.5×10^{-6}	3 400	1-2,2-1,2-3,3-2,5-2,7-4 4-1,4-3,4-4,4-5	Fracture zones No. 2 and No. 4 Vertical flow properties of rock mass
FS 4-2	83/10/25	1.0×10^{-5}	295	17-3 17-1,17-2,17-4	Fracture zones No. 2 and No. 4 Vertical flow properties of rock mass
FS 6-1	82/10/13-16	3.3×10^{-6}	4 400	2-1,10-4,11-2,13-4 6-2,6-3,6-4,10-3,10-4, 11-1,11-3,11-4	Fracture zone No. 3 Vertical flow properties of rock mass
FS 6-1	83/10/27	9.5×10^{-6}	770	11-2,15-3,16-3 11-1,11-3,11-4,15-1 15-2,15-4,16-1,16-2,16-4	Fracture zone No. 3 Vertical flow properties of rock mass
FS 11-2	82/10/27-29	3.5×10^{-6}	2 900	2-1,6-1,10-4,13-4 6-2,6-3,6-4,11-1,11-3 11-4	Fracture zone No. 3 Vertical flow properties of rock mass
FS 11-2	83/09/8-9	8.3×10^{-6}	1 240	6-1,15-3 6-2,15-1,15-2,15-4	Fracture zone No. 3 Vertical flow properties of rock mass
FS 15-3	83/10/24-26	1.7×10^{-5}	1 340	6-1,11-2 6-2,6-3,6-4,11-1,11-3 11-4,15-1,15-2,15-4	Fracture zone No. 3 Vertical flow properties of rock mass
FS 5-1	82/10/7-8	1.3×10^{-6}	1 380	5-2,5-3,5-4	Vertical flow properties of rock mass
FS 3-2	82/09/23-25	2.5×10^{-7}	2 800	3-1,3-3,3-4	Vertical flow properties of rock mass

*Constant drawdown test.

pump tests in fractured rock, when the location of fracture zones is poorly defined and the monitoring intervals are excessively long.

It is beyond the scope of this report to present the results of all the hydraulic interference tests completed at the CRNL ground-water flow study site. However, the results of most of the important tests conducted to evaluate the flow properties of the fracture zones are given. Several examples of vertical response to pumping the high hydraulic-conductivity fracture zones are also presented. Complete records of the vertical response for the entire study site are included in Appendix C.

The program of hydraulic interference testing identified four narrow fracture zones or large single fractures at the study site. These four fracture zones (identified as No. 1 to No. 4) have lateral extent greater than 50 m. Two of the fracture zones are subhorizontal (No. 1 and No. 2), one is inclined (No. 3) and the other is vertical (No. 4). The fracture zones are shown on a central north-south cross section of the study site in Figure 16. The results of the hydraulic interference tests are discussed for each fracture zone.

Fracture Zone No. 1

FS-10 Pump Tests

Fracture zone No. 1 is a narrow subhorizontal fracture zone intersected by nine test intervals (FS 5-1, 7-3, 8-2, 9-2, 10-1, 13-2, 15-1, 16-2 and 17-1) at depths of 33 to 50 m. The fracture zone is associated with a thin (<1 m thick) mafic layer and appears to be present throughout the study site. Two open-borehole pump tests were conducted from borehole FS-10 on August 20-27, 1982, and on September 27-29, 1983, to evaluate interborehole properties to test intervals FS 5-1, 7-3, 8-2, 9-2, and 13-2,

and FS 15-1, 16-2 and 17-1, respectively. The layout of test boreholes and plots of drawdown versus log-time for the two pump tests are shown in Figures 17 and 18. The second pump test was conducted because boreholes FS-15, 16 and 17 were not drilled at the time the first pump test was completed in borehole FS-10.

The drawdown responses shown in Figures 17 and 18 are similar and indicate (1) a straight line response at late time for both the pumping and observation intervals, (2) similar drawdown response for all observation test intervals regardless of position relative to the pumping borehole, and (3) a difference in drawdown of approximately 4 to 5 m between the pumping and observation interval responses.

Initial interpretation of the late-time drawdown responses using Cooper and Jacob (1946) approximation to the Theis solution suggests that the boreholes are located within a homogeneous isotropic fracture zone with transmissivity of $4 \times 10^{-6} \text{ m}^2 \cdot \text{s}^{-1}$ and variable storativity. Using the parallel-plate model, an equivalent single-fracture aperture $2b_{\text{esf}}$ may be determined from the transmissivity:

$$2b_{\text{esf}} = \left\{ \frac{12\mu T}{\rho g} \right\}^{1/3} \quad (7)$$

The late-time transmissivity is equivalent to a fracture opening of 190 μm . Results from injection tests and additional pump tests, however, indicate that the late-time data after approximately 500 to 1000 min reflect a reduced-permeability boundary and that interborehole permeabilities are significantly higher than an equivalent fracture aperture of 190 μm .

In the presence of a reduced-permeability boundary, early- to intermediate-time drawdown data are necessary to evaluate interborehole hydraulic properties. Early-time data, however, may be dominated by wellbore storage

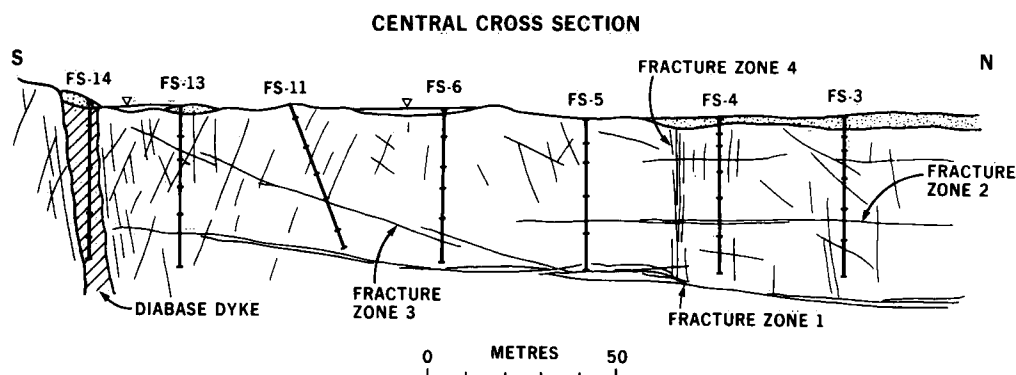


Figure 16. Vertical cross section through centre of CRNL ground-water flow study site showing four fracture zones identified from hydraulic testing.

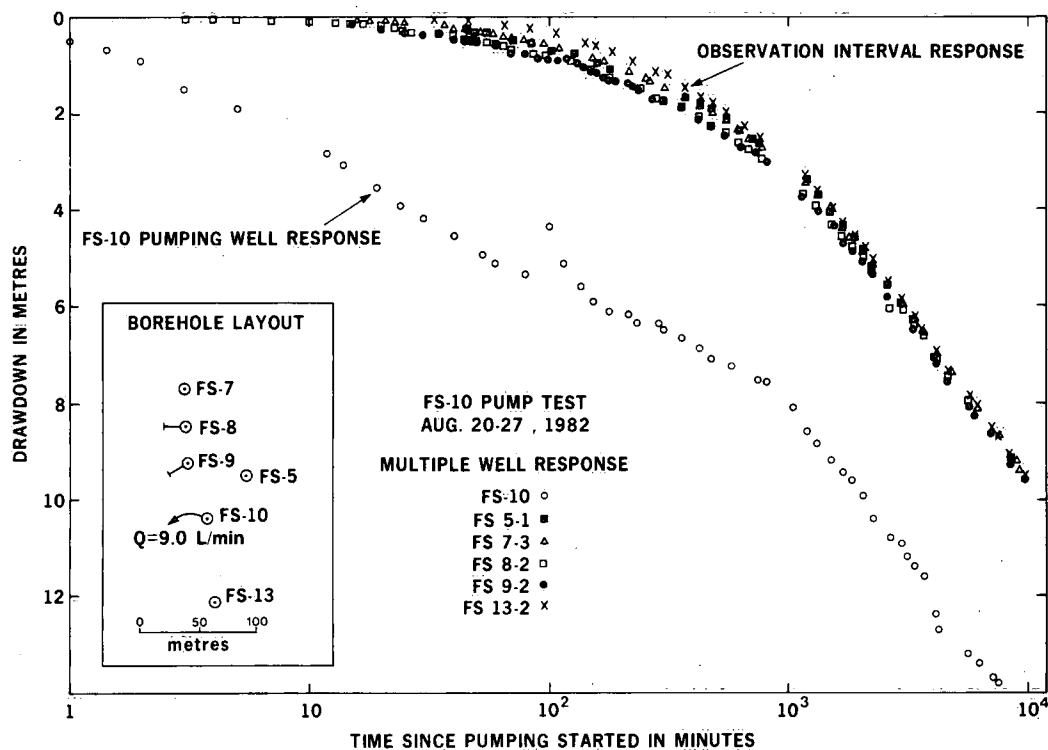


Figure 17. Drawdown versus log-time response for pumping borehole and observation intervals intersecting fracture zone No. 1, FS-10 pump test, August 20-27, 1982.

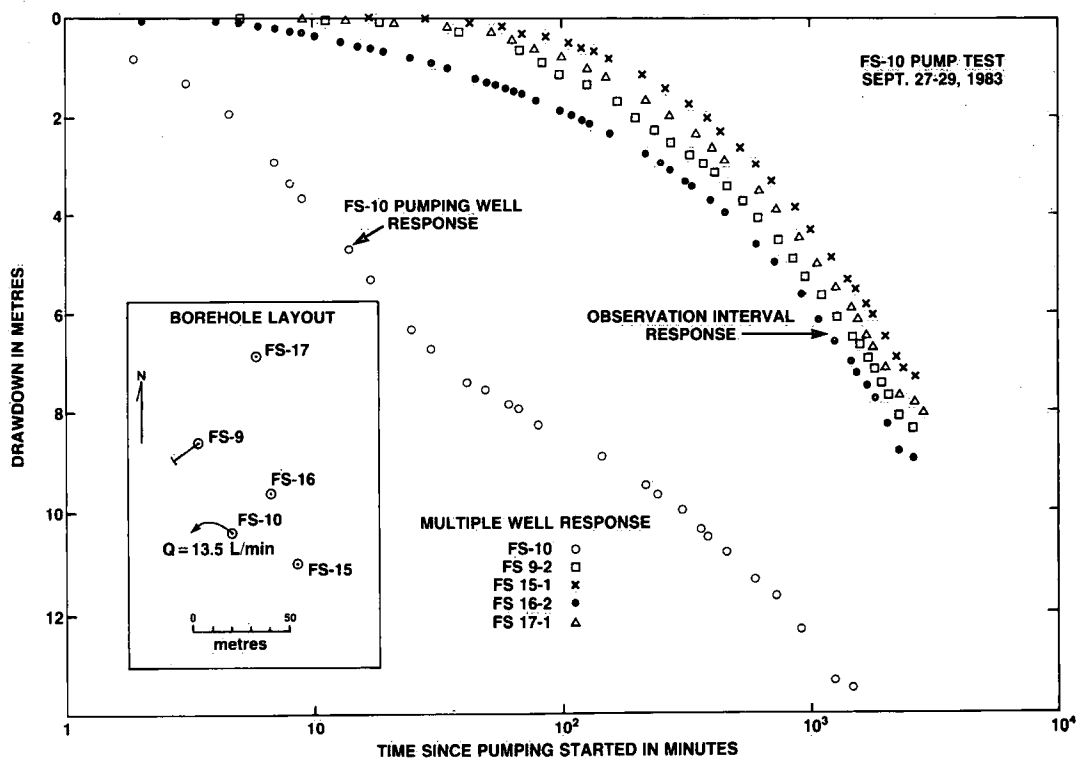


Figure 18. Drawdown versus log-time response for pumping borehole and observation intervals intersecting fracture zone No. 1, FS-10 pump test, September 27-29, 1983.

effects. Use of Equation 5 theoretically predicts that the storage effects in the activation wellbore may influence drawdown response up to and beyond 1000 min. Therefore, no portion of the drawdown curve may be analyzable for interborehole hydraulic properties. To confirm this theoretical prediction, the drawdown data for both FS-10 pump tests were plotted on log-drawdown versus log-time scales (Figs. 19 and 20). The log-log plot (Gringarten, 1982) permits identification of dominating flow regimes. Wellbore and/or fracture storage-dominated flow regimes are identified by a characteristic unit slope in the drawdown-time data on a log-log plot (Ramey, 1970). Wellbore storage effects are usually considered negligible 1 to 1.5 log cycles in time after the end of the unit slope (Earlougher, 1977). The unit slope is apparent in the drawdown responses (Figs. 19 and 20) of both the pumping well and in some of the observation intervals. Storage-dominated flow is persistent to approximately 100 to 500 min in both tests. Therefore, no portion of the drawdown curve may be reliably analyzed using conventional (Theis) techniques to determine interborehole hydraulic properties. These pump tests do, however, provide important qualitative information on interborehole hydraulic properties, types of boundaries, hydraulic connections and the behaviour of a large fracture zone subject to pumping. Based on the observed

drawdown response, fracture zone No. 1 shows high permeability in the vicinity of the test boreholes (in excess of 190 μm) and a far-field boundary of reduced permeability.

The 4- to 5-m drawdown offset observed in the pumping borehole is likely a consequence of a positive skin effect or reduced permeability in the immediate vicinity of the pumping borehole. A positive skin effect causes a drop in hydraulic head as fluid enters a borehole.

This permeability reduction may be due to clogging of fractures with drill cuttings or it may result from natural permeability heterogeneities within fractures. Van Everdingen (1953) and Hurst (1953) represented the skin effect as a skin factor, s , based on an infinitesimally thin layer with permeability differing from the medium permeability and located on the face of the borehole wall. The dimensionless skin factor, s , is related to the head loss (H_s) through the skin by:

$$s = \frac{2\pi TH_s}{Q} \quad (8)$$

where T is the medium transmissivity and Q is the borehole pumping rate.

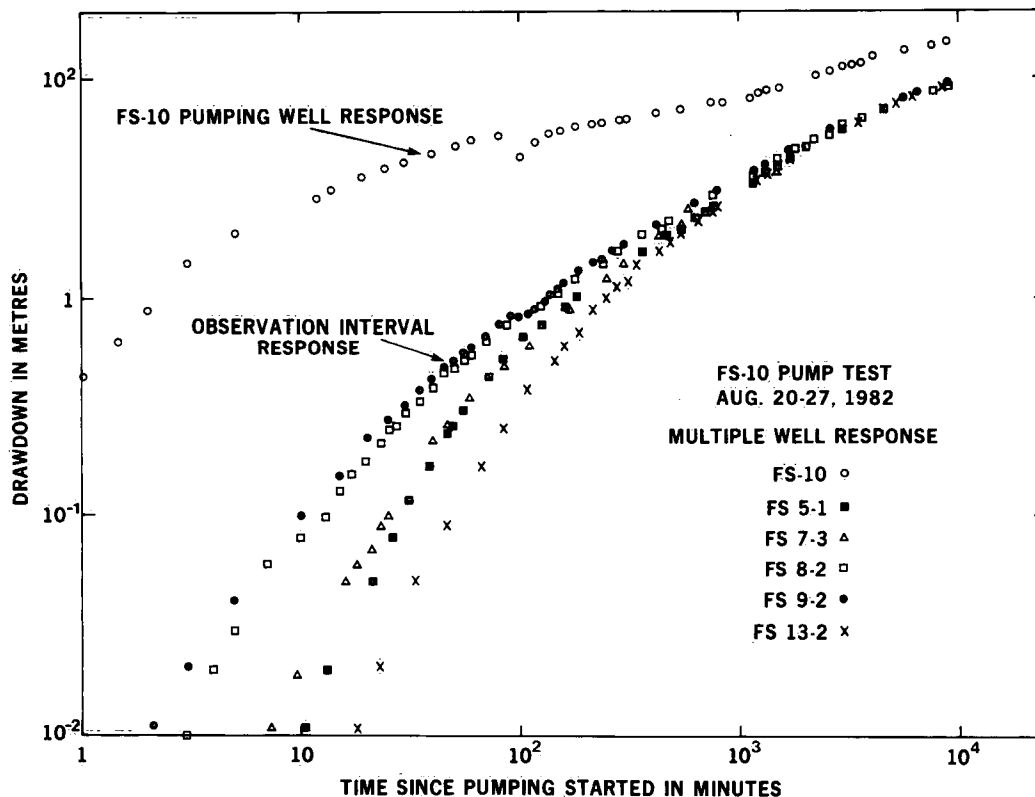


Figure 19. Log-drawdown versus log-time response for pumping borehole and observation intervals intersecting fracture zone No. 1, FS-10 pump test, August 20-27, 1982.

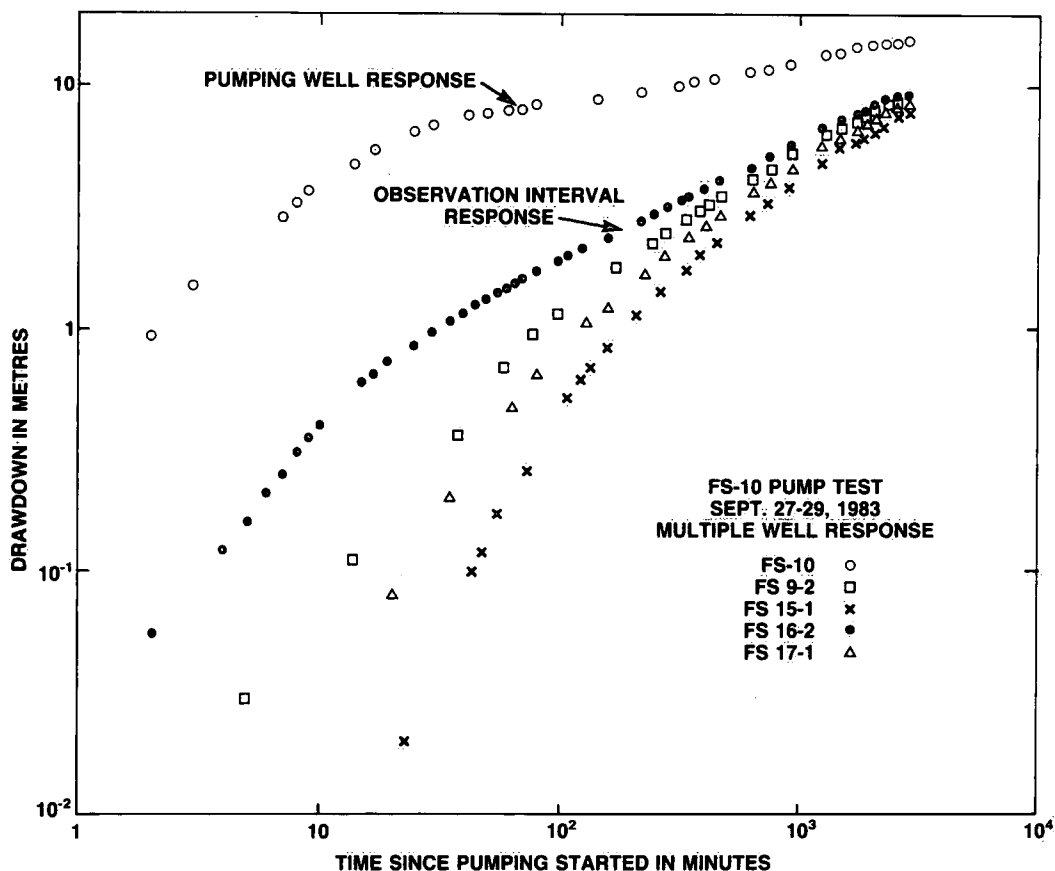


Figure 20. Log-drawdown versus log-time response for pumping borehole and observation intervals intersecting fracture zone No. 1, FS-10 pump test, September 27-29, 1983.

Evidence for the existence of a positive skin effect at the pumping borehole is shown clearly in Figure 21 in which water-level recovery data are plotted versus log-ratio of time since pumping started to time since pumping stopped. Recovery response of the pumping borehole (FS-10) is plotted with an observation-interval (FS 9-2) response representative of recovery within the fracture zone. At late-time or small-time ratio the recovery responses are identical. At early-time or large-time ratio, however, the responses differ by a maximum of about 4 to 5 m. This maximum difference represents the head loss, H_s , owing to a positive skin effect. Although not shown in this report, the skin factor may also be evaluated by plotting recovery data versus $t^{1/2}$ where t is time on a Cartesian plot (Raghavan, 1977). This analysis yields similar values of H_s for the pumping borehole and a small negative skin effect in the observation interval FS 9-2.

Using Equation 8 and assuming an average value of transmissivity determined from interference and injection tests, a skin factor of 5.6 is calculated for fracture zone No. 1 in borehole FS-10. This skin factor determined from the pumping test may also be checked with the results of straddle-packer injection tests which measure near-borehole fluid flow properties. Assuming all of the injection head

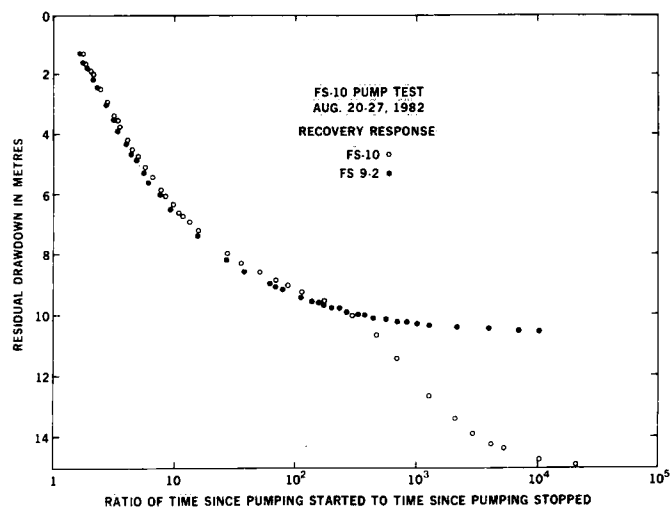


Figure 21. Recovery response for pumping borehole FS-10 and observation interval FS 9-2 intersecting fracture zone No. 1. The difference in recovery response at large-time ratio indicates a positive skin factor of 5.6 at the pumping borehole.

(ΔH) is dissipated during flow through the skin, the injection test data (Appendix B) yield an identical skin factor of 5.6, indicating that the H_s value determined from the pump test recovery data is reliable, and also that the head loss at the borehole-fracture interface is linearly proportional to flow rate in the range $6.7 \times 10^{-5} \text{ m}^3 \cdot \text{s}^{-1}$ (injection test) to $1.5 \times 10^{-4} \text{ m}^3 \cdot \text{s}^{-1}$ (pump test). This linearity in flow rate and head loss further suggests that the flow is laminar in the fracture zone in the vicinity of the pumping borehole.

Although the drawdown versus time data from both FS-10 tests are, in general, not useful in determining the interborehole hydraulic properties of fracture zone No. 1 by conventional methods, the data may be amenable to analysis using other models. In particular, the single, horizontal, uniform-flux fracture model (Gringarten and Ramey, 1974) may be appropriate in providing information on the anisotropic permeability (K_r , K_z) and storativity (S) of the rock mass in which the horizontal fracture zone No. 1 is imbedded. The flow conceptualization used in this model is schematically shown in Figure 22. A high-permeability fracture of radius r_f is imbedded in an anisotropic porous medium of infinite radial extent and thickness h . The porous medium is horizontally bounded by impermeable layers. The model further assumes that

the horizontal fracture has sufficient permeability that negligible hydraulic gradients exist along the fracture to the pumping borehole.

Available geologic and hydrogeologic information suggests that the Gringarten fracture model is applicable to the flow system tested by pumping fracture zone No. 1 from borehole FS-10. The near-uniform response in observation intervals intersecting the fracture zone indicates a negligible gradient within the fracture zone. Straddle-packer injection tests also show the high permeability of the fracture zone relative to the bulk of the rock mass. The rock mass also shows vertical flow regimes or drainage to the fracture zone during pumping.

The drawdown data for the fracture zone from the two FS-10 pump tests are shown in Figure 22 using data from observation intervals FS 8-2, FS 9-2 and FS 16-2. The drawdown data from the pumping borehole were not used because of the positive skin effect discussed previously. The data are plotted on a log-log plot with the visually best-fit type curves of Gringarten *et al.* (1972). The type curves show three distinct flow regimes; borehole and fracture storage-dominated flow at early time characterized by a unit slope, vertical linear flow to a horizontal fracture at

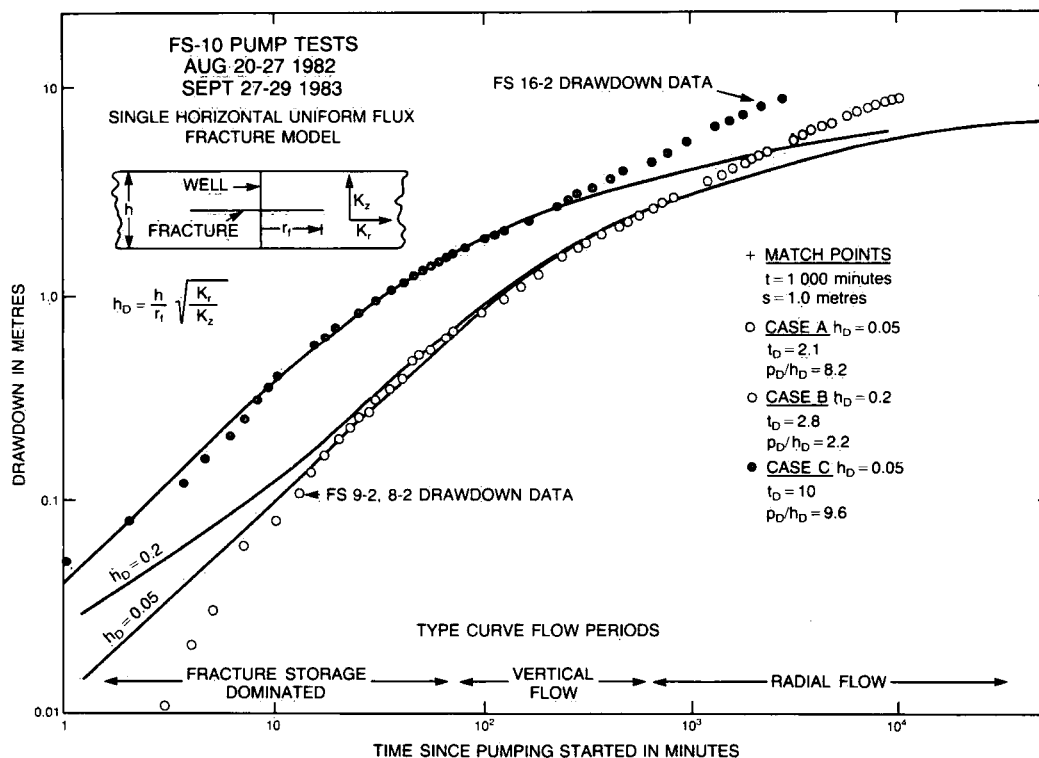


Figure 22. Log-drawdown versus log-time response in fracture zone No. 1 during two pump tests from borehole FS-10, with best-fit type curves of the Gringarten and Ramey (1974) single horizontal, uniform-flux fracture model.

intermediate times characterized by a half slope, and radial flow response at late times. The drawdown data for both pump tests show storage-dominated flow and vertical linear flow but do not indicate radial flow at late time. The drawdown data suggest the persistence of vertical linear flow from intermediate time to the end of the test.

The type curves of the Gringarten fracture model were visually fit to the drawdown data to determine hydraulic properties of the bulk rock mass. Fracture radius, r_f , was selected as 100 m based on available borehole information. A rock mass thickness, h , of 65 m, was used, based on observed vertical drawdown response during the pump tests. The resultant model parameters K_r , K_z and S are shown in Table 8. The three model fits indicate a vertical hydraulic conductivity of about $2 \times 10^{-5} \text{ m}\cdot\text{s}^{-1}$, a radial hydraulic conductivity of $2 \times 10^{-7} \text{ m}\cdot\text{s}^{-1}$, and a storativity of 2×10^{-5} . The calculated hydraulic conductivities indicate a ratio of vertical permeability to radial permeability of about 10 to 170.

The hydraulic conductivity values determined by the Gringarten model may be compared with the results of straddle-packer injection tests. The straddle-packer injection tests for the entire study site showed a geometric mean of hydraulic conductivity equal to $2.1 \times 10^{-9} \text{ m}\cdot\text{s}^{-1}$. Because most of the boreholes are vertical, the mean from the injection tests likely reflects the radial or horizontal hydraulic conductivity of the rock mass and to a lesser extent an average of both horizontal and vertical hydraulic conductivity. The Gringarten model yielded radial hydraulic conductivity of about $2 \times 10^{-7} \text{ m}\cdot\text{s}^{-1}$ and an average of radial and vertical hydraulic conductivity $(K_r K_z)^{1/2}$ in the range 5×10^{-7} to $3 \times 10^{-6} \text{ m}\cdot\text{s}^{-1}$. Therefore, the hydraulic conductivity of the rock mass determined by the Gringarten model is about two to three orders of magnitude higher than injection test results. The discrepancy in hydraulic conductivity determined by the two methods may result

from the presence of vertical high-permeability fractures. Vertical fractures would provide most of the flow to the horizontal fracture and to the pumping borehole, resulting in overestimation of the hydraulic conductivity of the rock mass between the vertical fractures. Alternatively, our injection tests likely measure the hydraulic conductivity of the rock mass between vertical fractures because most of the boreholes are drilled vertically. The estimate of storativity determined by the Gringarten model is probably also a measure of the storage properties of a rock mass containing vertical high-permeability fractures or fracture zones. It is likely an unreliable estimate of specific storage for uniformly fractured rock between vertical fractures or fracture zones.

FS 7-3, 8-2, 9-2 and 10-1 Pump Tests

Four pump tests were completed in fracture zone No. 1 using the multiple-packer, multiple-standpipe casing. The withdrawal flow rates were decreased to 3.0×10^{-5} and $6.0 \times 10^{-5} \text{ m}^3\cdot\text{s}^{-1}$ to reduce the onset of vertical flow regimes and far-field boundary effects and thus extend the period of infinite-acting radial flow in the fracture zone for analysis of interborehole hydraulic properties. Storage effects in activation test intervals were minimized by using air-lift pumping techniques in the 25-mm diameter standpipes.

The log-drawdown versus by log-time plots for these four pump tests are shown in Figures 23 to 26. Visually best-fit Theis curves through the data are also shown on these figures. The Theis curves generally provide a good fit to the drawdown data throughout the duration of the tests. Some early-time (less than 5 min) and late-time (greater than 100 min) deviations between the data and the type curves are evident. These deviations reflect storage-dominated flow at early time and far-field boundary or vertical leakage effects at late time.

Table 8. Hydraulic Properties of the Rock Mass Surrounding Fracture Zone No. 1 Determined from FS-10 Pump Tests Using Gringarten Uniform-Flux Fracture Model*

Data	h_D	Hydraulic conductivity ($\text{m}\cdot\text{s}^{-1}$)		Anisotropy K_z/K_r	Storativity
		K_r	K_z		
Case A					
FS 8-2, 9-2	0.05	1.5×10^{-7}	2.5×10^{-5}	165	3×10^{-5}
Case B					
FS 8-2, 9-2	0.2	1.6×10^{-7}	1.7×10^{-6}	10	2×10^{-5}
Case C					
FS 16-2	0.05	2.6×10^{-7}	4.4×10^{-5}	170	1×10^{-5}

*With $r_f = 100 \text{ m}$, $h = 65 \text{ m}$.

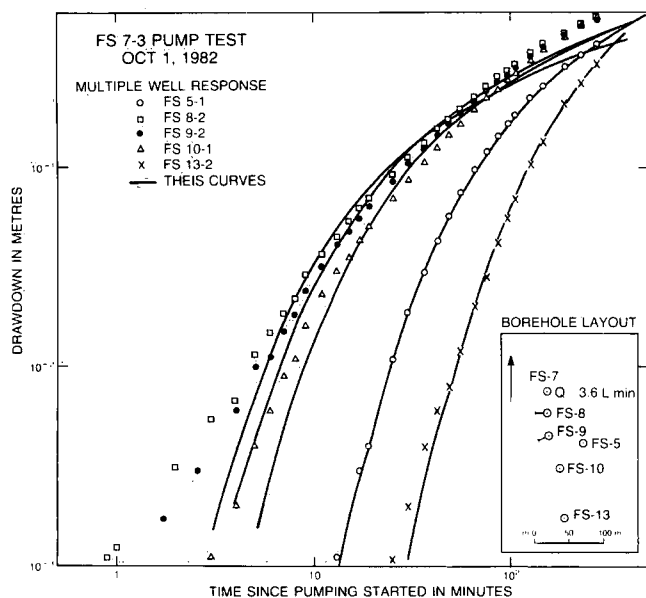


Figure 23. Log-drawdown versus log-time response for observation intervals intersecting fracture zone No. 1 with best-fit Theis curves, FS 7-3 pump test, October 1, 1982.

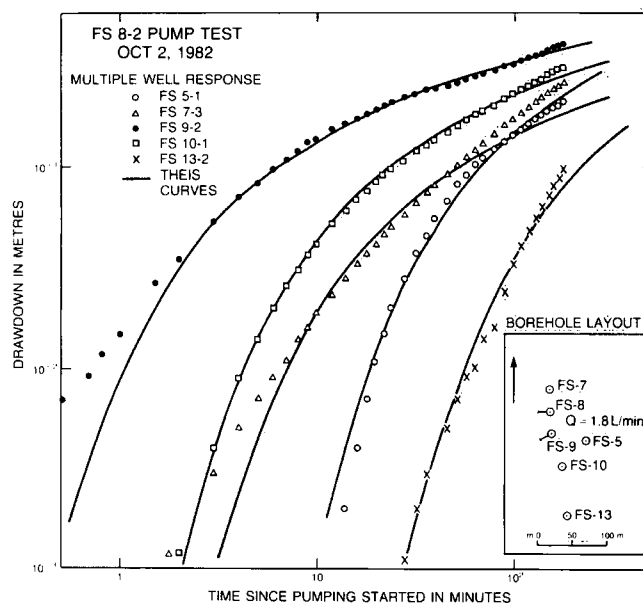


Figure 24. Log-drawdown versus log-time response for observation intervals intersecting fracture zone No. 1 with best-fit Theis curves, FS 8-2 pump test, October 2, 1982.

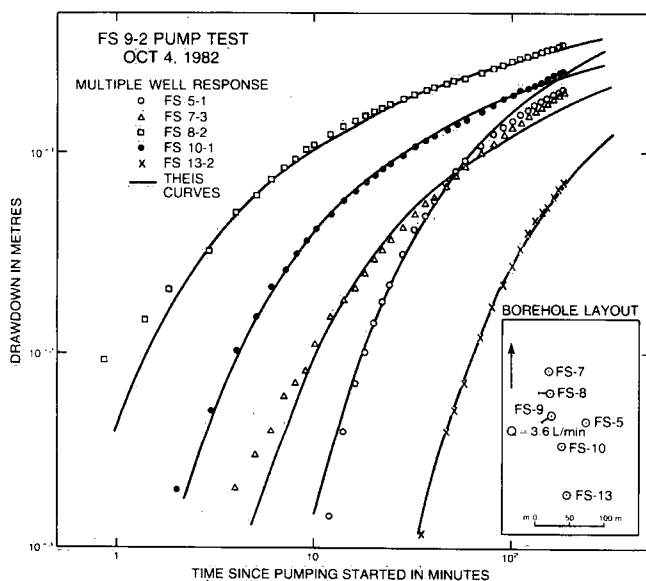


Figure 25. Log-drawdown versus log-time response for observation intervals intersecting fracture zone No. 1 with best-fit Theis curves, FS 9-2 pump test, October 4, 1982.

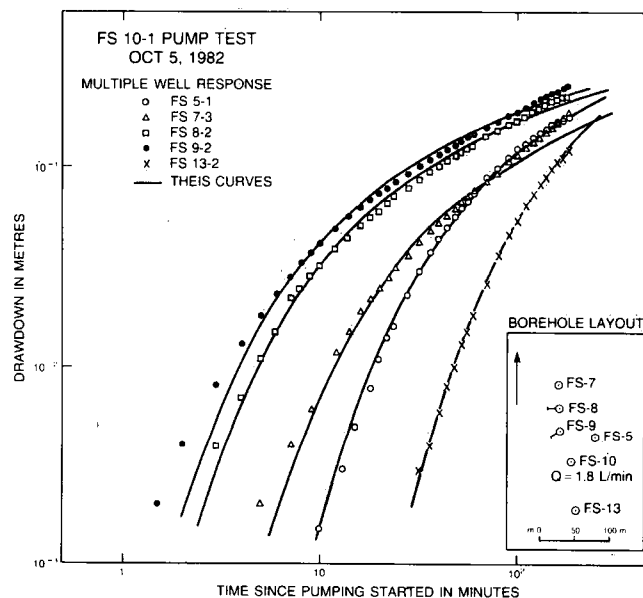


Figure 26. Log-drawdown versus log-time response for observation intervals intersecting fracture zone No. 1 with best-fit Theis curves, FS 10-1 pump test, October 5, 1982.

Fracture transmissivities and storativities were determined from the pump tests using conventional match-point calculations. The transmissivity data were expressed as equivalent single-fracture aperture $2b_{esf}$ using Equation 7. The equivalent single-fracture aperture and the storativity data for fracture zone No. 1 are listed in activation interval – observation interval matrices in Tables 9 and 10. Aperture

estimates in Table 9 listed for the same activation and observation interval were determined from the results of saddle-packer injection tests. The equivalent single-fracture apertures range from 45 to 900 μm , with highest values in the northwest corner of the study site and lowest values in the south. Fracture zone No. 1 has average aperture values of about 375 μm in the northern half of the study site and

150 μm in the southern half. The southern edge of the fracture zone is bound by an impermeable diabase dyke. Storativities range from 4×10^{-6} to 1×10^{-4} , with an average site value of about 2×10^{-5} .

Table 9. Equivalent Single-Fracture Aperture – Fracture Zone No. 1 ($2b_{\text{esf}}$ in μm)

Activation interval	Observation interval								
	FS 5-1	7-3	8-2	9-2	10-1	13-2	15-1	16-2	17-1
FS 5-1	105	—	—	—	—	—	—	—	—
FS 7-3	285	900	390	360	350	235	—	—	—
FS 8-2	290	385	290	390	350	305	—	—	—
FS 9-1	275	366	490	558	465	380	—	—	—
FS 10-1	325	390	380	400	350	260	420	490	410
FS 13-2	—	—	—	—	—	45	—	—	—
FS 15-1	—	—	—	—	—	—	130	—	—
FS 16-2	—	—	—	—	—	—	—	110	—
FS 17-1	—	—	—	—	—	—	—	—	190

Fracture Zone No. 2

Fracture zone No. 2 is a narrow, subhorizontal fracture zone intersected by seven test intervals (FS 1-2, 2-1, 3-2, 4-2, 5-2, 7-4, 17-3) at depths of 25 to 30 m. This fracture zone is located in the northern half of the study site.

A three-day duration pump test was conducted from test interval FS 4-2 to evaluate the interborehole hydraulic properties of fracture zone No. 2. Drawdown response was recorded in all six observation test intervals. Plots of log-drawdown versus log-time for the observation intervals FS 1-2, 2-1, 2-3, 3-2, 5-2 and 7-4 together with the visually best-fit Theis curves are shown in Figure 27.

Interpretation of the drawdown response in observation test intervals FS 2-1, 2-3, 7-4 and 17-3 is complicated by the proximity of vertical fracture zone No. 4 to these test intervals. Fracture zone No. 4 is the subsurface expression of a northwest trending lineament identified in Figures 4 and 9. Fracture zone No. 4 is located within a few metres for boreholes FS-7, FS-4 and FS-2. The lineament and presumably the fracture zone terminate in the vicinity of

borehole FS-2. Drawdown response in intervals FS 2-1, 2-3, 7-4 and 17-3 therefore reflects the combined hydraulic properties of fracture zones No. 2 and No. 4.

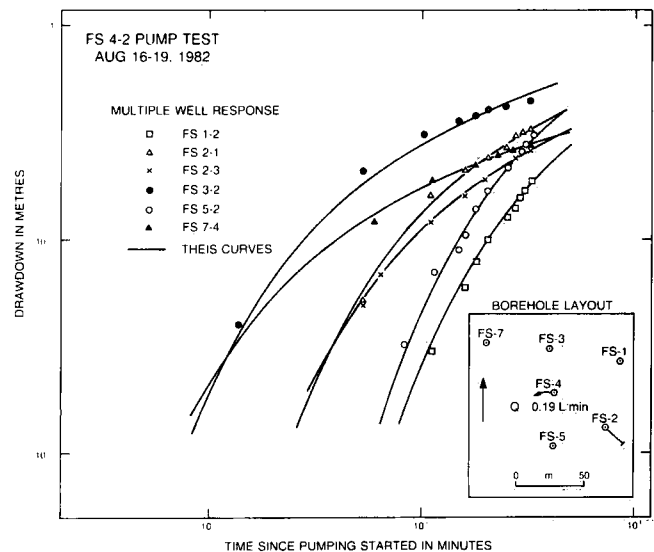


Figure 27. Log-drawdown versus log-time response for observation intervals intersecting fracture zone No. 2 with best-fit Theis curves, FS 4-2 pump test, August 16-19, 1982.

Equivalent single-fracture apertures $2b_{\text{esf}}$ and storativities were determined for fracture zones No. 2 and No. 4 from interference tests and are listed in Tables 11 and 12. Apertures listed for similar activation and observation test intervals in Table 11 were determined from straddle-packer injection tests. Tables 11 and 12 also include interference test data from a pump test completed from test interval FS 2-3 on September 25-28, 1982.

Estimates of equivalent single-fracture aperture for fracture zone No. 2 range from 13 to 355 μm with an average value of about 100 μm . The fracture zone has the highest permeability in the vicinity of boreholes FS-4, FS-7 and FS-17 and pinches out in all directions at a radial distance of about 50 m from boreholes FS-4 and FS-17. An average fracture storativity of 7×10^{-5} was determined for fracture zone No. 2 from three observation interval responses.

Table 10. Fracture Storativity – Fracture Zone No. 1

Activation interval	Observation interval								
	FS 5-1	7-3	8-2	9-2	10-1	13-2	15-1	16-2	17-1
FS 7-3	2×10^{-5}	—	6×10^{-5}	2×10^{-5}	8×10^{-6}	8×10^{-6}	—	—	—
FS 8-2	3×10^{-5}	5×10^{-5}	—	7×10^{-6}	5×10^{-6}	2×10^{-5}	—	—	—
FS 9-2	1×10^{-5}	2×10^{-5}	4×10^{-6}	—	3×10^{-5}	6×10^{-5}	—	—	—
FS 10-1	2×10^{-5}	1×10^{-5}	8×10^{-6}	1×10^{-5}	—	1×10^{-5}	1×10^{-4}	1×10^{-4}	9×10^{-6}

Table 11. Equivalent Single-Fracture Aperture — Fracture Zones Nos. 2 and 4 ($2b_{\text{esf}}$ in μm)

Activation interval	Observation interval								
	FS 1-2	2-1	2-3	3-2	4-2	4-4	5-2	7-4	17-3
FS 1-2	19*	—	—	—	—	—	—	—	—
FS 2-1	—	13*	—	—	—	—	—	—	—
FS 2-3	—	63†	—	—	195	116	116	—	—
FS 3-2	—	—	—	40*	—	—	—	—	—
FS 4-2	108*	123	140	131*	145*	60†	90*	165	196
FS 5-2	—	—	—	—	—	—	22*	—	—
FS 7-4	—	—	—	—	—	—	—	186*	—
FS 17-3	—	—	—	—	—	—	—	—	355*

*Property of fracture zone No. 2 only.

†Property of fracture zone No. 4 only determined from vertical pulse test.

Table 12. Fracture Storativity — Fracture Zones Nos. 2 and 4

Activation interval	Observation interval								
	FS 1-2	2-1	2-3	3-2	4-2	4-4	5-2	7-4	17-3
FS 2-3	—	—	—	—	1×10^{-4}	3×10^{-5}	2×10^{-4}	—	—
FS 4-2	9×10^{-5} *	6×10^{-5}	7×10^{-5}	4×10^{-5} *	—	—	1×10^{-4} *	1×10^{-5}	5×10^{-5}

*Property of fracture zone No. 2 only.

Fracture Zone No. 3

Fracture zone No. 3 is a narrow, inclined fracture zone intersected by seven test intervals (FS 2-1, 6-1, 10-4, 11-2, 13-4, 15-3 and 16-3) at depths of 18 to 38 m. Based on borehole data, the fracture zone is located in the southern and central areas of the study site, strikes northwest and dips about 25° to the northeast. The fracture zone is likely the subsurface expression of the northwest trending air photo lineament intersecting the southwest corner of the study area shown on Figures 4 and 9. Fracture zone No. 3 is also associated with thin mafic layering in the quartz monzonite of the study site.

Five pump tests were conducted in fracture zone No. 3 using test intervals FS 6-1, 11-2, and 15-3 as activation intervals. Observation interval responses to four of these pump tests are shown on log-log plots with visually best-fit Theis curves in Figures 28 to 31. Equivalent single-fracture apertures, $2b_{\text{esf}}$, and storativities were determined

from match-point calculations and are listed in Tables 13 and 14. Equivalent single-fracture apertures vary from 13 to $240 \mu\text{m}$, with average value of about $140 \mu\text{m}$ in the central and southern areas of the study site. The fracture zone appears to pinch out to the northeast and northwest. Storativities range from 1×10^{-6} to 1×10^{-4} with an average value of 1×10^{-5} .

Table 13. Equivalent Single-Fracture Aperture — Fracture Zone No. 3 ($2b_{\text{esf}}$ in μm)

Activation interval	Observation interval						
	FS 2-1	6-1	10-4	11-2	13-4	15-3	16-3
FS 2-1	13	—	—	—	—	—	—
FS 6-1	137	190	120	110	240	132	135
FS 10-4	—	—	14	—	—	—	—
FS 11-2	115	141	205	190	150	140	—
FS 13-4	—	—	—	—	96	—	—
FS 15-3	—	145	—	124	—	125	—
FS 16-3	—	—	—	—	—	—	42

Table 14. Fracture Storativity — Fracture Zone No. 3

Activation interval	Observation interval						
	FS 2-1	6-1	10-4	11-2	13-4	15-3	16-3
FS 6-1	3×10^{-5}	—	1×10^{-4}	1×10^{-6}	1×10^{-4}	7×10^{-6}	2×10^{-5}
FS 11-2	2×10^{-5}	1×10^{-5}	5×10^{-5}	—	4×10^{-4}	1×10^{-6}	—
FS 15-3	—	5×10^{-6}	—	5×10^{-6}	—	—	—

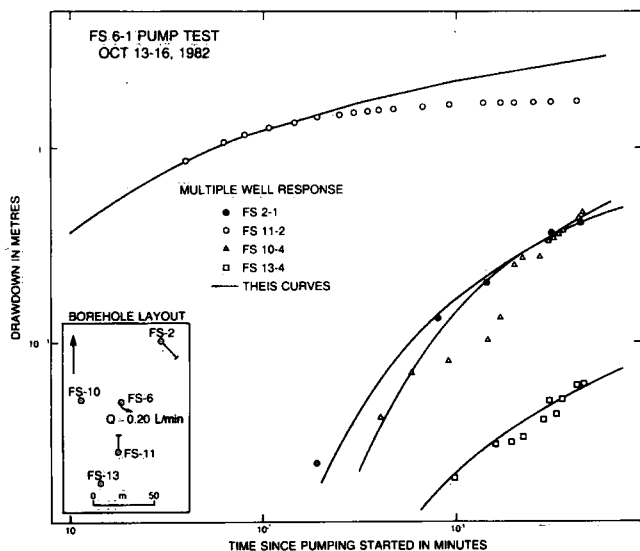


Figure 28. Log-drawdown versus log-time response for observation intervals intersecting fracture zone No. 3 with best-fit Theis curves, FS 6-1 pump test, October 13-16, 1982.

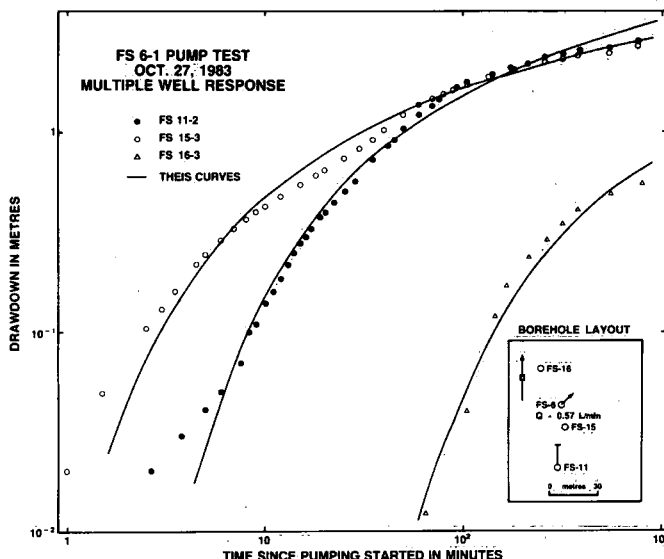


Figure 29. Log-drawdown versus log-time response for observation intervals intersecting fracture zone No. 3 with best-fit Theis curves, FS 6-1 pump test, October 27, 1983.

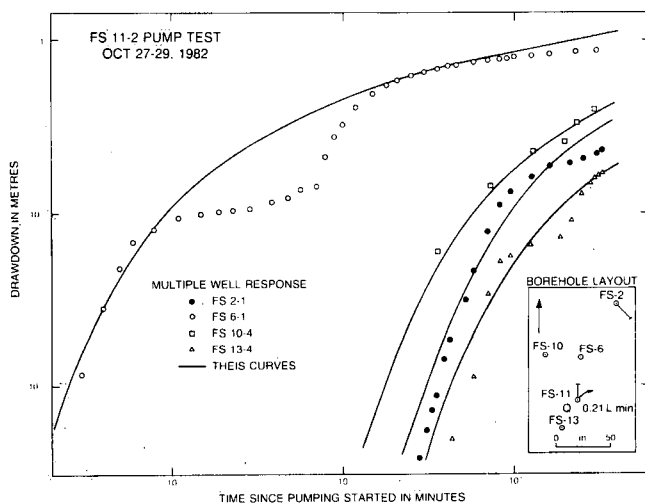


Figure 30. Log-drawdown versus log-time response for observation intervals intersecting fracture zone No. 3 with best-fit Theis curves, FS 11-2 pump test, October 27-29, 1982.

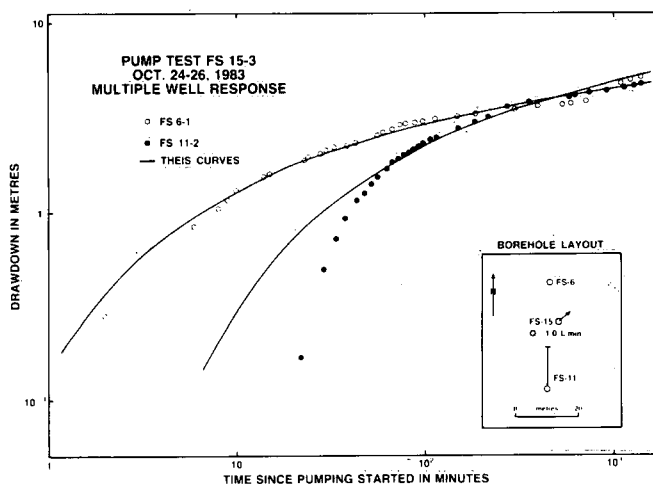


Figure 31. Log-drawdown versus log-time response for observation intervals intersecting fracture zone No. 3 with best-fit Theis curves, FS 15-3 pump test, October 24-26, 1983.

Fracture Zone No. 4

Fracture zone No. 4 is a narrow, vertical fracture zone striking northwesterly through the north and central sections of the study site. The fracture zone is the subsurface expression of the northwest trending lineament that intersects the northwest corner of the study site and was identified by air photo interpretation. Because the fracture zone is vertical, there are few, if any, borehole intersections. Borehole FS-17 may have intersected the fracture zone over

a length of 10 to 20 m near the bottom of the borehole. Fracture zone No. 4 is located about 1 to 2 m from boreholes FS-2, FS-4 and FS-7. The fracture zone likely intersects fracture zones No. 2 and No. 1 at depths of 25 and 45 m, respectively. Although the fracture zone has few borehole intersections, data from vertical interference tests, numerical ground-water flow modelling (Raven *et al.*, 1985) and hydraulic head monitoring (see section on "Hydraulic Head Monitoring") support the existence of a vertical high-permeability fracture zone in the location of the minor air photo lineament discussed above.

Vertical pulse interference tests were completed in boreholes FS-2 and FS-4 and analyzed using the methods of Hirasaki (1974) to determine a vertical hydraulic diffusivity κ_v . Vertical response measured in test intervals in boreholes FS-4 and FS-7, and FS-17 as a result of pumping fracture zone No. 1, were also analyzed to determine vertical diffusivity using the Neuman and Witherspoon (1972) ratio method (see the following section). The vertical diffusivity values were converted to equivalent single-fracture apertures $2b_{\text{eqf}}$ using Equation 7 and an estimate of storativity (5×10^{-5}) determined from interference tests in fracture zones No. 2 and No. 4. Apertures of 63 and 60 μm were calculated for the FS-2 and FS-4 pulse tests, respectively (Table 11). Vertical response measured in test intervals in boreholes FS-2, FS-4, FS-7 and FS-17 during pumping of fracture zone No. 1 yielded equivalent single fracture apertures of 53, 76, 115 and 94 to 165 μm , respectively. Numerical model simulations of flow at the study site required vertical permeabilities equivalent to single-fracture apertures of 140 to 200 μm to match the computed hydraulic head values with field hydraulic head distributions.

In summary, fracture zone No. 4 likely possesses equivalent single-fracture aperture of about 60 to 200 μm , with highest permeability in the northwest corner of the study site near boreholes FS-7 and FS-17 and lowest permeability in the vicinity of borehole FS-2. Combined equivalent single-fracture apertures and storativities determined from interference tests completed in fracture zones No. 2 and No. 4 are listed in Tables 11 and 12.

Vertical Flow Properties of the Rock Mass

During pumping of fracture zones No. 1, No. 2 and No. 3, drawdowns were monitored in the lower-permeability rock located above and below the fracture zones. Drawdowns in the surrounding low-permeability rock were typically delayed in time and of lower magnitude than drawdowns in the fracture zones, suggesting vertical flow in the surrounding rock mass. Figures 32 and 33 show the pattern of drawdown response in both the low-permeability rock surrounding fracture zone No. 1 and in fracture zone No. 1 during pumping from borehole FS-10. In Figure 32, fracture zone No. 1 is intersected by borehole FS-7. In Figure 33, fracture zone No. 1 is located below the bottom of borehole FS-3. Similar drawdown response is observed in the overlying rock mass in both boreholes, suggesting the response is likely a measure of vertical rock mass properties and not merely casing leaks or poor packer seals.

If we assume that the fracture zones and the surrounding low-permeability rock mass hydraulically behave as aquifers and aquitards, respectively (i.e., horizontal flow in the fracture zones, and vertical flow in the rest of the

rock mass), then the drawdown response in the fracture zones and the surrounding rock mass can be used to calculate the hydraulic diffusivity, κ , of the rock mass. The hydraulic diffusivity is defined as the ratio of the medium transmissivity to the storativity of the medium or the ratio of hydraulic conductivity (K) to specific storage (S_s).

$$\kappa = T/S = K/S_s \quad (9)$$

Several methods (Hirasaki, 1974; Wolfe, 1970; Hanshaw and Bredehoeft, 1968; Neuman and Witherspoon, 1972) can be used to determine the vertical diffusivity of low-permeability rock surrounding a high-permeability fracture zone. In general, the different methods yield similar values. In this report we have used the ratio method of Neuman and Witherspoon (1972) to determine vertical hydraulic diffusivity of the low-permeability rock surrounding fracture zone No. 1 during pumping from borehole FS-10. Although vertical drawdown responses were recorded for most of the other pumping tests completed in fracture zones No. 1, No. 2 and No. 3 (Table 7), it is beyond the scope of this report to present the analysis and interpretation of all the data. In using the Neuman and Witherspoon ratio method, we have assumed that both the high-permeability fracture zone No. 1 and the lower-permeability surrounding rock behave as equivalent porous media. It was further assumed that the measured drawdown response occurred approximately at the mid-point of each packer-isolated test interval. The ratio method requires drawdown data in both the low-permeability rock and the fracture zone, and the hydraulic diffusivity of the fracture zone. With additional information on vertical distance Z between the mid-point of the test interval and the fracture zone, application of the ratio method yields an average vertical hydraulic diffusivity κ_v . For a heterogeneous layered rock mass with N layers of thickness b_i , the vertical diffusivity of each layer, κ_{vi} , may be calculated from the average value κ_v , using (Neuman and Witherspoon, 1972):

$$\kappa_v = Z / \left(\sum_{i=1}^N \frac{b_i}{\kappa_{vi}} \right) \quad (10)$$

Drawdown data for test intervals that are located above and below fracture zone No. 1 and that showed response to FS-10 pump tests of fracture zone No. 1 are presented in Appendix C. Data for all boreholes are plotted as drawdown in metres versus log-time in minutes. No drawdowns were observed in boreholes FS-12 and FS-14, which were drilled into the impermeable diabase dyke. The drawdown data of Appendix C were analyzed using the ratio method and Equation 10 to determine the hydraulic diffusivity of the low-permeability rock. The results are shown on Table 15.

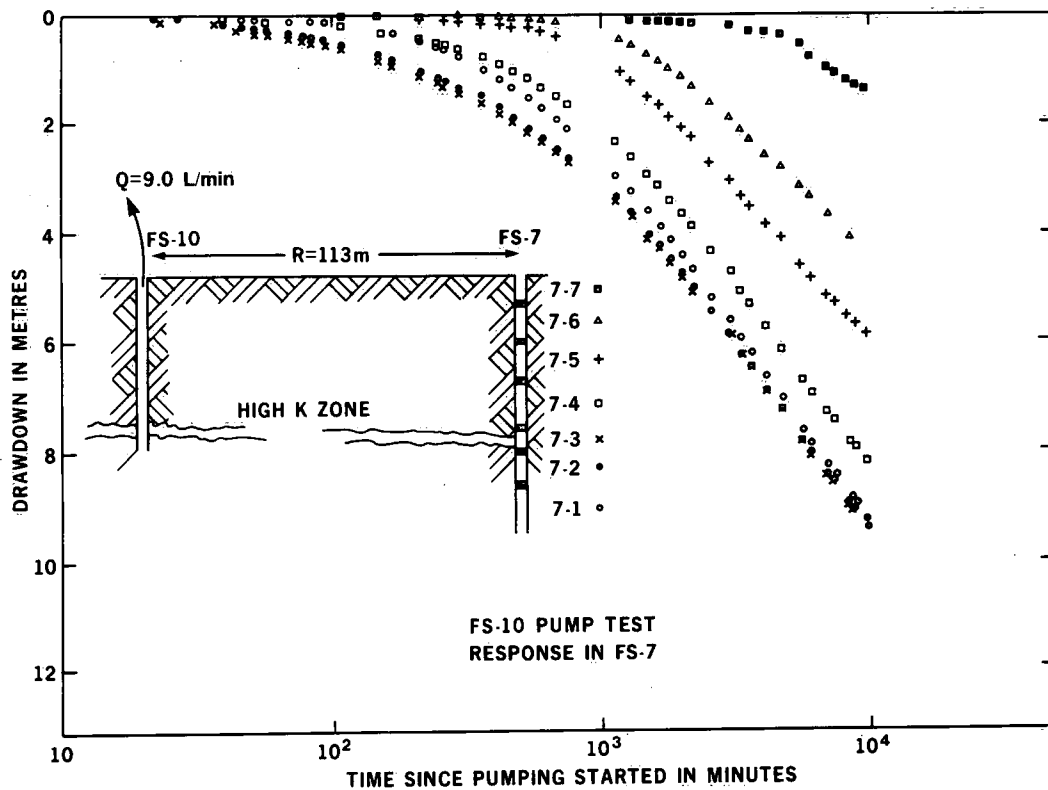


Figure 32. Drawdown versus log-time data for observation intervals in borehole FS-7 showing vertical response to pumping fracture zone No. 1 (high K zone) intersecting interval FS 7-3.

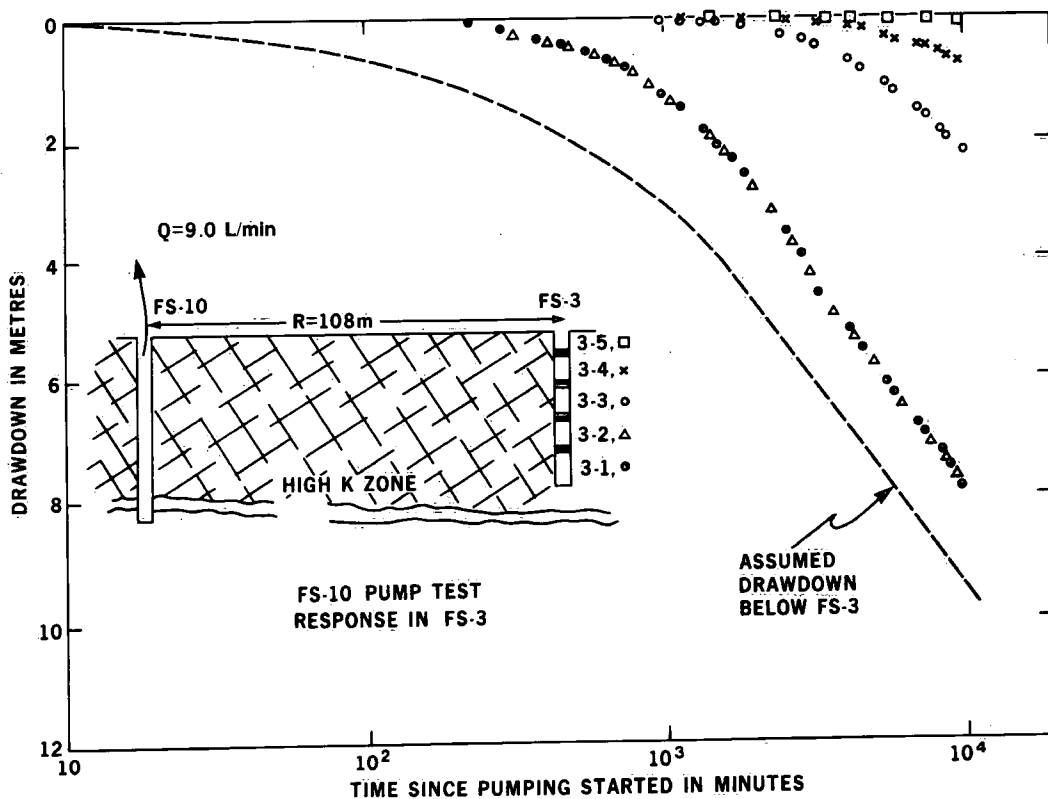


Figure 33. Drawdown versus log-time data for observation intervals in borehole FS-3 showing vertical response to pumping fracture zone No. 1 (high K zone) located below the bottom of borehole FS-3. Assumed drawdown in fracture zone No. 1 is plotted from Figure 32.

Table 15. Vertical Hydraulic Diffusivity

Borehole	Interval depth (m B.C.T.*)	κ_V ($\text{m}^2 \cdot \text{s}^{-1}$)
FS-1	11.7-24.0	1.1×10^{-4}
	24.0-30.0	1.3×10^{-4}
	30.0-53.0	1.9×10^{-3}
FS-2	11.8-19.0	2.4×10^{-5}
	19.0-48.7†	1.9×10^{-3}
	24.5-31.7	4.0×10^{-4}
	31.7-48.7‡	1.3×10^{-3}
FS-3	13.0-19.2	1.4×10^{-4}
	19.2-27.0	1.7×10^{-4}
	27.0-44.1	1.7×10^{-2}
	39.3-44.1‡	6.7×10^{-4}
FS-4	11.2-45.6†	4.5×10^{-3}
	18.5-27.4	1.1×10^{-3}
	27.4-45.6†	6.8×10^{-3}
	37.7-45.6‡	6.2×10^{-4}
FS-5	11.0-15.0	1.0×10^{-4}
	15.0-29.0	7.5×10^{-4}
	29.0-40.8§	2.4×10^{-4}
FS-6	12.0-19.0	5.0×10^{-5}
	19.0-42.0	4.0×10^{-4}
	25.0-35.0	7.0×10^{-5}
	35.0-42.0‡	2.0×10^{-4}
FS-7	5.0-11.0	4.0×10^{-4}
	11.0-25.0	5.4×10^{-3}
	25.0-37.0†	1.1×10^{-2}
FS-7	37.0-50.5†§	4.2×10^{-2}
	50.5-53.0†	2.6×10^{-3}
	50.5-67.0†	5.4×10^{-2}
FS-8	12.2-16.0	1.0×10^{-4}
	16.0-27.5	4.1×10^{-4}
	27.5-33.8§	7.1×10^{-4}
FS-9	10.3-25.4	1.6×10^{-3}
	25.4-31.2§	9.0×10^{-4}
	31.2-40.0†	1.6×10^{-1}
FS-11	8.4-12.4	1.8×10^{-5}
	12.4-21.5	2.0×10^{-4}
	21.5-32.7	1.2×10^{-4}
	32.6-41.1	5.0×10^{-4}
	36.4-41.1‡	2.0×10^{-4}
FS-13	19.0-27.0	2.6×10^{-5}
	27.0-33.0§	3.0×10^{-5}
	33.0-37.25	7.9×10^{-4}
FS-15	23.0-34.0	8.6×10^{-4}
	34.0-41.5	9.6×10^{-3}
	41.5-47.0§	3.8×10^{-2}
FS-16	23.0-33.5	5.4×10^{-4}
	33.5-40.0§	1.5×10^{-3}
	40.0-48.7	8.3×10^{-2}
FS-17	23.2-33.5	2.8×10^{-3}
	33.5-44.5†	1.1×10^{-2}
	44.5-52.0†§	6.2×10^{-2}

* Below casing top.

† High diffusivity pathway, likely the result of a high-permeability vertical fracture connecting the test interval and fracture zone No. 1.

‡ Depth of fracture zone No. 1 inferred from projections based on intersections in other boreholes.

§ Depth of fracture zone No. 1 interpreted from borehole hydraulic tests and fracture logs.

Vertical hydraulic diffusivities range from 2.4×10^{-5} to $1.6 \times 10^{-1} \text{ m}^2 \cdot \text{s}^{-1}$, with an average value of about $2 \times 10^{-4} \text{ m}^2 \cdot \text{s}^{-1}$. In several instances, the observed drawdowns suggested the existence of a high-diffusivity vertical fracture between the monitoring interval and fracture zone No. 1. These responses occurred in some intervals in boreholes FS-2, 3, 4, 6, 7 and 11. The responses observed in boreholes FS-2, 4 and 7 are likely the result of flow along the vertical fracture zone No. 4. The largest values of vertical hydraulic diffusivity were measured in test intervals in boreholes FS-7 and FS-17 located close to fracture zone No. 4.

HYDRAULIC HEAD MONITORING

Measurements of the spatial and temporal distributions of hydraulic head are essential in the study of ground-water flow. Spatial measurements of hydraulic head are necessary to determine the pattern of ground-water movement in a flow system as well as the degree of hydraulic connection or isolation between particular test intervals. Temporal variations in hydraulic head, in response to changing surface infiltration or pumping, provide valuable information on the boundary conditions and different hydrogeologic regimes within a ground-water flow system. Evaluation of numerical simulation models of ground-water flow under both steady-state and transient conditions further requires detailed and reliable field measurements of the spatial and temporal distribution of hydraulic head.

After casing installation, water levels were monitored more or less continuously in each test interval using an electric-contact, water-level tape. Water levels were recorded in test intervals in boreholes FS-1 to 9 from August 1981, in boreholes FS-10 to 14 from July 1982, and in boreholes FS-15 to 17 from August 1983. Measurements of water level in each of the 90 packer-isolated test intervals were converted to hydraulic head values and plotted against time on borehole hydrographs.

Hydraulic Head Distribution

Rock Mass

Hydrographs of borehole test intervals were used to identify periods with minimal hydraulic head transients for determination of equilibrium hydraulic head distributions. An example of the hydraulic head record for test intervals in borehole FS-2 during the period January 1982 to November 1984 is shown in Figure 34. It is beyond the scope of this report to present hydrographs for test intervals in all boreholes. Hydrographs for test intervals in boreholes FS-1 to 9 for the period August 1981 to March 1982 are given by Raven and Smedley (1982).

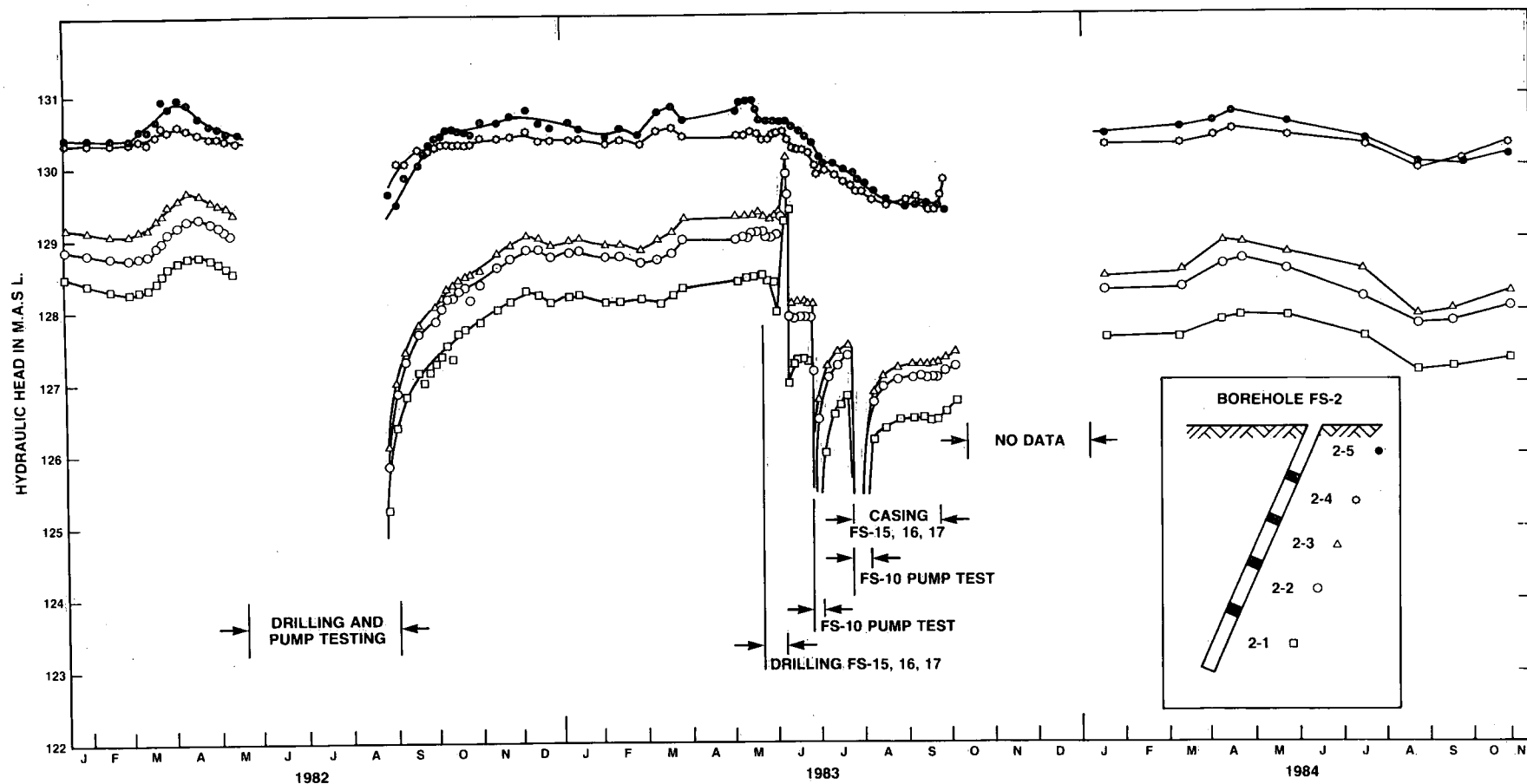


Figure 34. Hydrograph for test intervals in inclined borehole FS-2 for the period January 1982 to November 1984. Borehole activities that caused perturbations in the hydraulic head record are indicated.

Equilibrium hydraulic head data were determined for the entire study site on two dates: December 15, 1982, and November 1, 1984 (Table 16). As evident in Figure 34 for borehole FS-2, these dates are essentially free from hydraulic head transients introduced by borehole pumping or rapid changes in surface infiltration. The distribution of hydraulic head given in Table 16 indicates a relatively simple recharging ground-water flow system directed north and northwest toward Upper Bass Lake. The horizontal component of flow is governed by surface topography. Vertical and horizontal gradients at the site average 0.15 and 0.02, respectively.

Table 16. Equilibrium Hydraulic Head of FS Test Intervals

Interval	Hydraulic head (m.a.s.l.)	
	82/12/15	84/11/01
FS 1-1	125.89	125.64
FS 1-2	126.63	125.68
FS 1-3	127.42	126.77
FS 1-4	128.02	127.61
FS 1-5	128.70	128.23
FS 2-1	128.23	127.34
FS 2-2	128.66	128.09
FS 2-3	129.02	128.25
FS 2-4	130.37	130.31
FS 2-5	130.61	130.41
FS 3-1	126.44	125.49
FS 3-2	126.46	125.51
FS 3-3	127.50	126.52
FS 3-4	129.65	128.67
FS 3-5	N.A.*	N.A.
FS 3-6	130.20	129.97
FS 4-1	126.99	125.76
FS 4-2	127.02	125.81
FS 4-3	128.74	127.87
FS 4-4	128.79	127.90
FS 4-5	N.A.	N.A.
FS 4-6	130.40	131.21
FS 5-1	125.59	124.60
FS 5-2	128.13	127.12
FS 5-3	128.41	127.41
FS 5-4	129.06	128.05
FS 5-5	130.07	128.92
FS 6-1	129.58	128.44
FS 6-2	130.38	129.59
FS 6-3	130.48	129.92
FS 6-4	130.90	130.36
FS 6-5	132.32	130.51
FS 7-1	125.60	124.60
FS 7-2	125.59	124.61
FS 7-3	125.58	124.60
FS 7-4	126.16	125.34

* Test interval not accessed.

† Open borehole.

‡ Test interval recovering from pump test.

Note: Dashes indicate borehole not drilled at time of measurement.

Table 16. Continued

Interval	Hydraulic head (m.a.s.l.)	
	82/12/15	84/11/01
FS 7-5	126.42	125.60
FS 7-6	126.59	125.73
FS 7-7	127.91	125.94
FS 8-1	125.60	124.59
FS 8-2	125.58	124.60
FS 8-3	127.86	126.45
FS 8-4	129.15	127.31
FS 8-5	129.37	129.27
FS 9-1	125.59	124.58
FS 9-2	125.58	124.58
FS 9-3	125.69	124.62
FS 9-4	127.35	126.11
FS 9-5	130.70	131.32
FS 10-1	125.58	124.60†
FS 10-2	125.64	124.60
FS 10-3	130.26	124.60
FS 10-4	130.68	124.60
FS 10-5	130.67	124.60
FS 10-6	131.00	124.60
FS 11-1	129.86	129.16
FS 11-2	129.61	128.51
FS 11-3	130.62	129.86
FS 11-4	131.42	131.14
FS 11-5	133.30	133.40
FS 11-6	133.32	133.40
FS 12-1	135.20	134.28
FS 12-2	135.60	134.00
FS 12-3	135.38	134.17
FS 12-4	134.93	134.07
FS 12-5	133.56	133.13
FS 13-1	125.59	124.63
FS 13-2	125.61	124.65
FS 13-3	131.21	130.65
FS 13-4	133.04	132.87
FS 13-5	133.66	133.20
FS 13-6	133.68	133.66
FS 14-1	128.28‡	131.46
FS 14-2	132.70	132.30
FS 14-3	134.49	134.23
FS 14-4	134.47	134.32
FS 14-5	134.90	134.75
FS 15-1	—	125.50
FS 15-2	—	125.52
FS 15-3	—	128.54
FS 15-4	—	129.76
FS 15-5	—	131.95
FS 16-1	—	124.55
FS 16-2	—	124.60
FS 16-3	—	125.78
FS 16-4	—	127.53
FS 16-5	—	128.81
FS 17-1	—	124.60
FS 17-2	—	124.60
FS 17-3	—	125.35
FS 17-4	—	126.96
FS 17-5	—	128.37

All test intervals at the study site show rapid response to changing surface infiltration conditions. Typically, the test intervals show increased hydraulic head owing to increased surface infiltration during spring snow melt and also when evapo-transpiration is reduced in the fall. Decreased hydraulic head is observed with decreased surface infiltration during winter freeze-up and when potential evapo-transpiration exceeds precipitation in summer. These general trends are evident on the hydrograph for test intervals in borehole FS-2. Although these seasonal variations in hydraulic head may be as large as 1.0 to 1.5 m, they do not substantially change the general pattern of ground-water movement at the study site. The ground-water flow system remains dominated by vertical flow throughout the year.

The dominant vertical gradient at the study site is controlled by the presence of a flat-lying, high-permeability fracture zone (No. 1) of low hydraulic head located at a depth of 33 to 50 m. The fracture zone, which intersects the test intervals FS 5-1, 7-3, 8-2, 9-2, 10-1, 13-2, 15-1, 16-2 and 17-1, has uniform hydraulic head throughout the study site and acts as a boundary of constant hydraulic head. Analyses of the seasonal hydraulic head response in fracture zone No. 1 and in the overlying rock mass (Raven and Smedley, 1982) suggest that the hydraulic head within fracture zone No. 1 is controlled by surface infiltration and hydraulic head conditions acting in isolated areas within the study site or outside the investigation area of the study site. The influence of isolated or remote hydraulic head and infiltration characteristics on the study site flow system is also shown in Table 16. Hydraulic head data for fracture zone No. 1 and all intermediate to deep test intervals are approximately 1.0 m lower during November 1984 than during December 1982. Yet only a few near-surface test intervals show any significant hydraulic head variation between those two dates, suggesting relatively uniform conditions of surface infiltration throughout most of the study site. Therefore, the cause of the hydraulic head change at depth is isolated to selected areas within or remote from the study site. Test intervals in borehole FS-7, located adjacent to the vertical fracture zone No. 4 in the northwest corner of the study site, show the most consistent lowering of hydraulic head from surface to depth. These hydraulic response data in conjunction with other hydrogeologic data from hydraulic testing and ground-water sampling suggest the hydraulic head in fracture zone No. 1 and ultimately in all intermediate to deep test intervals is likely controlled through vertical fracture zone No. 4 by a swamp located immediately northwest of borehole FS-7.

The behaviour of the flow system studied at CRNL under varying infiltration conditions indicates that ground-water flow over an area of 200 m by 150 m and to a depth

of 50 m may be controlled by hydraulic head conditions in a remote, relatively small discharge area.

The hydraulic head record for intervals in borehole FS-2 also shows the important short-circuiting effect of open or uncased boreholes on the distribution of hydraulic head in adjacent cased boreholes. During May 1983, boreholes FS-15, 16 and 17 were drilled and left uncased until approximately mid-September, 1983. During diamond drilling of borehole FS-17, a sharp increase in hydraulic head was observed in test intervals FS 2-1, 2-2 and 2-3, confirming hydraulic connection between the test intervals and borehole FS-17. After completion of drilling the hydraulic head data for intervals FS 2-1, 2-2 and 2-3 were about 1.0 m lower than before drilling. This drop in hydraulic head is greater than that attributable to decreasing surface infiltration and reflects drainage of the rock mass in the vicinity of borehole FS-2 along fracture zones No. 2 and No. 4 to borehole FS-17 and down borehole FS-17 to fracture zone No. 1. With the installation of casing in borehole FS-17 in mid-September 1983, fluid levels in the test intervals FS 2-1, 2-2 and 2-3 began to rise to values more representative of the rock mass surrounding borehole FS-2.

Complete and detailed records of hydraulic head were collected for 90 test intervals during drawdown and recovery phases of pump tests from borehole FS-10 in August 1982 and in September 1983. The drawdown records of responding test intervals (all intervals except those in boreholes FS-12 and 14) are plotted on drawdown versus log-time diagrams in Appendix C. These plots are the most complete set of transient hydraulic head response data for the study site. These data are currently being used to evaluate specific storage properties of the rock mass and the ability of numerical models to simulate flow under transient conditions.

Fracture Zones Nos. 1, 2, 3 and 4

Equilibrium hydraulic head data were obtained from 9, 7 and 7 test intervals intersecting fracture zones Nos. 1, 2 and 3, respectively. Assuming the fracture zones are open or hydraulically connected at all points within the areas defined by borehole intersections, the hydraulic head data have been used to estimate the general pattern of ground-water movement within the fracture zones. No effort has been made to include far-field boundary conditions of each fracture zone on the resulting flow pattern diagrams.

Fracture zone No. 1 is intersected by test intervals FS 5-1, 7-3, 8-2, 9-2, 10-1, 13-2, 15-1, 16-2 and 17-1. As evident in Table 16, the hydraulic head values for all those test intervals except FS 15-1 are, within measurement limits (± 0.01 m), essentially identical. These hydraulic head

data suggest maximum hydraulic gradients of 0.0001 which are likely directed to the north. Test interval FS 15-1 shows an equilibrium hydraulic head 0.90 m higher than the value within the rest of the fracture zone. This suggests a region of reduced permeability in fracture zone No. 1 in the vicinity of borehole FS-15 with recharge effects dominating the local hydraulic head distribution within the fracture zone. The low hydraulic gradients throughout fracture zone No. 1 are consistent with the high hydraulic conductivity of the fracture zone measured by hydraulic testing.

Fracture zone No. 2 is intersected by test intervals FS 1-2, 2-1, 3-2, 4-2, 5-2, 7-4 and 17-3. As evident for fracture zone No. 1, equilibrium hydraulic heads within fracture zone No. 2 are approximately 1.0 m lower on November 1, 1984, than on December 15, 1982. However, the pattern of ground-water flow is similar on both dates. Figure 35 shows the estimated patterns of ground-water movement within the fracture zone on these dates. Ground-water flows to the north and northwest with an average hydraulic gradient of 0.01 to 0.02. Some local recharge indicated by hydraulic head mounding is evident in the vicinity of borehole FS-3 on November 1, 1984.

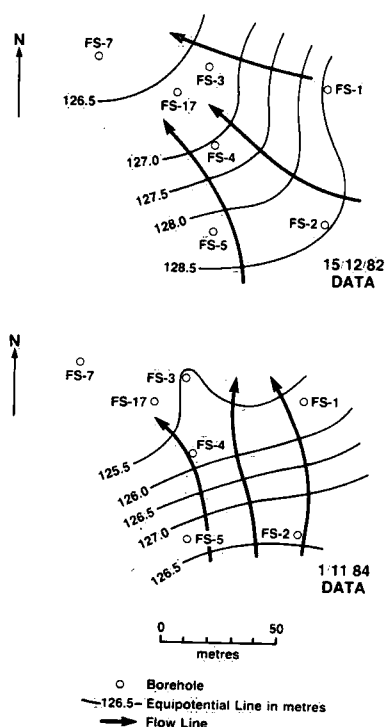


Figure 35. Patterns of ground-water flow in fracture zone No. 2 estimated from equilibrium hydraulic head data recorded on December 15, 1982, and on November 1, 1984.

Fracture zone No. 3 is intersected by test intervals FS 2-1, 6-1, 10-4, 11-2, 13-4, 15-3 and 16-3 and dips about

25° to the northeast. Hydraulic heads in this fracture zone are also about 1.0 m less on November 1, 1984, than on December 15, 1982. However, the patterns of ground-water movement are significantly different on these dates, principally as a result of lowering of hydraulic head in test interval FS 10-4. The hydraulic head in test interval FS 10-4 was lowered about 5 m by removing the borehole casing and permitting drainage between fracture zone No. 3 and No. 1. The patterns of ground-water movement in fracture zone No. 3 on these two dates are shown in Figure 36. On December 15, 1982, flow was directed down dip to the northeast with hydraulic gradients of 0.02 to 0.1. On November 1, 1984, ground-water movement was directed to the northwest toward borehole FS-10 with hydraulic gradients of 0.03 to 0.2. On both dates the lowest hydraulic gradients were observed in the areas of highest fracture permeability near boreholes FS-6, 11 and 15.

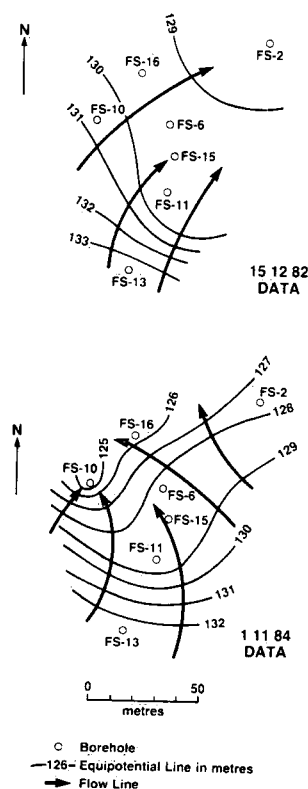


Figure 36. Patterns of ground-water flow in fracture zone No. 3 estimated from equilibrium hydraulic head data recorded on December 15, 1982, and on November 1, 1984. Borehole FS-10 was completed with multiple-packer casing on December 15, 1982, and was uncased or open on November 1, 1984.

Ground-water flow patterns within vertical fracture zone No. 4 are more difficult to evaluate because of limited borehole intersections. However, if we assume that the test intervals FS 4-2, 4-4, 7-1 to 7-7 and 17-1 to 17-3 are

sufficiently close to fracture zone No. 4 to reflect hydraulic head conditions within the fracture zone, we can make some general statements regarding ground-water motion. Ground water appears to flow principally down fracture zone No. 4 with a horizontal component directed toward the northwest. Average vertical gradients decrease from 0.1 to 0.02 from borehole FS-4 to FS-7, and average horizontal gradients between borehole FS-4 and FS-7 are about 0.02.

HYDRAULIC CONDUCTIVITY TENSOR DETERMINATIONS

The hydraulic conductivity of fractured crystalline rock is principally a function of the geometry (spacing, continuity, degree of interconnection and aperture) of the fracture system, as well as a function of the hydraulic conductivity of the rock matrix and any fracture infilling material present. In fractured crystalline rocks, matrix or intact rock permeability is usually negligible compared with the permeability resulting from the fractures. As fractures and their hydraulic properties are distributed three dimensionally in a rock mass, the hydraulic conductivity of a fractured crystalline rock will be both heterogeneous and anisotropic. Attempts to describe the anisotropy and heterogeneity of the hydraulic conductivity field require a three-dimensional characterization of the hydraulic properties of the rock mass. As a first attempt at describing the hydraulic conductivity field at the Chalk River study site, the results of straddle-packer injection tests and of borehole fracture logs have been integrated to develop a tensorial representation of the near-borehole hydraulic conductivity of each test interval.

Model Description

A fracture orientation-aperture (FOA) model (Snow, 1965; Rocha and Franciss, 1975) was used to calculate the hydraulic conductivity tensor for each test interval. The model assumes that fractures may be described as planar conduits continuous in their own planes and that mutual interference effects at fracture intersections are negligible. The model also assumes single phase, non-turbulent flow of an incompressible Newtonian fluid through rock fractures. Rock fractures are represented as smooth parallel plates with uniform separation or opening. The permeability or hydraulic conductivity (K_f) of a smooth parallel-plate fracture is:

$$K_f = \frac{(2b)^2 \rho g}{12 \mu} \quad (11)$$

where $2b$ = aperture or opening of fracture,
 g = acceleration of gravity,
 μ = dynamic viscosity of fluid, and
 ρ = fluid density.

The hydraulic conductivity tensor, or ellipsoid, for a test interval is determined by summing the permeability contribution of individual fractures within the test interval. The contribution of each fracture is determined by calculating the permeability of a cubic element of a continuous medium having sides equal to the effective fracture spacing. Thus discharge through the face of the cube is equal to discharge of the fracture under the same gradient.

For fracture orientation data collected from borehole investigations, the effective fracture spacing is the distance between a fracture and its repetition image at a distance L equal to the test interval or sampling line length (Bianchi and Snow, 1969). In equation form:

$$W = L |n_i \cdot D_i| \quad (12)$$

where W = effective fracture spacing,

L = test interval or sampling line length,

n_i = direction cosines of normal to fracture, and

D_i = direction cosines of sample line.

The contribution of a single fracture with aperture $2b$ to the continuous medium permeability tensor is (Snow, 1965):

$$K_{ij} = \frac{\rho g (2b)^3}{12 \mu L |n_i \cdot D_i|} (\delta_{ij} - M_{ij}) \quad (13)$$

where K_{ij} = hydraulic conductivity tensor of an equivalent continuous medium,

δ_{ij} = Kronecker delta, and

M_{ij} = a 3×3 matrix formed by the direction cosines of the normal to the conduit.

By summing the contribution of individual fractures and diagonalizing the resulting symmetric tensor, the principal hydraulic conductivities and associated principal directions of an equivalent continuous medium are calculated. Thus the FOA model employed in this analysis computes the permeability tensor of a continuous porous media equivalent to the rock mass. However, these calculations are based upon individual fracture characteristics. Because the fracture orientation-aperture model disregards finite fracture length it can generally be expected to overestimate rock mass hydraulic conductivity.

To determine the principal hydraulic conductivities, information on fracture aperture and orientation is required. Fracture orientation data were obtained from both borehole television and acoustic televiewer surveys. For this model, however, fracture orientations have been determined only from borehole acoustic televiewer surveys.

Fracture apertures were estimated indirectly from the results of injection tests. For this initial calculation we have assumed that all fractures within a 1.5- to 2.0-m injection test interval are equally conductive. It is recognized that fractures within an injection test interval probably do not contribute equally to flow. However, from a practical standpoint, given the close spacing of fractures in several borehole intervals, it would be impossible to resolve the individual permeabilities of fractures with small packer spacings and thus some averaging is inevitable. A distribution of fracture apertures is ensured in most casing test intervals, as these latter intervals generally are made up of several injection test intervals.

Individual fracture apertures were determined from flow rate per unit head data by the application of the following equation based on the parallel-plate model.

$$2b_{\text{eff}} = \left\{ \frac{Q}{\Delta H N} \frac{12\mu}{2\pi\rho g} \ln(r_b/r_w) \right\}^{1/3} \quad (14)$$

where $2b_{\text{eff}}$ = effective fracture aperture,
 r_b = radius of influence of injection test, assumed to be 10 m,
 r_w = radius of borehole,
 $Q/\Delta H$ = flow rate per unit injection head, and
 N = number of conductive fractures in an injection test interval.

As evident in Equation 14, no attempt has been made to correct fracture aperture estimates for fractures which intersect the borehole axis at angles other than 90° .

Over 1400 estimates of effective fracture aperture were determined from injection tests and borehole fracture logs measured in 17 boreholes. Calculated apertures ranged from 1.5 to 500 μm with a geometric mean of 11.8 μm . The distribution of effective fracture apertures for the entire study site is shown in Figure 37.

Results

A hydraulic conductivity tensor, K_{ij} , was determined for each packer-isolated test interval by summing the effective permeability contributions of individual fractures. The resultant symmetric tensor, K_{ij} , was diagonalized to determine the principal hydraulic conductivities (eigenvalues) and the principal directions (eigenvectors). The principal hydraulic conductivities (K_1 , K_2 and K_3) in three orthogonal directions define a hydraulic conductivity ellipsoid, as shown in Figure 38. The principal directions relative to three geographic reference axes are defined by three direction cosines (i.e. l_1 , m_1 , n_1 , for K_1). Geographic reference axes used in this report are X_1 pointing south, X_2 pointing

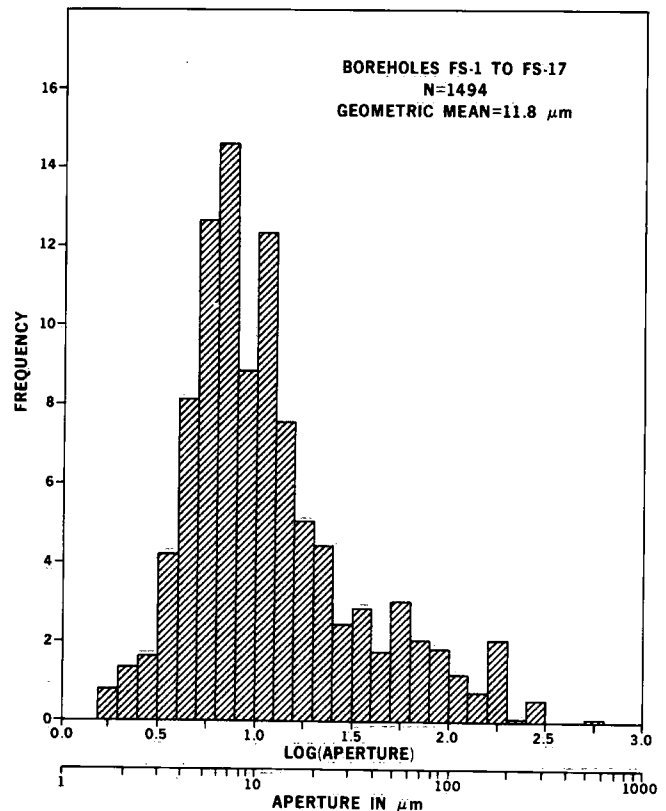


Figure 37. Distribution of the common logarithm of effective fracture aperture, $2b_{\text{eff}}$, in boreholes FS-1 to FS-17 determined from straddle-packer injection tests and borehole acoustic televiewer logs.

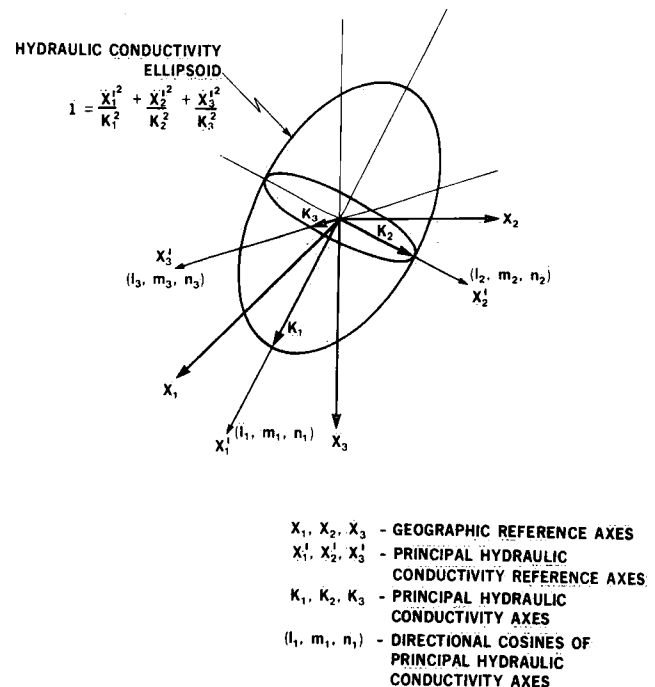


Figure 38. Hydraulic conductivity ellipsoid and reference axes in three directions.

east and X_3 pointing downward. The principal hydraulic conductivities and principal directions for each packer-isolated test interval are listed in Appendix D. The geometric mean of the K_1K_2 principal hydraulic conductivity plane and the anisotropy ratio K_1/K_3 were calculated and are also shown in Appendix D.

Principal hydraulic conductivities listed in Appendix D range from 10^{-11} to $10^{-5} \text{ m}\cdot\text{s}^{-1}$ with anisotropy ratios between 1 and 10, although some values in excess of 100 were calculated for test intervals with only a few fractures and all of them with a similar orientation. Because of the number and general scatter of fracture orientations (Figs. 8 and 9), the relatively low anisotropy ratios are not unexpected. However, it is important to note that the principal hydraulic conductivities shown in Appendix D do not consider the significant effect of individual high-permeability fractures such as fracture zones Nos. 1, 2, 3 and 4. The effects of these high-permeability fractures are averaged with other less-permeable fractures located within a straddle-packer test interval.

The hydraulic conductivity ellipsoids calculated for each test interval in Appendix D are generally spheroidal to oblate spheroidal. With increasing anisotropy ratio the spheroids become more oblate or flattened as the minor principal hydraulic conductivity K_3 decreases. In general, regardless of anisotropy ratio, the K_1 and K_2 hydraulic conductivities are similar for each test interval. Thus each hydraulic conductivity plane maybe defined in part by the major (K_1) and intermediate (K_2) principal hydraulic conductivities. The geometric mean and orientation of the K_1K_2 principal hydraulic conductivity plane have been used to compare hydraulic conductivity ellipsoids on stereographic plots.

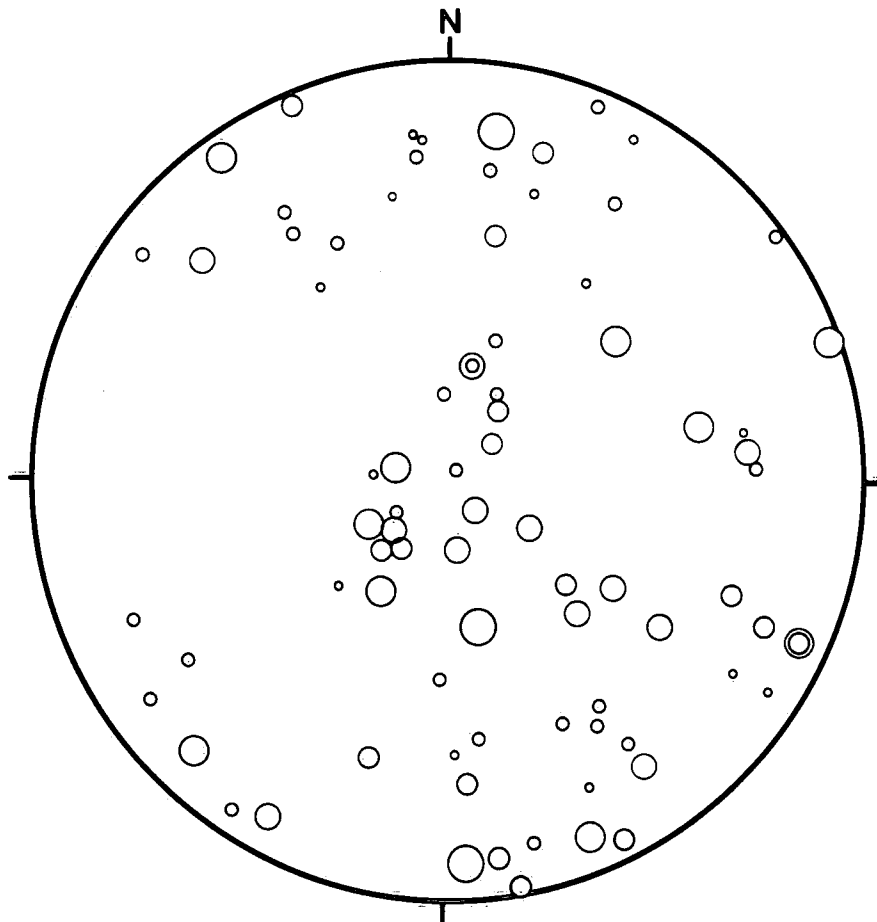
The poles to the K_1 , K_2 principal hydraulic conductivity planes, or K_3 axes, are plotted in Figure 39. The magnitude of geometric mean of the K_1K_2 plane has been represented by circles of variable diameter for each pole. The circle diameters are proportional to the common logarithm of the geometric mean of the K_1K_2 plane calculated in metres per second.

Figure 39 shows a large amount of scatter in the orientation of the principal hydraulic conductivity planes. Nevertheless, some clustering of K_3 poles is evident on the stereographic plot, suggesting preferred directions of permeability in the rock mass at the scale of the study site. From visual inspection of Figure 39, the permeability is greater in the following planes: subhorizontal, east-northeast striking and steeply dipping to the northwest, and to a lesser degree east-southeast striking and steeply dipping to the southwest. These directions of higher permeability correspond to the orientation of three major

fracture sets identified from borehole logging (Fig. 8 and Table 3). This correspondence is not unexpected, as the anisotropy of the hydraulic conductivity tensors is determined from the orientation of the borehole fractures. The large number of poles to the K_1K_2 principal hydraulic conductivity plane clustered in the centre of the plot relative to the borehole fracture polar plot (Fig. 8) suggests the subhorizontal fractures may possess larger apertures than the subvertical fracture sets. However, the higher permeabilities in the horizontal plane may also result from orientation bias. The Terzaghi correction for orientation bias was not used in calculating the permeability tensors of each test interval.

It is difficult to assess the reliability of the hydraulic conductivity tensors determined from the FOA model. Certainly, the geometric mean of the hydraulic conductivity ellipsoid, i.e. $(K_1K_2K_3)^{1/3}$ for each test interval, is, as expected, nearly identical with the equivalent rock mass hydraulic conductivity (K_{erm}) determined from injection tests (Table 6). However, an independent measure of the hydraulic conductivity properties of the rock mass is required for reliable assessment of the FOA model.

Vertical response in the rock mass from pumping fracture zone No. 1 provides an independent estimate of the vertical flow properties of the rock mass for comparison with the results from the fracture orientation-aperture model. However, the comparison is not straightforward. Vertical hydraulic diffusivity (see section on "Vertical Flow Properties of the Rock Mass") is determined from the vertical response monitoring, whereas vertical hydraulic conductivity is calculated from the FOA model. An estimate of specific storage, S_s , is required to calculate vertical hydraulic conductivity from vertical hydraulic diffusivity. To overcome this difficulty we have plotted (Fig. 40) vertical hydraulic diffusivity K_V calculated from pump test response (Table 6) against vertical hydraulic conductivity K_V determined from the fracture orientation-aperture model. Some averaging is necessary to compare the hydraulic diffusivity, which measures the vertical flow properties between FS test intervals, with the hydraulic conductivity, which is calculated for each FS test interval. The harmonic mean of vertical hydraulic conductivity was determined between FS test intervals for comparison with the vertical diffusivity in Figure 40. Lines identifying the range of specific storages required for the hydraulic diffusivity values to be equal to the hydraulic conductivity estimates are shown on Figure 40. Most of the data points fall between the specific storage lines 10^{-6} to 10^{-4} , but with significant scatter. The central or average value of specific storage is about 10^{-5} . The spread in data points is similar for test intervals that are close to high permeability fracture zones (i.e. fracture zone No. 4) and for test intervals in more uniformly fractured rock.



**POLES TO K_1, K_2 PRINCIPAL
HYDRAULIC CONDUCTIVITY PLANE.
LOWER HEMISPHERE
EQUAL AREA PROJECTION.**

**LOGARITHM OF
GEOMETRIC MEAN OF
 K_1, K_2 PRINCIPAL HYDRAULIC
CONDUCTIVITY AXES
IN m/s, $\text{Log } (K_1 K_2)^{1/2}$**

- < -9.0
- $-9.0 - -8.0$
- $-8.0 - -7.0$
- $-7.0 - -6.0$
- $-6.0 - -5.0$
- > -5.0

**Figure 39. Stereographic plot of poles to K_1, K_2 principal hydraulic conductivity planes for FS test intervals.
Hydraulic conductivity tensors determined from acoustic televiewer fracture logs and injection test data.**

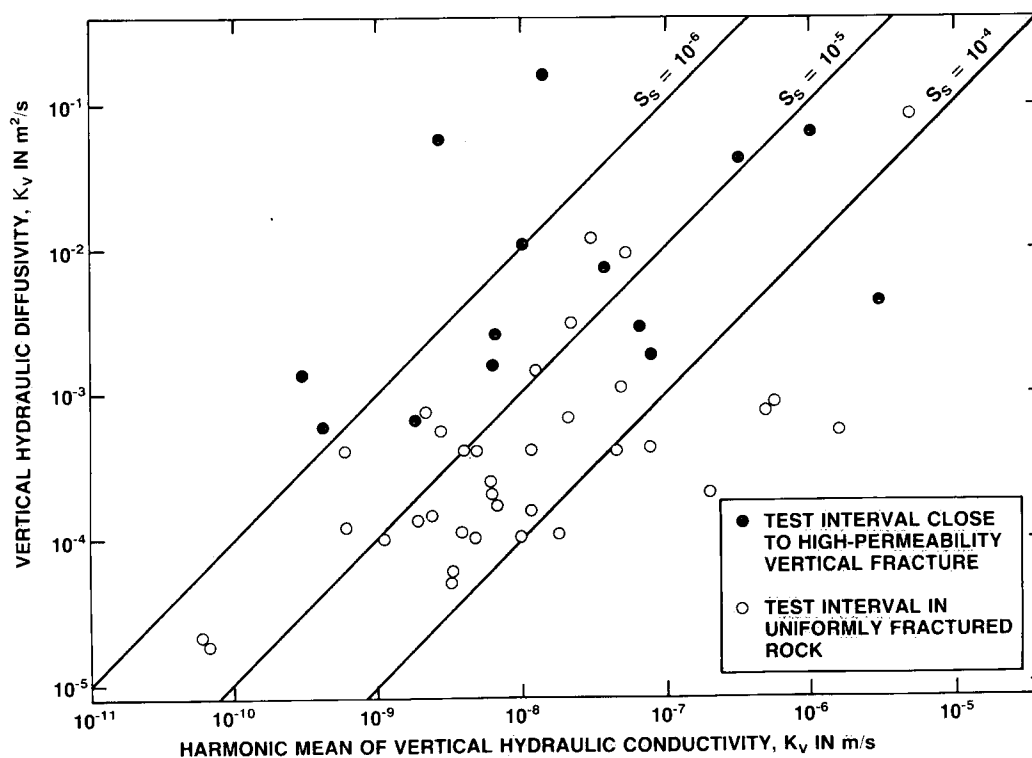


Figure 40. Plot of vertical hydraulic diffusivity determined from pump tests versus the harmonic mean of vertical hydraulic conductivity calculated from the fracture orientation-aperture model. Lines identify values of specific storage required for the vertical hydraulic conductivity to equal the vertical hydraulic diffusivity.

The range of specific storages required for equivalence between the hydraulic diffusivity and conductivity values is consistent with storage values determined from other hydraulic interference tests. Interference tests completed in fracture zones Nos. 1, 2, 3 and 4 yielded storativities of 10^{-4} to 10^{-6} with an average value of 10^{-5} (results of hydraulic interference tests). For these fracture zones the effective width is unity and therefore the storativities are equal to specific storages:

Two-dimensional numerical simulations of steady-state (Raven *et al.*, 1985) and transient ground-water flow at the study site were compared with field hydraulic head data to evaluate the reliability of the hydraulic properties determined by the fracture orientation-aperture model. The results of the steady-state modelling suggest that the FOA model provides reasonable estimates of anisotropic hydraulic conductivity for the upper 30 m of the rock mass but overestimates hydraulic conductivity below the 30-m depth. The transient ground-water flow modelling indicated that an average specific storage value of 10^{-5} was appropriate in describing the drawdown response in the rock mass above fracture zone No. 1.

In summary, the FOA model used in this study appears, based on independent hydraulic property measurement and numerical model simulations, to provide an adequate description of the anisotropic hydraulic conductivity of uniformly fractured rock masses above the 30-m depth. The FOA model is expected to be less reliable in describing the vertical flow properties of a rock mass intersected by high-permeability vertical fracture zones and investigated with vertical boreholes. There is, however, evidence (Fig. 40) to indicate the FOA model may provide a reasonable estimate of the higher vertical hydraulic conductivity resulting from the presence of vertical fractures near the investigating boreholes.

SUMMARY

The hydraulic characteristics of a block of fractured monzonitic gneiss, 200 m by 150 m by 50 m deep, have been measured using surface and borehole methods as part of a study investigating ground-water flow systems in fractured rock. The surface and borehole methods included air photo and geophysical lineament analysis, fracture

mapping and logging, injection and interference testing, and hydraulic head monitoring. The results of these investigations have been combined and interpreted to provide a three-dimensional picture of the ground-water flow system at Chalk River. The investigations also provided fundamental information on ground-water flow systems in fractured rock and the usefulness of various investigative techniques in defining such systems.

The results of studies summarized in this report indicate that large structural features such as fracture zones, faults and dykes play an important role in controlling flow systems in fractured rock. In the CRNL study, large structural discontinuities hydraulically behaved as (1) short-circuiting ground-water flow pathways (i.e. fracture zone No. 4); (2) impermeable ground-water flow boundaries (i.e. diabase dykes); and (3) constant potential ground-water flow boundaries (i.e. fracture zone No. 1). Because of their hydrogeological significance, identification of major structural discontinuities is important in any detailed hydrogeologic study. Air photo lineament analysis, surface and airborne EM-VLF surveys, and surface mapping were valuable tools in identifying and predicting the occurrence of major structural discontinuities in the subsurface. All inclined and steeply dipping major structural discontinuities intersected by boreholes were also identified by these techniques. Subhorizontal fracture zones intersected by boreholes were not detected from surface investigations.

The flow properties of the rock blocks defined by major structural discontinuities result from the interconnection of smaller-scale discontinuous fractures. Statistical characterization of this fracture system is important in estimating hydraulic properties and interpreting hydraulic tests. Several methods of fracture system characterization were successfully used at the CRNL study site. Surface fracture mapping using scan-line surveys identified all major inclined fracture sets to depths of 50 m. Borehole television surveys and borehole acoustic-televiwer logging identified all major fracture sets, both horizontal and inclined. Borehole acoustic-televiwer logging provided superior fracture detection capability in mafic or dark-coloured rock.

Detailed analysis of fracture orientation data from three subareas showed that the fracture system is not statistically homogeneous at the scale of the study site. This spatial variation in fracture characteristics is in part related to the presence or absence of major structural discontinuities in different subareas. This nonhomogeneity in fracture characteristics at the site scale suggests that different parameters or parameter distributions would be required to model reliably the CRNL study site using equivalent porous medium or discrete-stochastic fracture flow modelling methods. Analysis of individual borehole

fracture data (Lau *et al.*, 1984) indicates the suitable size for discretization or characterization of flow properties for use with equivalent porous median models is likely less than a characteristic length determined by average borehole spacing (25-50 m). For the hydraulic conductivity tensors determined in the section on "Hydraulic Conductivity Tensor Determinations," characteristic lengths were determined by the location of casing packers and ranged between 3 and 13 m.

Single-borehole injection tests and multiple-borehole interference tests have proven extremely useful in defining the hydraulic properties of the rock mass. Injection tests provide cost-effective and reliable information on the hydraulic conductivity of the rock mass in the immediate vicinity of the boreholes. Interference tests, which are more difficult to complete and to interpret, provide information on interborehole hydraulic properties. Interference tests require careful design to minimize the effect of borehole and far-field boundary conditions on interborehole hydraulic response.

A fracture orientation-aperture model has been used to integrate fracture orientation and injection test data and calculate a hydraulic conductivity tensor for each FS test interval. The hydraulic conductivity tensors calculated by the model are not highly anisotropic. Also, based on numerical model simulations and independent hydraulic tests, these conductivity tensors appear to provide a reasonable estimate of hydraulic properties of the rock mass above the 30-m depth at CRNL. Below the 30-m depth the model apparently overestimates hydraulic conductivity.

The results of hydraulic testing, fracture logging and hydraulic head monitoring indicate a simple gravity-controlled ground-water flow system occurs at the CRNL study site. Flow in this system is primarily vertical to a low-hydraulic head fracture zone (No. 1) located at 33- to 50-m depth. The horizontal component of flow is directed to the northwest and reflects surface topography. An east-west striking diabase dyke forms a southern impermeable boundary for the flow system. The location of the low-head fracture zone and the diabase dyke is shown together with study site boreholes in Figure 41. The location and orientation of fracture zone No. 1 shown in Figure 41 were determined from nine borehole intersections and various hydraulic interference tests. Hydraulic head within fracture zone No. 1 and most of the intermediate to deep test intervals appear to be controlled through a vertical fracture zone (No. 4) by a surface bog located northwest of the study site.

Four major fracture zones of high permeability (No. 1 to No. 4) were identified at the study site. The locations of

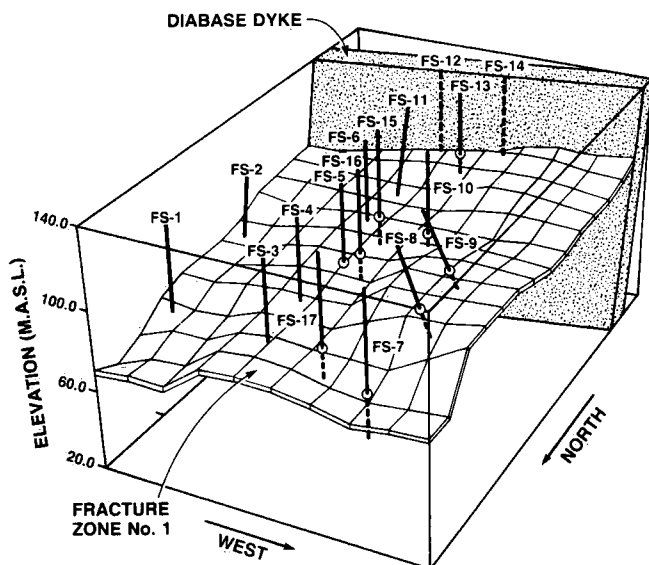


Figure 41. Isometric sketch of CRNL ground-water flow study site showing the location of test boreholes, fracture zone No. 1 and diabase dyke.

fracture zones Nos. 2, 3 and 4 are shown together with study site boreholes in Figure 42. Fracture zones No. 1 and No. 3 and portions of fracture zone No. 2 are characterized by high permeability and the presence of thin (<1 m thick) mafic layers in the monzonitic gneiss. These mafic zones are clearly important hydrogeological features at the CRNL study site.

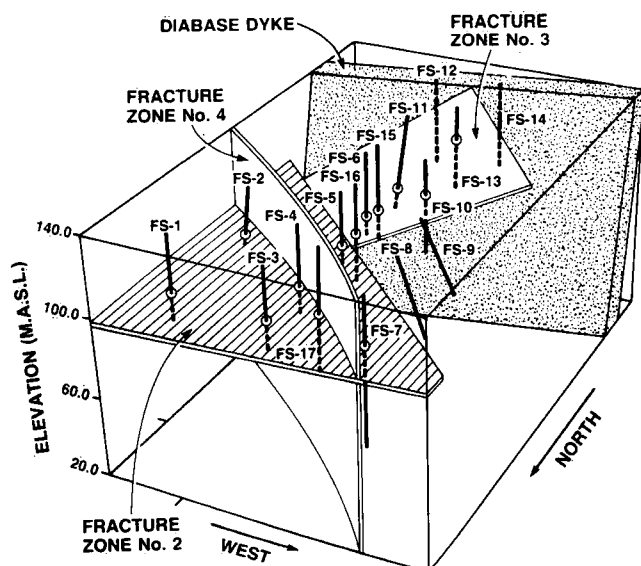


Figure 42. Isometric sketch of CRNL ground-water flow study site showing the location of test boreholes, fracture zones Nos. 2, 3 and 4, and diabase dyke.

The results of this study also suggest that undetected vertical fractures may play an important role in controlling flow within the shallow system at CRNL. Hydraulic interference tests to measure vertical hydraulic diffusivity indicate the presence of vertical fractures and fracture zones (i.e. No. 4). However, the ability to detect vertical fracturing at CRNL is limited by the dominant borehole orientation, i.e., vertical to steeply plunging. Future investigations should include a higher percentage of inclined boreholes in spite of the added difficulty associated with drilling, logging and testing in such boreholes.

REFERENCES

- Argarwal, R.G., R. Al-Hussainy and H.J. Ramey, Jr. 1970. An investigation of wellbore storage and skin effect in unsteady liquid flow. 1. Analytical treatment. *Soc. Pet. Eng. J.* 10(3): 279-290.
- Bianchi, L. and D.T. Snow. 1969. Permeability of crystalline rock interpreted from measured orientations and apertures of fractures. *Ann. Arid Zone*, 8(2): 231-245.
- Brown, P.A. and N.A.C. Rey. 1984. Geologic and structural conditions at Chalk River. *Proc. Workshop on Geophysical and Related Geoscientific Studies at Chalk River*, December, M.D. Thomas and D.F. Dixon (eds.). In press.
- Brown, P.A. and R.H. Thivierge. 1977. General geology, fracturing and drill site selection — CRNL. *Geol. Surv. Can.* unpublished report GD-PR-817.
- Cooper, H.H., Jr. and C.E. Jacob. 1946. A generalized graphical method for evaluating formation constants and summarizing well field history. *Trans. Am. Geophys. Union*, 27: 526-534.
- Dence, M.R. and W.J. Scott. 1980. The Use of Geophysics in the Canadian Nuclear Fuel Waste Management Program with Examples from the Chalk River Research Areas. *At. Energy Can. Ltd. Technical Record*, TR-102.¹
- Earlougher, R.C., Jr. 1977. Advances in well test analysis. *Soc. Pet. Eng. of AIME Special Monograph*, Volume 5.
- Gale, J.E. 1977. A numerical, field and laboratory study of flow in rocks with deformable fractures. *Scientific Series No. 72*, National Hydrology Research Institute, Inland Waters Directorate, Environment Canada, Ottawa.
- Gale, J.E., C. Forster and R. Nadon. 1979. Permeability of fractured low-permeability rocks. *Final Report to Lawrence Berkeley Laboratory, Waterloo Research Institute Project No. 803-12*, University of Waterloo, Waterloo, Ontario.
- Gringarten, A.C. 1982. Flow-test evaluation of fractured reservoirs. In *Geol. Soc. Am. Special Pap. 189, Recent Trends in Hydrogeology*, pp. 237-263.
- Gringarten, A.C. and H.J. Ramey, Jr. 1974. Unsteady-state pressure distributions created by a well with a single horizontal fracture, partial penetration, or restricted entry. *Soc. Pet. Eng. J.* 14(4): 413-426.
- Gringarten, A.C., H.J. Ramey, Jr. and R. Raghavan. 1972. Pressure analysis for fractured wells. *Soc. Pet. Eng. Pap. 4051* presented SPE AIME 47th annual meeting, San Antonio, Texas, October.

¹Atomic Energy of Canada Limited Technical Records are unrestricted, unpublished reports available from the Scientific Documents Distribution Office, Atomic Energy of Canada Limited Research Company, Chalk River, Ontario, K0J 1J0.

- Hanshaw, B.B. and J.D. Bredehoeft. 1968. On the maintenance of anomalous fluid pressures. II. Source layer at depth. *Geol. Soc. Am. Bull.* 79: 1107-1122.
- Hirasaki, G.J. 1974. Pulse tests and other early transient pressure analyses for in-situ estimation of vertical permeability. *Soc. Pet. Eng. J. Trans.* 257: 75-90.
- Hurst, W. 1953. Establishment of the skin effect and its impediment to fluid flow in a wellbore. *Pet. Eng.* 25: B-6.
- Hvorslev, M.J. 1951. Time lag and soil permeability in groundwater observations. *Bull.* 36, Waterways Experiment Station, U.S. Army Corps Eng., Vicksburg, Mississippi.
- Jargon, J.R. 1976. Effect of wellbore storage and wellbore damage at the active well on interference test analysis. *J. Pet. Technol.*, pp. 851-858.
- Lau, J.S.O. 1980. Borehole Television Survey, Underground Rock Engineering, *CIM Special Volume* 22, pp. 204-210.
- Lau, J.S.O., L.F. Auger and J.G. Bisson. 1984. Borehole television survey and acoustic televiewer logging at the National Hydrology Research Institute's hydrogeologic test site at Chalk River. *Proc. Workshop on Geophysical and Related Geoscientific Studies at Chalk River*, M.D. Thomas and D.F. Dixon (eds.). In press.
- Lumbers, S.B. 1974. Precambrian geology, Mattawa - Deep River Area, District of Nipissing and County of Renfrew, Ontario Department of Mines Miscellaneous Pap. 59.
- Neuman, S.P. and P.A. Witherspoon. 1972. Field determination of the hydraulic properties of leaky multiple aquifer systems. *Water Resour. Res.* 8(5): 1284-1298.
- Papadopoulos, I.S. and H.H. Cooper, Jr. 1967. Drawdown in a well of large diameter. *Water Resour. Res.* 3(1): 241-244.
- Priest, S.D. and J.A. Hudson. 1981. Estimation of discontinuity spacing and trace length using scanline surveys. *Int. J. Rock Mech. Min. Sci. and Geomech. Abstr.* 18, pp. 183-197.
- Raghavan, R. 1977. Pressure behaviour of wells intercepting fractures. *Proc. Invitational Well-Testing Symp.*, October 19-21, Berkeley, California, Lawrence Berkeley Laboratory Rep. 7027, pp. 117-160.
- Ramey, H.J., Jr. 1970. Short time well test data interpretation in the presence of skin effect and wellbore storage. *J. Pet. Technol.* 22(1): 97-104.
- Raven, K.G. 1980. Studies in Fracture Hydrology at Chalk River Nuclear Laboratories: 1977/78/79. *At. Energy Can. Ltd. Technical Record*, TR-113.¹
- Raven, K.G. and J.A. Smedley. 1982. CRNL ground water flow study - summary of FY 1981 research activities, unpublished National Hydrology Research Institute report submitted to Atomic Energy of Canada Ltd. for publication as AECL Technical Record.¹
- Raven, K.G., J.A. Smedley, R.A. Sweezey and K.S. Novakowski. 1985. Field investigations of a small ground water flow system in fractured monzonitic gneiss. *Proc. 17th Int. Assoc. of Hydrogeologists Meeting, Hydrogeology of Rocks of Low Permeability*, Tucson, Arizona, January 7-11.
- Rocha, M. and F. Franciss. 1975. Determination of permeability in anisotropic rock masses from integral samples. *Rock Mech.* 9: 67-93.
- Rouleau, A. 1984. Statistical characterization and numerical simulation of a fracture system - application to groundwater flow in the Stripa granite. Ph.D. Thesis, University of Waterloo, Waterloo, Ontario.
- Scott, W.J. 1984. VLF surveys at Chalk River. *Proc. Workshop on Geophysical and Related Geoscientific Studies at Chalk River*, December, M.D. Thomas and D.F. Dixon (eds.). In press.
- Sinha, A.K. and J.G. Hayles. 1984. Surface electromagnetic surveys at Chalk River. *Proc. Workshop on Geophysical and Related Geoscientific Studies at Chalk River*, December, M.D. Thomas and D.F. Dixon (eds.). In press.
- Snow, D.T. 1965. A parallel plate model of fractured permeable media. Ph.D. Thesis, University of California, Berkeley.
- Terzaghi, R.D. 1965. Sources of error in joint surveys. *Geotechnique*, 15: 287-304.
- van Everdingen, A.F. 1953. The skin effect and its influence on the productive capacity of a well. *Am. Inst. Min. Eng. Trans.* 198: 171-176.
- Wolfe, R.G. 1970. Field and laboratory determination of the hydraulic diffusivity of a confining bed. *Water Resour. Res.* 6(1): 194-202.
- Zemanek, J., R.L. Caldwell, E.E. Glen, S.V. Halcomb, L.J. Norton and A.J.D. Strauss. 1969. The borehole televiewer - a new logging concept for fracture location and other types of borehole inspection. *J. Pet. Technol.* 21: 762-774.

Appendix A
Fracture Hydrology Logs, Boreholes
FS-1 to FS-17

APPENDIX A

FRACTURE HYDROLOGY LOGS, BOREHOLES FS-1 TO FS-17

Lithologic data were determined from 1.5-m interval chip samples collected during drilling for boreholes FS-1 to FS-14 and from recovered core for boreholes FS-15 to FS-17.

Fractures and veins identified by borehole television are plotted as a straight line connecting the high and low points of the elliptical borehole wall trace.

Fractures and veins identified by acoustic televiewer are

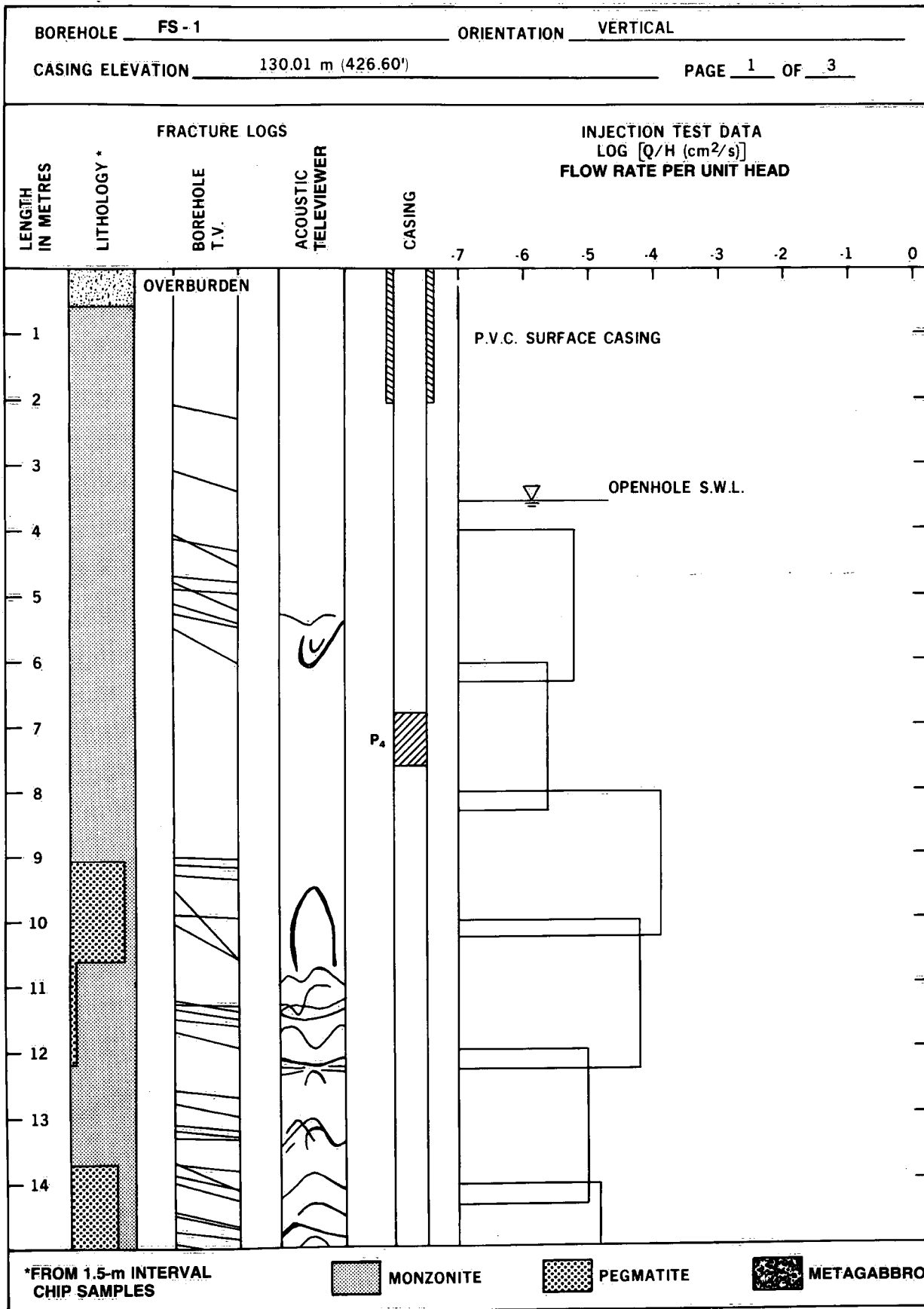
schematically represented as they appeared on the 360° photographs of the borehole wall over 0.5-m intervals.

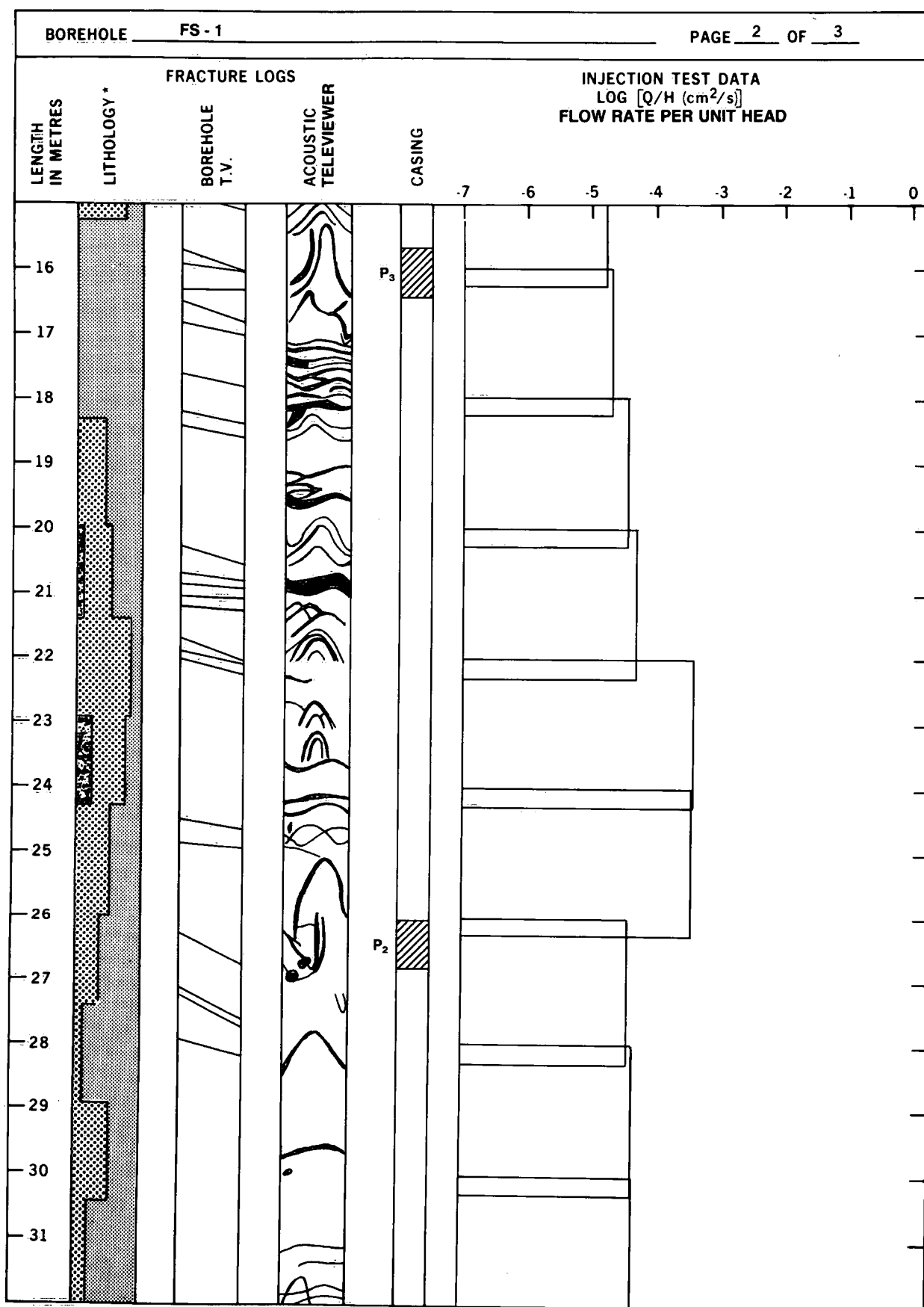
Borehole casing packers are identified as P₁, P₂, etc.

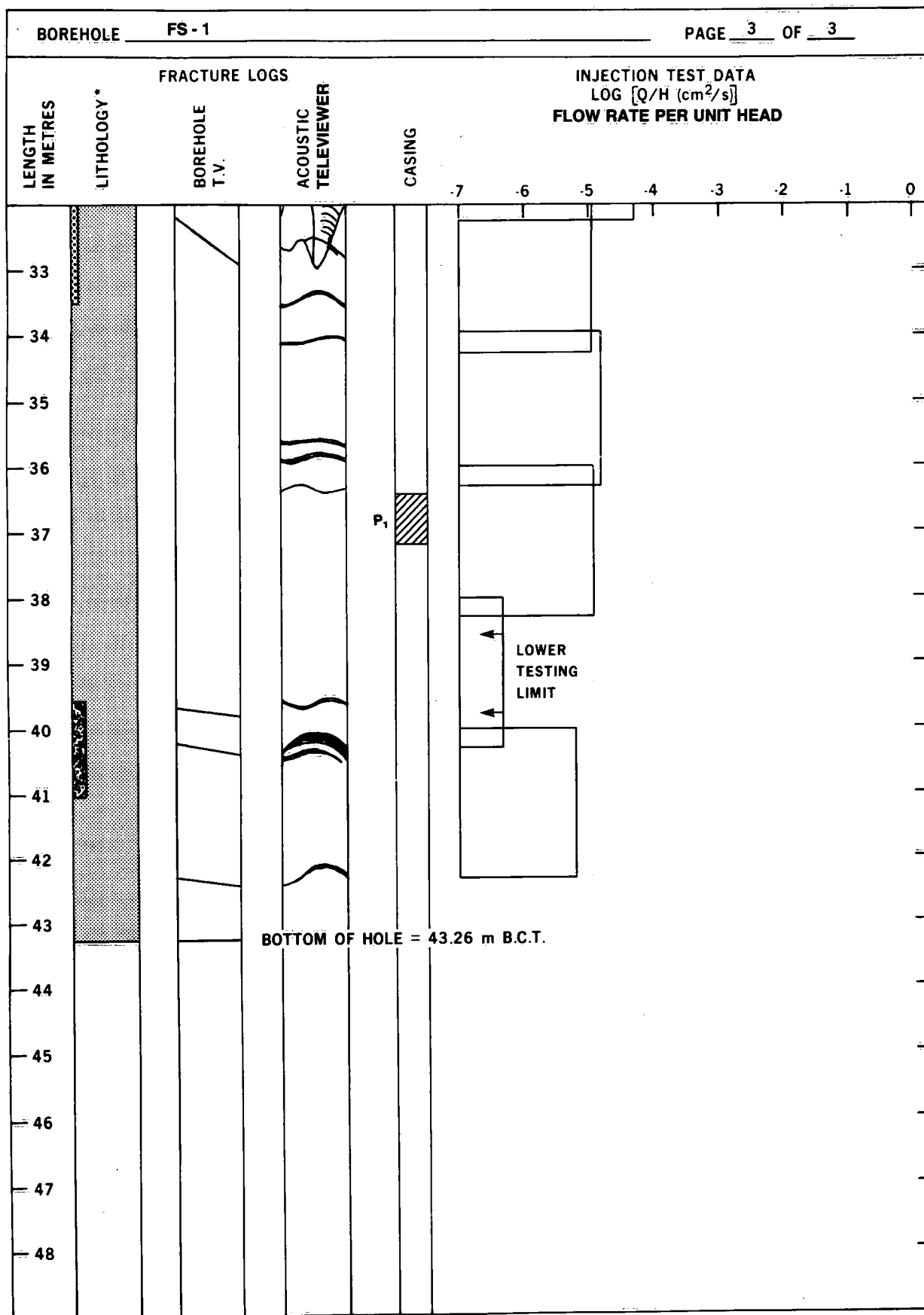
Flow rate per unit head data are from short-term, straddle-packer injection tests.

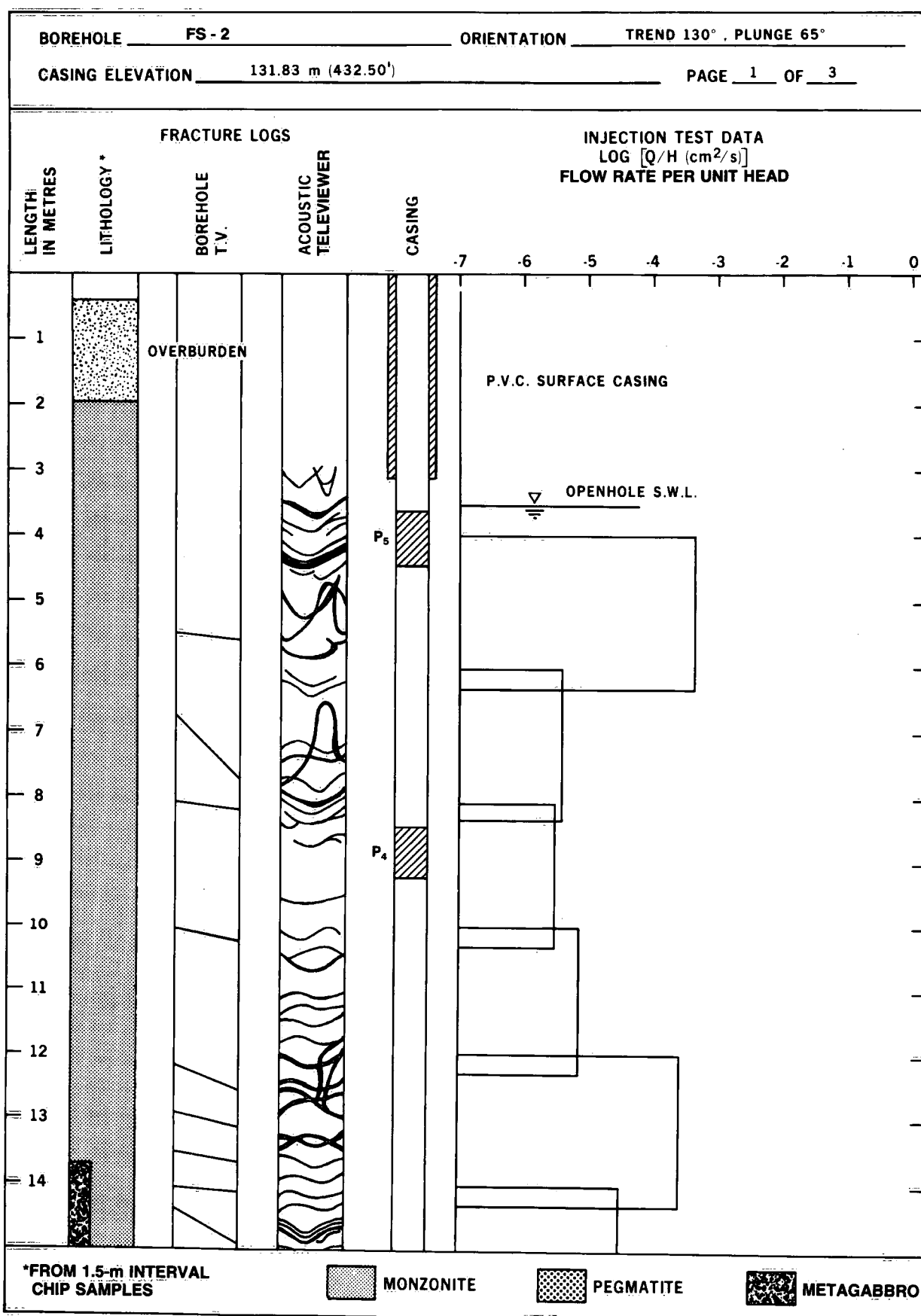
S.W.L. — Static water level.

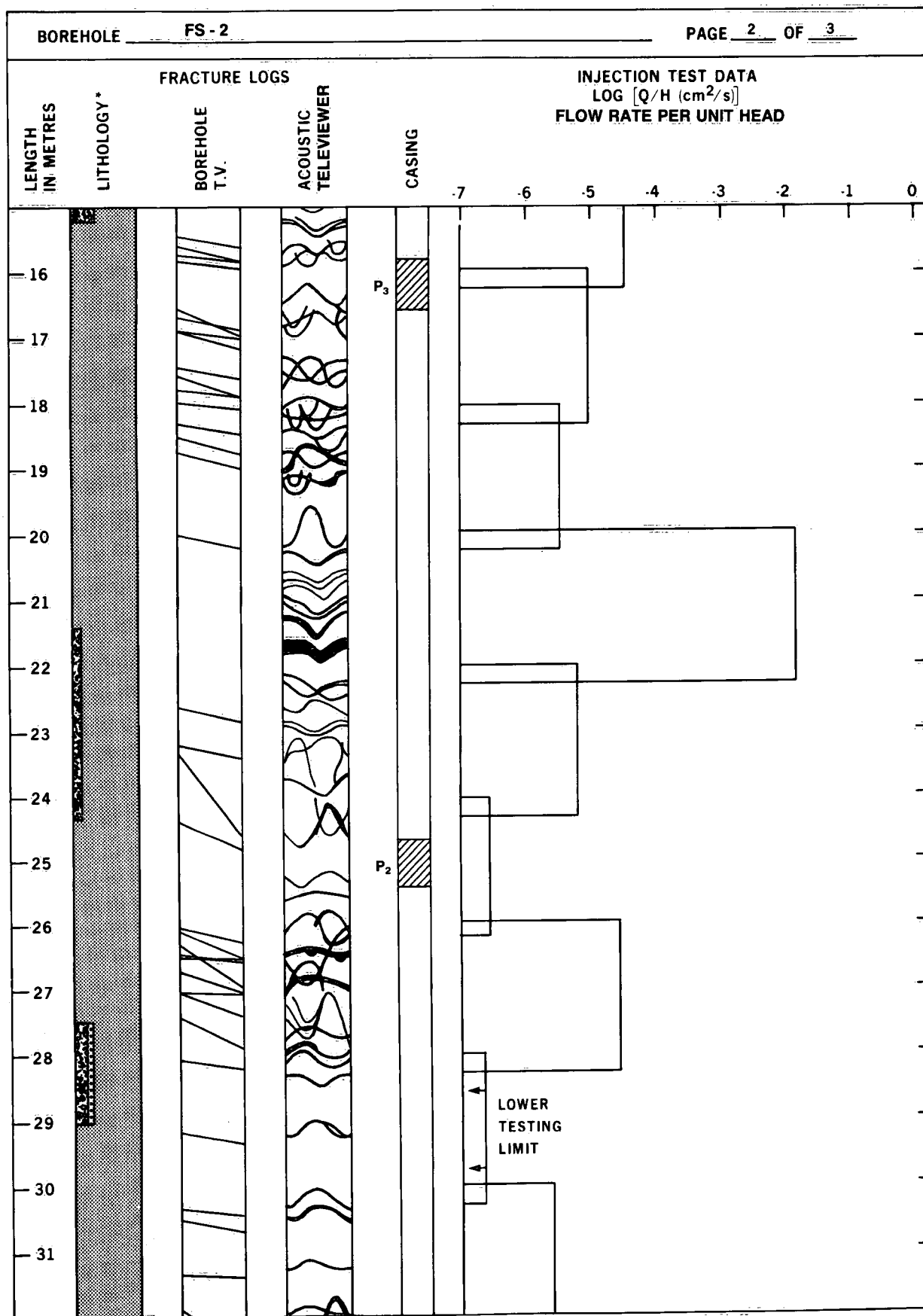
B.C.T. — Below casing top.

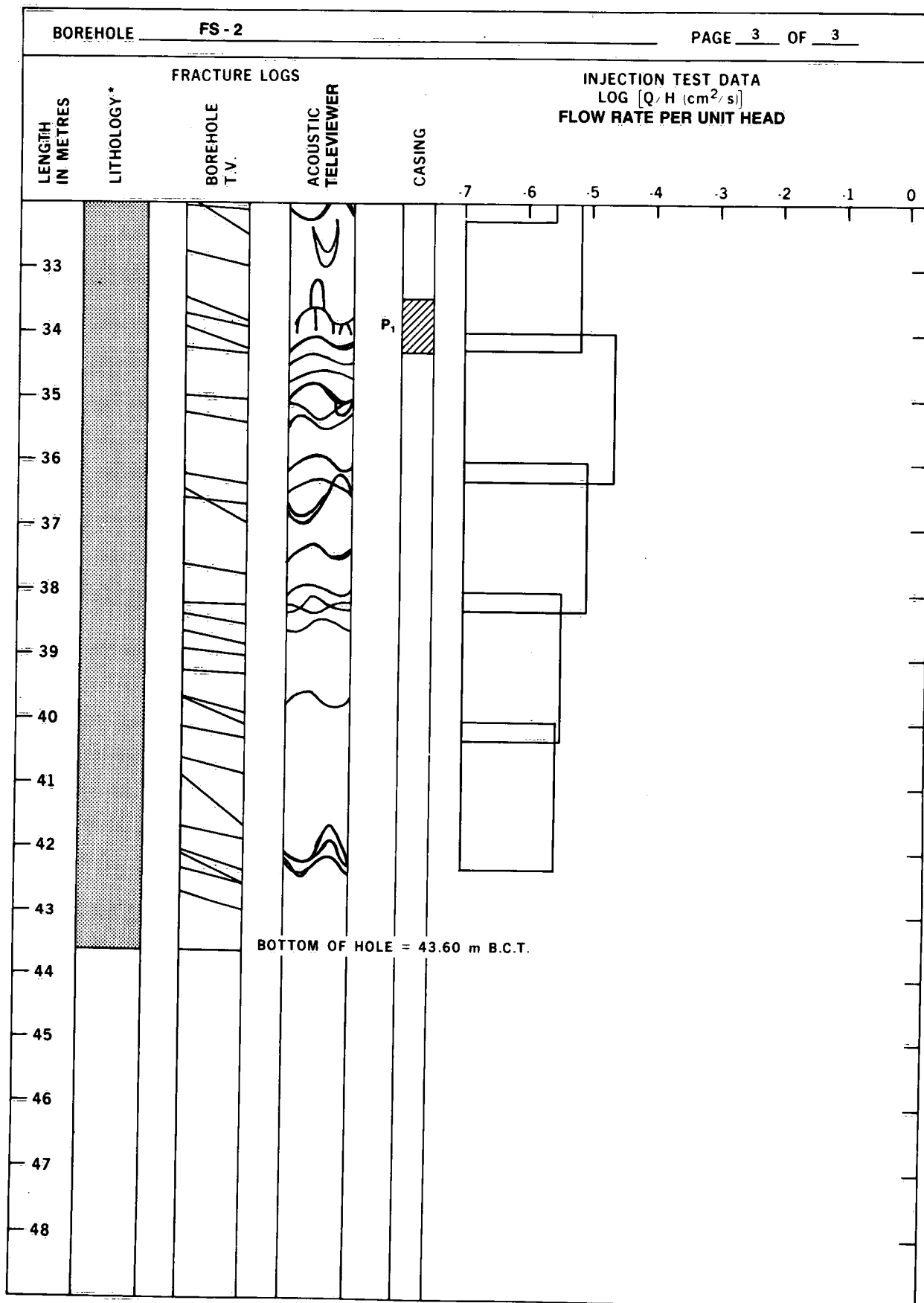


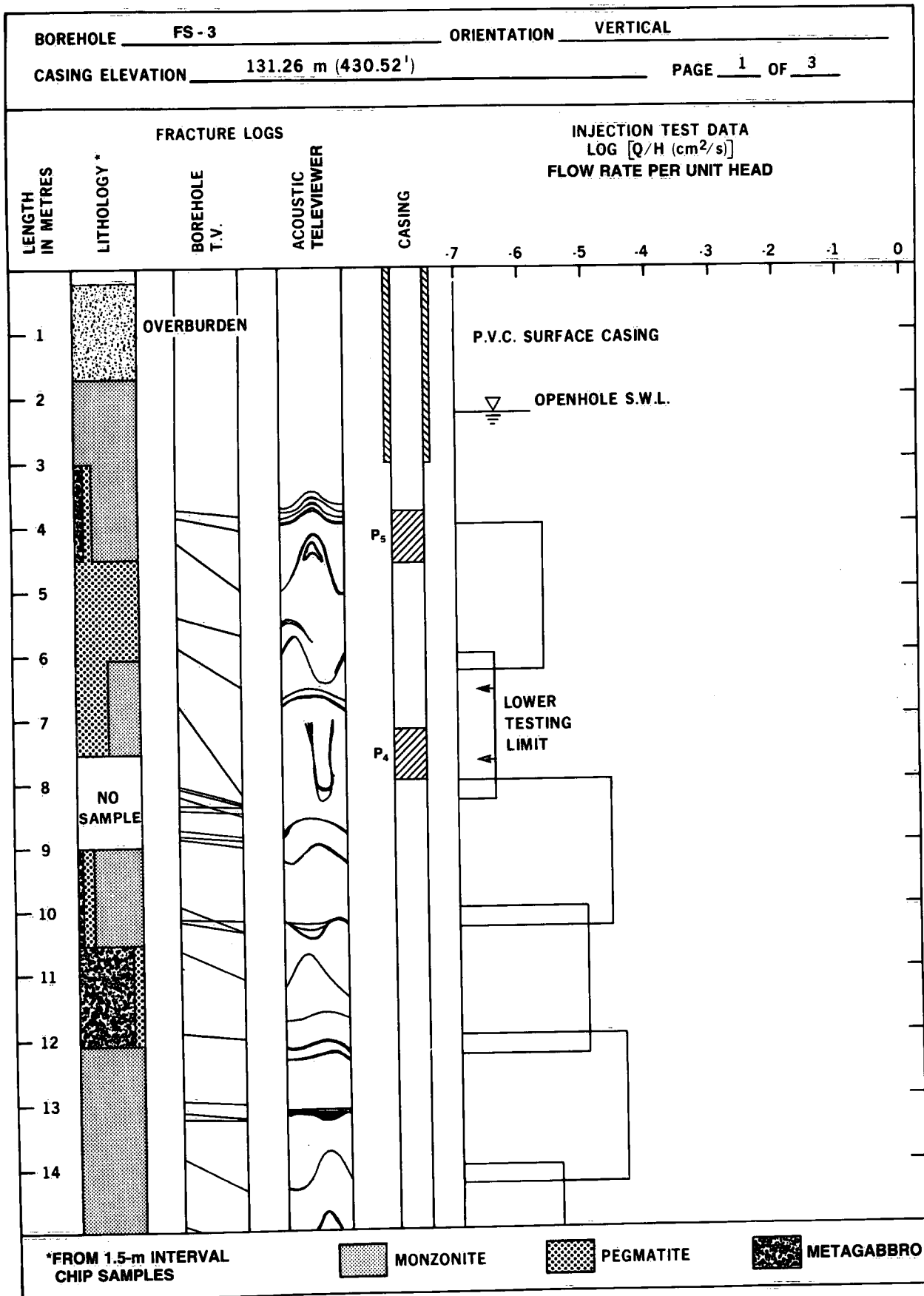


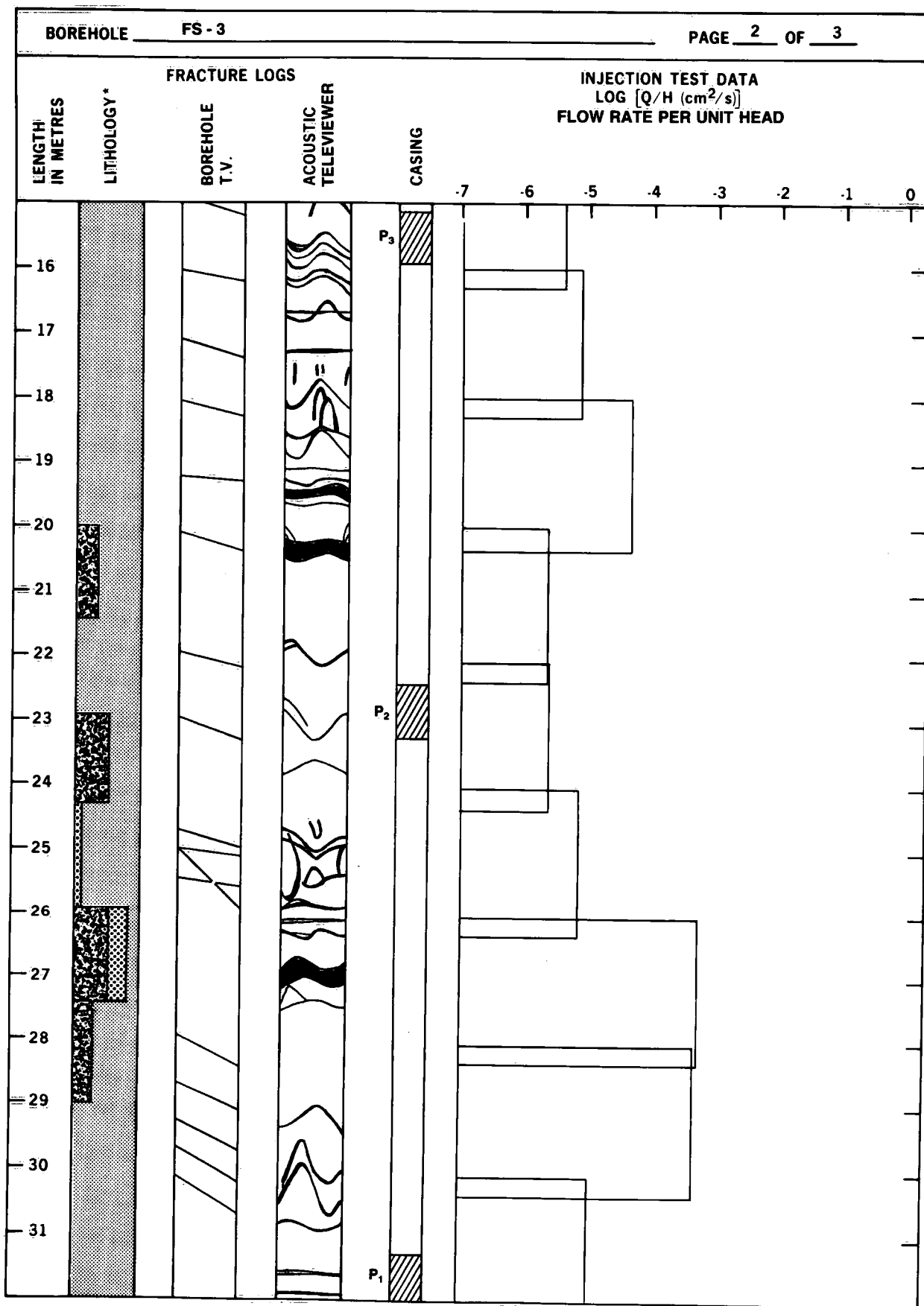


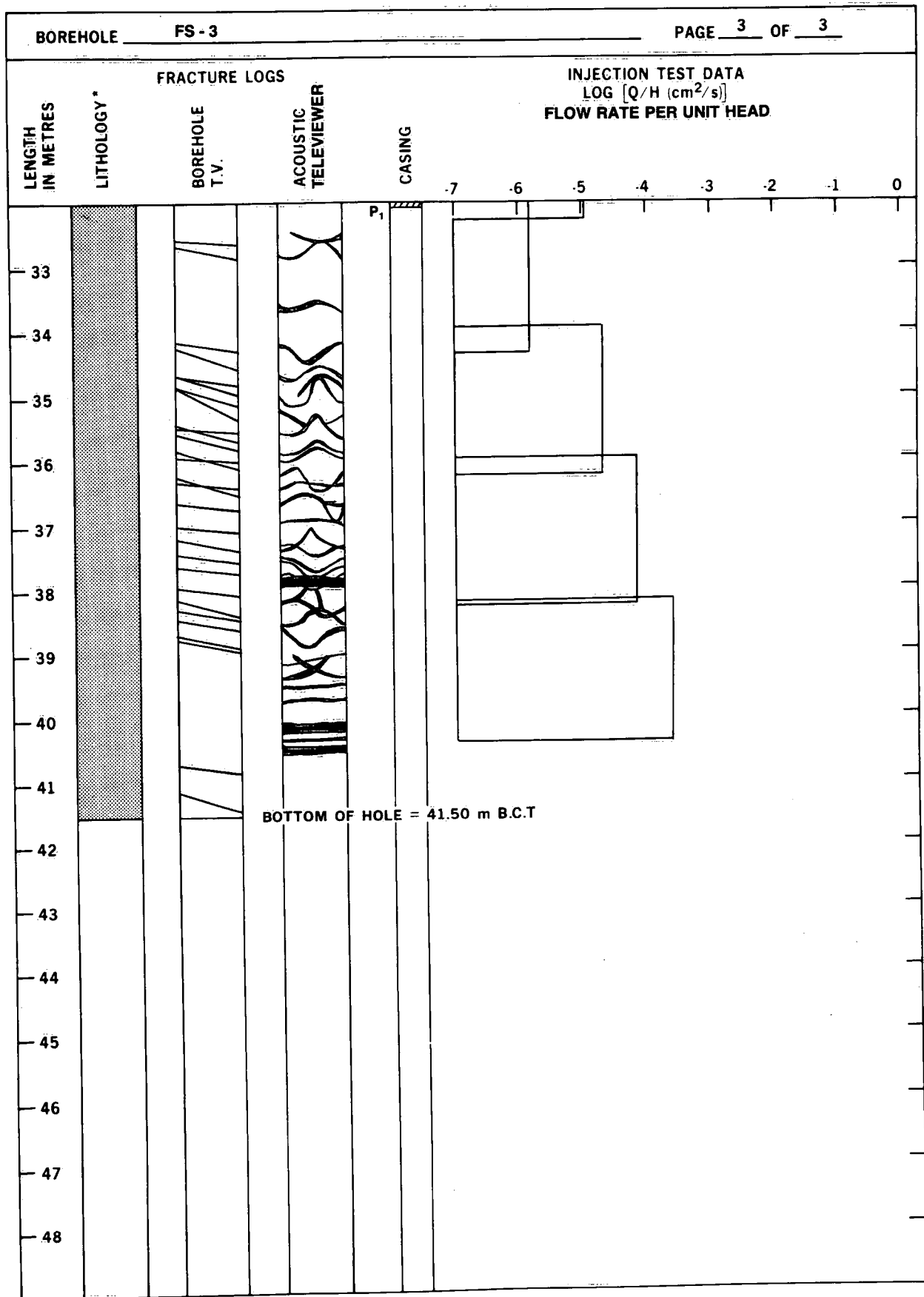


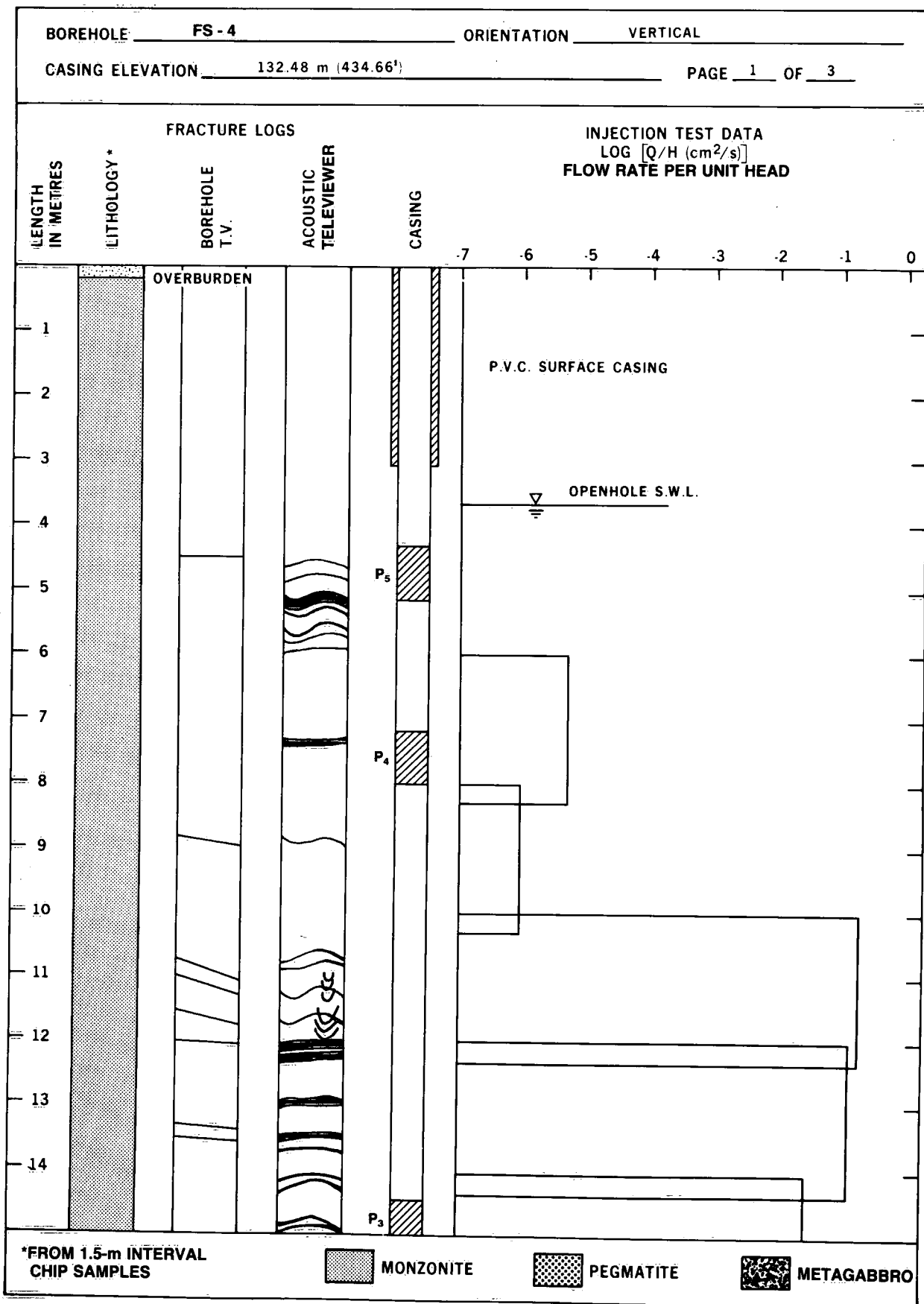


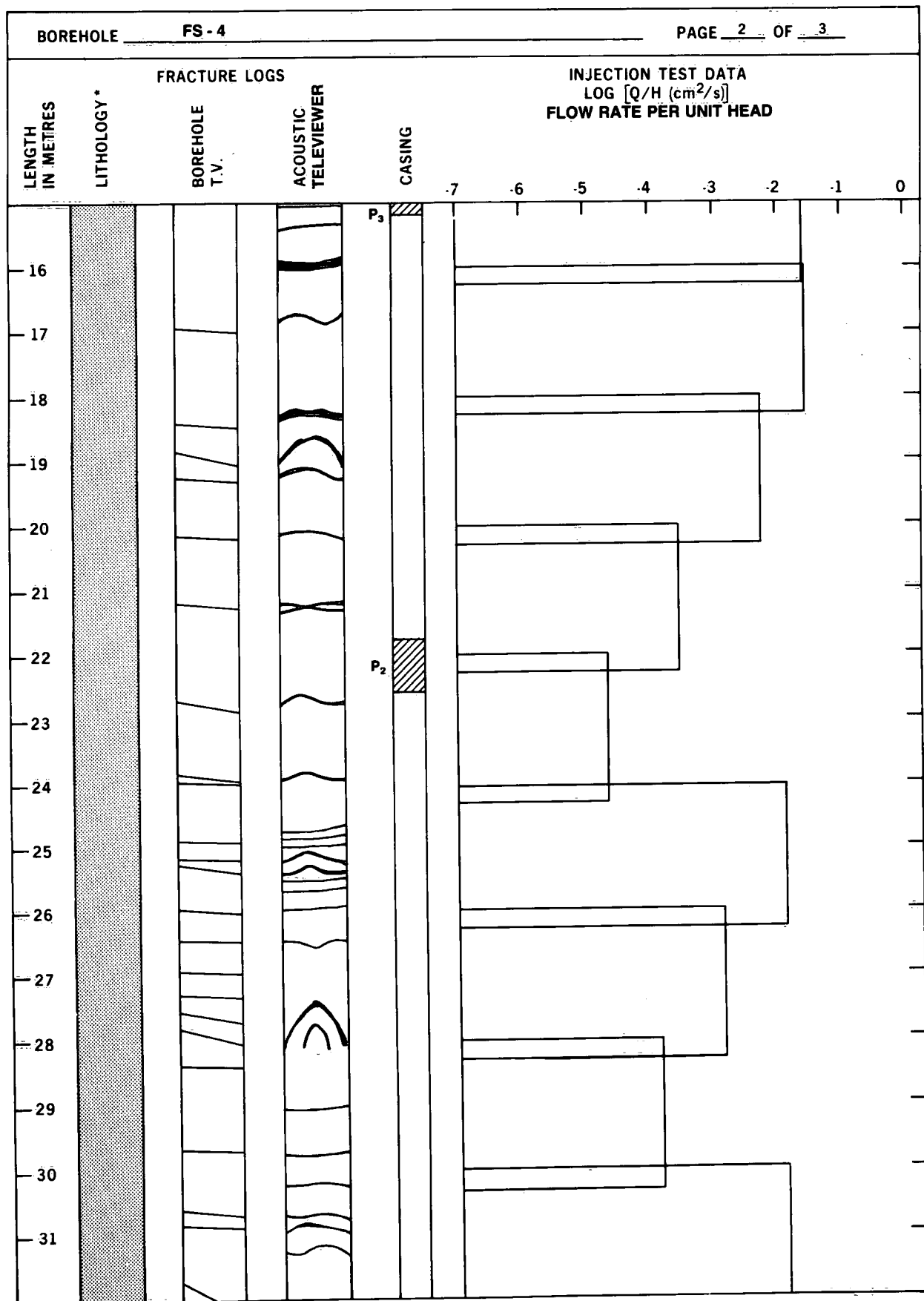


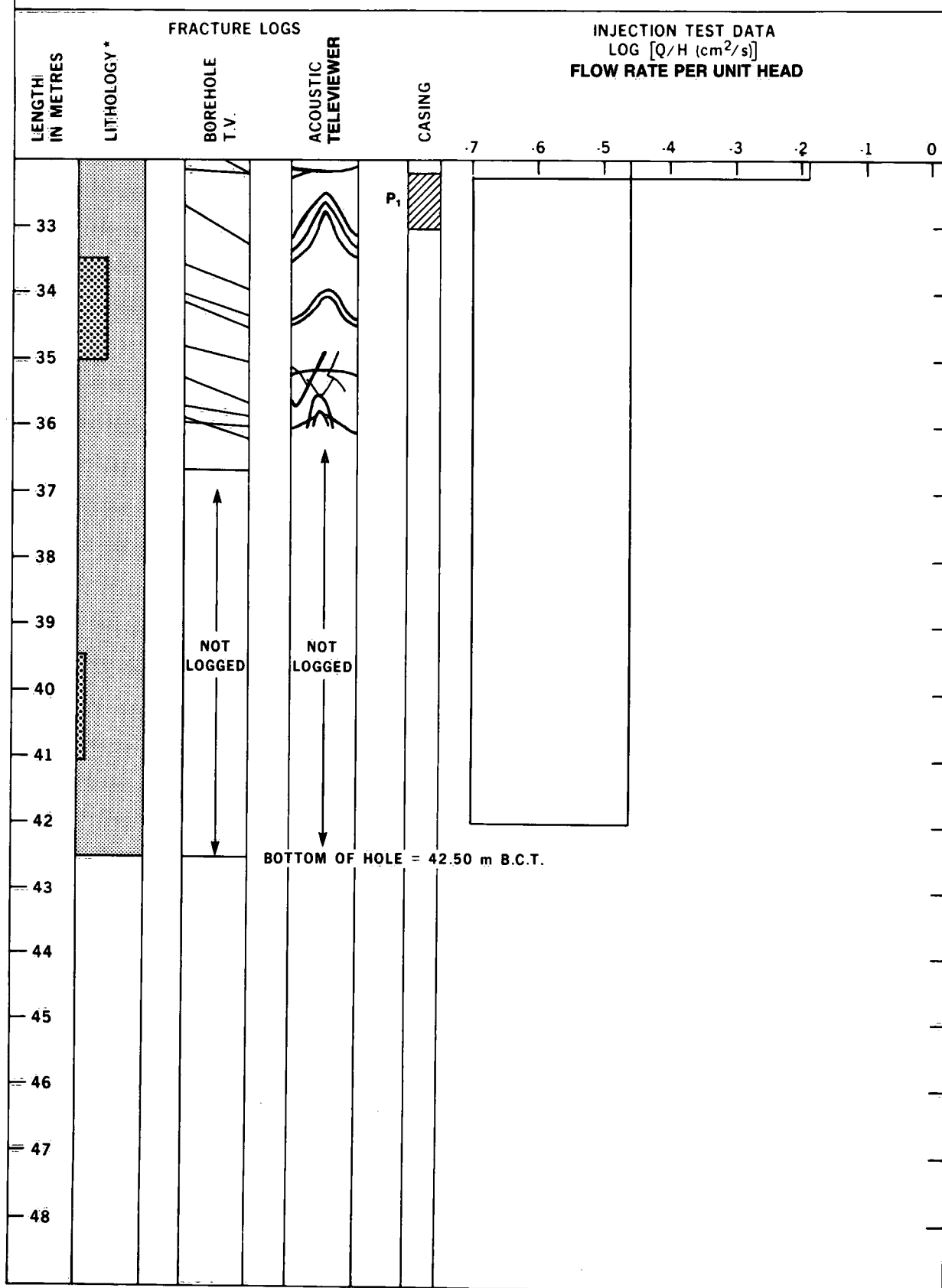


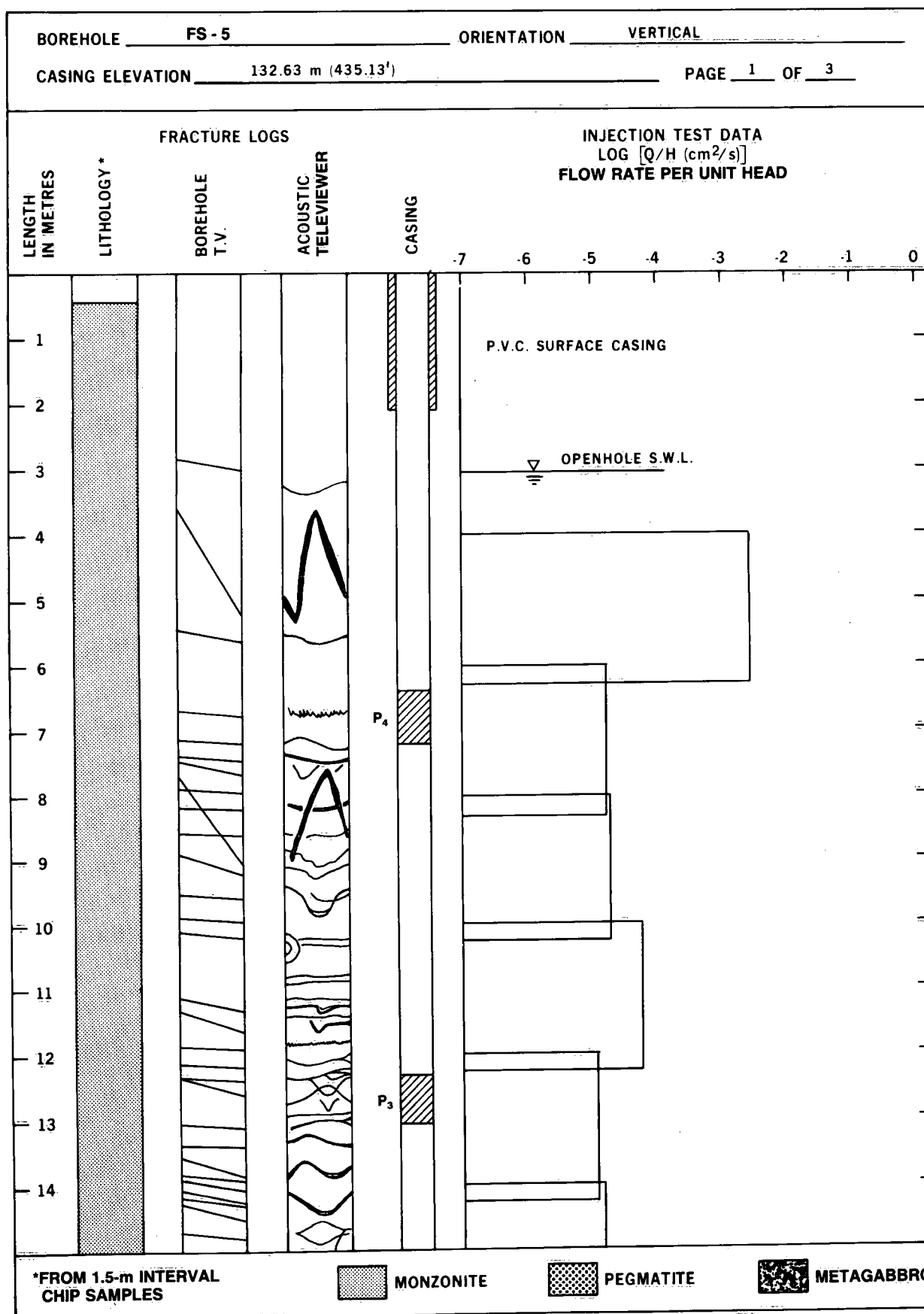


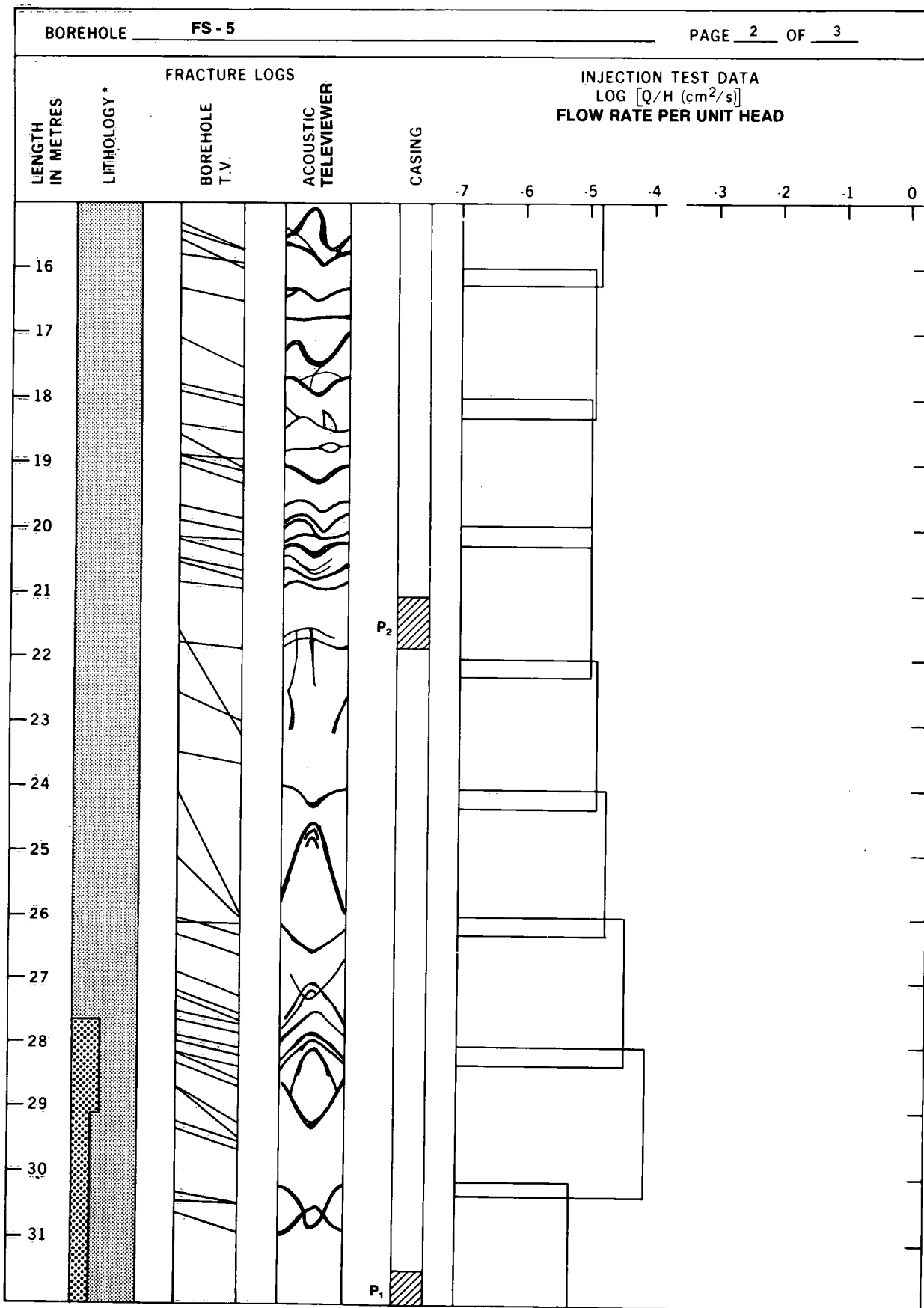


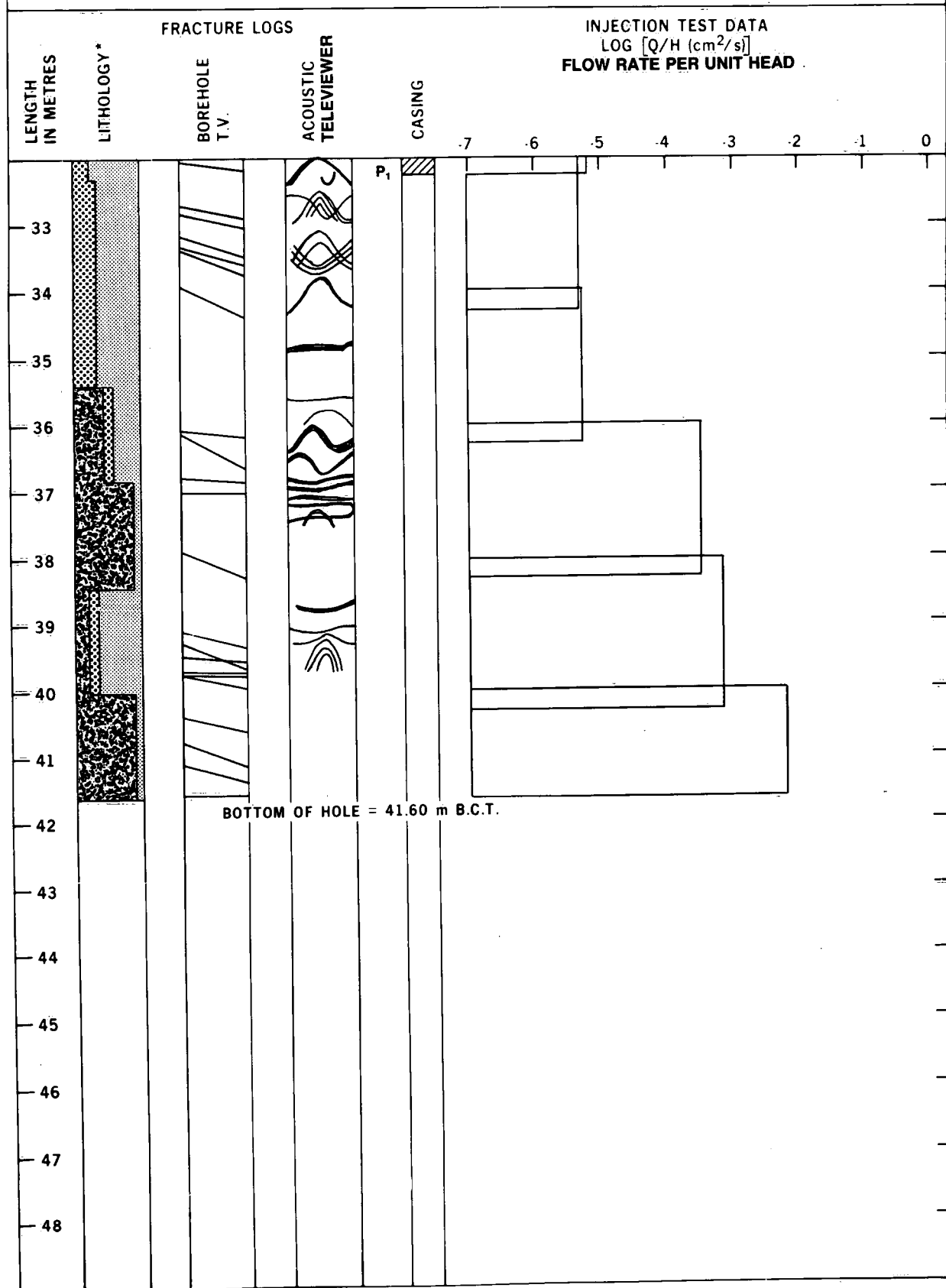


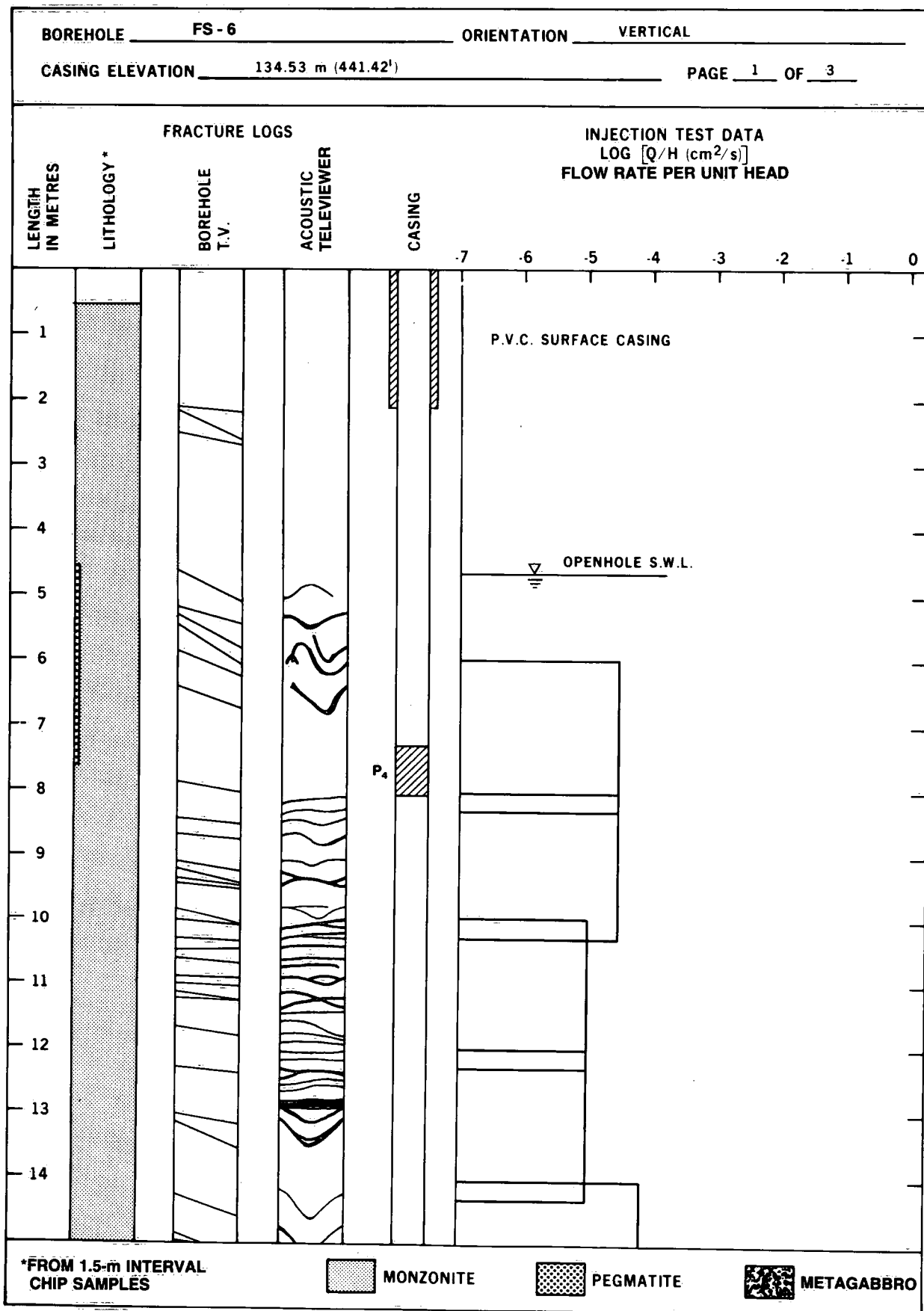


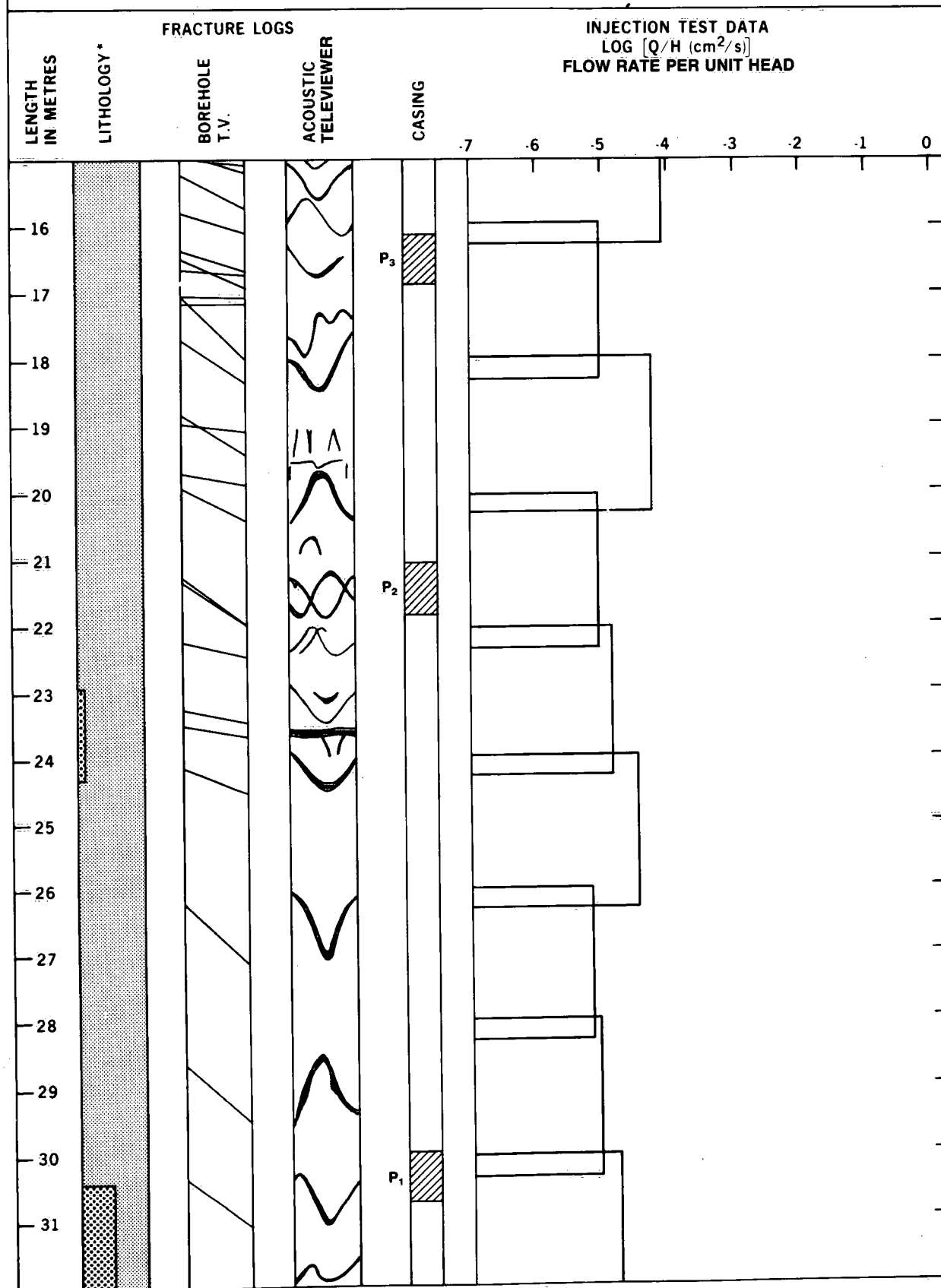


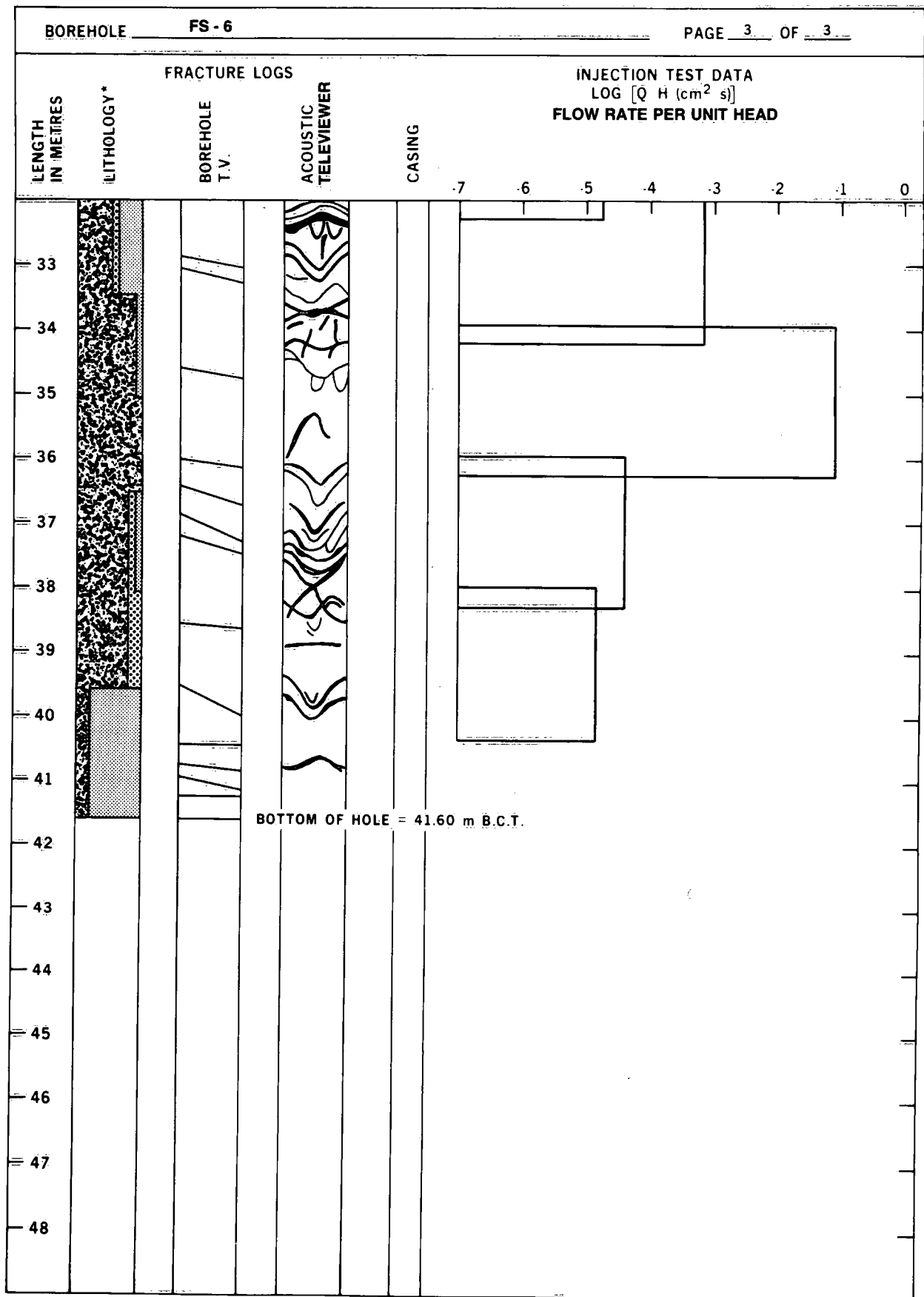


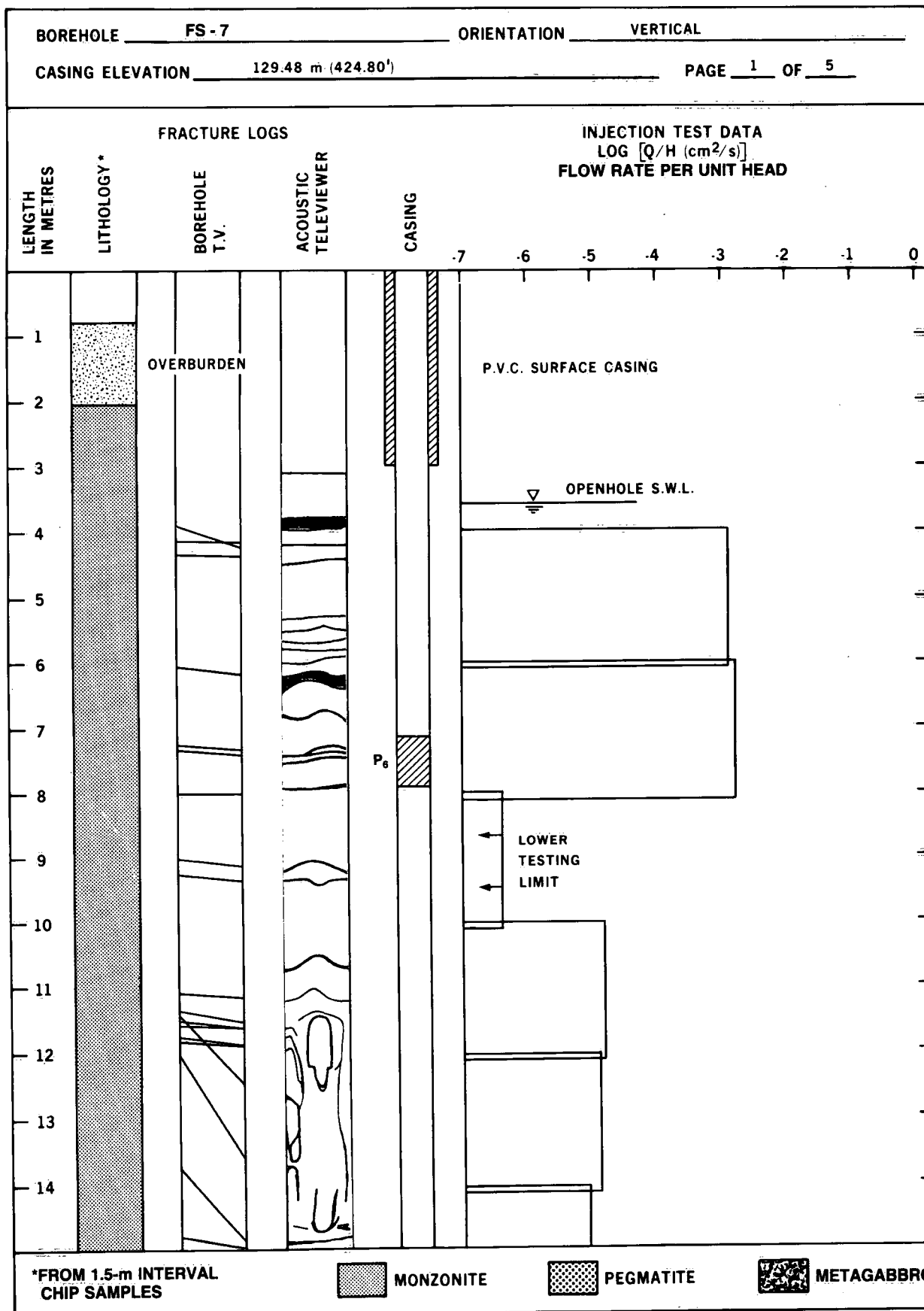


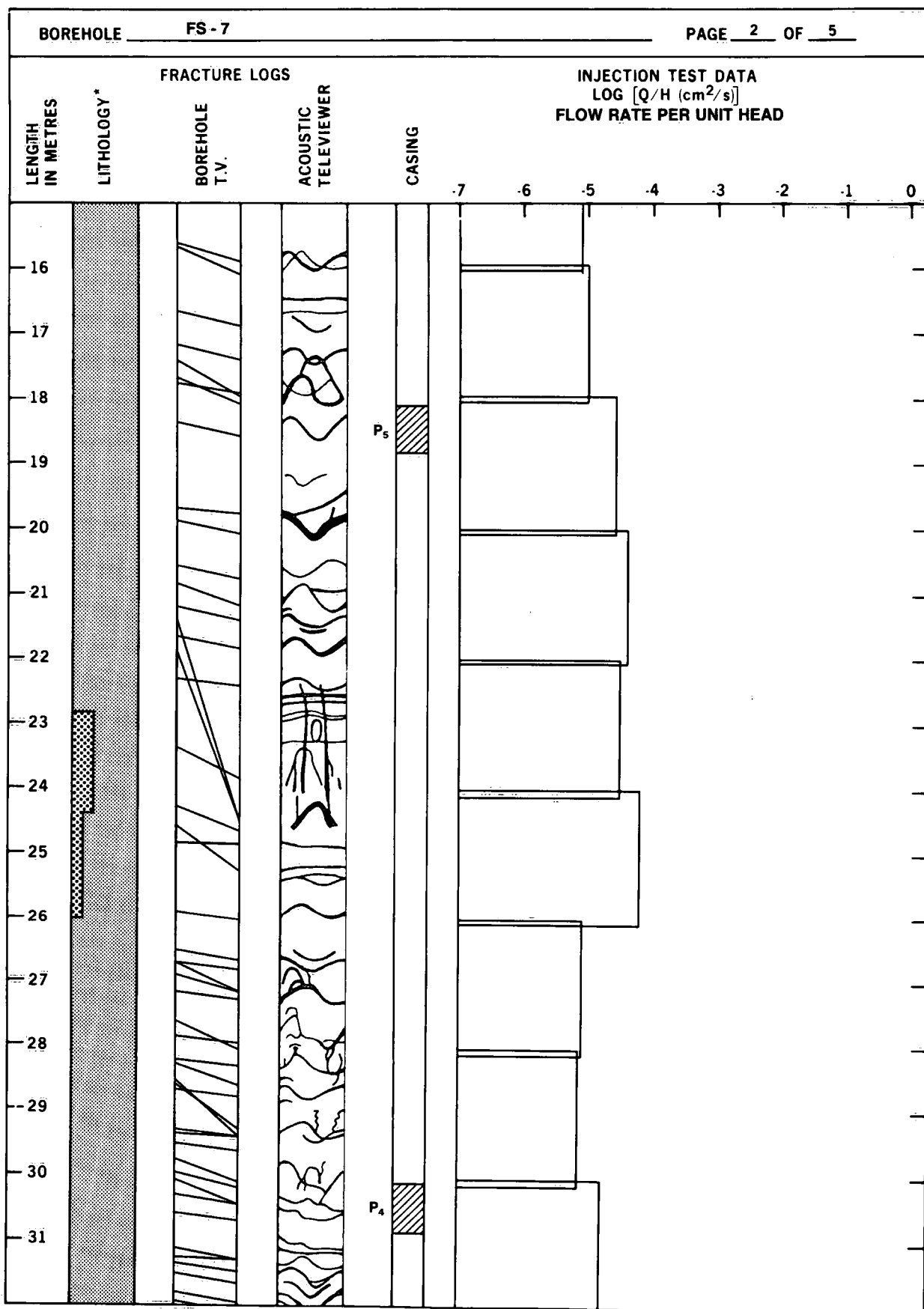


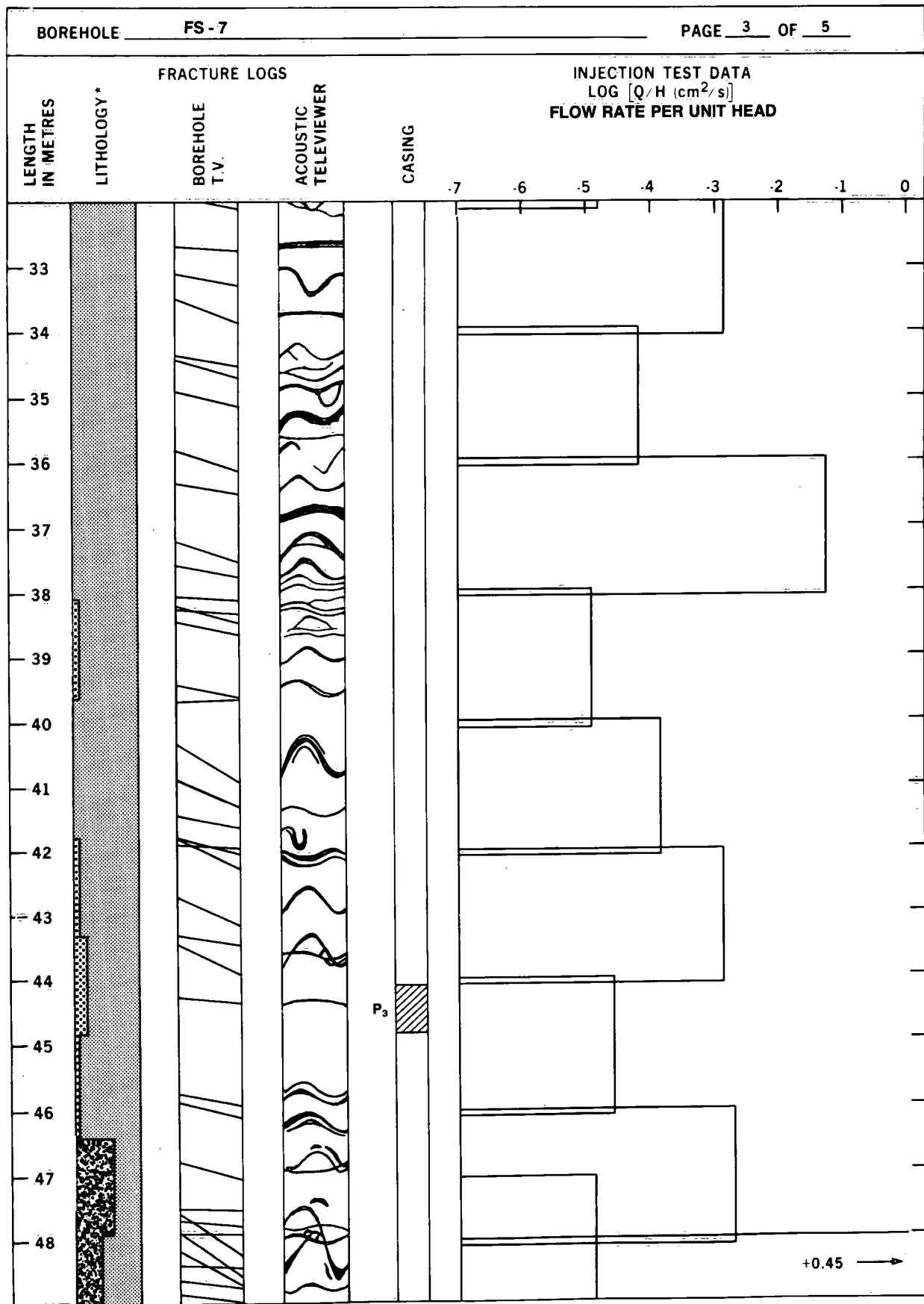


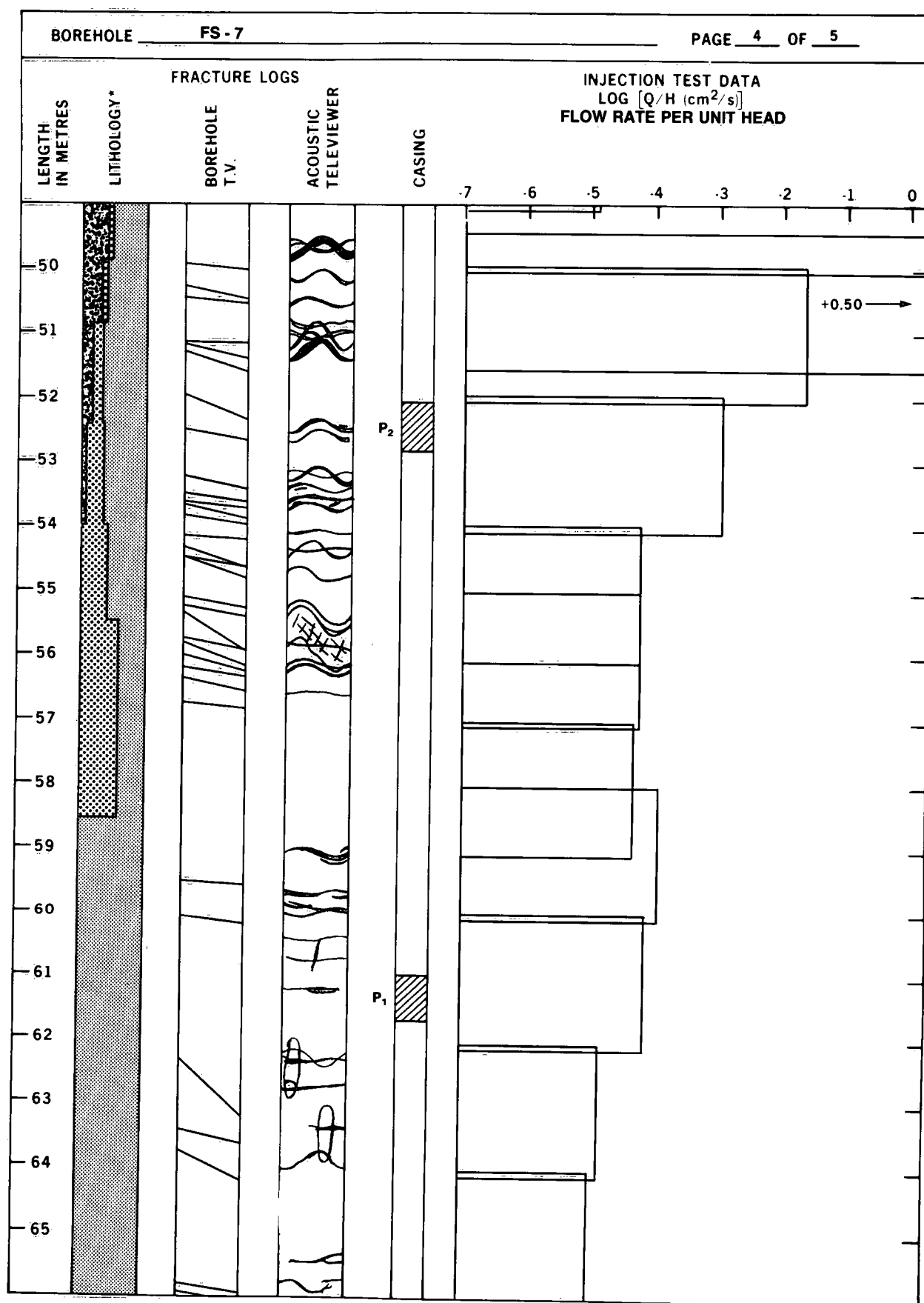


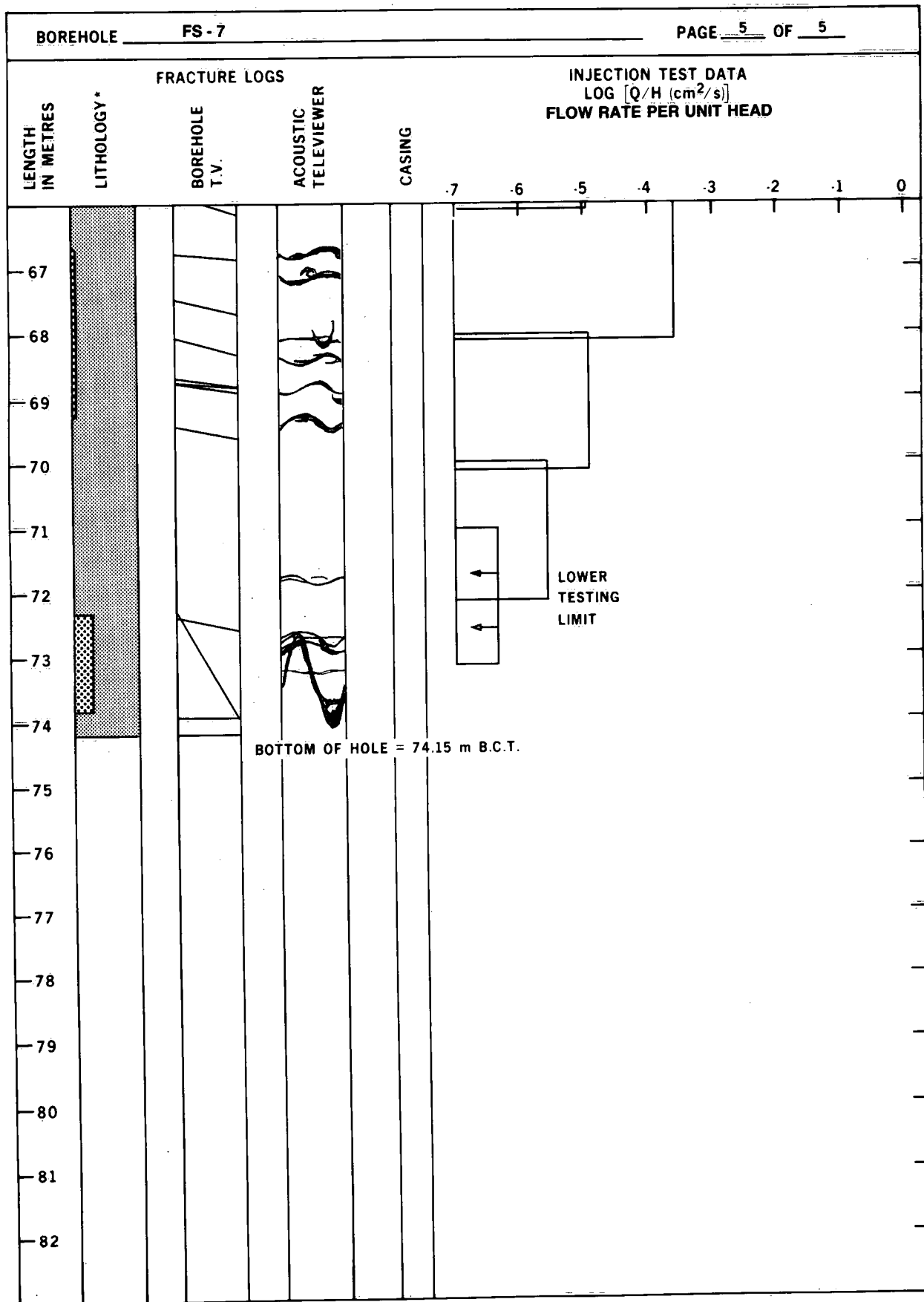


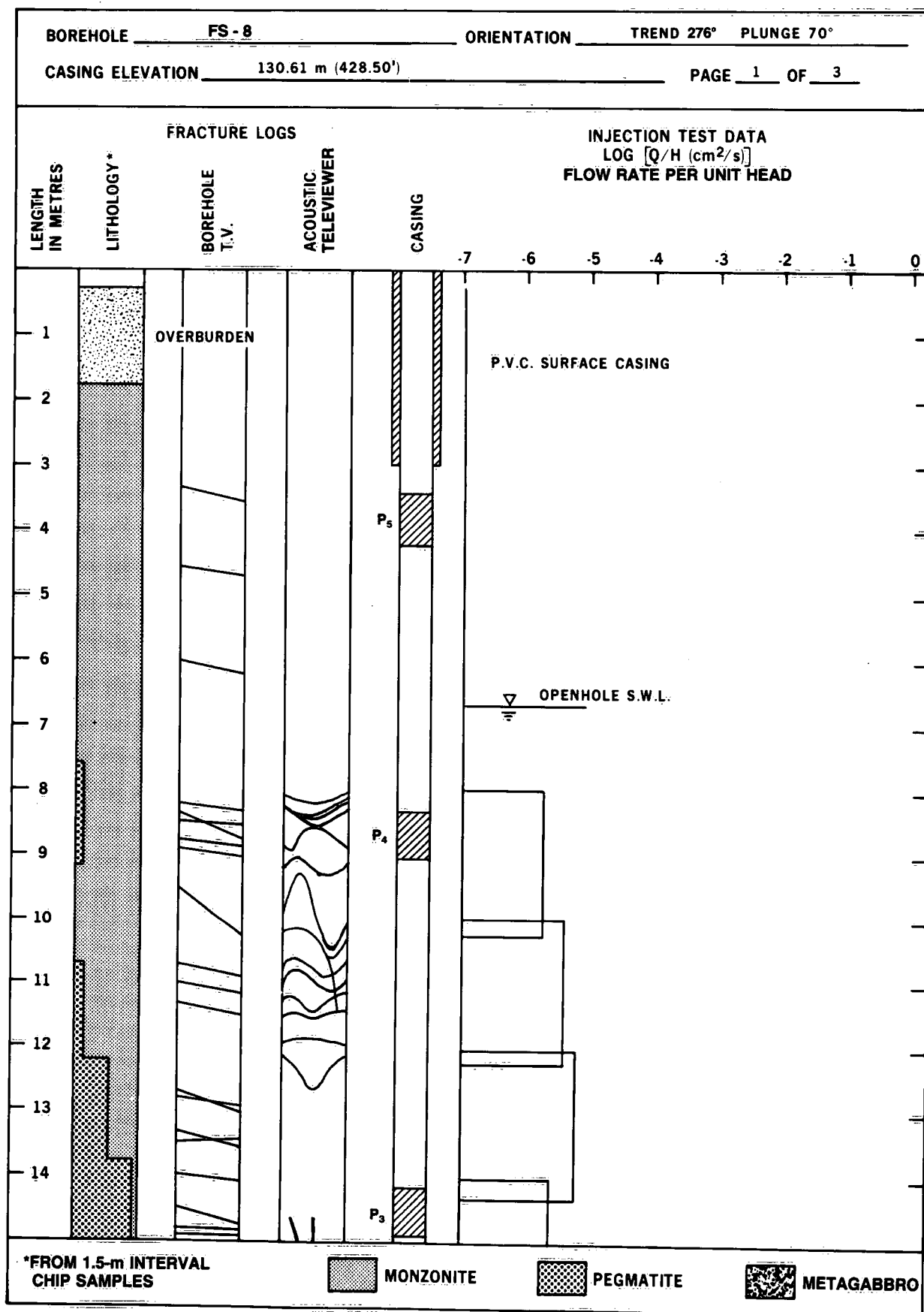


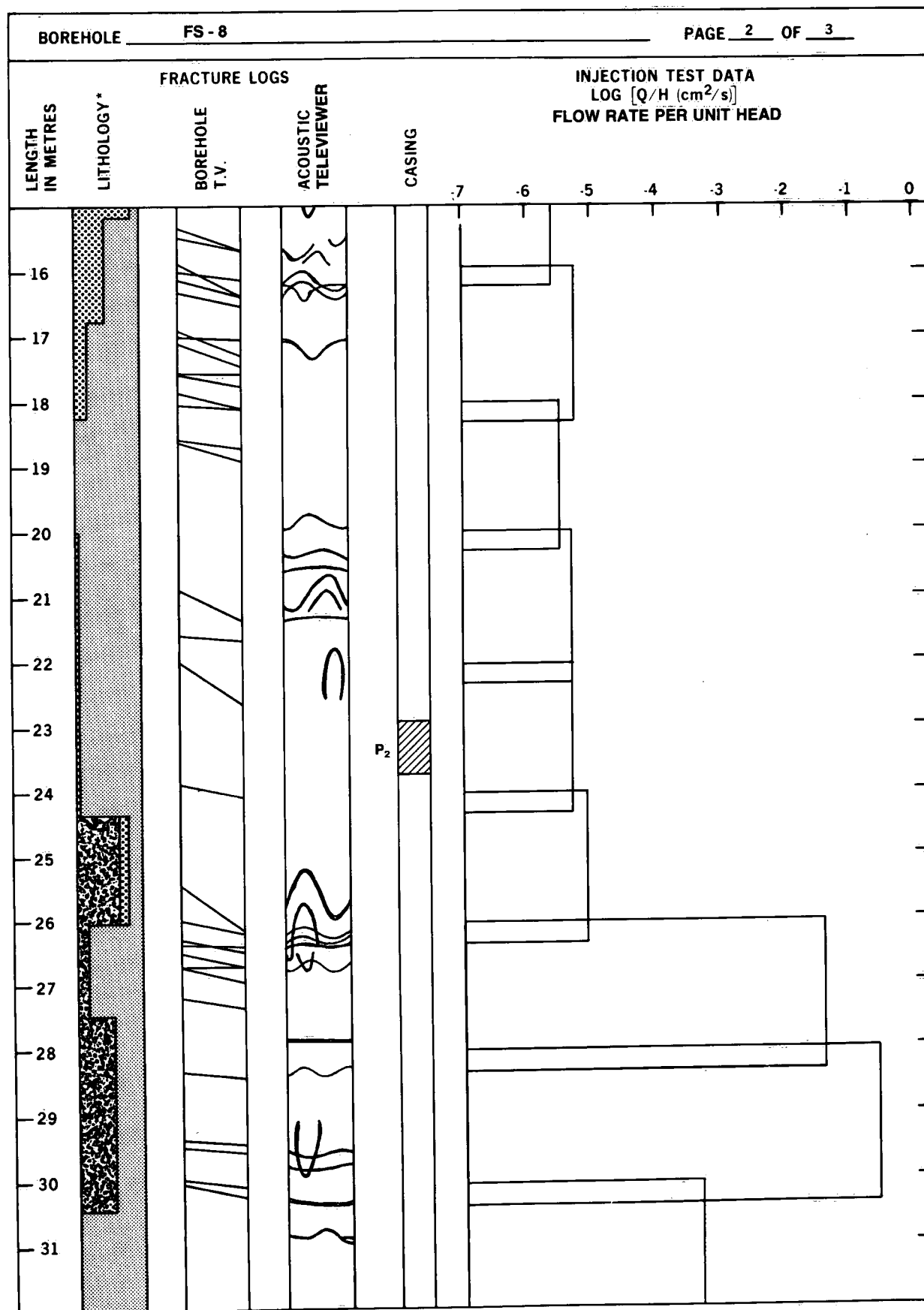


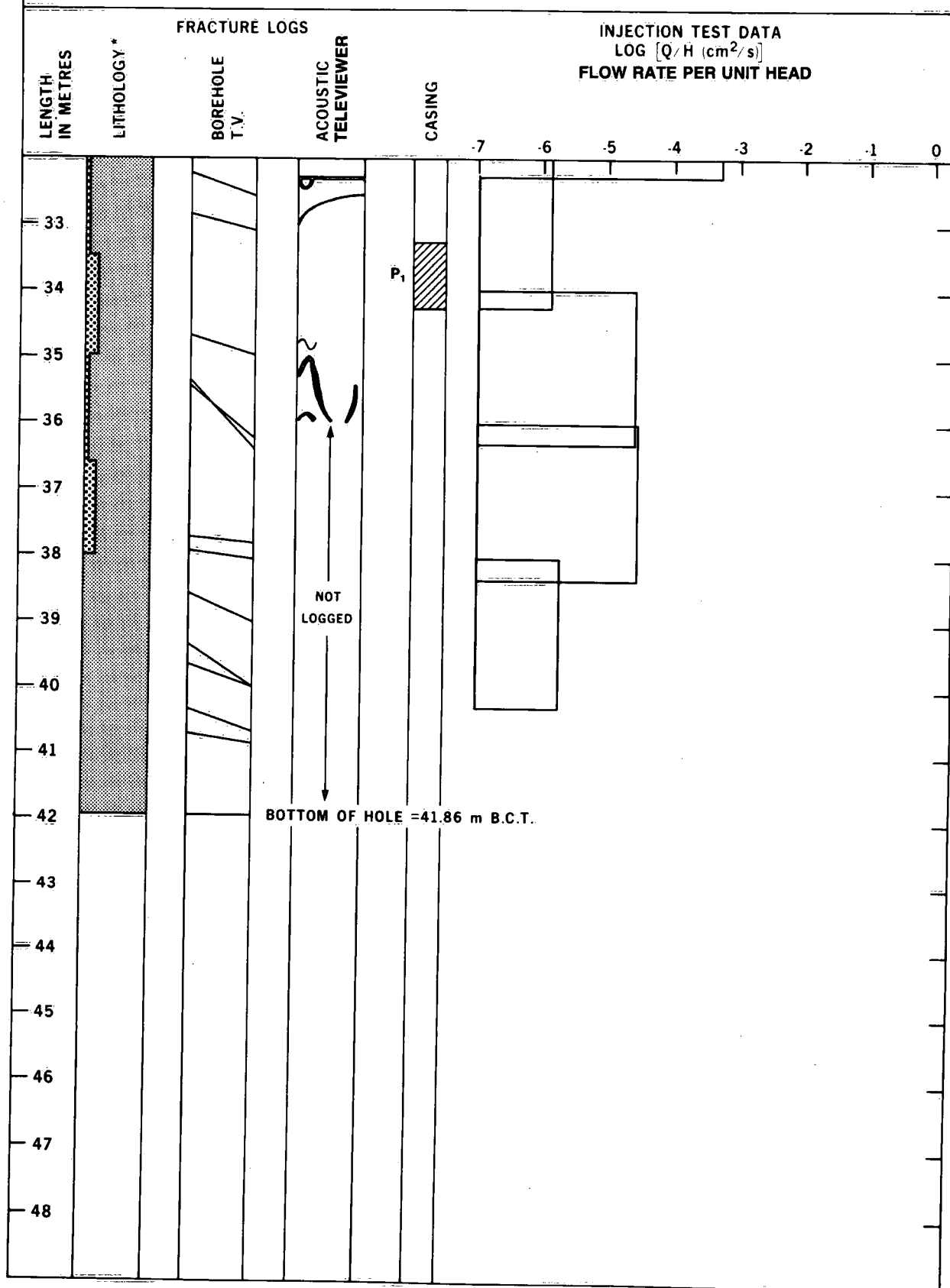


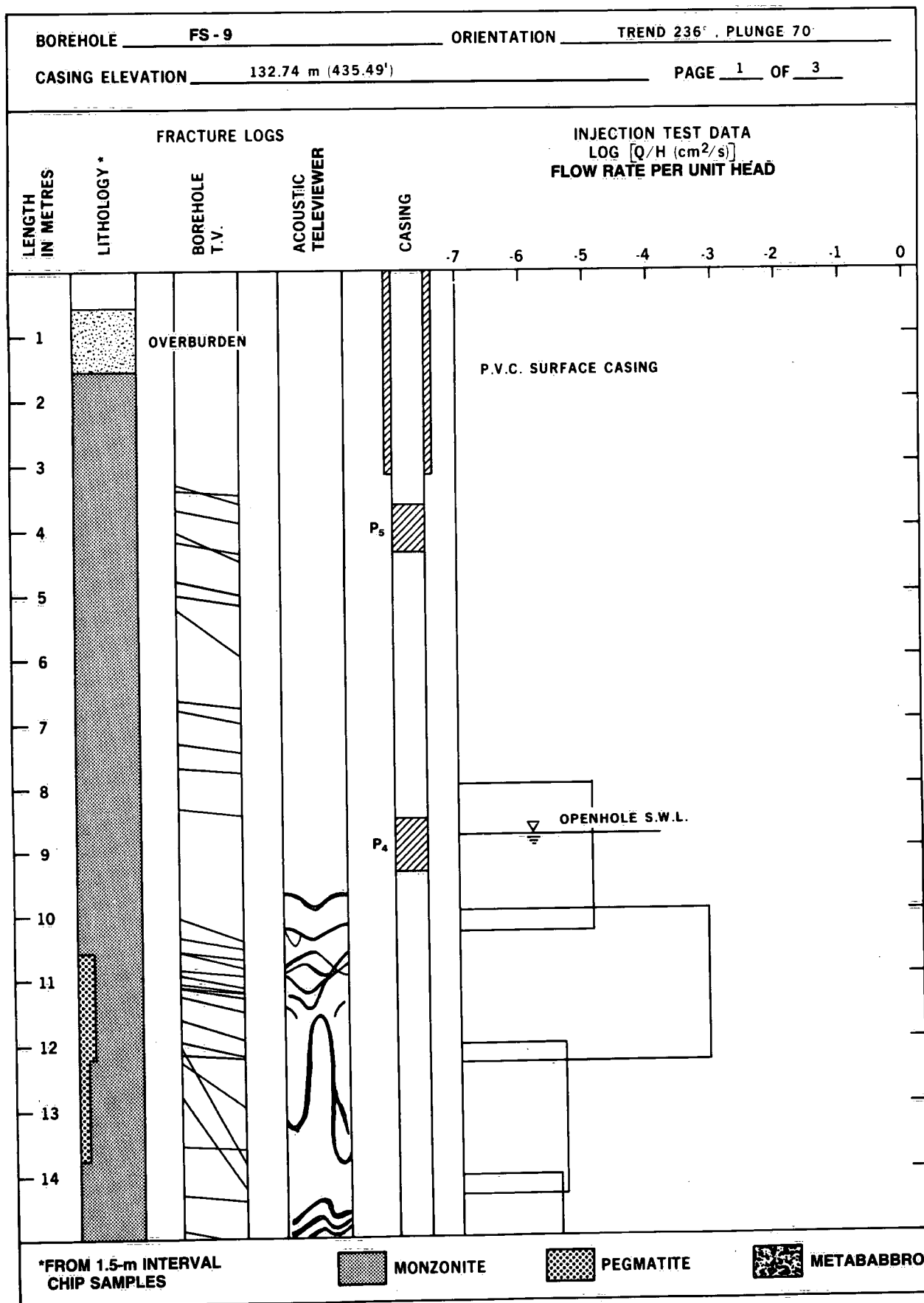


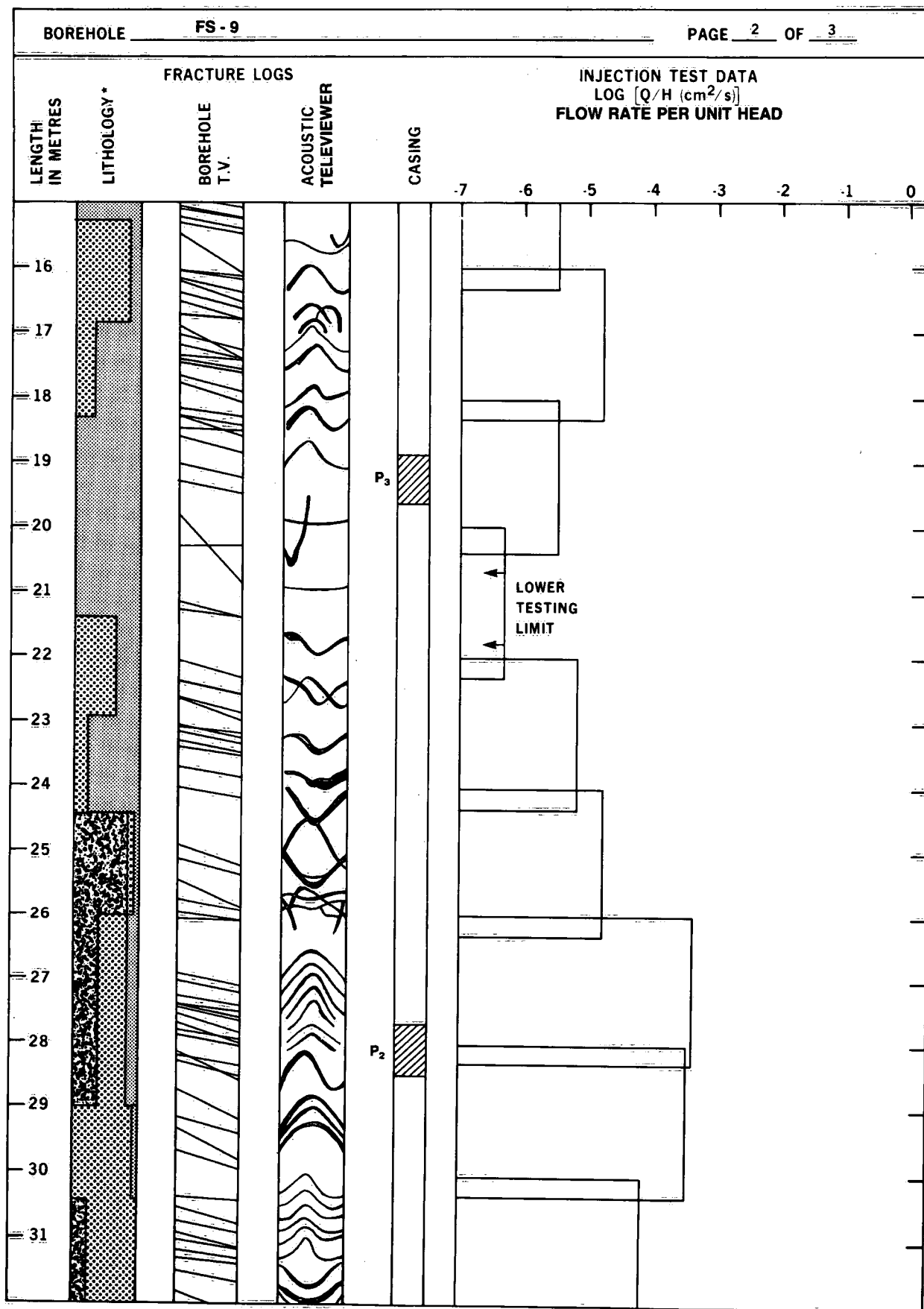


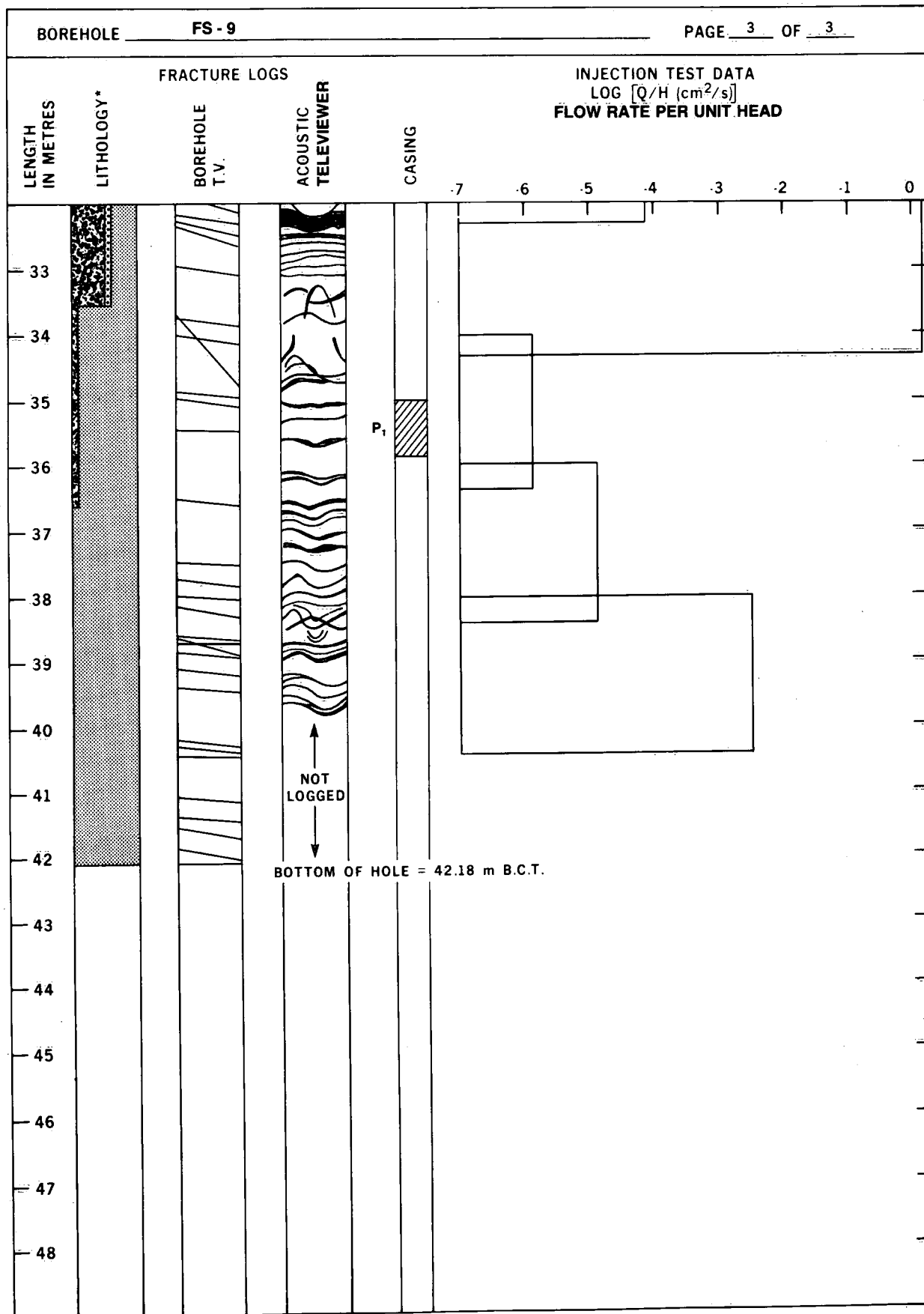


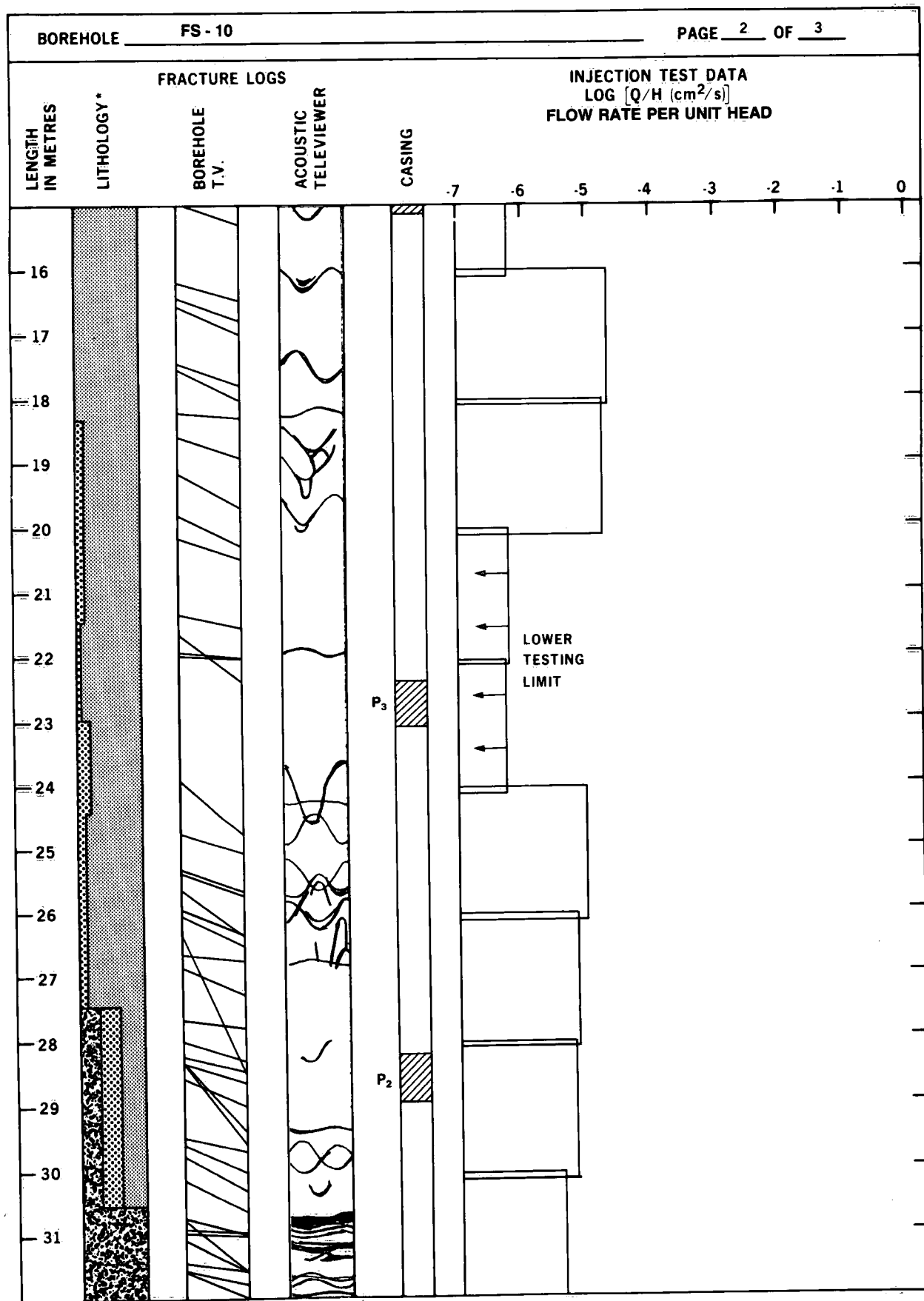


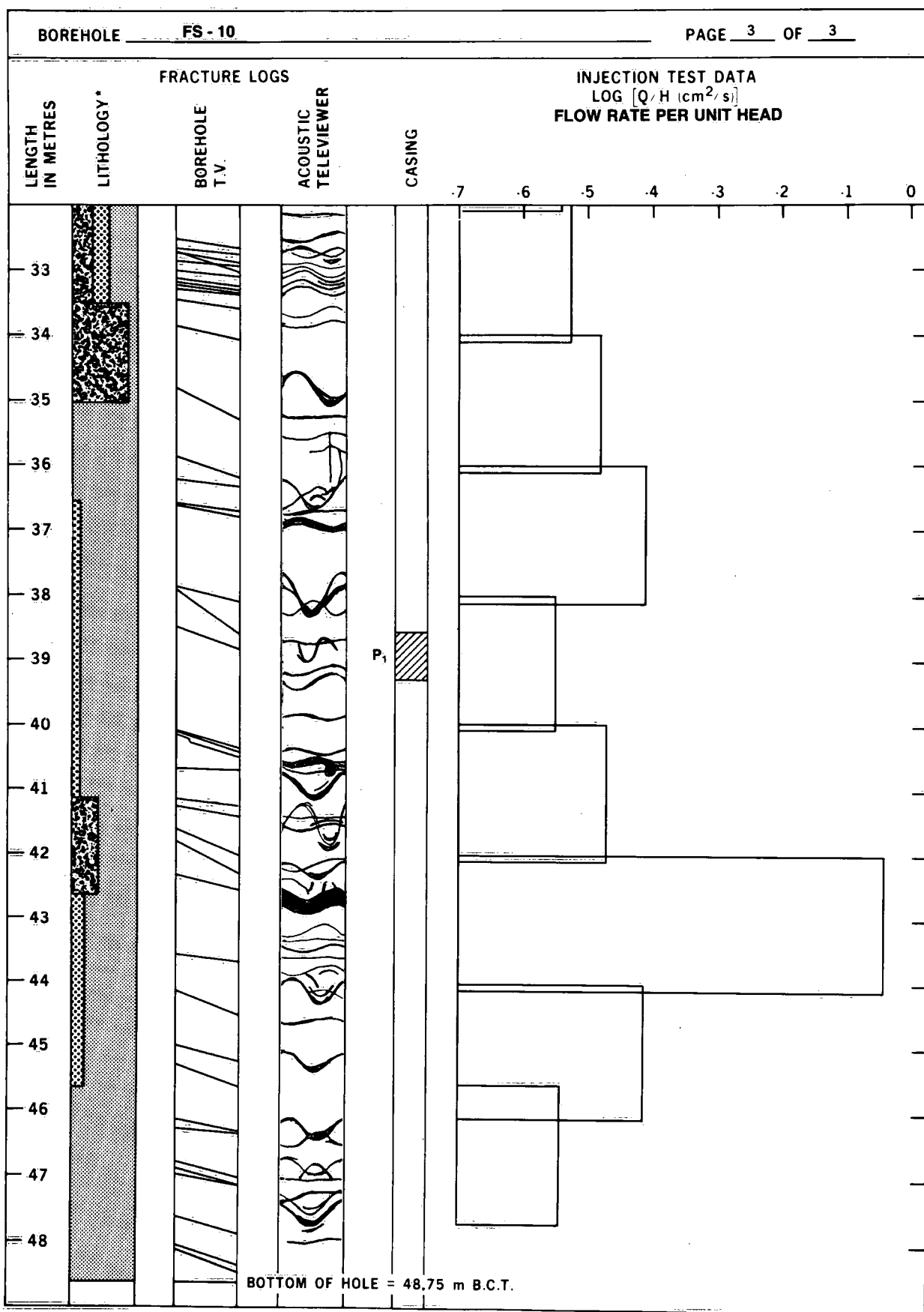


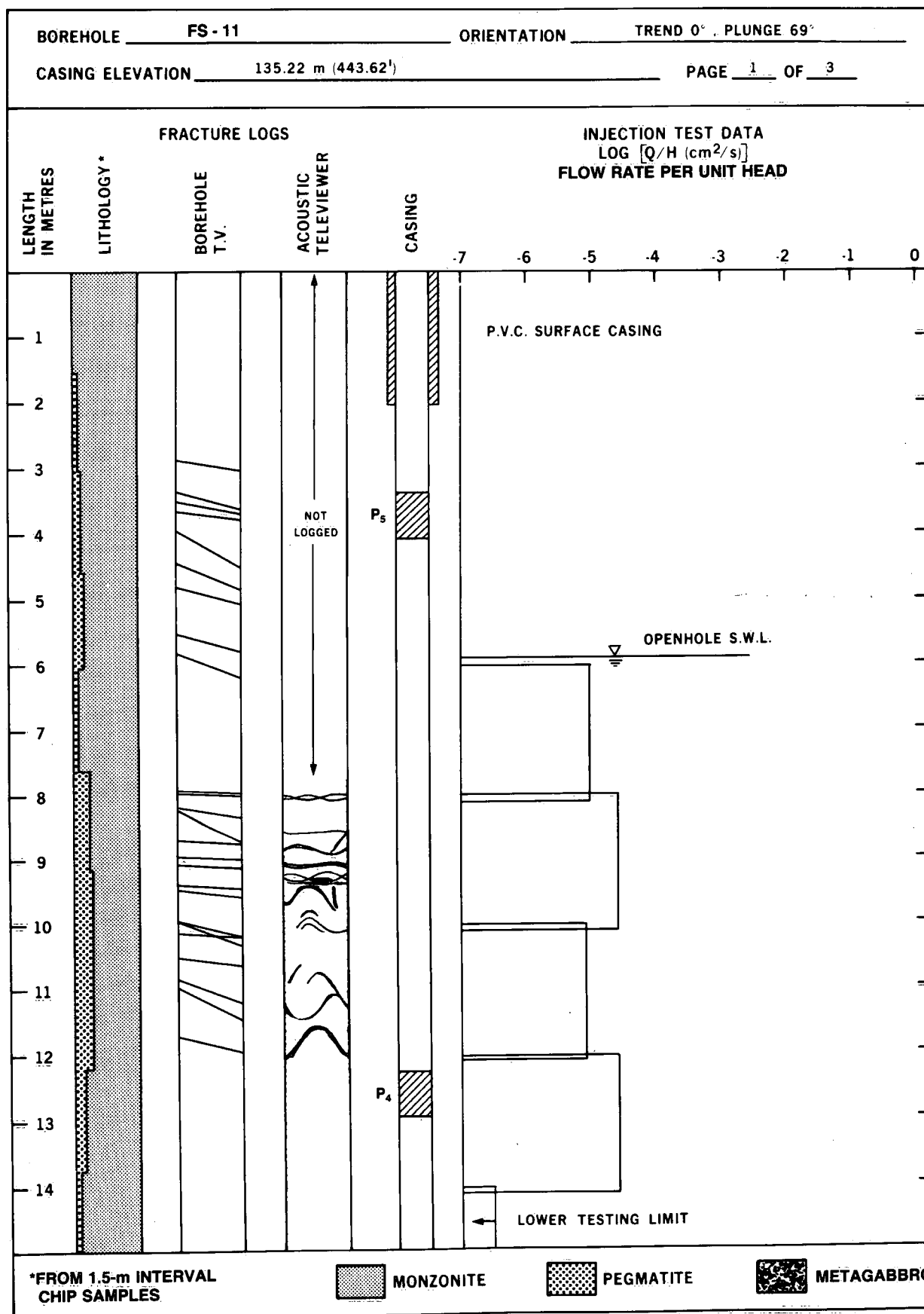


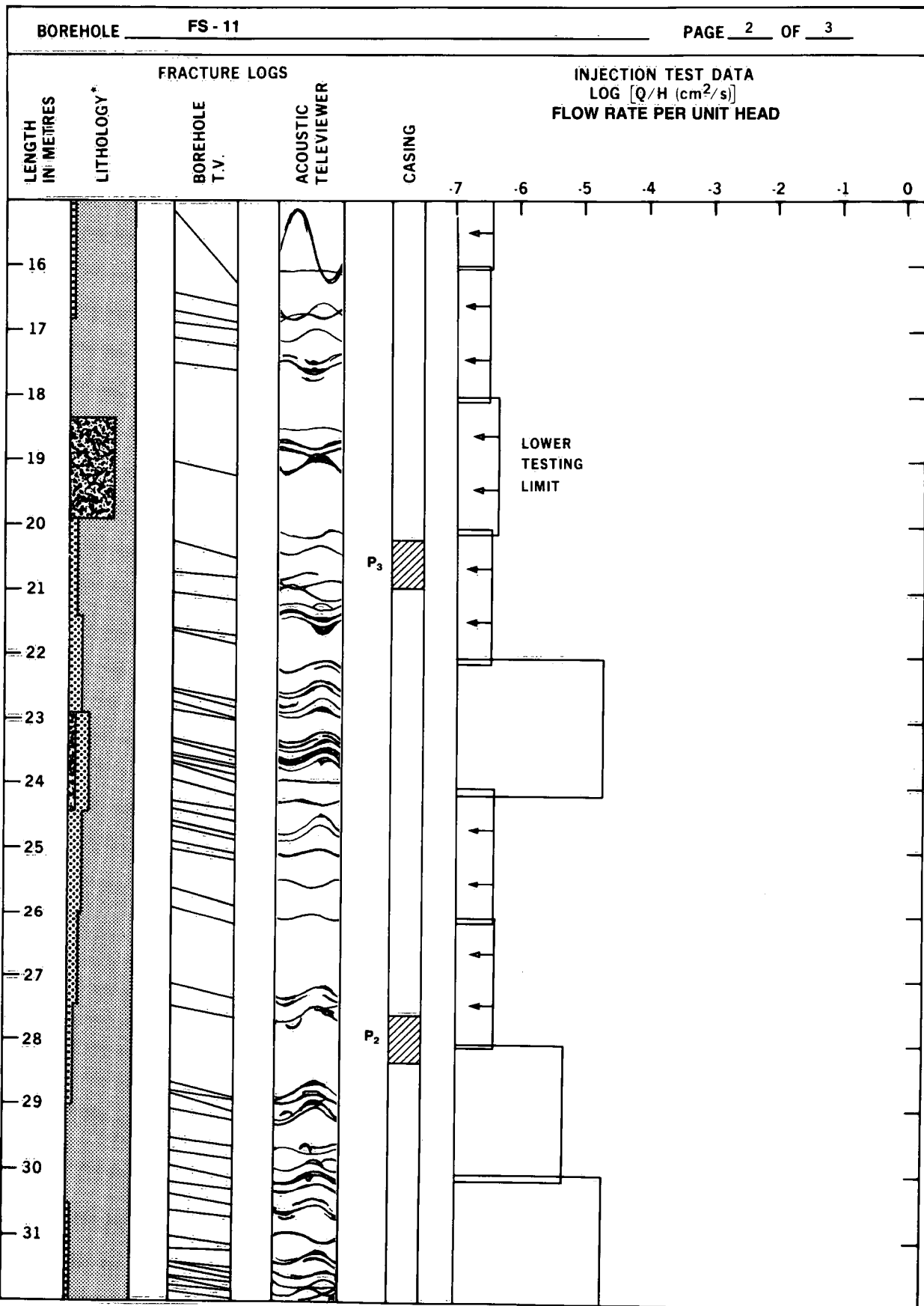


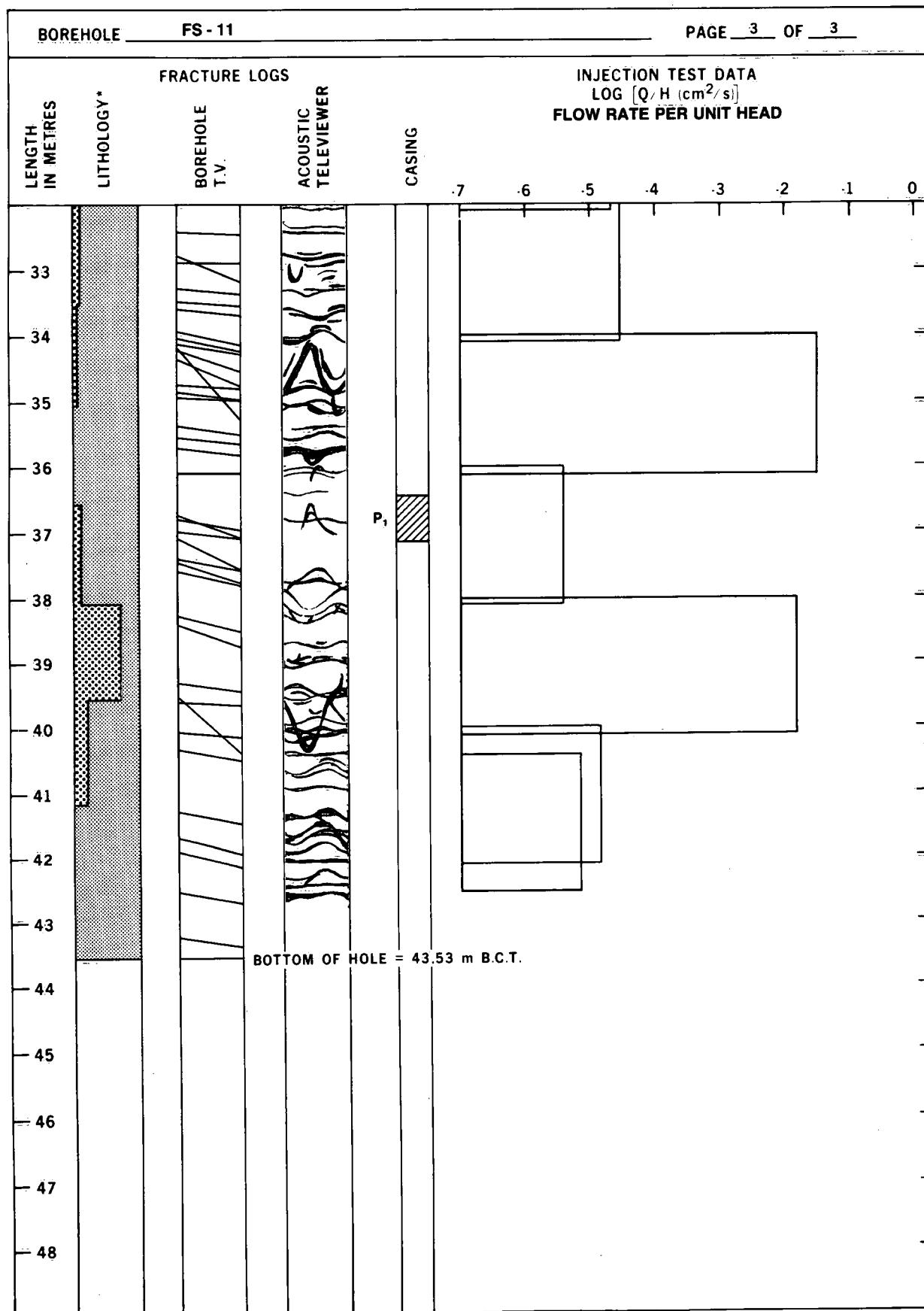


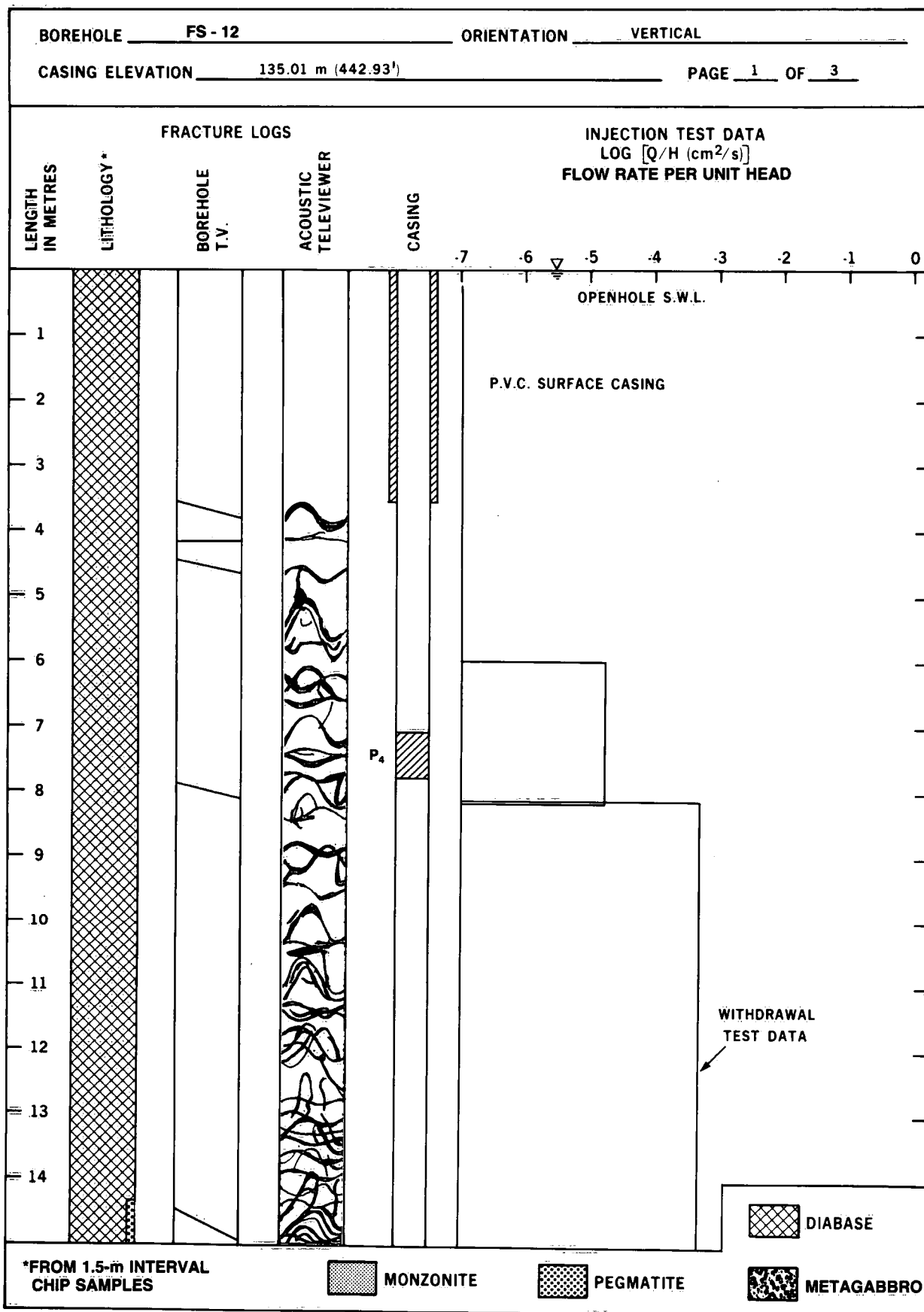


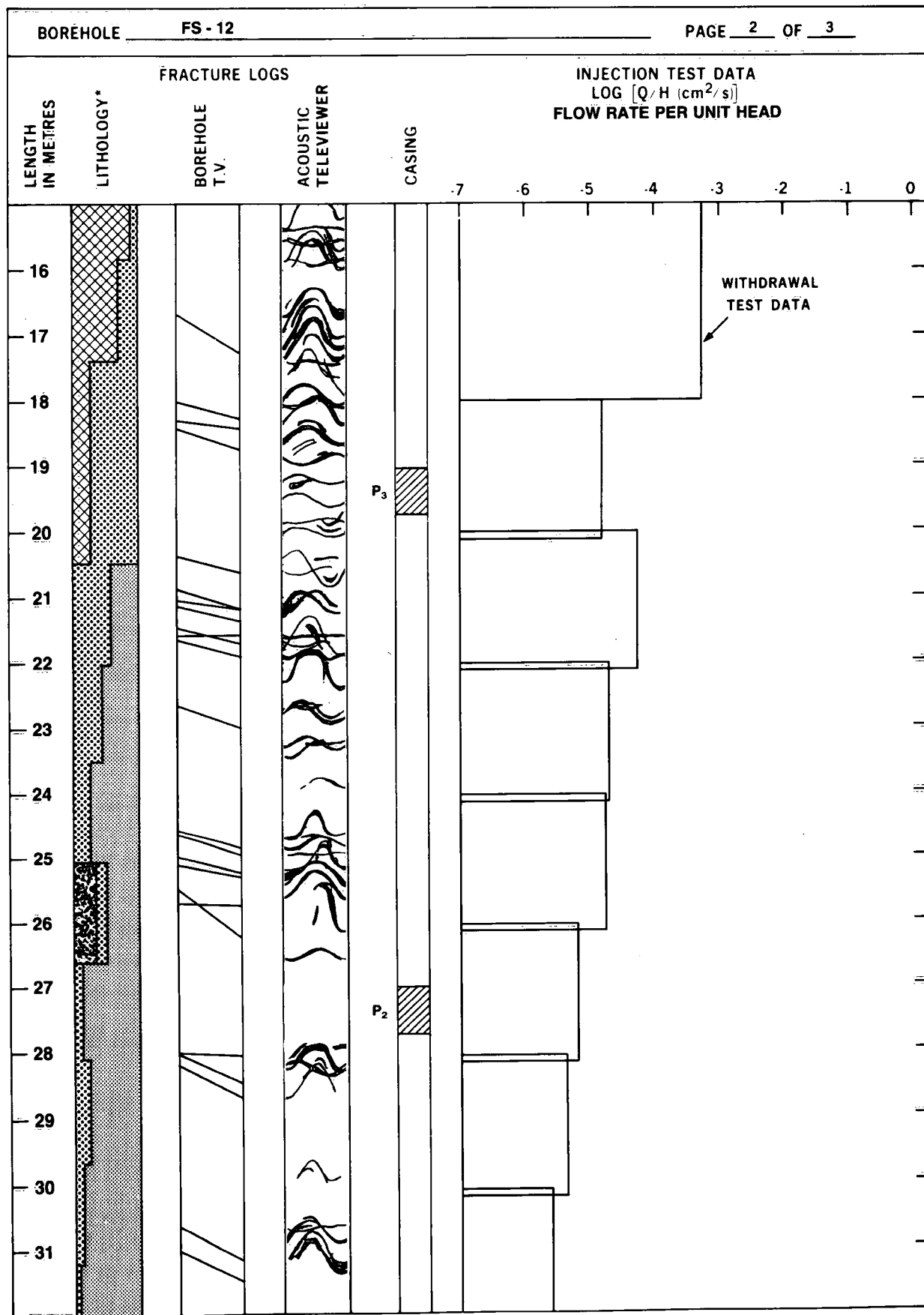


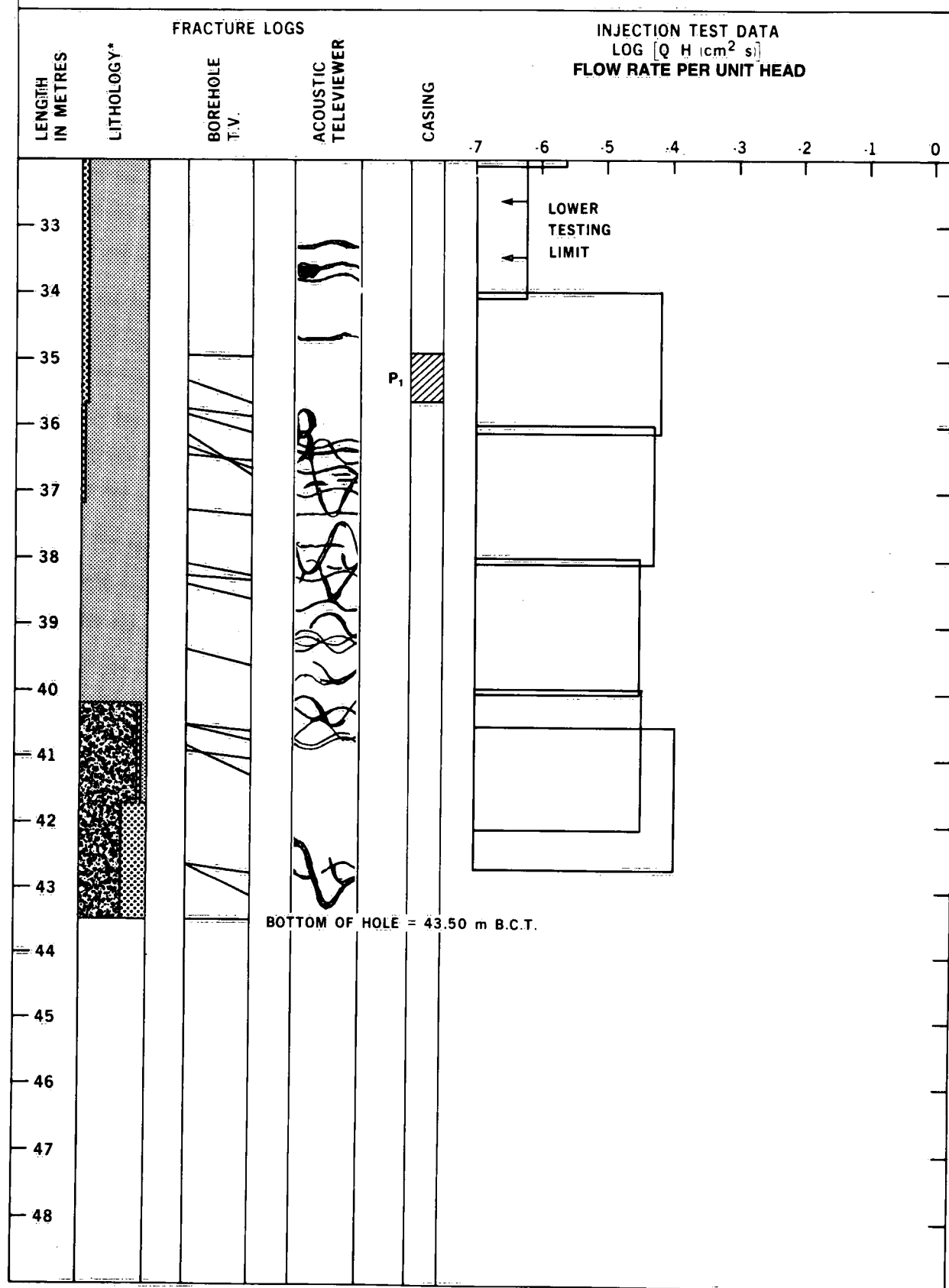


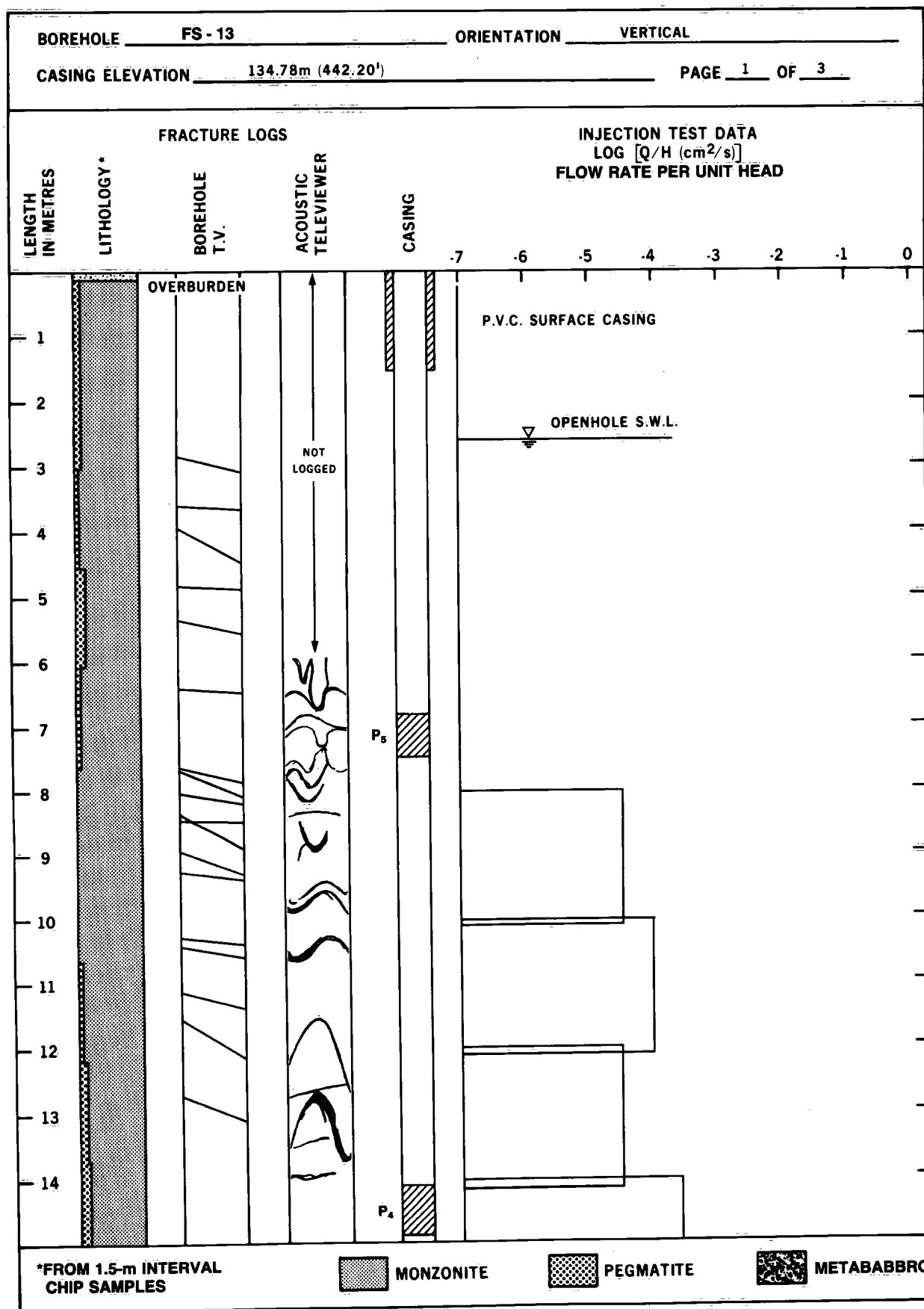


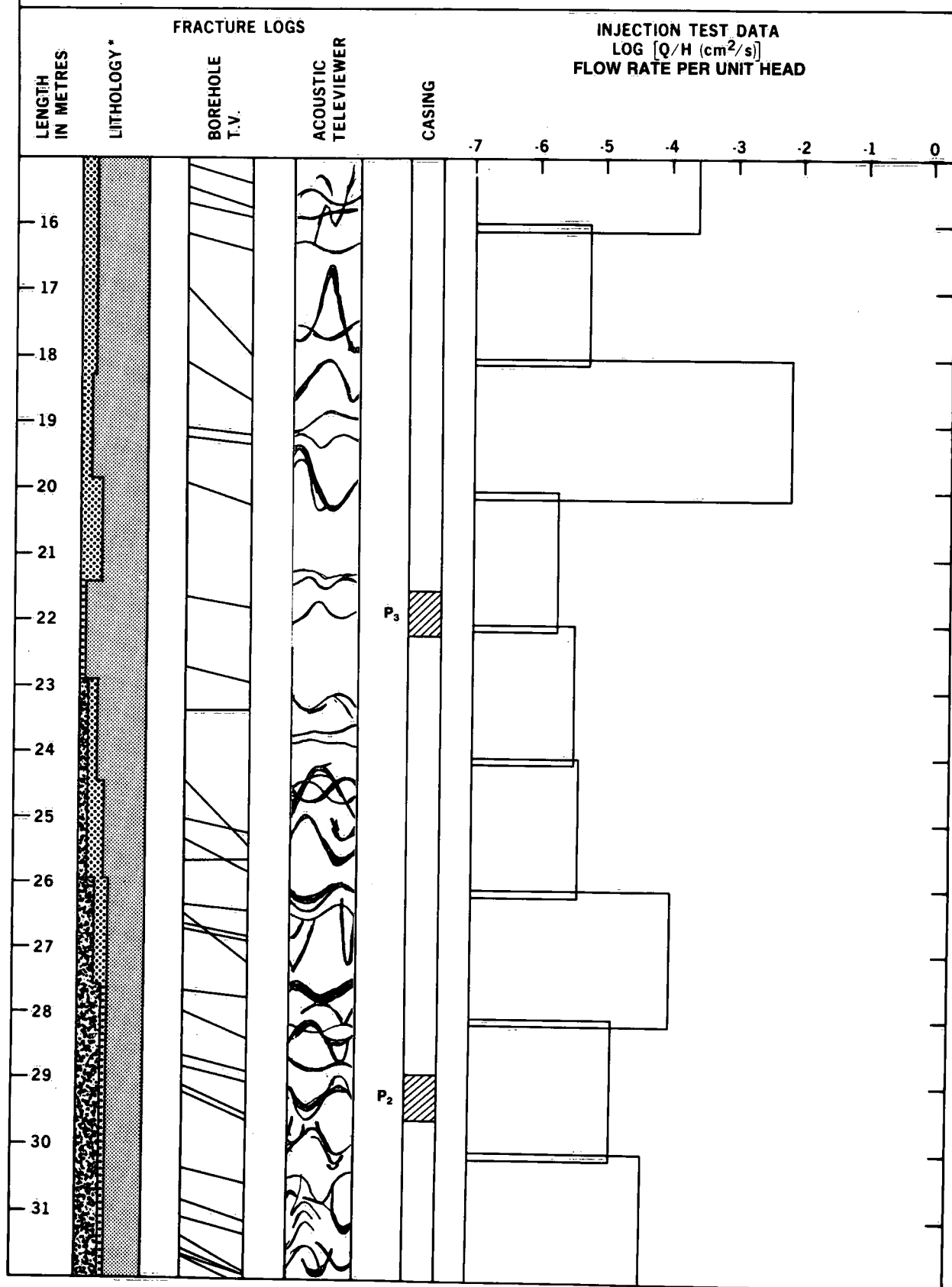


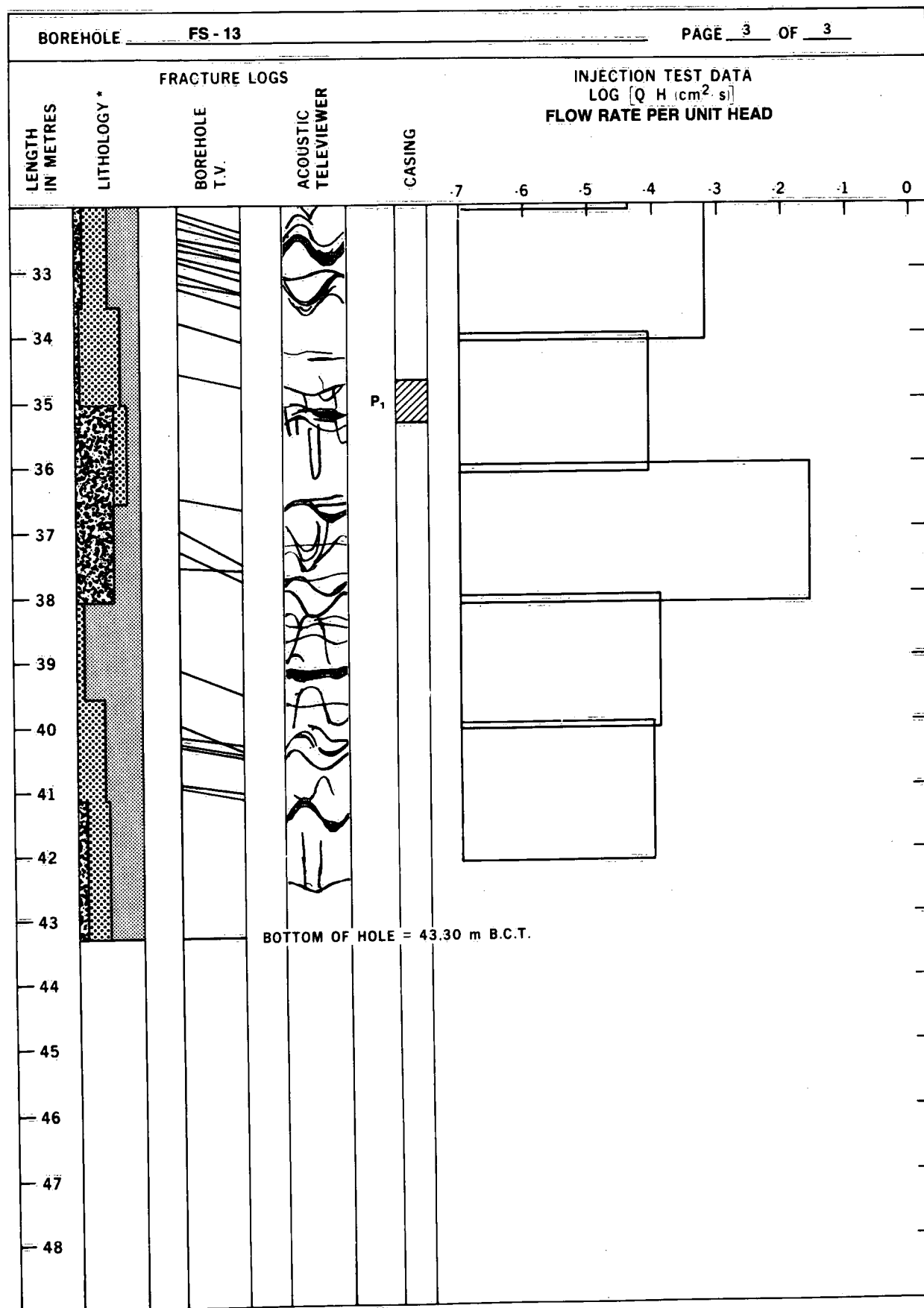


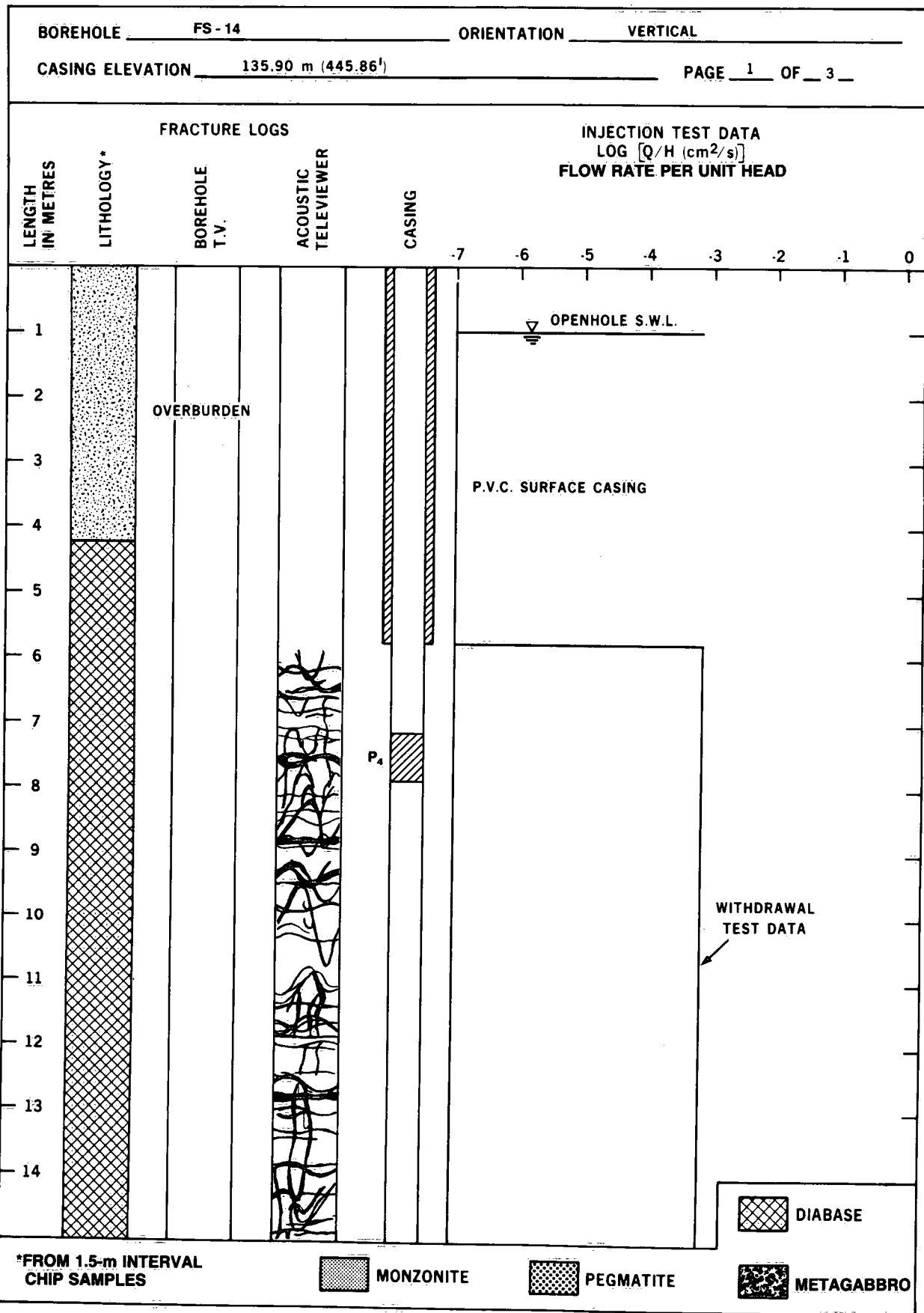


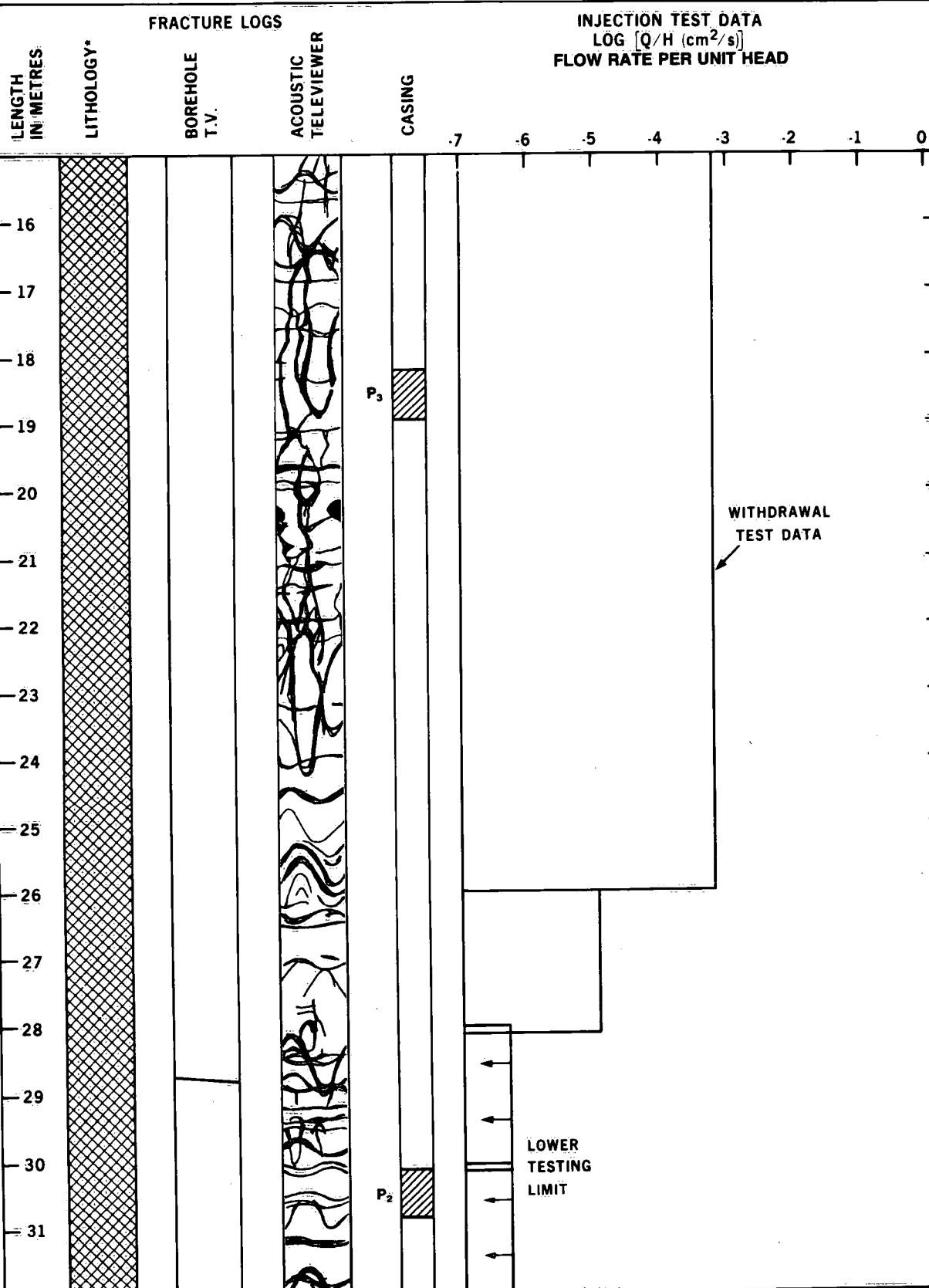


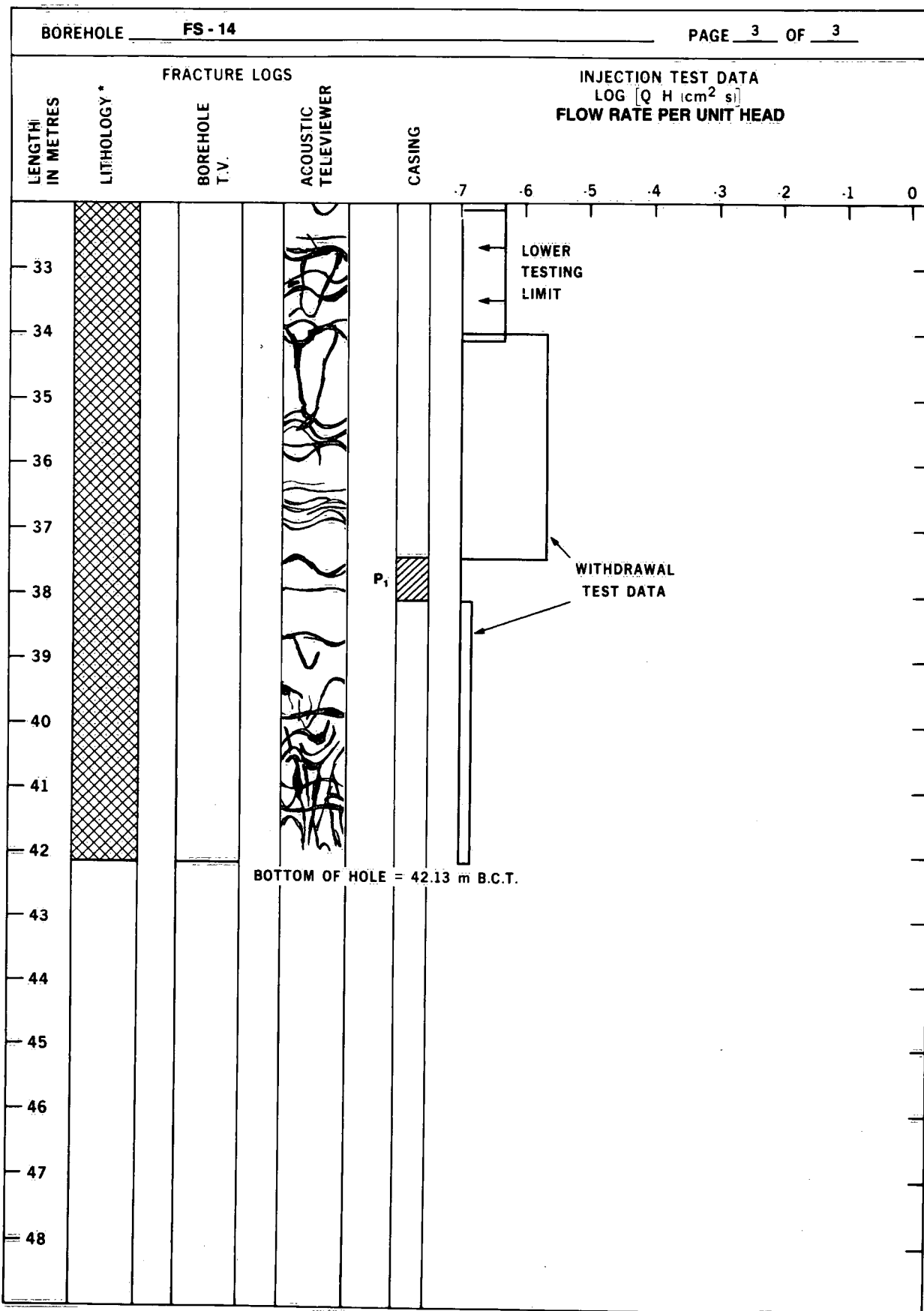


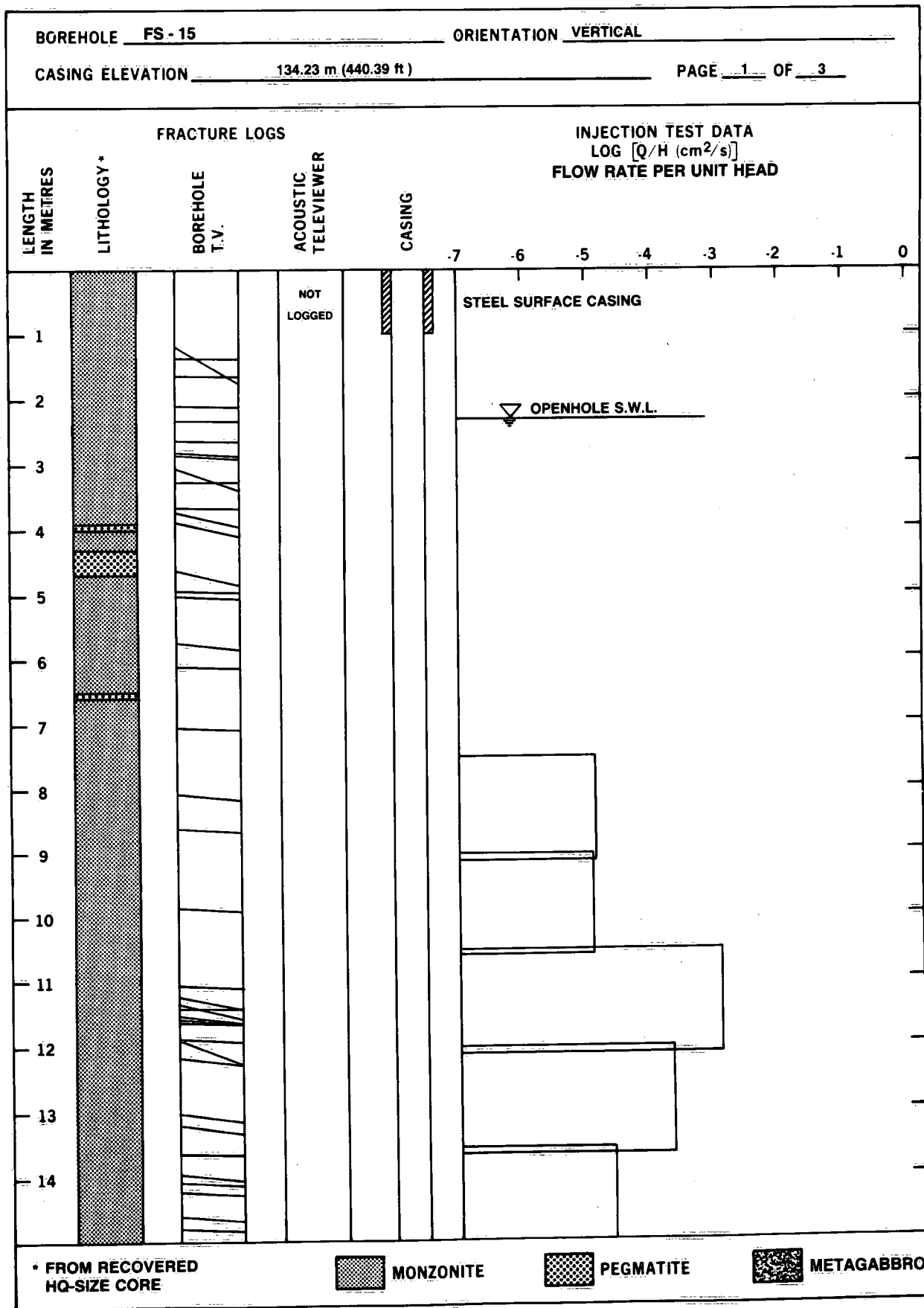


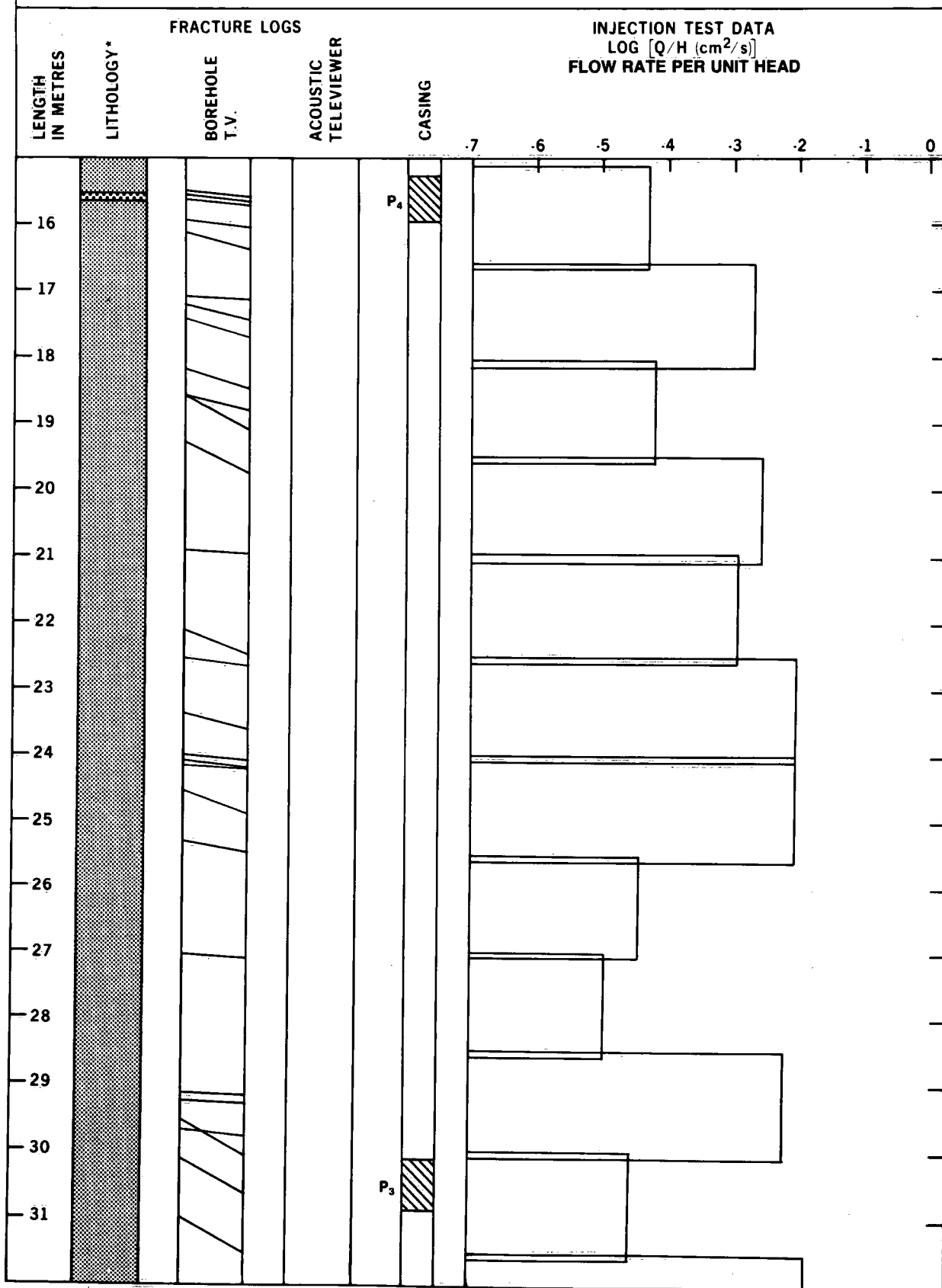


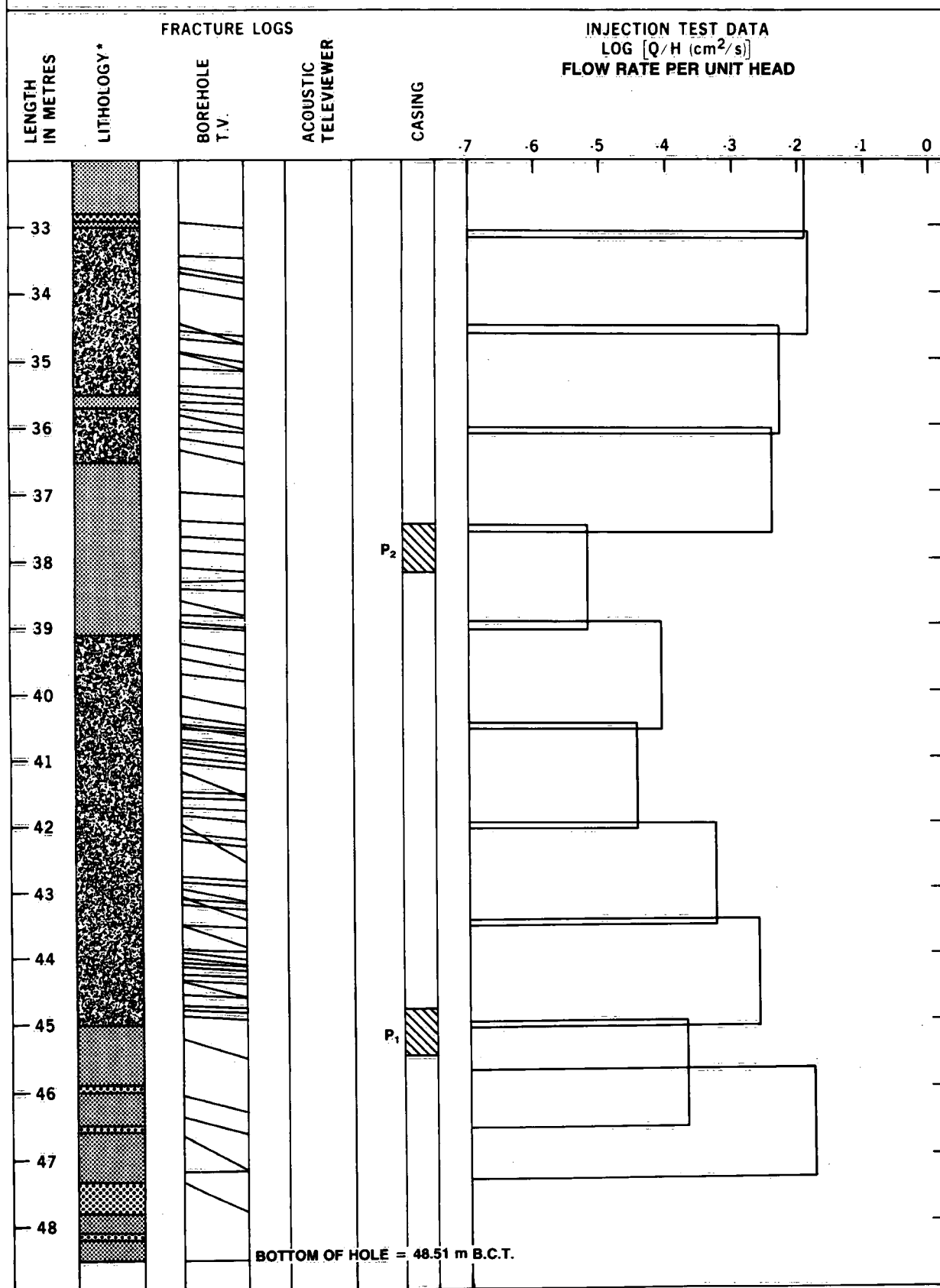


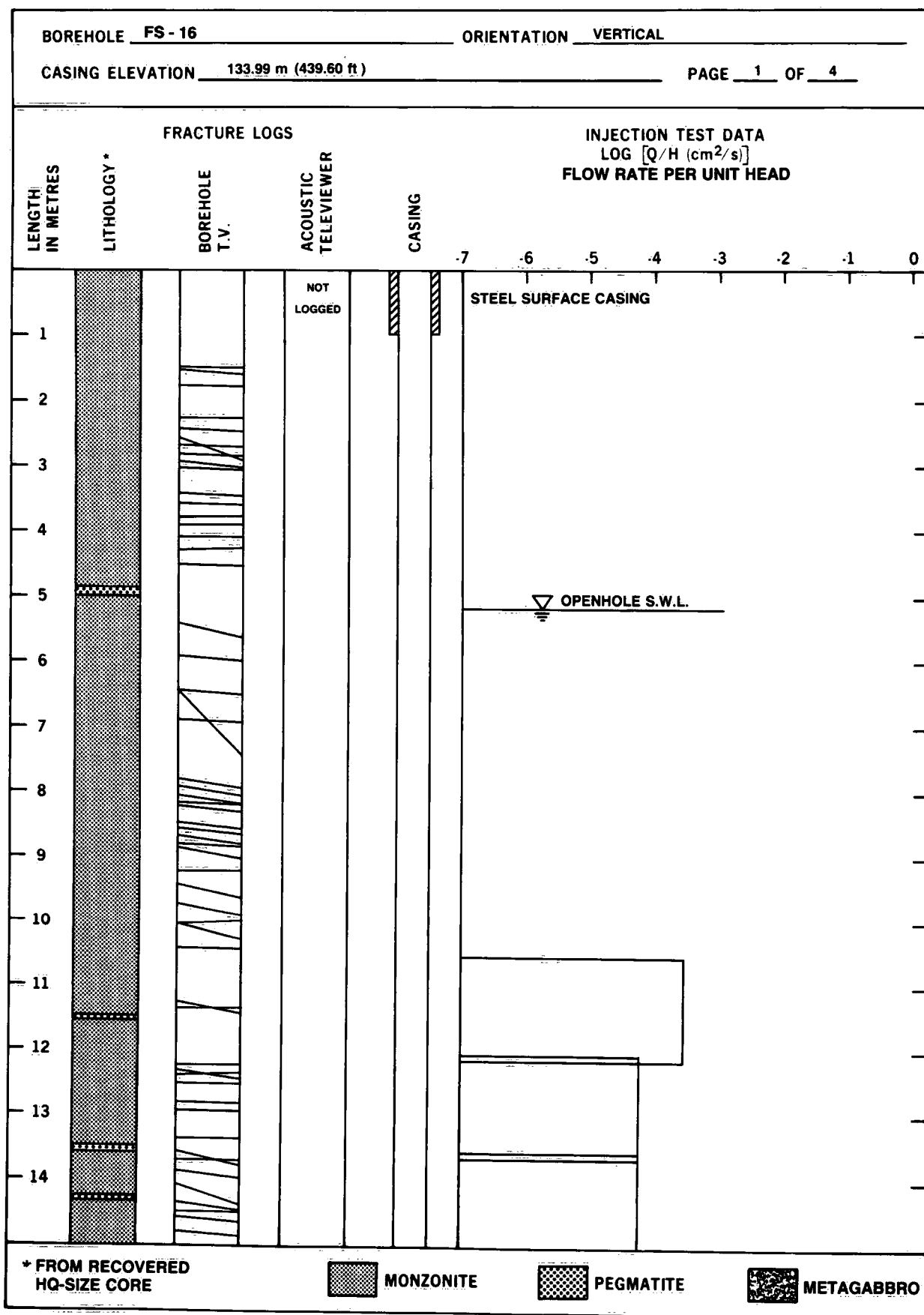


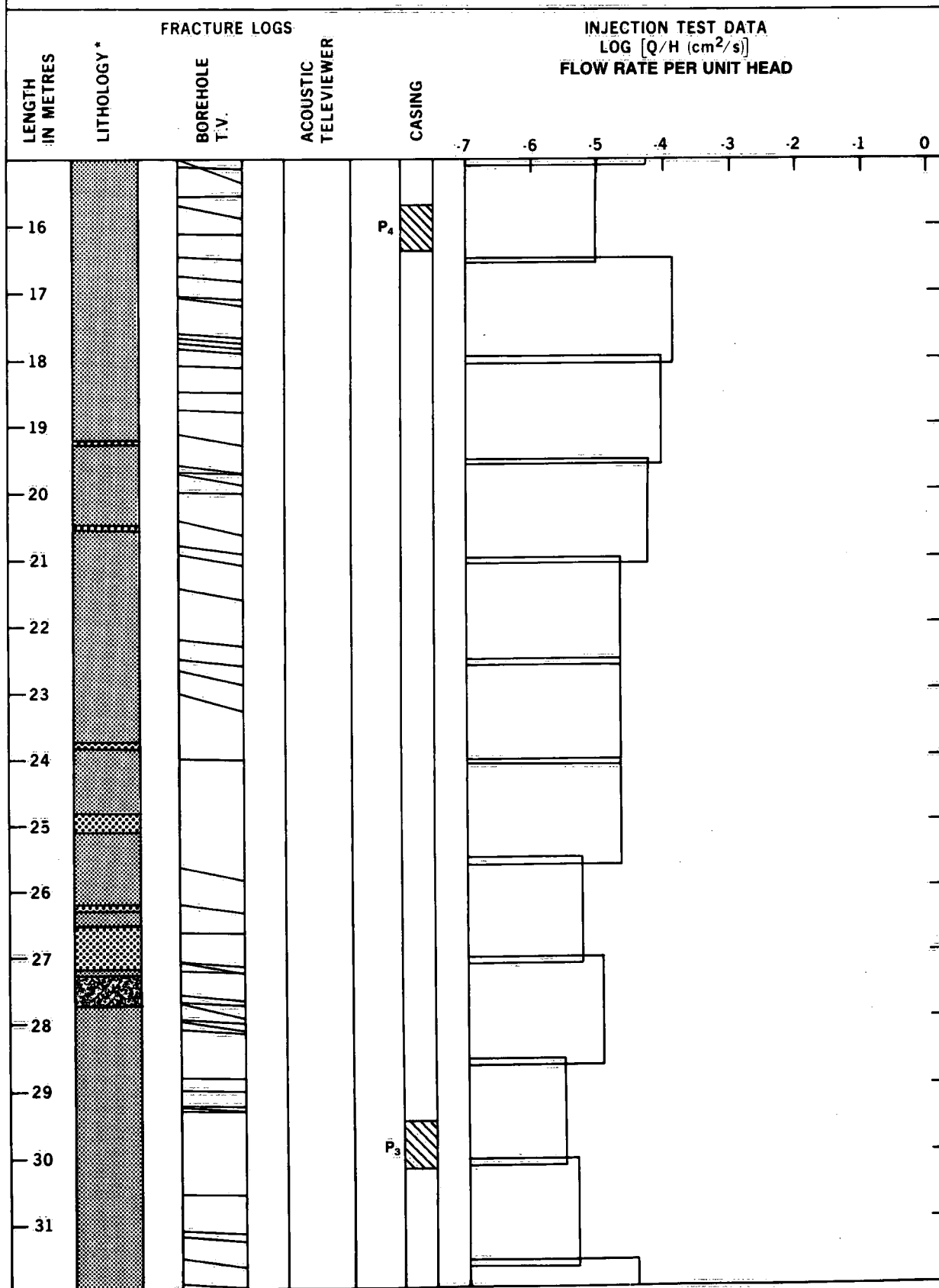


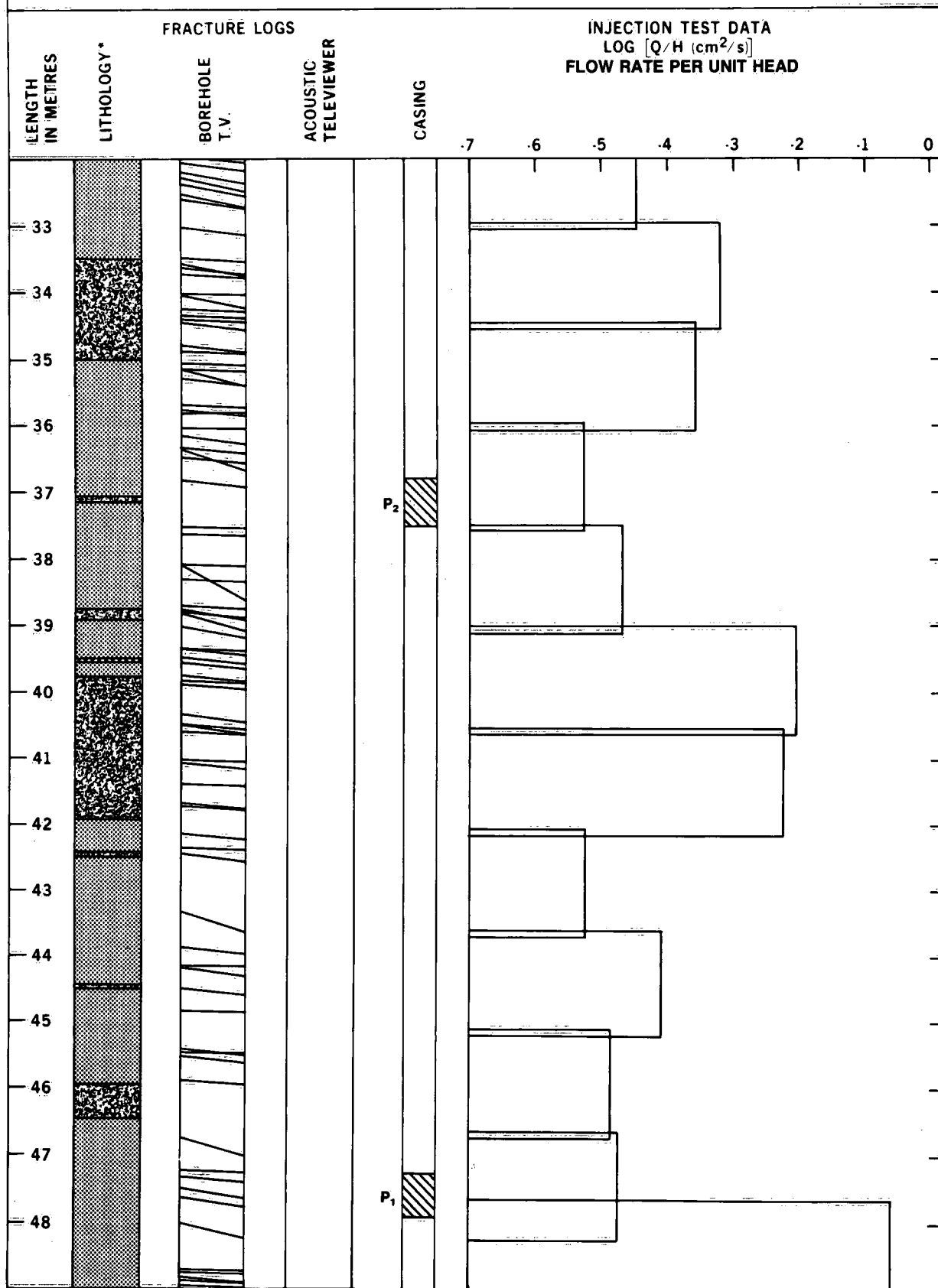












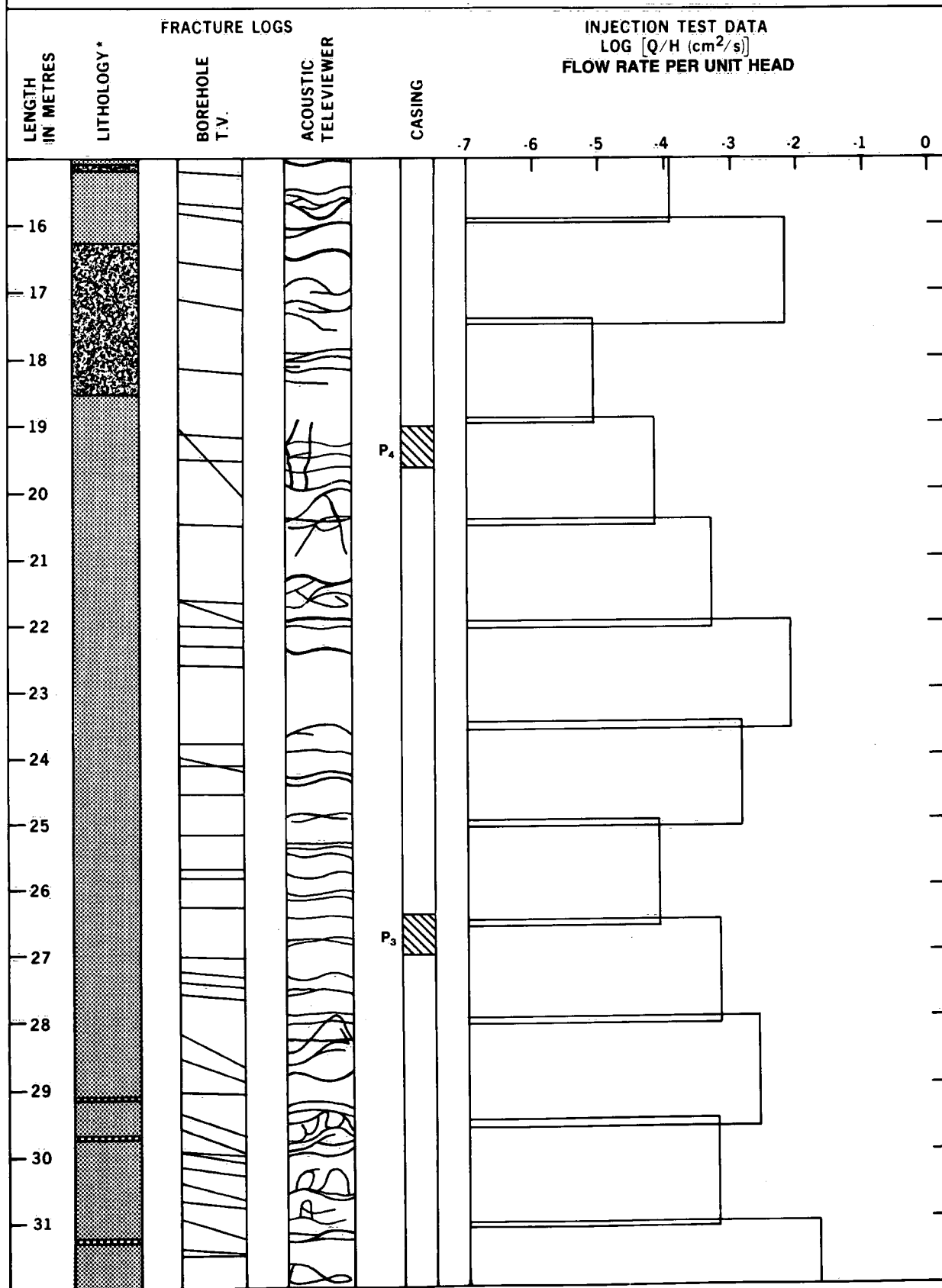
BOREHOLE FS - 16				PAGE 4 OF 4									
LENGTH IN METRES	LITHOLOGY *	FRACTURE LOGS				INJECTION TEST DATA							
		BOREHOLE T.V.	ACOUSTIC TELEVIEWER	CASING		LOG [Q/H (cm ² /s)]							
						FLOW RATE PER UNIT HEAD							
						-7	-6	-5	-4	-3	-2	-1	0
50													
51													
52													
53													
54													
55													
56													
57													
58													
59													
60													
61													
62													
63													
64													
65													

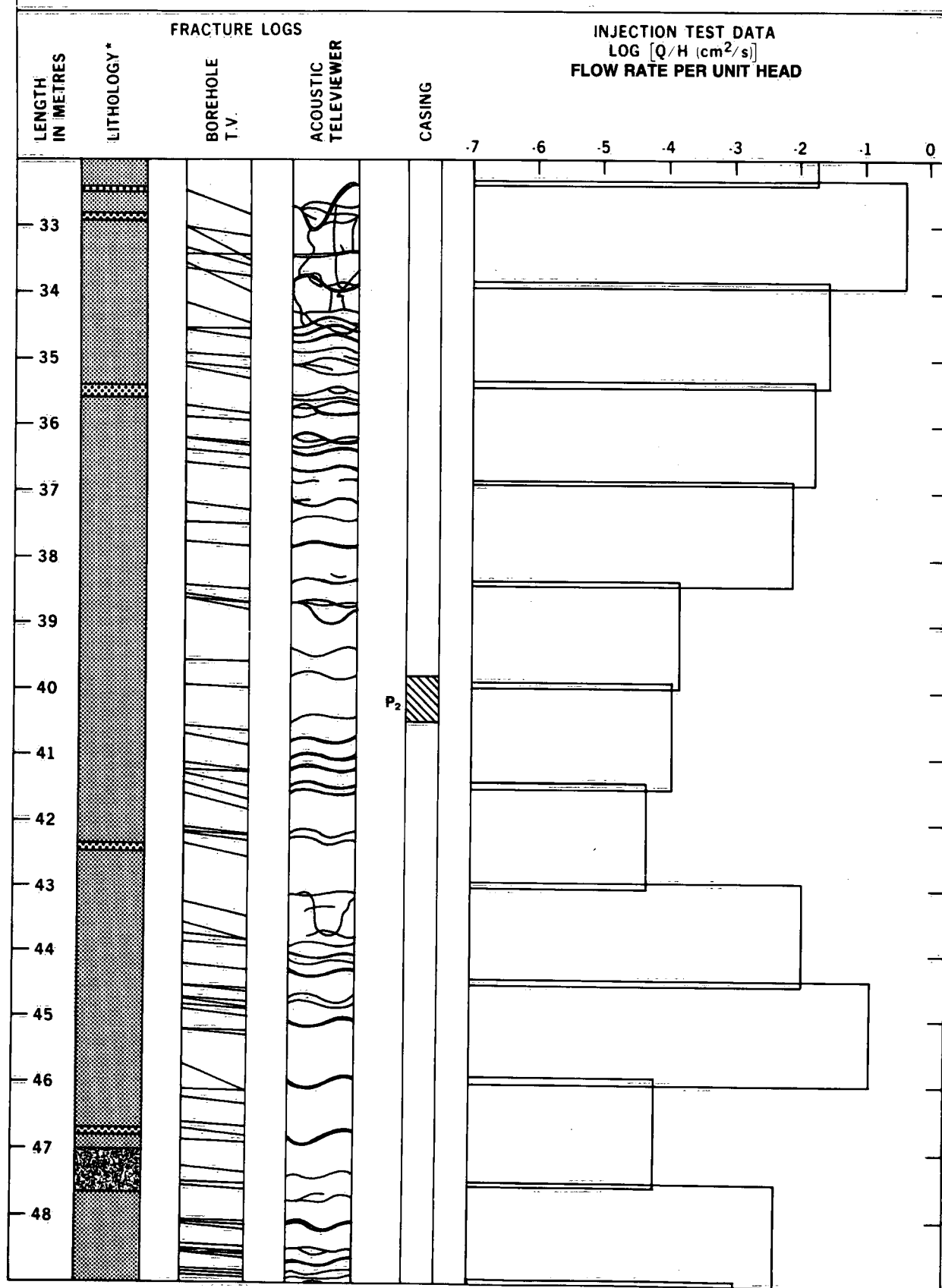
BOTTOM OF HOLE = 50.34 m B.C.T.

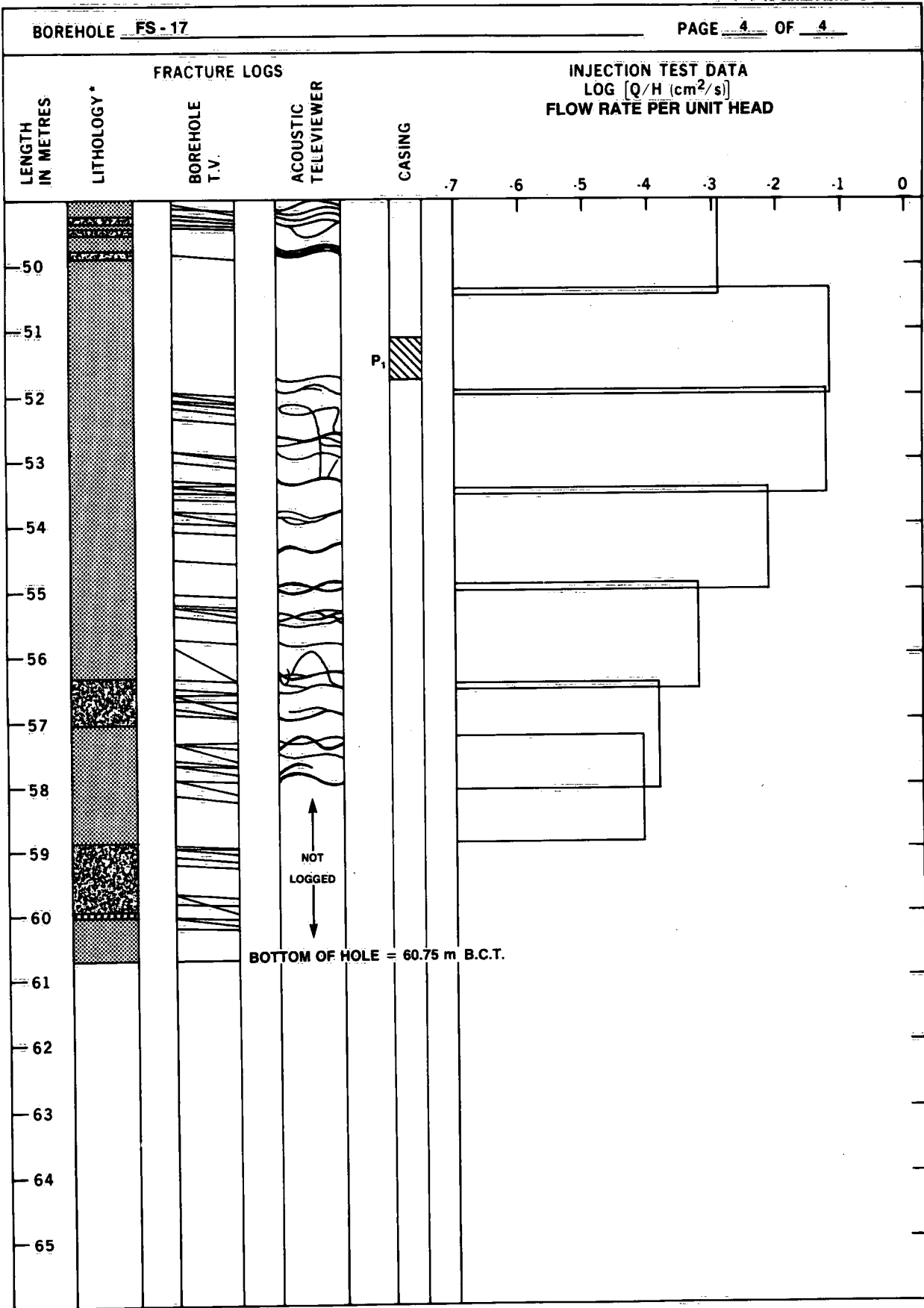
ORIENTATION VERTICAL

PAGE 1 OF 4









Appendix B
Straddle-Packer Injection Test Data,
Boreholes FS-1 to FS-17

Table B-1. Injection Test Summary Borehole FS-1

Depth of test interval (m B.C.T. *)	Injection head ΔH (m)	Flow rate Q ($m^3 \cdot s^{-1}$)	Flow rate per unit head $Q/\Delta H$ ($m^2 \cdot s^{-1}$)
4.00- 6.27	18.6	1.0×10^{-8}	5.5×10^{-10}
6.00- 8.27	18.3	4.1×10^{-9}	2.2×10^{-10}
8.00-10.27	18.8	2.1×10^{-7}	1.1×10^{-8}
10.00-12.27	19.0	1.1×10^{-7}	5.7×10^{-9}
12.00-14.27	18.7	1.7×10^{-8}	9.1×10^{-10}
14.00-16.27	18.3	2.7×10^{-8}	1.5×10^{-9}
16.00-18.27	18.3	3.4×10^{-8}	1.9×10^{-9}
18.00-20.27	17.8	5.7×10^{-8}	3.2×10^{-9}
20.00-22.27	17.8	7.6×10^{-8}	4.3×10^{-9}
22.00-24.27	18.7	6.7×10^{-7}	3.4×10^{-8}
24.00-26.27	18.8	6.2×10^{-7}	3.3×10^{-8}
26.00-28.27	18.3	6.7×10^{-8}	3.7×10^{-9}
28.00-30.27	18.0	7.9×10^{-8}	4.4×10^{-9}
30.00-32.27	17.5	8.0×10^{-8}	4.6×10^{-9}
32.00-34.27	18.4	1.9×10^{-8}	1.1×10^{-9}
34.00-36.27	17.3	2.5×10^{-8}	1.4×10^{-9}
36.00-38.27	18.3	1.9×10^{-8}	1.1×10^{-9}
38.00-40.27	17.3	$7.6 \times 10^{-10} \dagger$	4.4×10^{-11}
40.00-42.27	18.1	1.1×10^{-8}	5.9×10^{-10}

*Below casing top.

 \dagger Lowest measurable flow rate.

Table B-2. Injection Test Summary Borehole FS-2

Depth of test interval (m B.C.T. *)	Injection head ΔH (m)	Flow rate Q ($m^3 \cdot s^{-1}$)	Flow rate per unit head $Q/\Delta H$ ($m^2 \cdot s^{-1}$)
4.00- 6.27	15.5	5.9×10^{-7}	3.8×10^{-8}
6.00- 8.27	15.6	5.7×10^{-9}	3.6×10^{-10}
8.00-10.27	15.7	5.0×10^{-9}	3.1×10^{-10}
10.00-12.27	15.5	1.2×10^{-8}	7.7×10^{-10}
12.00-14.27	15.2	6.2×10^{-7}	4.1×10^{-8}
14.00-16.27	14.8	4.3×10^{-8}	2.9×10^{-9}
16.00-18.27	14.3	1.3×10^{-8}	8.8×10^{-10}
18.00-20.27	14.5	5.3×10^{-9}	3.7×10^{-10}
20.00-22.27	10.4	1.1×10^{-5}	1.1×10^{-6}
22.00-24.27	14.7	7.6×10^{-9}	5.2×10^{-10}
24.00-26.27	15.2	$3.8 \times 10^{-10} \dagger$	2.5×10^{-11}
26.00-28.27	14.8	3.7×10^{-8}	2.5×10^{-9}
28.00-30.27	18.1	$3.8 \times 10^{-10} \dagger$	2.1×10^{-11}
30.00-32.27	15.7	3.8×10^{-9}	2.4×10^{-10}
32.00-34.27	15.8	9.1×10^{-9}	5.8×10^{-10}
34.00-36.27	15.6	2.7×10^{-8}	1.7×10^{-9}
36.00-38.27	16.1	1.2×10^{-8}	7.5×10^{-10}
38.00-40.27	16.3	5.2×10^{-9}	3.2×10^{-10}
40.00-42.27	16.5	4.7×10^{-9}	2.8×10^{-10}

*Below casing top.

 \dagger Lowest measurable flow rate.

Table B-3. Injection Test Summary Borehole FS-3

Depth of test interval (m B.C.T. *)	Injection head ΔH (m)	Flow rate Q ($m^3 \cdot s^{-1}$)	Flow rate per unit head $Q/\Delta H$ ($m^2 \cdot s^{-1}$)
4.00- 6.27	8.50	1.9×10^{-9}	2.3×10^{-10}
6.00- 8.27	9.60	$3.8 \times 10^{-10} \dagger$	4.0×10^{-11}
8.00-10.27	9.20	2.3×10^{-8}	2.5×10^{-9}
10.00-12.27	15.6	1.6×10^{-8}	1.0×10^{-9}
12.00-14.27	15.5	6.3×10^{-8}	4.1×10^{-9}
14.00-16.27	16.2	6.4×10^{-9}	3.9×10^{-10}
16.00-18.27	17.5	1.3×10^{-8}	7.4×10^{-10}
18.00-20.27	15.4	6.0×10^{-8}	3.9×10^{-9}
20.00-22.27	15.5	3.0×10^{-9}	2.0×10^{-10}
22.00-24.27	18.0	3.6×10^{-9}	2.0×10^{-10}
24.00-26.27	15.6	1.0×10^{-8}	6.5×10^{-10}
26.00-28.27	16.4	7.2×10^{-7}	4.4×10^{-8}
28.00-30.27	16.4	6.4×10^{-7}	3.9×10^{-8}
30.00-32.27	16.0	1.5×10^{-8}	9.5×10^{-10}
32.00-34.27	16.4	2.3×10^{-9}	1.4×10^{-10}
34.00-36.27	15.8	2.9×10^{-8}	1.8×10^{-9}
36.00-38.27	15.8	9.9×10^{-8}	6.3×10^{-9}
38.20-40.47	15.3	3.5×10^{-7}	2.3×10^{-8}

*Below casing top.

 \dagger Lowest measurable flow rate.

Table B-4. Injection Test Summary Borehole FS-4

Depth of test interval (m B.C.T. *)	Injection head ΔH (m)	Flow rate Q ($m^3 \cdot s^{-1}$)	Flow rate per unit head $Q/\Delta H$ ($m^2 \cdot s^{-1}$)
4.00- 6.02	9.70	$3.8 \times 10^{-10} \dagger$	3.9×10^{-11}
6.00- 8.27	14.4	5.7×10^{-9}	3.9×10^{-10}
8.00-10.27	14.9	1.1×10^{-9}	7.3×10^{-11}
10.00-12.27	3.80	3.9×10^{-5}	1.0×10^{-5}
12.00-14.27	4.10	3.3×10^{-5}	7.9×10^{-6}
14.00-16.27	9.30	1.7×10^{-5}	1.8×10^{-6}
16.00-18.27	9.70	1.8×10^{-5}	1.9×10^{-6}
18.00-20.27	13.0	5.2×10^{-6}	4.0×10^{-7}
20.00-22.27	14.1	3.1×10^{-7}	2.2×10^{-8}
22.00-24.27	15.4	2.9×10^{-8}	1.9×10^{-9}
24.00-26.27	12.5	1.3×10^{-5}	1.0×10^{-6}
26.00-28.27	14.0	1.7×10^{-6}	1.2×10^{-7}
28.00-30.27	14.9	1.9×10^{-7}	1.2×10^{-8}
30.00-32.27	12.9	1.3×10^{-5}	1.0×10^{-6}
32.00-34.27	14.1	3.1×10^{-8}	2.2×10^{-9}
34.00-42.50	17.6	3.0×10^{-8}	1.7×10^{-9}

*Below casing top.

 \dagger Lowest measurable flow rate.

Table B-5. Injection Test Summary Borehole FS-5

Depth of test interval (m B.C.T. *)	Injection head ΔH (m)	Flow rate Q ($m^3 \cdot s^{-1}$)	Flow rate per unit head $Q/\Delta H$ ($m^2 \cdot s^{-1}$)
4.00- 6.27	10.3	2.4×10^{-6}	2.3×10^{-7}
6.00- 8.27	15.4	1.9×10^{-8}	1.2×10^{-9}
8.00-10.27	15.4	2.6×10^{-8}	1.7×10^{-9}
10.00-12.27	15.7	9.0×10^{-8}	5.7×10^{-9}
12.00-14.27	15.5	1.7×10^{-8}	1.1×10^{-9}
14.00-16.27	15.5	2.2×10^{-8}	1.4×10^{-9}
16.00-18.27	15.5	1.9×10^{-8}	1.2×10^{-9}
18.00-20.27	15.4	1.8×10^{-8}	1.2×10^{-9}
20.00-22.27	15.4	1.6×10^{-8}	1.1×10^{-9}
22.00-24.27	15.2	2.0×10^{-8}	1.3×10^{-9}
24.00-26.27	15.2	2.7×10^{-8}	1.8×10^{-9}
26.00-28.27	14.8	5.7×10^{-8}	3.9×10^{-9}
28.00-30.27	15.5	1.2×10^{-7}	8.0×10^{-9}
30.00-32.27	16.7	9.9×10^{-9}	5.9×10^{-10}
32.00-34.27	18.1	7.9×10^{-9}	4.4×10^{-10}
34.00-36.27	16.8	8.0×10^{-9}	4.8×10^{-10}
36.00-38.27	18.8	5.4×10^{-7}	2.9×10^{-8}
38.00-40.27	18.5	1.0×10^{-6}	5.5×10^{-8}
40.00-41.60	0.30	1.7×10^{-7}	5.6×10^{-7}

* Below casing top.

Table B-6. Injection Test Summary Borehole FS-6

Depth of test interval (m B.C.T. *)	Injection head ΔH (m)	Flow rate Q ($m^3 \cdot s^{-1}$)	Flow rate per unit head $Q/\Delta H$ ($m^2 \cdot s^{-1}$)
6.00- 8.27	15.5	3.8×10^{-8}	2.5×10^{-9}
8.00-10.27	14.0	3.4×10^{-8}	2.4×10^{-9}
10.00-12.27	14.2	1.1×10^{-8}	8.0×10^{-10}
12.00-14.27	14.3	1.1×10^{-8}	8.0×10^{-10}
14.00-16.27	13.4	9.1×10^{-8}	6.8×10^{-9}
16.00-18.27	14.5	1.1×10^{-8}	7.2×10^{-10}
18.00-20.27	14.3	7.6×10^{-8}	5.3×10^{-9}
20.00-22.27	14.6	1.3×10^{-8}	8.8×10^{-10}
22.00-24.27	14.1	1.8×10^{-8}	1.2×10^{-9}
24.00-26.27	8.20	2.7×10^{-8}	3.3×10^{-9}
26.00-28.27	8.00	5.3×10^{-9}	6.7×10^{-10}
28.00-30.27	7.00	4.9×10^{-9}	7.1×10^{-10}
30.00-32.27	6.60	3.5×10^{-9}	1.4×10^{-9}
32.00-34.27	6.10	3.3×10^{-9}	5.4×10^{-8}
34.00-36.27	2.90	1.5×10^{-5}	5.1×10^{-6}
36.00-38.27	5.10	1.6×10^{-8}	3.1×10^{-9}
38.00-40.27	4.80	6.0×10^{-9}	1.3×10^{-9}

* Below casing top.

Table B-7. Injection Test Summary Borehole FS-7

Depth of test interval (m B.C.T. *)	Injection head ΔH (m)	Flow rate Q ($m^3 \cdot s^{-1}$)	Flow rate per unit head $Q/\Delta H$ ($m^2 \cdot s^{-1}$)
4.00- 6.10	19.0	2.6×10^{-6}	1.3×10^{-7}
6.00- 8.10	19.3	3.1×10^{-6}	1.6×10^{-7}
8.00-10.10	15.7	$6.7 \times 10^{-10} \dagger$	4.3×10^{-11}
10.00-12.10	19.7	2.7×10^{-8}	1.4×10^{-9}
12.00-14.10	20.3	2.4×10^{-8}	1.2×10^{-9}
14.00-16.10	20.2	1.7×10^{-8}	8.3×10^{-10}
16.00-18.10	6.20	6.1×10^{-9}	9.8×10^{-10}
18.00-20.10	6.30	1.5×10^{-8}	2.4×10^{-9}
20.00-22.10	21.6	8.7×10^{-8}	4.0×10^{-9}
22.00-24.10	22.1	6.9×10^{-8}	3.1×10^{-9}
24.00-26.10	21.2	1.4×10^{-7}	6.4×10^{-9}
26.00-28.10	22.1	1.9×10^{-8}	8.5×10^{-10}
28.00-30.10	22.9	1.8×10^{-8}	7.6×10^{-10}
30.00-32.10	23.5	3.9×10^{-8}	1.7×10^{-9}
32.00-34.10	21.6	2.6×10^{-6}	1.2×10^{-7}
34.00-36.10	22.0	1.4×10^{-7}	6.2×10^{-9}
36.00-38.10	8.40	4.0×10^{-5}	4.8×10^{-6}
38.00-40.10	22.2	2.6×10^{-8}	1.2×10^{-9}
40.00-42.10	21.1	2.6×10^{-7}	1.2×10^{-8}
42.00-44.10	20.4	2.6×10^{-6}	1.3×10^{-7}
44.00-46.10	20.6	5.0×10^{-8}	2.4×10^{-9}
46.00-48.10	19.3	3.6×10^{-6}	1.9×10^{-7}
48.00-50.10	0.20	6.5×10^{-5}	2.8×10^{-4}
47.00-49.10	20.3	2.5×10^{-8}	1.2×10^{-9}
49.50-51.60	0.14	7.0×10^{-5}	5.0×10^{-4}
50.00-52.10	14.2	3.2×10^{-5}	2.3×10^{-6}
52.00-54.10	24.2	2.7×10^{-6}	1.1×10^{-7}
54.00-56.10	25.0	1.5×10^{-7}	6.1×10^{-9}
55.00-57.10	24.2	1.5×10^{-7}	6.1×10^{-9}
57.00-59.10	23.6	1.1×10^{-7}	4.7×10^{-9}
58.00-60.10	23.4	2.8×10^{-7}	1.2×10^{-8}
60.00-62.10	23.5	1.7×10^{-7}	7.4×10^{-9}
62.00-64.10	23.9	3.7×10^{-8}	1.6×10^{-9}
64.00-66.10	23.3	2.6×10^{-8}	1.1×10^{-9}
66.00-68.10	22.5	5.7×10^{-7}	2.5×10^{-8}
68.00-70.10	23.1	2.9×10^{-8}	1.3×10^{-9}
70.00-72.10	21.9	6.0×10^{-9}	2.7×10^{-10}
71.00-73.10	22.9	$6.7 \times 10^{-10} \dagger$	2.9×10^{-11}

*Below casing top.

†Lowest measurable flow rate.

Table B-8. Injection Test Summary Borehole FS-8

Depth of test interval (m B.C.T. *)	Injection head ΔH (m)	Flow rate Q ($m^3 \cdot s^{-1}$)	Flow rate per unit head $Q/\Delta H$ ($m^2 \cdot s^{-1}$)
8.00-10.27	14.8	2.7×10^{-9}	1.8×10^{-10}
10.00-12.27	14.8	5.7×10^{-9}	3.9×10^{-10}
12.00-14.27	17.4	9.5×10^{-9}	5.5×10^{-10}
14.00-16.27	17.5	4.2×10^{-9}	2.4×10^{-10}
16.00-18.27	16.9	9.5×10^{-9}	5.6×10^{-10}
18.00-20.27	17.0	5.3×10^{-9}	3.1×10^{-10}
20.00-22.27	16.7	7.6×10^{-9}	4.6×10^{-10}
22.00-24.27	18.6	7.6×10^{-9}	4.1×10^{-10}
24.00-26.27	16.7	1.3×10^{-8}	8.0×10^{-10}
26.00-28.27	9.80	2.6×10^{-5}	2.6×10^{-6}
28.00-30.27	2.30	4.2×10^{-5}	1.8×10^{-5}
30.00-32.27	16.8	6.2×10^{-7}	3.7×10^{-8}
32.00-34.27	17.8	1.9×10^{-9}	1.1×10^{-10}
34.00-36.27	17.7	3.6×10^{-8}	2.0×10^{-9}
36.00-38.27	16.0	3.4×10^{-8}	2.1×10^{-9}
38.00-40.27	16.5	2.7×10^{-8}	1.6×10^{-10}

*Below casing top.

Table B-9. Injection Test Summary Borehole FS-9

Depth of test interval (m B.C.T. *)	Injection head ΔH (m)	Flow rate Q ($m^3 \cdot s^{-1}$)	Flow rate per unit head $Q/\Delta H$ ($m^2 \cdot s^{-1}$)
8.00-10.27	12.6	1.3×10^{-8}	1.0×10^{-9}
10.00-12.27	13.9	8.2×10^{-7}	5.6×10^{-8}
12.00-14.27	15.4	5.7×10^{-9}	3.7×10^{-10}
14.00-16.27	14.7	4.6×10^{-9}	3.1×10^{-10}
16.00-18.27	15.1	2.2×10^{-8}	1.5×10^{-10}
18.00-20.27	14.2	4.2×10^{-9}	3.0×10^{-10}
20.00-22.27	16.6	7.6×10^{-10}	4.6×10^{-11}
22.00-24.27	16.1	9.1×10^{-9}	5.7×10^{-10}
24.00-26.27	15.3	2.1×10^{-8}	1.4×10^{-9}
26.00-28.27	14.3	4.7×10^{-7}	3.3×10^{-8}
28.00-30.27	13.9	4.3×10^{-7}	3.1×10^{-8}
30.00-32.27	14.7	8.6×10^{-8}	5.9×10^{-9}
32.00-34.27	0.40	5.1×10^{-5}	1.3×10^{-4}
34.00-36.27	14.7	1.5×10^{-9}	1.0×10^{-10}
36.00-38.27	14.3	1.7×10^{-8}	1.2×10^{-9}
38.00-40.27	15.3	3.4×10^{-6}	2.2×10^{-7}

*Below casing top.

Table B-10. Injection Test Summary Borehole FS-10

Depth of test interval (m B.C.T. *)	Injection head ΔH (m)	Flow rate Q ($m^3 \cdot s^{-1}$)	Flow rate per unit head $Q/\Delta H$ ($m^2 \cdot s^{-1}$)
12.00-14.10	11.3	9.4×10^{-9}	8.3×10^{-10}
14.00-16.10	11.5	$6.7 \times 10^{-10} \dagger$	5.9×10^{-11}
16.00-18.10	10.7	2.0×10^{-8}	1.9×10^{-9}
18.00-20.10	12.2	2.1×10^{-8}	1.8×10^{-9}
20.00-22.10	12.5	$6.7 \times 10^{-10} \dagger$	5.4×10^{-11}
22.00-24.10	13.2	$6.7 \times 10^{-10} \dagger$	5.1×10^{-11}
24.00-26.10	12.4	1.1×10^{-8}	8.7×10^{-10}
26.00-28.10	14.4	8.7×10^{-9}	6.1×10^{-10}
28.00-30.10	14.9	8.7×10^{-9}	5.9×10^{-10}
30.00-32.10	15.6	5.4×10^{-9}	3.5×10^{-10}
32.00-34.10	15.6	7.4×10^{-9}	4.7×10^{-10}
34.00-36.10	12.8	1.8×10^{-8}	1.4×10^{-9}
36.00-38.10	12.6	8.7×10^{-8}	6.9×10^{-9}
38.00-40.10	14.7	4.0×10^{-9}	2.7×10^{-10}
40.00-42.10	12.3	1.9×10^{-8}	1.5×10^{-9}
42.00-44.10	2.00	6.7×10^{-5}	3.4×10^{-5}
44.00-46.10	22.2	1.5×10^{-7}	6.7×10^{-9}
45.58-47.68	25.8	1.0×10^{-8}	3.9×10^{-10}

*Below casing top.

 \dagger Lowest measurable flow rate.

Table B-11. Injection Test Summary Borehole FS-11

Depth of test interval (m B.C.T. *)	Injection head ΔH (m)	Flow rate Q ($m^3 \cdot s^{-1}$)	Flow rate per unit head $Q/\Delta H$ ($m^2 \cdot s^{-1}$)
6.00- 8.10	17.2	1.7×10^{-8}	9.7×10^{-10}
8.00-10.10	10.6	2.7×10^{-8}	2.5×10^{-9}
10.00-12.10	17.2	1.3×10^{-8}	7.8×10^{-10}
12.00-14.10	17.7	4.8×10^{-8}	2.7×10^{-9}
14.00-16.10	19.2	$6.7 \times 10^{-10} \dagger$	3.5×10^{-11}
16.00-18.10	20.0	$6.7 \times 10^{-10} \dagger$	3.4×10^{-11}
18.00-20.10	14.8	$6.7 \times 10^{-10} \dagger$	4.5×10^{-11}
20.00-22.10	18.8	$6.7 \times 10^{-10} \dagger$	3.6×10^{-11}
22.00-24.10	16.6	2.8×10^{-8}	1.7×10^{-9}
24.00-26.10	17.7	$6.7 \times 10^{-10} \dagger$	3.8×10^{-11}
26.00-28.10	18.1	$6.7 \times 10^{-10} \dagger$	3.7×10^{-11}
28.00-30.10	17.8	8.1×10^{-9}	4.5×10^{-10}
30.00-32.10	18.9	3.6×10^{-8}	1.9×10^{-9}
32.00-34.10	14.5	4.0×10^{-8}	2.8×10^{-9}
34.00-36.10	8.10	2.2×10^{-5}	2.7×10^{-6}
36.00-38.10	18.8	6.7×10^{-9}	3.6×10^{-10}
38.00-40.10	11.7	1.7×10^{-5}	1.5×10^{-6}
40.00-42.10	23.9	3.1×10^{-8}	1.3×10^{-9}
40.42-42.52	23.5	1.5×10^{-8}	6.3×10^{-10}

*Below casing top.

 \dagger Lowest measurable flow rate.

Table B-12. Injection Test Summary Borehole FS-12

Depth of test interval (m B.C.T. *)	Injection head ΔH (m)	Flow rate Q ($\text{m}^3 \cdot \text{s}^{-1}$)	Flow rate per unit head $Q/\Delta H$ ($\text{m}^2 \cdot \text{s}^{-1}$)
6.00- 8.10	5.80	1.0×10^{-8}	1.7×10^{-9}
8.00-18.00†	7.46	3.3×10^{-7}	4.4×10^{-8}
18.00-20.10	13.2	1.7×10^{-8}	1.4×10^{-9}
20.00-22.10	12.1	6.1×10^{-8}	1.0×10^{-8}
22.00-24.10	13.0	2.2×10^{-8}	1.7×10^{-9}
24.00-26.10	13.2	1.9×10^{-8}	1.4×10^{-9}
26.00-28.10	13.1	6.7×10^{-9}	5.1×10^{-10}
28.00-30.10	13.3	4.7×10^{-9}	3.5×10^{-10}
30.00-32.10	12.4	2.7×10^{-9}	2.2×10^{-10}
32.00-34.10	12.6	$6.7 \times 10^{-10} \ddagger$	8.0×10^{-11}
34.00-36.10	11.8	7.1×10^{-8}	6.0×10^{-9}
36.00-38.10	12.7	6.4×10^{-8}	5.0×10^{-9}
38.00-40.10	12.9	3.4×10^{-8}	2.6×10^{-9}
40.00-42.10	12.8	3.6×10^{-8}	2.8×10^{-9}
40.55-42.65	11.9	1.2×10^{-7}	9.7×10^{-9}

* Below casing top.

† Withdrawal test data.

‡ Lowest measurable flow rate.

Table B-13. Injection Test Summary Borehole FS-13

Depth of test interval (m B.C.T. *)	Injection head ΔH (m)	Flow rate Q ($\text{m}^3 \cdot \text{s}^{-1}$)	Flow rate per unit head $Q/\Delta H$ ($\text{m}^2 \cdot \text{s}^{-1}$)
8.00-10.10	16.2	5.2×10^{-8}	3.2×10^{-9}
10.00-12.10	16.9	1.7×10^{-7}	1.0×10^{-8}
12.00-14.10	16.8	5.4×10^{-8}	3.2×10^{-9}
14.00-16.10	16.5	4.0×10^{-7}	2.0×10^{-8}
16.00-18.10	16.6	8.1×10^{-9}	4.9×10^{-10}
18.00-20.10	13.4	8.7×10^{-6}	6.5×10^{-7}
20.00-22.10	15.5	2.7×10^{-9}	1.7×10^{-10}
22.00-24.10	15.5	4.7×10^{-9}	3.0×10^{-10}
24.00-26.10	14.7	5.4×10^{-9}	3.7×10^{-10}
26.00-28.10	11.2	1.1×10^{-7}	9.8×10^{-9}
28.00-30.10	13.6	1.7×10^{-8}	1.2×10^{-9}
30.00-32.10	12.2	4.6×10^{-8}	3.8×10^{-9}
32.00-34.10	12.1	7.6×10^{-7}	6.3×10^{-8}
34.00-36.10	15.1	1.1×10^{-7}	7.5×10^{-9}
36.00-38.10	11.5	2.8×10^{-5}	2.4×10^{-6}
38.00-40.10	14.3	1.6×10^{-7}	1.1×10^{-8}
40.00-42.10	17.0	1.6×10^{-7}	9.5×10^{-9}

* Below casing top.

Table B-14. Injection Test Summary Borehole FS-14

Depth of test interval (m B.C.T. *)	Injection head ΔH (m)	Flow rate Q ($\text{m}^3 \cdot \text{s}^{-1}$)	Flow rate per unit head $Q/\Delta H$ ($\text{m}^2 \cdot \text{s}^{-1}$)
5.80-26.00†	8.43	5.6×10^{-7}	6.6×10^{-8}
26.00-28.10	14.1	1.5×10^{-8}	1.0×10^{-9}
28.00-30.10	14.5	$6.7 \times 10^{-10} \ddagger$	4.6×10^{-11}
30.00-32.10	14.9	$6.7 \times 10^{-10} \ddagger$	4.5×10^{-11}
32.00-34.10	14.4	$6.7 \times 10^{-10} \ddagger$	4.7×10^{-11}
34.00-37.41†	9.71	1.9×10^{-9}	2.0×10^{-10}
38.10-42.13†	12.9	1.9×10^{-10}	1.5×10^{-11}

* Below casing top.

† Withdrawal test data.

‡ Lowest measurable flow rate.

Table B-15. Injection Test Summary Borehole FS-15

Depth of test interval (m B.C.T. *)	Injection head ΔH (m)	Flow rate Q ($\text{m}^3 \cdot \text{s}^{-1}$)	Flow rate per unit head $Q/\Delta H$ ($\text{m}^2 \cdot \text{s}^{-1}$)
7.50- 9.05	19.6	2.4×10^{-8}	1.2×10^{-9}
9.00-10.55	20.8	2.5×10^{-8}	1.2×10^{-9}
10.50-12.05	13.4	1.6×10^{-6}	1.2×10^{-7}
12.00-13.55	14.8	2.8×10^{-7}	1.9×10^{-8}
13.50-15.05	15.2	3.6×10^{-8}	2.4×10^{-9}
15.00-16.55	16.7	8.5×10^{-8}	5.1×10^{-9}
16.50-18.05	7.28	1.6×10^{-6}	2.2×10^{-7}
18.00-19.55	8.32	5.1×10^{-8}	6.1×10^{-6}
19.50-21.05	7.16	1.9×10^{-6}	2.7×10^{-7}
21.00-22.55	9.97	1.0×10^{-6}	1.0×10^{-7}
22.50-24.05	14.4	1.1×10^{-5}	8.0×10^{-7}
24.00-25.55	15.7	1.3×10^{-5}	8.2×10^{-7}
25.50-27.05	14.9	4.9×10^{-9}	3.3×10^{-9}
27.00-28.55	15.6	1.7×10^{-8}	1.1×10^{-9}
28.50-30.05	17.0	8.7×10^{-6}	5.3×10^{-7}
30.00-31.55	11.8	3.3×10^{-8}	2.8×10^{-9}
31.50-33.05	14.1	1.8×10^{-5}	1.3×10^{-6}
33.00-34.55	14.3	2.0×10^{-5}	1.4×10^{-6}
34.50-36.05	9.28	5.1×10^{-6}	5.5×10^{-7}
36.00-37.55	13.2	5.7×10^{-6}	4.3×10^{-7}
37.50-39.05	18.1	1.2×10^{-8}	6.7×10^{-10}
39.00-40.55	20.2	1.7×10^{-7}	8.6×10^{-9}
40.50-42.05	19.7	7.4×10^{-8}	3.8×10^{-9}
42.00-43.55	18.8	1.0×10^{-6}	5.5×10^{-8}
43.50-45.05	16.2	4.0×10^{-6}	2.5×10^{-7}
45.00-46.55	20.5	4.0×10^{-7}	1.9×10^{-8}
46.55-48.05	12.7	2.0×10^{-5}	1.6×10^{-6}

* Below casing top.

Table B-16. Injection Test Summary Borehole FS-16

Depth of test interval (m B.C.T.)*	Injection head ΔH (m)	Flow rate Q ($m^3 \cdot s^{-1}$)	Flow rate per unit head $Q/\Delta H$ ($m^2 \cdot s^{-1}$)
10.50-12.05	20.9	4.9×10^{-7}	2.4×10^{-8}
12.00-13.55	19.6	9.9×10^{-8}	5.1×10^{-9}
13.50-15.05	19.4	9.9×10^{-8}	5.1×10^{-9}
15.00-16.55	25.6	2.1×10^{-8}	8.3×10^{-10}
16.50-18.05	23.8	2.3×10^{-7}	9.9×10^{-9}
18.00-19.55	24.1	1.7×10^{-7}	7.2×10^{-9}
19.50-21.05	22.4	1.1×10^{-7}	4.9×10^{-9}
21.00-22.55	24.0	4.9×10^{-8}	2.1×10^{-9}
22.50-24.05	23.7	4.9×10^{-8}	2.1×10^{-9}
24.00-25.55	23.2	4.6×10^{-8}	2.0×10^{-9}
25.50-27.05	23.6	1.2×10^{-8}	5.0×10^{-10}
27.00-28.55	23.2	2.3×10^{-8}	9.8×10^{-10}
28.50-30.05	23.3	5.2×10^{-9}	2.2×10^{-10}
30.00-31.55	24.4	1.1×10^{-8}	4.3×10^{-10}
31.50-33.05	24.2	7.4×10^{-8}	3.1×10^{-9}
33.00-34.55	23.6	1.3×10^{-6}	5.6×10^{-8}
34.50-36.05	23.7	5.2×10^{-7}	2.2×10^{-8}
36.00-37.55	24.9	1.3×10^{-8}	5.1×10^{-10}
37.50-39.05	25.0	4.9×10^{-8}	2.0×10^{-9}
39.00-41.55	20.9	1.8×10^{-5}	8.6×10^{-7}
40.50-42.05	17.6	1.0×10^{-5}	5.8×10^{-7}
42.00-43.55	15.8	9.1×10^{-9}	5.8×10^{-10}
43.50-45.05	9.22	9.4×10^{-8}	8.1×10^{-9}
45.00-46.55	10.0	1.4×10^{-8}	1.4×10^{-9}
46.50-48.05	8.94	1.6×10^{-8}	1.8×10^{-9}
47.48-49.03	1.57	3.6×10^{-5}	2.3×10^{-5}

*Below casing top.

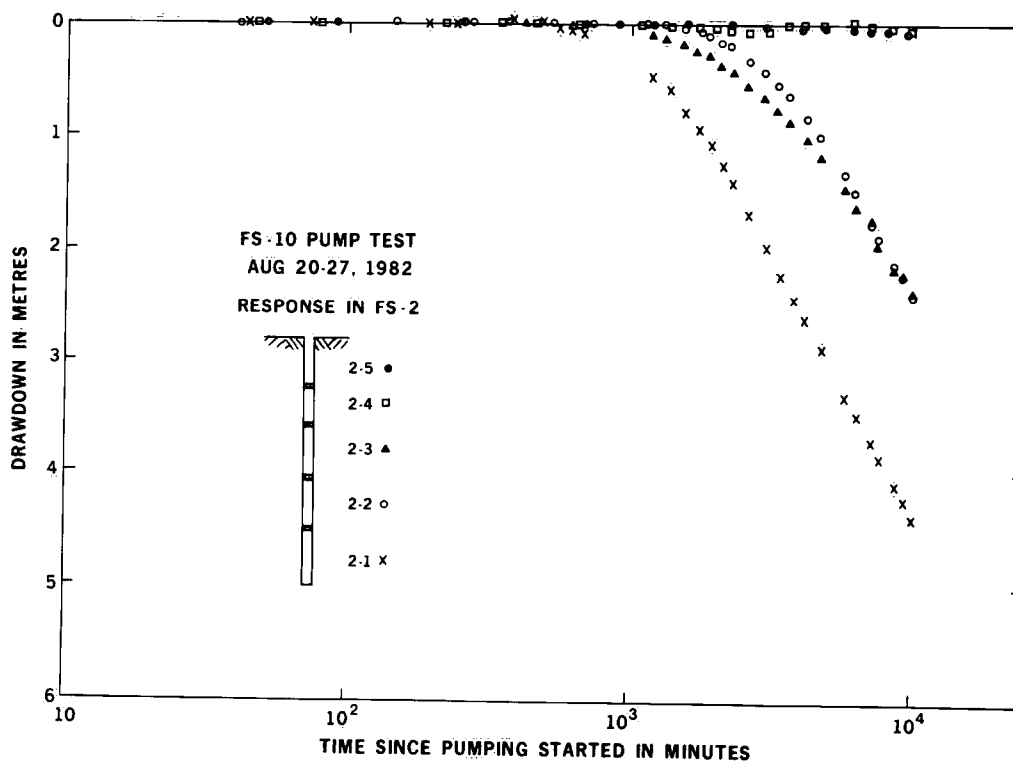
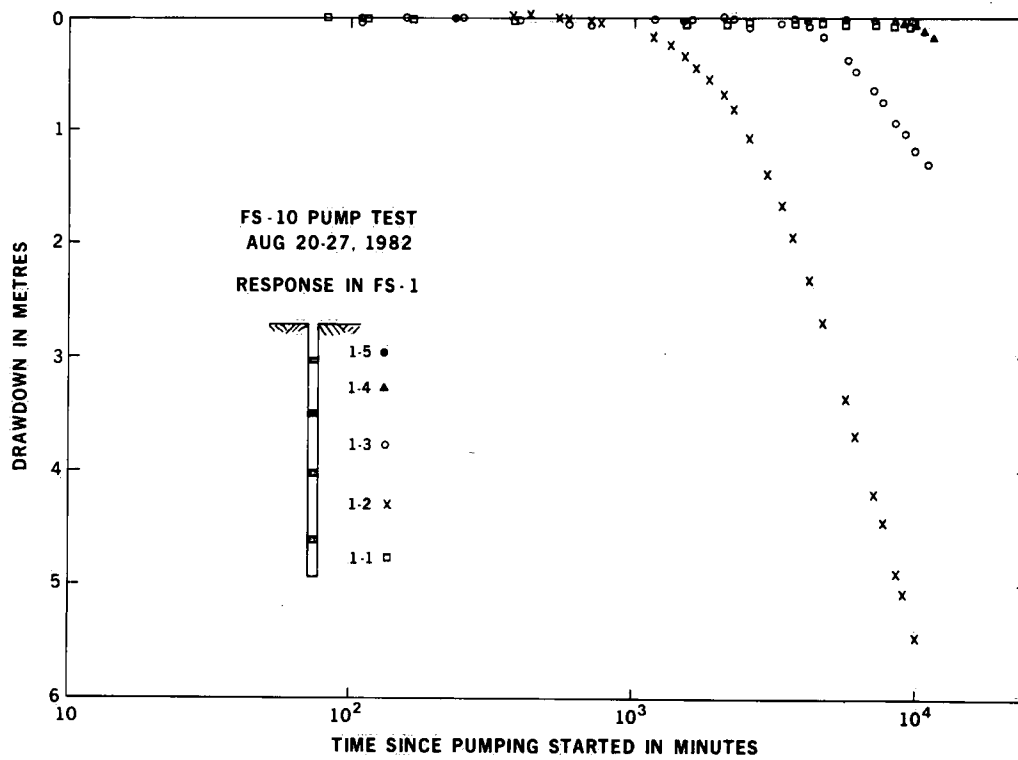
Table B-17. Injection Test Summary Borehole FS-17

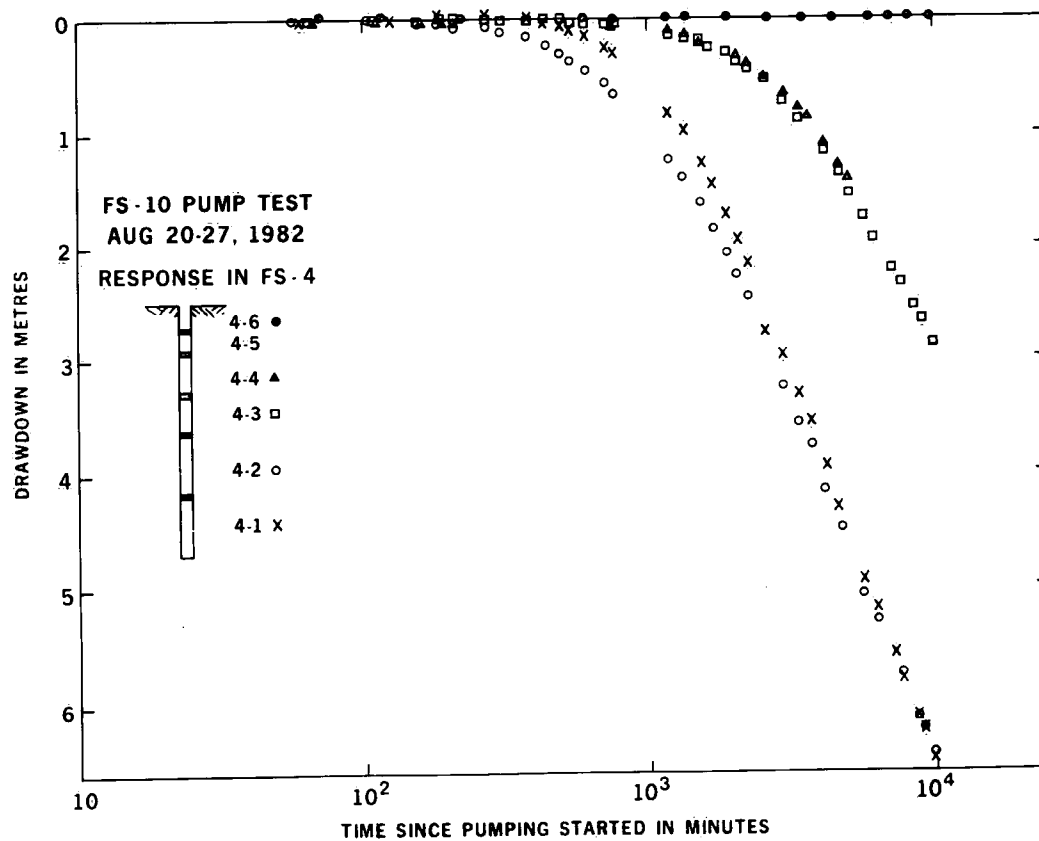
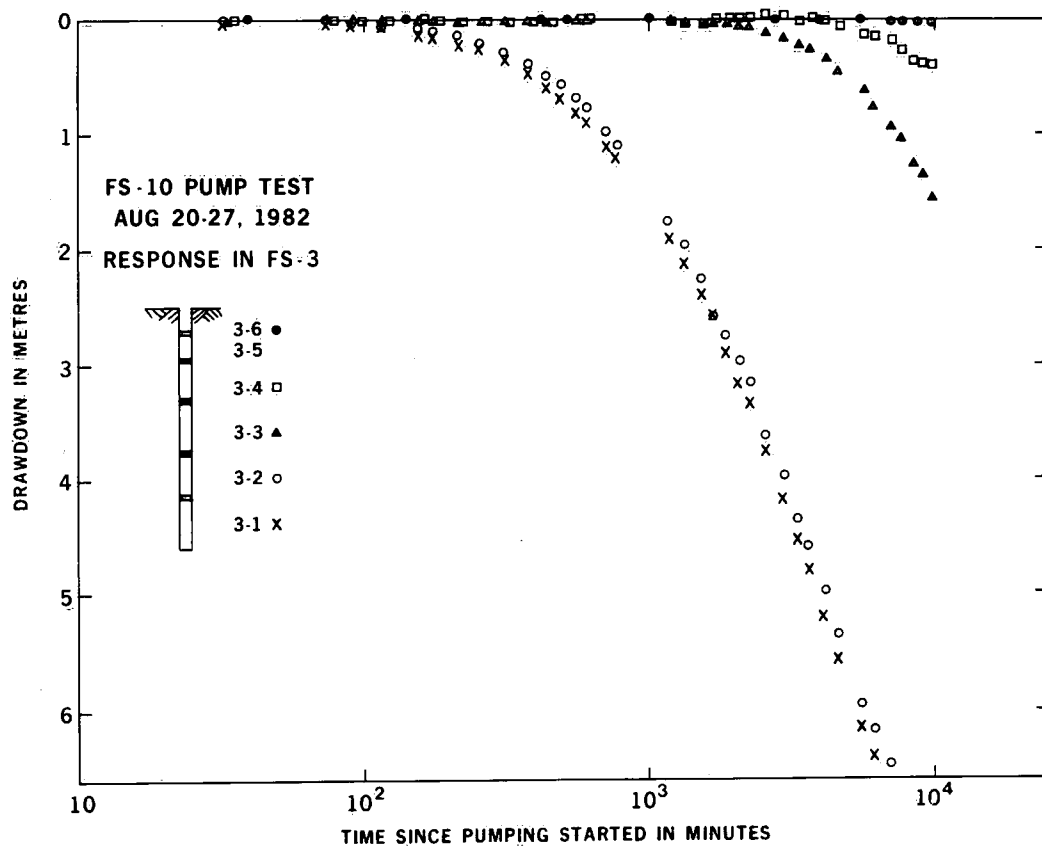
Depth of test interval (m B.C.T.*)	Injection head ΔH (m)	Flow rate Q ($m^3 \cdot s^{-1}$)	Flow rate per unit head $Q/\Delta H$ ($m^2 \cdot s^{-1}$)
8.38- 9.93	12.6	8.1×10^{-9}	6.4×10^{-10}
9.88-11.43	12.4	3.5×10^{-9}	2.8×10^{-10}
11.38-12.93	11.9	2.0×10^{-7}	1.7×10^{-8}
12.88-14.43	11.2	2.9×10^{-7}	2.6×10^{-8}
14.38-15.93	12.2	1.2×10^{-7}	9.5×10^{-9}
15.88-17.43	12.1	6.3×10^{-6}	5.2×10^{-7}
17.38-18.93	11.4	6.5×10^{-6}	5.7×10^{-7}
18.88-20.43	14.8	9.0×10^{-8}	6.1×10^{-9}
20.38-21.93	14.7	6.3×10^{-7}	4.3×10^{-8}
21.88-23.43	12.2	8.8×10^{-6}	7.1×10^{-7}
23.38-24.93	13.8	1.7×10^{-6}	1.2×10^{-7}
24.88-26.43	14.9	9.9×10^{-8}	6.6×10^{-9}
26.38-27.93	13.4	7.8×10^{-7}	5.8×10^{-8}
27.88-29.43	11.7	2.3×10^{-6}	1.9×10^{-7}
29.38-30.93	13.3	6.4×10^{-7}	4.8×10^{-8}
30.88-32.43	8.80	1.4×10^{-5}	1.6×10^{-6}
32.38-33.93	1.04	3.6×10^{-5}	3.4×10^{-5}
33.88-35.43	11.6	2.7×10^{-5}	2.3×10^{-6}
35.38-36.93	12.1	1.7×10^{-5}	1.4×10^{-6}
36.88-38.43	13.9	9.0×10^{-6}	6.5×10^{-7}
38.38-39.93	17.3	2.4×10^{-7}	1.4×10^{-8}
39.88-41.43	19.1	2.1×10^{-7}	1.1×10^{-8}
41.38-42.93	18.8	8.7×10^{-8}	4.6×10^{-9}
42.88-44.43	12.5	1.1×10^{-5}	9.2×10^{-7}
44.38-45.93	2.97	2.9×10^{-5}	9.9×10^{-6}
45.88-47.43	18.2	1.1×10^{-7}	6.0×10^{-9}
47.38-48.93	17.1	6.3×10^{-5}	3.7×10^{-7}
48.88-50.43	16.7	1.7×10^{-6}	9.9×10^{-8}
50.38-51.93	6.03	2.9×10^{-5}	4.9×10^{-6}
51.88-53.43	5.82	2.7×10^{-5}	4.6×10^{-6}
53.38-54.93	14.7	8.3×10^{-6}	5.6×10^{-7}
54.88-56.43	16.5	8.4×10^{-7}	5.1×10^{-8}
56.38-57.93	19.0	2.5×10^{-7}	1.3×10^{-8}
57.18-58.73	18.7	1.4×10^{-7}	7.3×10^{-9}

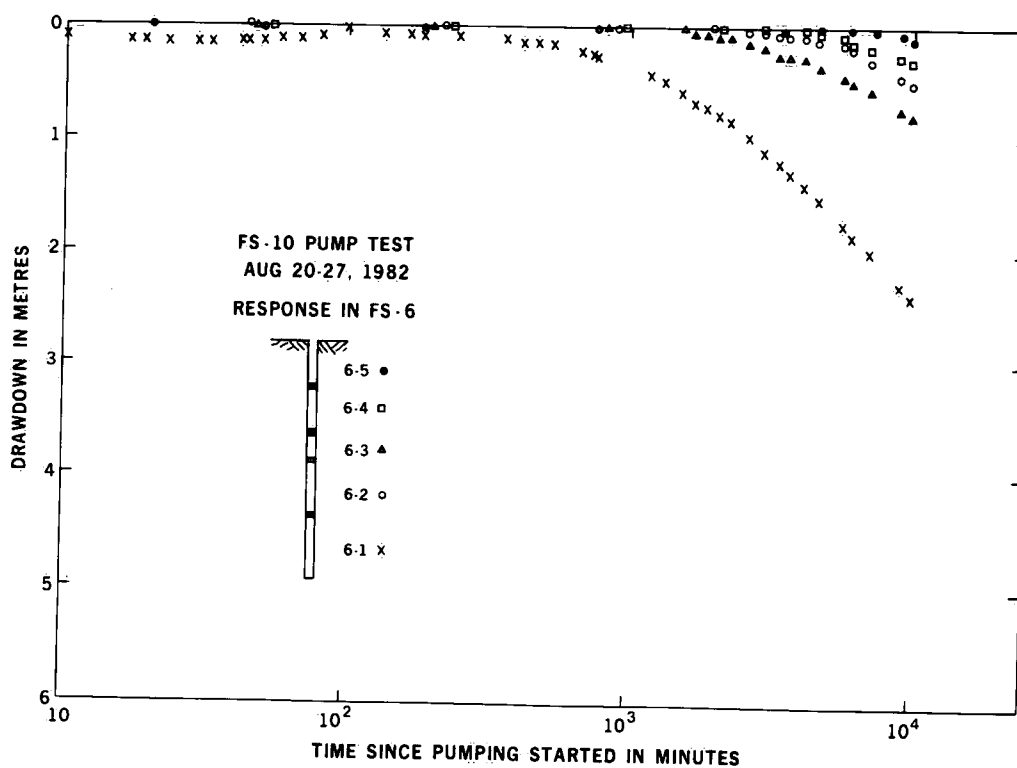
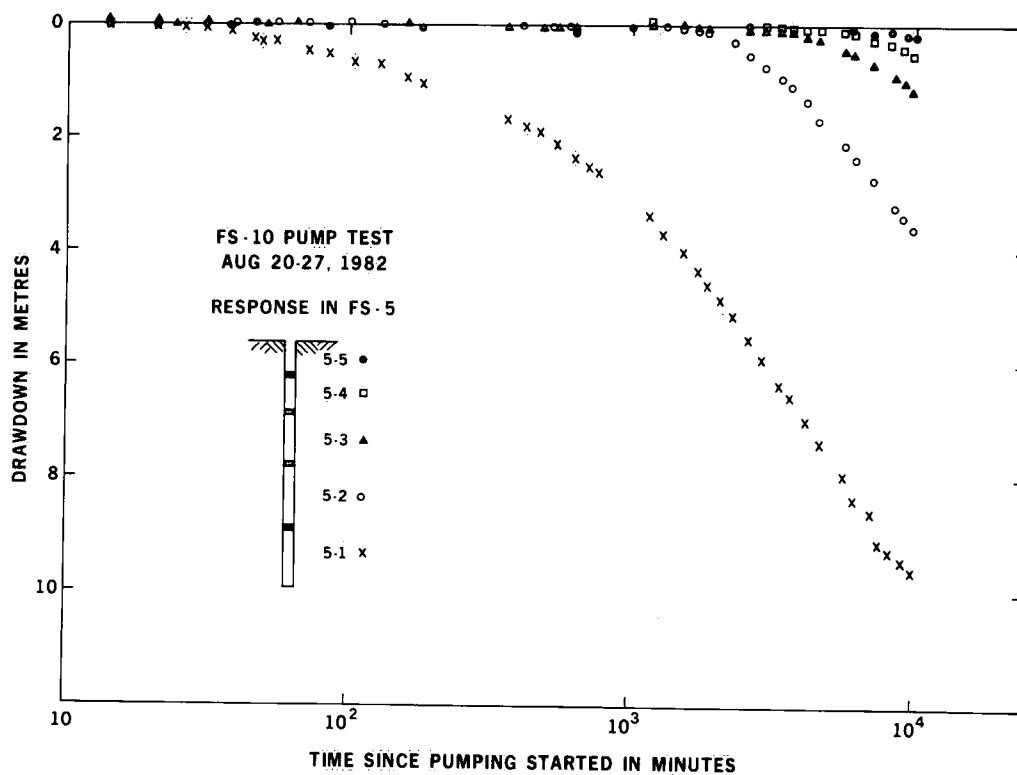
*Below casing top.

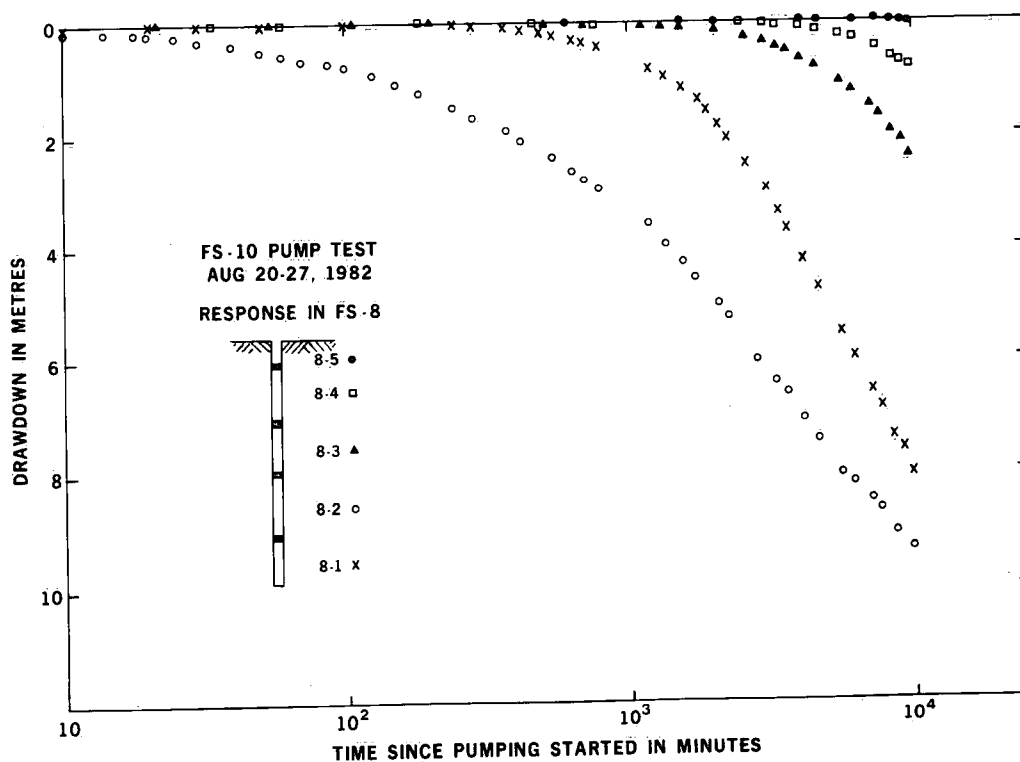
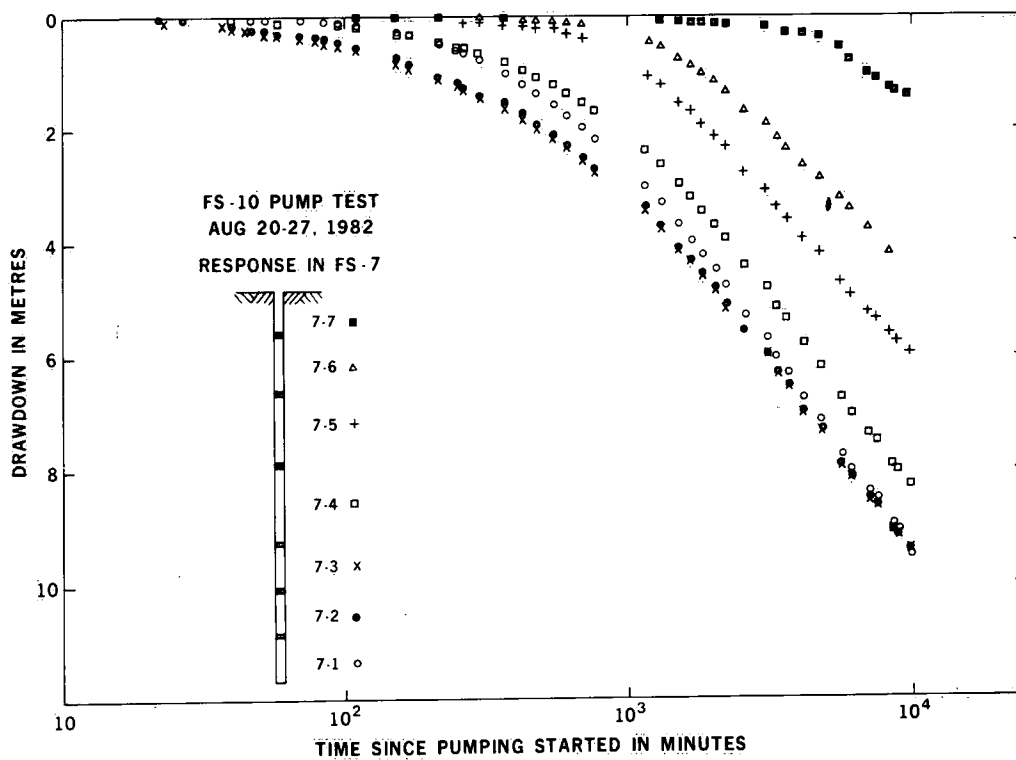
Appendix C contains plots of drawdown versus log time in response to pump tests of fracture zone No. 1 from borehole FS-10, August 20-27, 1982, and September 27-29, 1983.

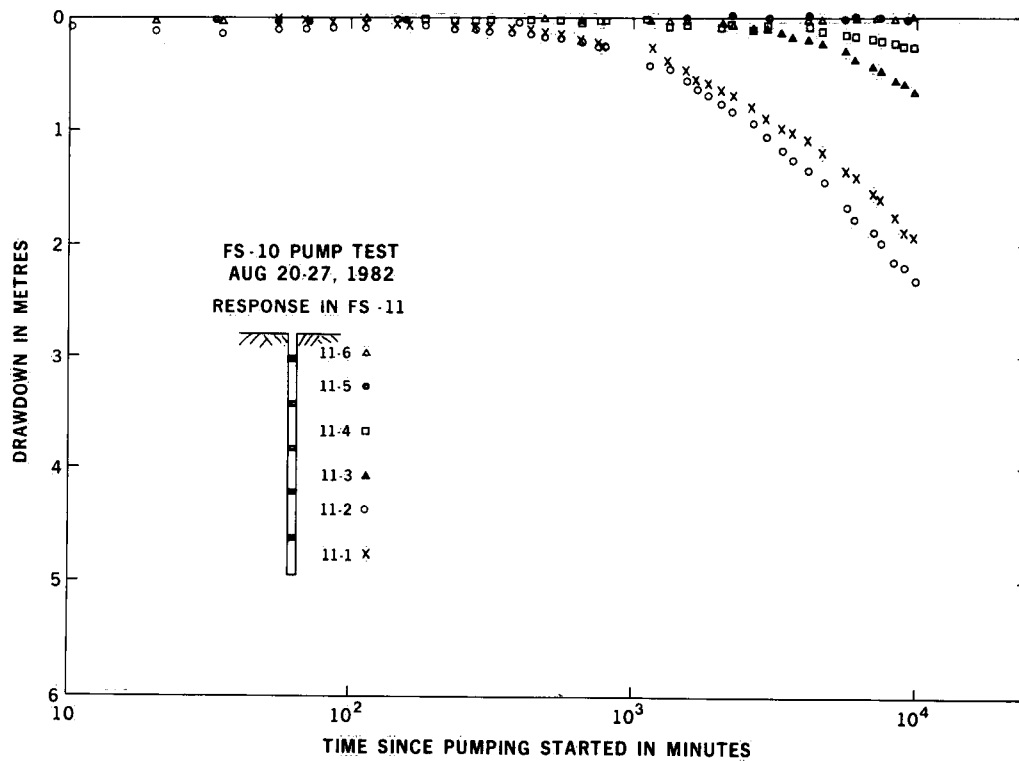
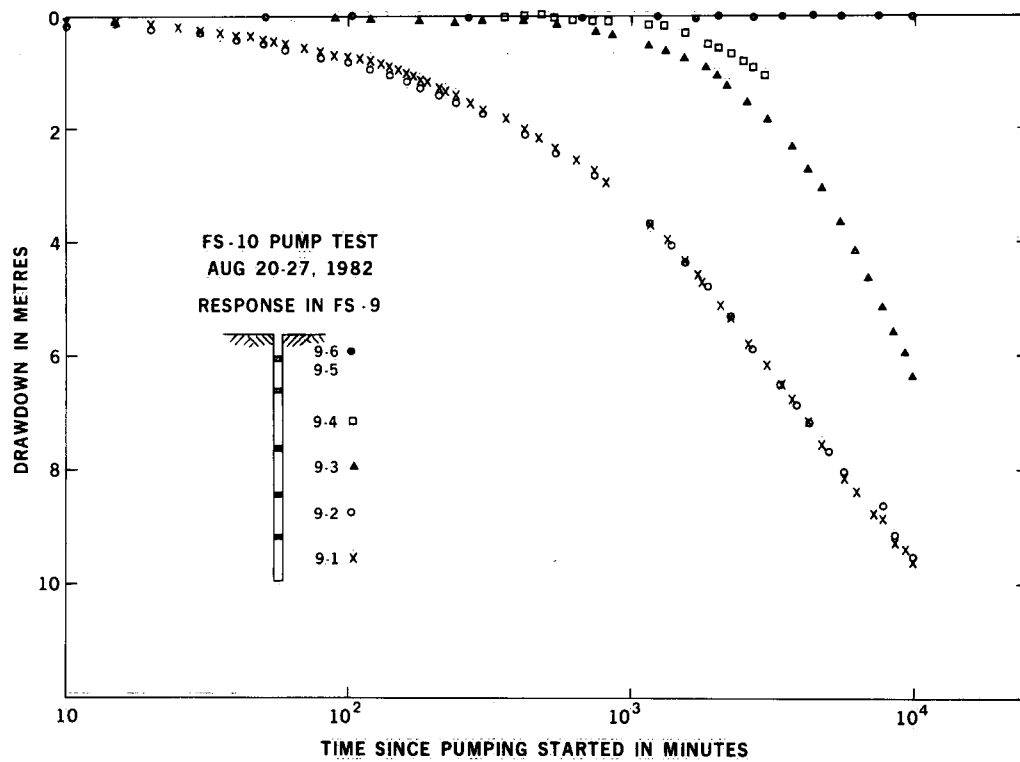
Appendix C
Plots of Drawdown Versus Log Time,
Borehole FS-10

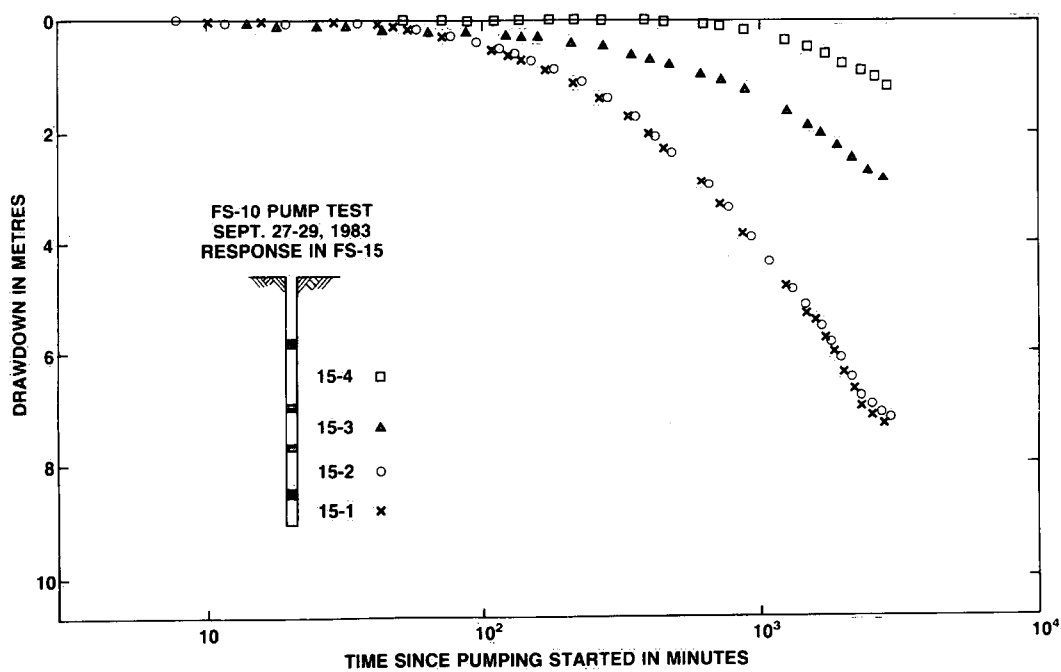
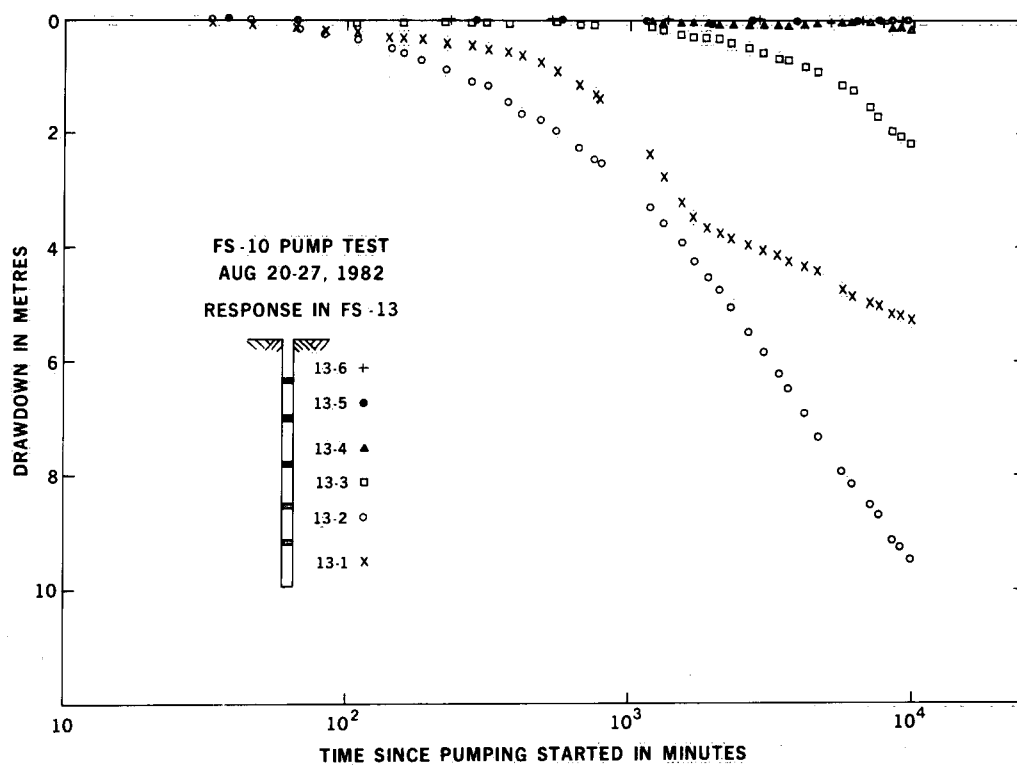


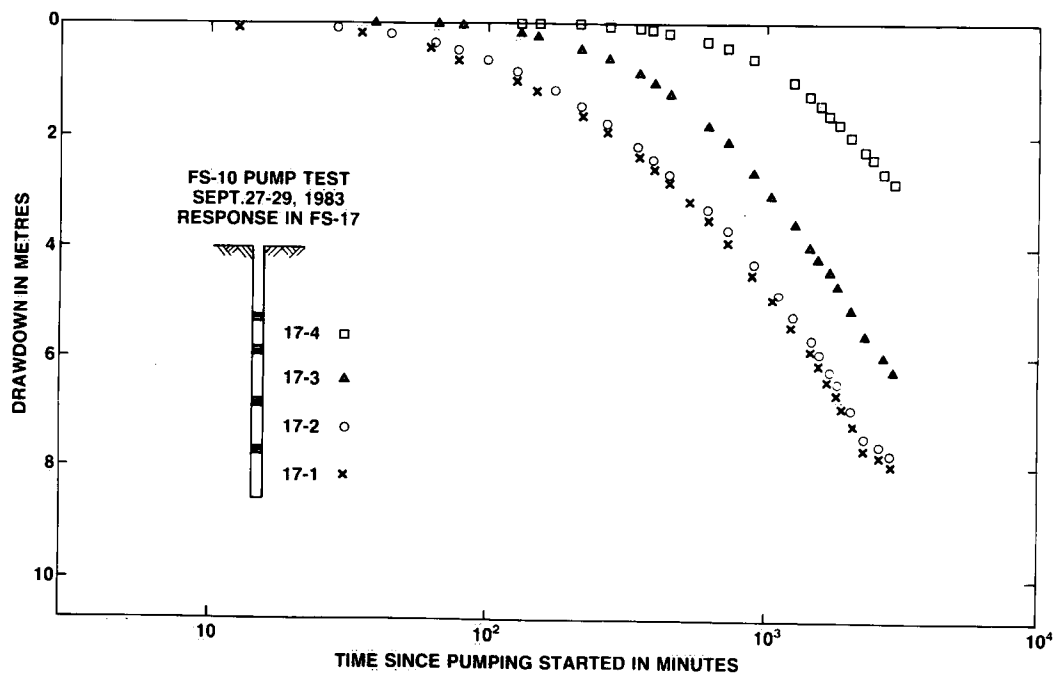
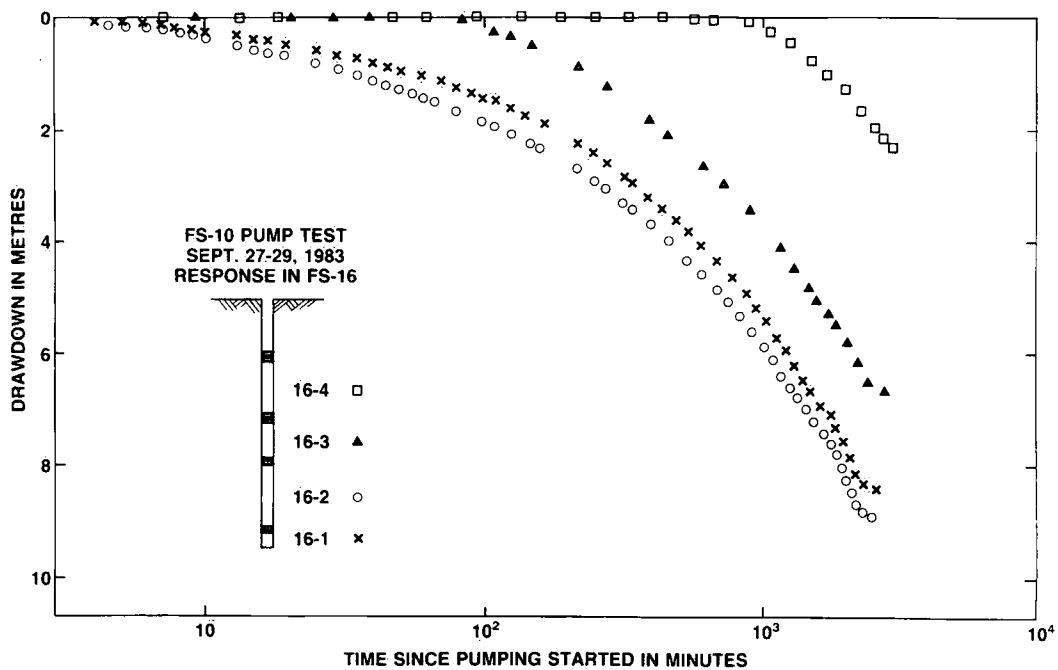












Appendix D contains hydraulic conductivity tensors determined for FS test intervals based on injection test data and borehole acoustic televiewer fracture logs.

Appendix D

Hydraulic Conductivity Tensors

Table D-1. Principal Hydraulic Conductivities and Principal Directions

Interval	K_1 ($\text{m}\cdot\text{s}^{-1}$)	Principal hydraulic conductivities and principal directions*					Geometric mean ($K_1 K_2$) ^{1/2} ($\text{m}\cdot\text{s}^{-1}$)	Anisotropy ratio K_1/K_3
		l_1^* m_1 n_1	K_2 ($\text{m}\cdot\text{s}^{-1}$)	l_2 m_2 n_2	K_3 ($\text{m}\cdot\text{s}^{-1}$)	l_3 m_3 n_3		
FS 1-1	1.1×10^{-10}	-0.157 -0.873 -0.462	1.1×10^{-10}	-0.883 -0.086 -0.462	4.0×10^{-14}	0.443 -0.480 -0.757	1.1×10^{-10}	2750.0
FS 1-2	1.5×10^{-9}	0.216 -0.933 -0.288	1.4×10^{-9}	0.591 0.359 -0.722	4.4×10^{-10}	0.777 -0.014 0.630	1.5×10^{-9}	3.4
FS 1-3	1.9×10^{-8}	0.308 -0.316 -0.897	1.8×10^{-8}	-0.040 -0.947 0.319	4.9×10^{-9}	0.950 0.063 0.305	1.9×10^{-8}	3.9
FS 1-4	3.3×10^{-9}	0.325 -0.834 -0.447	2.0×10^{-9}	-0.311 -0.540 0.782	1.7×10^{-9}	0.893 0.115 0.434	2.7×10^{-9}	1.9
FS 1-5	3.7×10^{-10}	-0.247 -0.599 0.762	3.2×10^{-10}	-0.410 -0.648 -0.642	6.0×10^{-11}	-0.878 0.471 0.086	3.5×10^{-10}	6.2
FS 2-1	4.3×10^{-10}	-0.022 -0.723 0.691	2.8×10^{-10}	0.718 0.470 0.514	1.7×10^{-10}	0.696 -0.507 -0.508	3.67×10^{-10}	2.5
FS 2-2	7.3×10^{-9}	-0.272 -0.317 -0.909	6.7×10^{-9}	-0.876 -0.310 0.370	9.3×10^{-10}	0.399 -0.896 0.193	7.0×10^{-9}	7.8
FS 2-3	1.4×10^{-7}	0.527 -0.705 -0.475	1.3×10^{-7}	-0.817 -0.574 -0.057	6.1×10^{-8}	0.232 -0.418 0.878	1.4×10^{-7}	2.3
FS 2-4	8.6×10^{-8}	-0.310 -0.917 -0.252	8.4×10^{-8}	-0.090 0.293 -0.952	5.8×10^{-9}	0.946 -0.273 -0.173	8.5×10^{-8}	14.8
FS 2-5	2.1×10^{-10}	0.123 -0.933 -0.399	1.5×10^{-10}	-0.992 -0.103 -0.077	8.1×10^{-11}	-0.037 -0.346 0.938	1.8×10^{-10}	2.6
FS 3-1	3.4×10^{-9}	-0.169 -0.973 0.155	2.5×10^{-9}	0.907 -0.093 0.411	1.6×10^{-9}	-0.385 0.210 0.899	3.0×10^{-9}	2.1
FS 3-2	2.3×10^{-8}	-0.273 0.418 -0.866	1.9×10^{-8}	-0.894 0.223 0.389	7.3×10^{-9}	-0.356 -0.881 -0.313	2.1×10^{-8}	3.2
FS 3-3	4.4×10^{-9}	-0.805 -0.379 0.133	4.1×10^{-9}	-0.055 -0.150 -0.987	4.4×10^{-10}	0.591 -0.801 0.089	4.3×10^{-9}	10.0
FS 3-4	2.2×10^{-9}	-0.787 -0.602 -0.135	1.6×10^{-9}	0.270 -0.140 -0.953	7.5×10^{-10}	0.554 -0.786 0.273	1.9×10^{-9}	2.9
FS 3-5	3.9×10^{-10}	0.095 0.243 -0.966	3.7×10^{-10}	-0.462 0.870 0.173	2.1×10^{-11}	-0.882 -0.429 -0.195	3.8×10^{-10}	18.6
FS 4-1	5.3×10^{-10}	0.290 0.644 -0.708	5.2×10^{-10}	-0.282 0.765 0.579	2.7×10^{-11}	-0.914 -0.032 -0.404	5.3×10^{-10}	20.

*Direction cosines relative to geographic reference axes.

Table D-1. Continued

Interval	K_1 ($\text{m}\cdot\text{s}^{-1}$)	Principal hydraulic conductivities and principal directions*					Geometric mean ($K_1 K_2$) ^{1/2} ($\text{m}\cdot\text{s}^{-1}$)	Anisotropy ratio K_1/K_3
		l_1^* m_1 n_1	K_2 ($\text{m}\cdot\text{s}^{-1}$)	l_2 m_2 n_2	K_3 ($\text{m}\cdot\text{s}^{-1}$)	l_3 m_3 n_3		
FS 4-2	1.9×10^{-7}	-0.982 -0.087 0.169	1.8×10^{-7}	-0.108 0.987 -0.118	3.1×10^{-8}	0.157 0.135 0.978	1.9×10^{-7}	6.1
FS 4-3	3.0×10^{-7}	-0.463 -0.773 0.435	2.9×10^{-7}	-0.858 0.515 0.002	1.7×10^{-8}	0.225 0.372 0.901	3.0×10^{-7}	18.0
FS 4-4	4.6×10^{-6}	0.871 0.352 -0.342	3.1×10^{-6}	-0.455 0.321 -0.830	1.7×10^{-6}	-0.183 0.879 0.440	3.9×10^{-6}	2.7
FS 5-1	1.7×10^{-7}	-0.716 -0.175 0.642	1.7×10^{-7}	-0.691 0.153 -0.706	9.6×10^{-9}	0.096 -0.949 -0.300	1.7×10^{-7}	18.0
FS 5-2	6.1×10^{-9}	-0.233 -0.278 0.932	5.0×10^{-9}	-0.496 -0.790 -0.360	1.8×10^{-9}	-0.836 0.546 -0.046	5.6×10^{-9}	3.4
FS 5-3	1.6×10^{-9}	-0.391 -0.822 0.415	1.4×10^{-9}	-0.393 -0.258 -0.882	4.0×10^{-10}	0.832 -0.508 -0.222	1.5×10^{-9}	4.0
FS 5-4	2.0×10^{-9}	-0.211 -0.977 -0.011	1.2×10^{-9}	0.839 -0.187 0.512	8.4×10^{-10}	-0.503 0.100 0.859	1.6×10^{-9}	2.4
FS 5-5	1.8×10^{-7}	-0.455 -0.849 0.269	1.6×10^{-7}	0.116 0.243 0.963	2.5×10^{-8}	-0.883 0.470 -0.012	1.7×10^{-7}	7.2
FS 6-1	6.1×10^{-6}	0.120 -0.163 0.979	5.5×10^{-6}	0.574 -0.794 -0.202	7.4×10^{-7}	-0.810 -0.586 0.002	5.8×10^{-6}	8.2
FS 6-2	1.7×10^{-9}	-0.225 0.691 -0.687	1.5×10^{-9}	0.098 0.718 0.689	3.2×10^{-10}	0.969 0.087 -0.230	1.6×10^{-9}	5.3
FS 6-3	4.5×10^{-8}	0.010 0.005 -0.999	4.1×10^{-8}	-0.180 0.984 0.004	4.2×10^{-9}	0.984 0.180 0.011	4.3×10^{-8}	10.0
FS 6-4	2.4×10^{-9}	-0.070 -0.975 0.212	2.0×10^{-9}	0.322 0.179 0.930	4.8×10^{-10}	-0.944 0.133 0.301	2.2×10^{-9}	5.0
FS 7-1	3.0×10^{-9}	-0.996 -0.058 0.061	1.9×10^{-9}	0.075 -0.281 0.957	1.3×10^{-9}	-0.039 0.958 0.284	2.5×10^{-9}	2.3
FS 7-2	1.4×10^{-8}	-0.496 0.830 -0.257	1.3×10^{-8}	-0.749 -0.258 0.611	1.2×10^{-9}	0.440 0.495 0.749	1.4×10^{-8}	12.0
FS 7-3	2.0×10^{-5}	-0.034 0.989 -0.146	2.0×10^{-5}	-0.775 0.066 0.629	1.0×10^{-7}	0.631 0.135 0.764	2.0×10^{-5}	200.0
FS 7-4	4.9×10^{-7}	0.076 0.670 -0.738	4.4×10^{-7}	-0.914 0.344 0.218	6.2×10^{-8}	-0.400 -0.658 -0.639	4.7×10^{-7}	8.1

Table D-1. Continued

Interval	K_1 ($\text{m}\cdot\text{s}^{-1}$)	Principal hydraulic conductivities and principal directions*					Geometric mean ($K_1 K_2$) ^{1/2} ($\text{m}\cdot\text{s}^{-1}$)	Anisotropy ratio K_1/K_3
		l_1^* m_1 n_1	K_2 ($\text{m}\cdot\text{s}^{-1}$)	l_2 m_2 n_2	K_3 ($\text{m}\cdot\text{s}^{-1}$)	l_3 m_3 n_3		
FS 7-5	5.4×10^{-9}	-0.109 -0.387 0.916	4.7×10^{-9}	-0.362 -0.842 -0.399	1.9×10^{-9}	-0.926 0.375 0.049	5.1×10^{-9}	2.8
FS 7-6	6.9×10^{-9}	-0.745 -0.667 -0.003	4.4×10^{-9}	0.667 -0.745 0.020	2.7×10^{-9}	-0.015 0.013 1.000	5.7×10^{-9}	2.6
FS 7-7	4.0×10^{-8}	-0.835 -0.534 0.134	4.0×10^{-8}	0.443 -0.795 -0.414	9.3×10^{-10}	0.328 -0.287 0.900	4.0×10^{-8}	43.0
FS 8-1	No televiewer data							
FS 8-2	4.2×10^{-5}	-0.076 0.992 0.103	4.1×10^{-5}	0.076 0.108 -0.991	1.4×10^{-6}	-0.994 -0.067 -0.084	4.2×10^{-5}	30.0
FS 8-3	1.2×10^{-8}	0.045 0.280 -0.959	1.2×10^{-8}	-0.183 0.946 0.268	4.7×10^{-10}	-0.982 -0.164 -0.094	1.2×10^{-8}	25.0
FS 8-4	3.1×10^{-9}	-0.209 0.955 -0.213	3.1×10^{-9}	0.171 -0.178 -0.969	4.3×10^{-11}	-0.963 -0.239 -0.126	3.1×10^{-9}	72.0
FS 9-1	4.1×10^{-8}	-0.214 -0.966 0.148	3.1×10^{-8}	0.919 -0.148 0.364	1.1×10^{-8}	-0.330 0.214 0.920	3.6×10^{-8}	3.7
FS 9-2	3.2×10^{-5}	-0.106 -0.984 0.146	1.9×10^{-5}	-0.198 -0.123 -0.973	1.4×10^{-5}	-0.975 0.132 0.182	2.5×10^{-5}	2.3
FS 9-3	5.9×10^{-9}	-0.075 0.886 -0.457	5.8×10^{-9}	0.507 -0.360 -0.783	3.1×10^{-10}	-0.858 -0.291 -0.423	5.9×10^{-9}	19.0
FS 9-4	1.0×10^{-8}	0.586 -0.687 0.430	7.6×10^{-9}	0.041 -0.505 -0.862	6.2×10^{-9}	-0.809 -0.523 0.268	8.7×10^{-9}	1.6
FS 10-1	3.5×10^{-6}	-0.079 -0.961 -0.266	2.5×10^{-6}	-0.996 0.085 -0.013	1.1×10^{-6}	-0.035 -0.264 0.964	3.0×10^{-6}	3.2
FS 10-2	1.6×10^{-9}	-0.605 0.445 -0.660	1.2×10^{-9}	-0.049 0.807 0.589	5.8×10^{-10}	-0.795 -0.389 0.466	1.4×10^{-9}	2.8
FS 10-3	2.3×10^{-9}	0.384 -0.254 0.888	2.2×10^{-9}	0.718 -0.523 -0.460	2.4×10^{-10}	-0.581 -0.814 0.019	2.3×10^{-9}	9.6
FS 10-4	7.6×10^{-10}	-0.563 0.826 0.023	7.0×10^{-10}	-0.449 -0.282 -0.848	7.4×10^{-11}	-0.695 -0.487 0.529	7.3×10^{-10}	10.0
FS 10-5	4.0×10^{-10}	-0.987 -0.119 -0.106	3.9×10^{-10}	0.061 0.336 -0.940	4.9×10^{-12}	0.148 -0.934 -0.325	4.0×10^{-10}	81.0

Table D-1. Continued

Interval	K_1 ($\text{m}\cdot\text{s}^{-1}$)	Principal hydraulic conductivities and principal directions*					Geometric mean ($K_1 K_2$) ^{1/2} ($\text{m}\cdot\text{s}^{-1}$)	Anisotropy ratio K_1/K_3
		l_1^* m_1 n_1	K_2 ($\text{m}\cdot\text{s}^{-1}$)	l_2 m_2 n_2	K_3 ($\text{m}\cdot\text{s}^{-1}$)	l_3 m_3 n_3		
FS 11-1	4.2×10^{-7}	-0.809 0.542 0.227	3.5×10^{-7}	-0.234 -0.652 0.722	9.4×10^{-8}	0.539 0.531 0.654	3.8×10^{-7}	4.5
FS 11-2	1.6×10^{-6}	-0.479 0.387 0.788	1.6×10^{-6}	0.505 -0.613 0.608	3.8×10^{-9}	-0.718 0.689 -0.099	1.6×10^{-6}	420.
FS 11-3	3.4×10^{-10}	-0.366 -0.894 -0.261	3.4×10^{-10}	-0.210 0.352 -0.912	4.3×10^{-12}	0.907 -0.279 -0.317	3.4×10^{-10}	79.0
FS 11-4	3.6×10^{-11}	-0.845 0.466 -0.262	3.4×10^{-11}	0.247 -0.094 -0.964	1.2×10^{-11}	-0.474 -0.880 -0.036	3.5×10^{-11}	3.0
FS 11-5	5.8×10^{-10}	0.402 -0.369 0.838	3.1×10^{-10}	0.024 -0.911 -0.412	2.9×10^{-10}	-0.916 -0.185 0.357	4.2×10^{-10}	2.0
FS 12-1	3.9×10^{-9}	-0.607 -0.468 0.643	3.5×10^{-9}	-0.530 -0.365 -0.766	1.5×10^{-9}	-0.593 0.805 0.027	3.7×10^{-9}	2.6
FS 12-2	1.3×10^{-9}	0.464 -0.836 -0.293	1.2×10^{-9}	-0.872 -0.490 0.018	1.5×10^{-10}	0.159 -0.247 0.956	1.3×10^{-9}	8.7
FS 12-3	3.8×10^{-9}	-0.122 -0.496 0.860	2.7×10^{-9}	-0.642 0.701 0.313	1.5×10^{-9}	0.757 0.514 0.403	3.2×10^{-9}	2.5
FS 12-4	7.2×10^{-9}	0.491 -0.177 -0.853	7.0×10^{-9}	-0.380 0.838 -0.393	2.1×10^{-9}	-0.784 -0.517 -0.344	7.1×10^{-9}	3.4
FS 13-1	5.7×10^{-7}	0.629 -0.368 0.685	4.3×10^{-7}	0.441 -0.556 -0.704	2.1×10^{-7}	-0.640 -0.745 0.188	5.0×10^{-7}	2.7
FS 13-2	2.4×10^{-8}	0.691 -0.419 0.589	1.7×10^{-8}	0.602 -0.118 -0.790	7.1×10^{-9}	-0.400 -0.900 -0.171	2.0×10^{-8}	3.4
FS 13-3	1.2×10^{-8}	-0.634 0.269 0.726	1.2×10^{-8}	0.668 -0.284 0.688	1.6×10^{-9}	-0.391 -0.920 -0.001	1.3×10^{-8}	8.1
FS 13-4	1.7×10^{-7}	0.484 0.182 -0.856	1.3×10^{-7}	-0.719 0.641 -0.270	6.9×10^{-8}	-0.500 -0.746 -0.441	1.5×10^{-7}	2.5
FS 13-5	6.6×10^{-9}	0.507 -0.268 -0.819	5.4×10^{-9}	-0.382 0.782 -0.492	1.3×10^{-9}	-0.773 -0.562 -0.294	6.0×10^{-9}	5.1
FS 14-1	9.1×10^{-12}	-0.203 0.706 -0.679	8.2×10^{-12}	0.090 0.704 0.705	1.4×10^{-12}	0.975 0.083 -0.206	8.7×10^{-12}	6.5
FS 14-2	6.5×10^{-11}	0.084 0.629 0.773	6.5×10^{-11}	0.203 -0.770 0.605	3.7×10^{-11}	-0.976 -0.106 0.192	6.5×10^{-11}	1.8

Table D-1. Concluded

Interval	K_1 ($\text{m}\cdot\text{s}^{-1}$)	Principal hydraulic conductivities and principal directions*					Geometric mean ($K_1 K_2$) ^{1/2} ($\text{m}\cdot\text{s}^{-1}$)	Anisotropy ratio K_1/K_3
		l_1^* m_1 n_1	K_2 ($\text{m}\cdot\text{s}^{-1}$)	l_2 m_2 n_2	K_3 ($\text{m}\cdot\text{s}^{-1}$)	l_3 m_3 n_3		
FS 14-3	1.7×10^{-8}	-0.088	1.5×10^{-8}	-0.451	2.6×10^{-9}	-0.888	1.6×10^{-8}	6.5
		0.258		0.851		-0.458		
		-0.962		0.269		-0.042		
FS 14-4	3.7×10^{-8}	0.059	3.1×10^{-8}	0.394	8.1×10^{-9}	-0.917	3.4×10^{-8}	4.6
		-0.128		-0.908		-0.399		
		0.990		-0.141		0.003		
FS 15-1	2.0×10^{-6}	0.775	1.7×10^{-6}	0.493	3.2×10^{-7}	-0.397	1.9×10^{-6}	6.3
		-0.355		-0.182		-0.917		
		0.524		-0.851		-0.034		
FS 15-2	5.2×10^{-8}	0.482	4.1×10^{-8}	-0.862	2.6×10^{-8}	-0.157	4.7×10^{-8}	2.0
		-0.840		-0.506		0.198		
		0.250		-0.037		0.968		
FS 15-3	4.5×10^{-7}	0.535	3.3×10^{-7}	0.273	3.0×10^{-7}	-0.799	3.9×10^{-7}	1.5
		-0.814		-0.085		-0.575		
		0.225		-0.958		-0.177		
FS 15-4	1.8×10^{-6}	0.247	1.5×10^{-6}	0.321	3.7×10^{-7}	-0.914	1.7×10^{-6}	4.9
		-0.729		-0.561		-0.394		
		0.639		-0.763		-0.096		
FS 15-5	1.7×10^{-8}	-0.083	1.4×10^{-8}	0.511	4.2×10^{-9}	-0.856	1.6×10^{-8}	4.1
		-0.986		0.085		0.147		
		0.147		0.855		0.497		
FS 16-1	6.6×10^{-6}	0.069	6.1×10^{-6}	-0.874	4.7×10^{-6}	0.481	6.4×10^{-6}	1.4
		0.956		-0.080		-0.281		
		0.284		0.479		0.831		
FS 16-2	2.0×10^{-7}	0.707	1.4×10^{-7}	-0.482	1.3×10^{-7}	0.517	1.7×10^{-7}	1.5
		-0.510		-0.855		-0.100		
		0.490		-0.193		-0.850		

Environment Canada Library, Burlington



3 9055 1017 2912 6

